THE UNIVERSITY *of* EDINBURGH

Measuring the self-interaction cross-section of dark matter with astronomical particle colliders

David Richard Harvey

A thesis submitted in fulfilment of the requirements
for the degree of Doctor of Philosophy
to the
University of Edinburgh
2014

Abstract

The dark matter paradigm has been a great source of speculation in both the 20th and 21st Centuries. Since its proposed existence in 1933, the mounting evidence has led to this theoretical particle becoming one of the greatest mysteries of modern physics. However, despite its dominant presence in the Universe, little is known about its nature and how it behaves. In this thesis I critically analyse one particular property of dark matter: the self-coupling.

The self-interacting dark matter paradigm hypothesises that dark matter is not collisionless as assumed in most cosmological simulations, and in-fact has some probability that it will scatter off itself. Such a self-coupling will resolve many discrepancies that exist between observations and theory, particularly on small, non-linear scales. Moreover, any detection of a self-interaction cross-section will place considerable limitations on the acceptable particle physics models of dark matter and hence has grown to become an important question.

In this thesis I develop and implement a method to constrain the self-interaction cross-section of dark matter that exploits continually accreting and merging groups of galaxies as they fall into galaxy clusters. Utilising the ubiquitous nature of accreting substructure, I measure the offsets between dark matter and baryonic gas as they become separated due to their differing interaction properties. Studying this effect over a sample of events, I will be able to make the first ever statistical estimate of the cross-section of dark matter, while averaging over many different unknown merging scenarios.

I begin my thesis by deriving an analytical description of sub-halo in-fall, allowing me to constrain dark matter self-interaction models directly from observations. In this study, I find that current archival data should be able to detect a difference in the dynamical behaviour of dark matter and standard model particles at 6σ, and measure the total interaction cross-section $\sigma_{\rm DM}/m$ with 68%

confidence limits of $\pm 1\,\mathrm{cm}^2\mathrm{g}^{-1}$.

Having constructed a new method to derive constraints on the cross-section of dark matter I carry out a study into the potential systematics that may affect a measurement. I determine the accuracy of weak gravitational lensing, which is the distortion of light due to intervening mass, as a tool to estimate the positions of substructure in galaxy clusters. I find that the public `Lenstool` software can measure the position of individual $1.5 \times 10^{13} M_{\odot}$ peaks with $\sim 0.3''$ systematic bias, as long as they are at least $\sim 30''$ from the cluster centre.

Finally, I develop a pipeline that can analyse a sample of inhomogeneous observations from *The Hubble Space Telescope* and the Chandra X-ray Observatory. By measuring the positions of dark matter, gas and galaxies for 68 individual merging events, from a total of 28 galaxy clusters, I detect a 7.4σ offset between gas and an unobserved dark mass. I make the first ever measurement of cross-section of dark matter from a sample of clusters finding $\sigma_{\mathrm{DM}} < 0.50\mathrm{cm}^2/\mathrm{g}$ [95% CL], the best constraints to date. In addition to this I find that the brightest group galaxy infact tends to lead the dark matter halo during merging events. Although evidence for the existence of interacting dark matter, I conclude that the astrophysics of the BCG is complicated, and that this apparent directional bias should be considered in all galaxy cluster analyses. Moreover, I show that this technique is easily extendable for future surveys that have larger samples of galaxy clusters, with constraints of $\sigma_{\mathrm{DM}} < 0.001\mathrm{cm}^2/\mathrm{g}$ potentially attainable.

Declaration

I hereby declare that my dissertation entitled *"Using astronomical particle colliders to constrain the self-interaction cross-section of dark matter"* is not substantially the same as any that I have submitted for a degree or diploma or other qualification at any other University. I further state that no part of my thesis has already been or is being concurrently submitted for any such degree, diploma or other qualification. This dissertation is the result of my own work and includes nothing which is the outcome of work done in collaboration, unless stated explicitly. Those parts of this dissertation which have been published, or are in press, are listed below:

- The work in chapter 4 draws on the published work in *'On the cross-section of dark matter using substructure infall into galaxy clusters'* with Eric Tittley, Richard Massery, Thomas Kitching, Andy Taylor, Simon Pike; Scott Kay, Erwin Lau and Daisuke Nagai, *MNRAS*, **441**, 404. The initial idea to extend the bulleticity idea was drawn up between myself and Richard Massey. The following framework was developed between myself, Andy Taylor, Eric Tittley and Tom Kitching. The simulations were run by an external group; Simon Pike and Scott Kay, from which we used the resulting data. The method to convert these into shear maps was developed by myself with aid of Richard Massey.

- The work in chapter 5 draws on the published work in *'Dark matter astrometry: accuracy of subhalo positions for the measurement of self-interaction cross-sections'*, with Richard Massey, Thomas Kitching, Andy Taylor, Eric Jullo, Jean-Paul Kneib, Eric Tittley and Philip Marshall, *MNRAS*, **433**, 151. The simulations were written and run by myself. Tom Kitching and Richard Massey helped in the complexities of the simulations

adding input for noise parameters. Phil Marshal was instrumental in coordinating with Eric Jullo and Jean-Paul Kneib to use LENSTOOL. LENSTOOL is a code that was written entirely by Phil Marshall, Eric Jullo and Jean-Paul Kneib.

- The work in chapter 6 draws on the submitted work in *'Astronomical Particle Colliders' submitted to Nature*, with Richard Massey, Thomas Kitching, Andy Taylor and Eric Tittley. The work for this Chapter was mainly carried out by myself. I developed the X-ray pipeline with aid from Eric Tittley. I constructed the HST ACS pipeline to reduce and drizzle images, using the online tools. The shape measurement algorithm, although in its raw nature was drawn from Richard Massey, I adapted this on my own to utilise for the sample in question. I constructed mass models, X-ray maps and optical maps for each cluster by myself. All authors contributed to the interpretation of the observations.

- The work in chapter A draws on the published work in *'Observing Dark Worlds: A crowdsourcing experiment for dark matter mapping* with Thomas Kitching, Joyce Noah-Vanhoucke, Ben Hamner, Tim Salimans and Ana Pires, *Astronomy & Computing*, **5**, 35. This work was a joint collaboration between my self and Tom Kitching. Although I analysed all the data and wrote the manuscript Tom Kitching was vital in the construction of the competition and the interpretation of the analysis. The other authors contributed to the construction and completetion of the competition, however had no real contribution to the analysis and publication.

David Harvey
Edinburgh
May 2014

Acknowledgements

There are a whole host of people that have contributed to my academic success and mental sanity over the last 3.5 years and to acknowledge them all here would require another thesis, so for those who I forget, please forgive me.

I would like to initially thank Andy Taylor, Tom Kitching, Eric Tittley and Richard Massey for the advice and support that they have given me. I want to specifically thank Tom (and Kaggle) for giving me the opportunity to take time out of my PhD and go to San Francisco for 3 months and Guy and Rowan Cavet for showing me incredible friendship and trust to take me in when I had nowhere to stay. It truly was one of the best times of my life. I also want to say a big thank you to Richard for his continual enthusiasm and excitement about this project. It truly did drive my enthusiasm even in the dark depths of second year. In addition to the silly number of advisors, I want to thank Eric Jullo, Catherine Heymanns, Alan Heavens and Jim Dunlop for continual advice and support throughout.

Working at the Observatory would have not been possible if it was't for the continual emotional support and terrible banter. I want to thank Paula Wilkie for providing endless crosswords at lunchtime, Victoria Bruce for mainly lifts home when I was too tired to walk (but also great support during job applications) and the rest of the team in my year, including Chris Duncan, Alex Mead, Rebecca Bowler and Sandy Rogers. I do want to say a specific thank you to Trevor Back and Jack Mayo for some, at times, awful chat, which gave a real break from the studies.

Aside from the Observatory, I must thank the "Square". Marco Petrucci who was definitely a better friend than landlord, Chris Swales for never reading any

of my papers, but for always calling and visiting just to abuse me. Jay Jonjo Harman, Rob Anderson, Matt Holroyd, Soupy, KP and #BonorCond you have provided some truly epic nights, and some even better times on the hockey pitch. I wouldn't have made it this far without them and the rest of EUHC.

I want to say a huge thank you to Tim Richardson who recently passed away. His enthusiasm made the change from Business to Physics so easy, and his advice, tutoring and passion for the subject inspired me to take on my PhD. Thank you.

I must mention my parents, if it wasn't for them I wouldn't have had the opportunity to do Physics, let alone a PhD in Astrophysics. The support, love, visits and money they have given me have been vital to my happiness.

Finally I want to thank Alice Hazelton for the love and support, for trekking up north and sticking with me. For reading work that you never cared about and for giving me the opportunity to follow my passion that is Astronomy.

To everyone, this has truly been a experience that I won't forget.

Thank you
David Harvey

Contents

Abstract i

Declaration iv

Acknowledgements vii

Contents x

List of figures xiv

List of tables xxv

1 Introduction for non-specialists 1
- 1.1 The big bang theory . . . 1
- 1.2 What is dark matter? . . . 2
- 1.3 Astronomical particle colliders . . . 3

2 Background Cosmology 5
- 2.1 Cosmology and the large scale structure . . . 7
  - 2.1.1 Universal geometry . . . 7
  - 2.1.2 The matter dominated universe . . . 9
  - 2.1.3 Cosmological distances . . . 11
  - 2.1.4 In the beginning . . . 16
  - 2.1.5 Separating the land from the sea . . . 18
  - 2.1.6 Letting the dry land appear . . . 19
  - 2.1.7 Precision cosmology . . . 23
- 2.2 Dark matter . . . 27
  - 2.2.1 Theories and candidates . . . 28
  - 2.2.2 Weakly Interacting Massive Particles . . . 28
  - 2.2.3 Detection . . . 34
- 2.3 Residual problems with the ΛCDM Universe . . . 39
  - 2.3.1 Self-Interacting Dark Matter . . . 40
  - 2.3.2 Bulleticity . . . 44

2.3.3 The differential cross-section 46
2.3.4 Scientific aims of this thesis 48

3 Gravitational Lensing 51
3.1 The basics of gravitational lensing 52
3.2 Observing gravitational lensing 56
3.3 Dark matter mass mapping 60
3.3.1 Direct inversion : Kaiser and Squires 62
3.3.2 Aperture mass 63

4 On the cross-section of dark matter 70
4.1 Dark matter in minor mergers 70
4.2 Methodology 75
4.2.1 Calibrating $\sigma_{\rm DM}/m$ with relative distances 76
4.2.2 A physical model of dark matter and gas infall 77
4.2.3 Instantaneous quasi-equilibrium 85
4.3 Applying the method to simulations 88
4.3.1 Hydrodynamical simulations of clusters 88
4.3.2 Component offsets in noise-free simulations 92
4.3.3 Robustness to astrophysical effects 97
4.3.4 Total matter vs. dark matter systematic bias? 98
4.4 Prospects for measuring signal with realistic noise 99
4.4.1 Signal as a function of cluster redshift 99
4.4.2 Noise in X-ray and Galaxy observations 101
4.4.3 Expected statistical precision 101
4.5 Conclusions 102

5 Accuracy of sub-halo positions in galaxy clusters 106
5.1 Dark matter astrometry 106
5.2 Methodology 108
5.2.1 Simulated shear fields 108
5.2.2 Mass reconstruction 114
5.3 Results 116
5.3.1 Accuracy as a function of distance from the cluster and mass fraction 124
5.3.2 Cluster member inclusion 126
5.4 Precision of lenstool 127
5.5 Discussion 128
5.6 Conclusions 130

6 Constraints on the self-interaction cross-section of dark matter 132
6.1 Constraining the cross-section of dark matter with 28 galaxy clusters 132
6.2 Data 133

6.3 Method . . . 134
6.3.1 X-ray analysis technique . . . 134
6.3.2 Weak Lensing Analysis . . . 136
6.3.3 Mass reconstruction . . . 142
6.3.4 Galaxy Distribution . . . 142
6.4 Results . . . 145
6.4.1 Individual Cluster Analysis . . . 147
6.4.2 Estimating errors in offsets . . . 179
6.4.3 Dark matter exists . . . 182
6.4.4 Removing line of sight projections with β . . . 183
6.4.5 Cross-Section . . . 185
6.5 Astrophysical Implications . . . 186
6.5.1 Interpretation 1: Self-Interacting Dark Matter . . . 188
6.5.2 Interpretation 2: Bias of the BGG . . . 189
6.5.3 Interpretation 3: Statistical Fluctuation . . . 189
6.5.4 Interpretation 4: Unknown Astrophysical Process . . . 189
6.6 Conclusions . . . 191

7 Conclusions & Future Work **193**

A Observing Dark Worlds:
A crowdsourcing experiment for dark matter mapping **199**
A.1 Introduction . . . 199
A.1.1 Standard approaches to dark matter reconstruction . . . 200
A.1.2 Expert citizen science . . . 201
A.2 Observing Dark Worlds . . . 203
A.2.1 The Competition . . . 203
A.2.2 The Data . . . 204
A.2.3 The Metric . . . 206
A.3 Results . . . 209
A.3.1 Metric Stability . . . 213
A.4 Successful Algorithms . . . 215
A.4.1 First place: Tim Salimans . . . 217
A.4.2 Second place: Iain Murray . . . 218
A.4.3 Third place: Ana Pires . . . 219
A.5 Implications for future competitions . . . 220
A.6 Conclusions . . . 221

Bibliography **223**

Publications **233**

List of Figures

1.1 How we are able to map out the dark matter in the Universe. The shear mass of dark matter heavily distorts space around the cluster, causing light rays passing close by to be bent. By measuring the apparent deformation of the background galaxies we can infer the distribution of dark matter in the galaxy cluster. 2

1.2 Colliding galaxy clusters are ideal laboratories to study the subtle properties of dark matter. Here, two galaxy clusters have passed through one another, causing the gas to separate from its associated dark matter cloud. The dark matter still remains coincident with the collisionless galaxies. By measuring the three different components of a galaxy cluster, I shall study the properties of dark matter in this thesis. 4

2.1 Using the Friedmann equation (equation (2.14)) it is possible to determine the affect of cosmological parameters on the age and fate of the Universe. Any total density greater than unity will result in the Universe coming together in 'the Big Crunch', and any open universe will continue to expand at an every increasing rate. . . . 12

2.2 The dimensionless proper angular diameter distances for different cosmologies. Since matter will bend the light as it travels through the Universe, the apparent size something is will depend on the matter content of the Universe at that redshift. In each case a flat universe is shown, with the black solid line showing a vacuum energy dominated, the blue dotted line showing a radiation dominated and the red dashed, a matter dominated universe. . . 14

2.3 Planck Power Spectrum. This show shows the coefficient of each angular multiple measured from the temperature fluctuations of the CMB. The resulting power spectrum can be used to extract cosmological parameters. 25

2.4 The merging cluster 1E0657-55, (Bullet Cluster). This is a typical example of a post-merging galaxy cluster. In the red is the hot X-ray emitting baryonic gas, and in the blue is the dark matter. It can be seen that during the merger the gas is shocked in to a bullet form, and the dark matter has separated from its associated gas. Clowe et al. (2006) find an 8σ offset between gas and an unobservable dark mass. 29
2.5 The WIMP is a heavily favoured candidate for dark matter. On the left hand y-axis is the comoving number density of dark matter particles, and on the right hand side is the resulting relic density today. These are being shown as a function of temperature of the Universe (bottom) and time (top). At early times, dark matter will have annihilated with itself until the expansion rate of the Universe exceeded the annihilation cross-section causing the number density to freeze out. If the annihilation cross-section was higher it would push the black line and shaded contours down. The black line here shows the annihilation cross-section that returns the correct relic density today with the yellow, green and blue contours representing annihilation cross-sections a factor of 10, 100 and 1000 different. (Feng, 2010) 31
2.6 A diagram to show the different ways dark matter can couple to standard model particles and to itself. Different terrestrial and space-based experiments are attempting to constrain the standard model coupling, however it is only possible to constrain the self-interaction cross-section via astronomical observations. (Livio & Silk, 2014) 35
2.7 A summary of all the current best direct detection experiments, with the lines showing the constraints set by the experiment in the event of a non-detection, and the shaded regions are the parts of the parameter space where the experiment has claimed a detection. Clearly, none of the claimed detection regions overlap, providing further evidence that these are false positives, and not a real detection. 37
2.8 The effect of two different scattering mechanisms on the distribution of dark matter. Each panel shows the same merging system, A520, with the blue showing the resulting distribution of interacting dark matter and the orange showing the resulting galaxy particle distribution (assumed collisionless). The top panel shows the 1D distribution of dark matter particles for a scattering mechanism that occurs rarely with large amounts of momentum exchange. The bottom panel shows the resulting 1D distribution of dark matter in the event it interacts often with small amounts of momentum exchange. 47

3.1 Typical geometry of a gravitational lens. 53

3.2 The effect of gravitational shear, γ on a circularly symmetric galaxy. A positive (negative) γ_1 corresponds to a stretching along the x (and y) axis, and positive (negative) γ_2 corresponds to a stretching along the 45° (135°). 56

3.3 The main effects on a galaxy image as it traverses the Universe. The initial galaxy, with some intrinsic ellipticity is sheared, the galaxy is then blurred by the point spread function of the telescope due to either abnormalities in the optics or the atmosphere, and then the image is pixelised and made noisy (Kitching et al., 2010). The aim is to reverse the observed effects to measure the initial shearing. 57

3.4 The results of a ray tracing simulation. Each tick mark represents the ellipticity of a galaxy caused by the background over density (white diffuse clouds). The correlated shapes of galaxies can be clearly seen at the over densities of matter. These correlated shapes can be used to map out the dark matter on large scales, extracting cosmological parameters, and on small to test the nature of dark matter (Jain et al., 2000). 61

3.5 Two methods to reconstruct the dark matter in the galaxy cluster 1E0657-55 (the Bullet Cluster). The top panel shows, in blue, the best fitting model as returned by LENSTOOL in units of projected mass density ($10^8 M_\odot$/arcsecond^2) and the lower panel, in green, is the result of the direct inversion (non-parametric) using the Kaiser Squires formalism, in units of dimensionless convergence from Clowe et al. (2006) (the white is the one, two and 3 σ contour regions of their best fitting position. It can be seen that although both methods return similar mass distributions, the Kaiser-Squires method is not a parametric fit. The white bar in the bottom panel represents 200kpc and both panels have the same scale. 68

4.1 Cartoon illustrating how I propose to use all three components of in-falling substructure. The vector from galaxies to gas defines an (approximate) direction of infall. Dark matter should lie some fraction along this vector, depending upon its interaction cross section. The observed positions will be noisy, so in practice I will measure the parallel and perpendicular vectors from galaxies to dark matter. If $\sigma_{\rm DM}$= 0, these should both average to zero. Throughout this chapter I adopt shorthand subscript notation G for gas, D for dark matter, I for the intersection point closest to the dark matter in the direction towards the gas, and S ("stars") for galaxies. 73

4.2 Generic behaviour of drag force acting on dark matter substructure, as a function of interaction cross-section. We propose an interpolation function between the two well-understood extremes based on optical depth. This function is essential to calibrate the observed behaviour of the DM against the behaviour of the gas. . 79

4.3 The gravitational force that an extended dark matter halo has on an extended gas halo (solid line) and galaxies (dashed line), as a function of their separation. In this particular case, I model the force on substructure gas (solid line) and stars (dashed line) due to substructure DM, using representative component sizes discussed in the text. The dashed vertical lines delineate the regimes set out in the text. 83

4.4 Hydrodynamical simulation of a galaxy cluster growing through minor mergers. The inset zooms into one piece of in-falling substructure. Blue shows the projected distribution of dark matter, red shows the standard model baryonic gas, and white shows galaxies. In this simulation, the dark matter is non-interacting, and therefore is expected to lie in the same place as the galaxies. However, there is a clear separation between in-falling substructure's galaxies and baryonic gas. 89

4.5 Projected offsets $d_{\rm SG}$ between galaxies and gas in substructure around 30 clusters in hydrodynamical simulations that include the effects of gas cooling, star formation, supernova feedback and AGN feedback. In each case the black points are the results from clusters at a redshift of 0 and the blue points are from haloes at a redshift of 0.6. The left panel shows the offset as a function of the projected distance from the cluster in units of r_{500}, the radius inside which the density is 500 times greater than the mean density in the Universe. The dashed lines show earlier predictions from MKN. The centre panel shows the offset as a function of the mass of the sub-halo (see equation 4.35). The right panel shows the offset as a function of its parent cluster mass, M_{500}, the total mass inside a sphere of radius r_{500}. Each point shows the weighted mean of offsets within that particular radial or mass bin, with the error bars representing the one-sigma error. 90

4.6 Projected offsets between substructure galaxies and the intersection point with DM in the direction towards the gas (SI) for $z = 0$ and $z = 0.6$. In real data, this distance will probe the finite cross-section of DM. Since the simulations explicitly use collisionless DM, I expect these offsets to be consistent with zero. Each point shows the weighted mean of offsets within that particular mass bin, with the error bars representing the one sigma error. 94

4.7 Projected, transverse offsets between DM and the intersection point (DI) for $z = 0$ and $z = 0.6$, which tests for potential systematics. Under the assumption that over an ensemble average there is no preferred in-fall direction and there is no systematic bias in the positional estimates of DM, this parameter should be consistent with zero. Each point shows the weighted mean of offsets within that particular mass bin, with the error bars representing the one-sigma error. 95

4.8 The observed offsets in substructure components appear broadly robust to astrophysical processes. The panels show the projected offsets $d_{\rm GI}$ between gas and dark matter (in the direction towards the galaxies) in substructure around 30 simulated clusters at $z = 0$ (left) and $z = 0.6$ (right), assuming different models of baryonic physics. Dashed lines show earlier predictions from MKN, for reference and ease of comparison. 96

4.9 Bias induced in measurements of $\beta_{\parallel}$ by assuming that gravitational lensing measures only DM (blue, diagonally down hatching), rather that the total mass (red, diagonally up hatching). This is *an order of magnitude below* the expected statistical precision for 30 clusters. We can only detect this systematic effect in the *noise-free* simulations – note the change of scale on the horizontal-axis is compared to Figure 4.10. Only in very large, future surveys, will it be necessary to simultaneously fit (and subtract) the mass in the other substructure components. 100

4.10 Potential constraints on $\beta_{\parallel}$ from a sample of 60 minor mergers in the presence of realistic observational noise. Hatched regions show the integrated 68% confidence limits. The different colours show expected constraints if the clusters were all at redshift $z_{\rm lens} = 0.2$, 0.4 or 0.6, where the tall Gaussian with diagonally down hatching is $z = 0.2$, the middle peak with diagonally upward hatching is $z = 0.4$, and the smallest peak with diagonally downward hatching is $z = 0.6$. We have explicitly removed all redshift-dependence of the physical signal; the changing errors here are due to the apparent angular size and the lensing geometry at different distances from the observer. All the distributions are consistent with zero, as expected from the collisionless dark matter used in the simulations. 104

4.11 Potential constraints on the self-interaction cross-section of DM $\sigma_{\rm DM}/m$ from a sample of 60 minor mergers in the presence of realistic observational noise. Hatched regions show the integrated 68% confidence limits, where the tall Gaussian with diagonally down hatching is $z = 0.2$, the middle peak with diagonally upward hatching is $z = 0.4$, and the smallest peak with diagonally downward hatching is $z = 0.6$.. This is a propagation of Figure 4.10 using equation 4.9, assuming $\sigma^\star/m = 4.5\pi\,{\rm cm}^2{\rm g}^{-1}$. For clusters at redshift $z = 0.2$ the constraints are much tighter implying potentially a limit of $< 1{\rm cm}^2{\rm g}^{-1}$ to 68% confidence. 105

5.1 The reduced shear signal of a simulated cluster with a NFW profile. The main halo has a M_{200} of $8 \times 10^{14} M_\odot$ and is positioned at (0,0) and the sub-halo, $8 \times 10^{13} M_\odot$, is positioned at (0,49). The field of view represents that of a Hubble Space telescope Advanced Camera for Surveys with a typical density of galaxies of 80/square arc minute. The circles are a guide for where they are placed and have no physical significance. 109

5.2 Main halo positional estimates 117

5.3 Sub-halo positional estimates 117

5.4 The likelihood surface for the main (top) and sub (bottom) halo positions in the case of zero noise (gravitational shear only). The binned histograms show the true posteriors and their maximum likelihoods as the solid line. The dotted line is the true position. The left hand panels are the position in the radial direction and the right hand panels are tangential direction. In the case of no noise the likelihood surface derived from LENSTOOL exhibits no bias around the maximum likelihood. 117

5.5 **Intrinsic ellipticities only**: The left and right hand panel show the positional estimates of the main and sub-halo respectively. In this initial test the background galaxies only contained a Gaussian intrinsic ellipticity distribution. The mass of the respective haloes are shown, in all cases the sub-halo was 10 times less massive than the main halo. (So results at $8 \times 10^{14} M_\odot$ main halo in the left hand panel are from the same simulation as those shown at $8 \times 10^{13} M_\odot$ in the right hand panel). A variety of configurations were tested with the cartoon inset showing the setup in each case. For each configuration, 100 noise realisations were run at the mass scale, the position of each halo estimated and then averaged over the all configurations. (so each point reflects 400 averaged simulations). 118

5.6 **Intrinsic ellipticities and shape measurement bias**: The left and right hand panel are the positional estimates of the main and sub-halo respectively. In each case the mass is given and the main halo is 10 times more massive than the sub-halo. The main halo is elliptical and the background galaxies have shape measurement bias and intrinsic ellipticities. In this case 100 realisations were run and the average position at each mass scale calculated. 119

5.7 **Intrinsic ellipticities, shape measurement bias and source galaxy redshift distribution**: The left and right hand panel are the positional estimates of the main and sub-halo respectively. In each case the mass is given and the main halo is 10 times more massive than the sub-halo. The main halo is elliptical and the background galaxies have shape measurement bias, a distribution in their redshift and intrinsic ellipticities. In this case 100 realisations were run and the average position at each mass scale calculated. 120

5.8 **Dual sub-halo simulation, with intrinsic ellipticities, shear measurement bias and source galaxy redshift distribution**: The top left panel shows the positional estimates of the main halo, the top right the estimates of *sub-halo 1* and the bottom panel gives the estimates of *sub-halo 2*. The masses of the haloes are given. In each case the sub-haloes are 10 times smaller in mass (so they are equal size) than the main halo. The background galaxies have intrinsic ellipticities, shape measurement bias and a redshift distribution. The plots show 3 different configurations (given by the dashed circles). In each case *sub-halo 1* is kept in the same place as shown in the cartoon inset, and for each of the 3 scenarios *sub-halo 2* is positioned as shown. In each scenario 100 noise realisations are run and the positions averaged over all configurations and noise realisations. 121

5.9 **Simulated SIE haloes, with intrinsic ellipticities, source galaxy redshift distribution and shape measurement bias**: The left hand panel and right hand panel show the main and sub-halo positional estimates respectively. In this scenario a SIE profile is simulated and NFW fitted imitating profile misidentification in real data. The main halo is always 10 times larger than the sub-halo, and the source galaxies have shape measurement bias, intrinsic ellipticities and a redshift distribution. 100 noise realisations were run and the average position estimated in each case. 122

5.10 **Weak lensing accuracy as a function of the radial position from the cluster and mass fraction ($M_{\rm sub}/M_{\rm main}$).** In each case the background galaxies have intrinsic ellipticities, redshift distribution and shape measurement bias. The first two panels (main and sub-halo respectively) show an $8 \times 10^{13} M_{\odot}$ cluster (with associated 10 times large parent halo), simulated at various distances from the main halo. The catastrophic failure at $< 30''$ is due to the sub-halo position overlapping with the parent halo. The second two panels show the positional estimates of a main halo of 8×10^{14} and sub-halo with an increasing sub-halo mass (decreasing ratio). It is shown that the bias is mass fraction independent and is robust to minor mergers as well as substructure infall. 125

5.11 Main (top) and Sub (bottom panel) position as function of cluster member contamination expressed as a percentage of the total background galaxy number. 126

5.12 1 The error in the mean position for various sample sizes. In order to detect an overall offset between baryonic and dark matter the error in the mean of the sample size needs to be less than the expected signal. For clusters at redshift $z = 0.6$, the bulleticity is $\sim 2''$, and for a redshift $z = 0.3$ this increases to $3.5''$. A sample of ~ 50 offsets should yield a significant detection of bulleticity, and LENSTOOL can measure these offsets with subdominant systematic bias. 128

6.1 The redshift distribution of the clusters used in this work. 134

6.2 An example PSF model that is implemented at the *Wavdetect* stage. The image shows a combined exposure map weighted PSF map stacked for the various observations of the cluster A520. . . 137

6.3 The distribution of best fitting focus positions for the acquired HST observations. Each colour represents the distribution of best fitting focus positions for each cluster over the various observations. To determine the best fitting focus position the ellipticity of the stars was compared to that of the Tiny Tim model for the given filter. 140

6.4 An example of the PSF model for the cluster MACSJ0416. Each mark shows the position of an object returned by SEXTRACTOR. Not all of these objects are galaxies and have sufficient exposures, therefore many of the objects will not be in the final shear catalogue. Each tick mark shows the ellipticity of the PSF at that position in the field. Many more objects are found in the edges since there are less exposures and hence higher noise. 141

6.5 A comparison between the measured shears for the cluster A3827 in the F814W and the F606W ACS filter. 143

6.6 Illustration of how I propose to use all three components of infalling substructure, with the sign of each vector shown with the potential centroid of the measured dark matter. The vector, $\delta_{\rm SG}$, from galaxies (green) to gas (red) defines our coordinate system and the assumed direction of infall. This is always positive. Theoretically, dark matter should lie some fraction along this vector, depending upon its interaction cross section. However, the observed position will be noisy, so in practice I will measure the parallel, $\delta_{\rm SI}$, and perpendicular, $\delta_{\rm DI}$, vectors from galaxies to dark matter (blue). In the event that for an individual system I measure the dark matter position to be in front of the galaxies and be above the vector, $\delta_{\rm SG}$, then $\delta_{\rm SI}$ will be negative and $\delta_{\rm DI}$ shall be positive. The diagram shows how the sign for each of these vectors change with each potential position of dark matter. 146
6.7 1E0657 149
6.8 A1758 150
6.9 A2163 151
6.10 A2744 152
6.11 A370 153
6.12 A3827 154
6.13 A520 155
6.14 A781 156
6.15 DLSCLJ0916 157
6.16 El Gordo 158
6.17 MACSJ0025 159
6.18 MACSJ0152 160
6.19 MACSJ0358 161
6.20 MACSJ0416 162
6.21 MACSJ0417 163
6.22 MACSJ0553 164
6.23 MACSJ0717 165
6.24 MACSJ0911 166
6.25 MACSJ1006 167
6.26 MACSJ1226 168
6.27 MACSJ1354 169
6.28 MACSJ1731 170
6.29 MACSJ2243 171
6.30 MS1054 172
6.31 RXCJ0105 173
6.32 RXCJ0638 174
6.33 RXJ1000 175
6.34 SPTCL2332 176
6.35 ZWCL1234 177

6.36 ZWCL1358 178

6.37 An overview of the 68 extracted merging haloes. In each case I show the magnitude separation between galaxies and gas, $\delta_{\rm SG}$, and associated error in red, and the separation of the dark matter with respect to the galaxies, projected onto the SG vector, $\delta_{\rm SI}$ and associated error in blue. The error bars show the locally estimated errors. 180

6.38 The distribution of each mass offset from the previous figure, binned to show overall distributions. From the top panel down, the panels show the distribution of $\delta_{\rm DI}$, $\delta_{\rm SI}$, $\delta_{\rm GI}$ and then finally $\delta_{\rm SG}$. The important panel here is the second panel as any noticeable offset will be evidence for interacting dark matter. The different colours represent the different proxies for the galaxy distribution. In green is the flux weighted number density. the red is the number weighted density and the blue is the BGG proxy. 181

6.39 The expected bias on β caused by the gas halo shifting the estimated lensing peak, as a function of the distance the gas peak from the dark matter peak. 184

6.40 The probability distribution of β. Green represents the estimate using the flux weighted sample of galaxies, the red the number density and the blue to BGG. I observe a slight tendency for the dark matter to be offset from the BGG at the 1.8σ confidence level. 184

6.41 Here I test the affect of $\sigma^*_{\rm DM}$, on the estimation of the cross-section of dark matter. The top panel shows the corresponding values of $\sigma^*_{\rm DM}$ for different halo masses assuming a mass - concentration relation. The bottom panel shows how a few of those values affect the estimation of the cross-section. I find that the effect is not significant, and sub-dominant to the statistical error. For the final estimation I therefore use a value of $\sigma^*_{\rm DM} = 6.5{\rm cm}^2/{\rm g}$, corresponding to $M = 10^{14} M_\odot$. 187

6.42 The PDFs for the cross-section of dark matter assuming $\sigma^*_{\rm DM} = 6.5{\rm cm}^2/{\rm g}$. The green represents the PDF using the flux weighted estimator for the galaxy distribution, the red shows the PDF of the number density estimator and blue, the brightest group galaxy estimator. 188

6.43 It seems that the two estimations of the distribution of galaxies is coincident with the dark matter, however the BGG seems to be slightly offset from the dark matter, with the non-baryonic component lagging behind the galaxy implying some non-zero dark matter cross-section. 190

A.1 An example of one of the training skies given to the participants. Here there are three haloes, with these positions shown by the red triangles. The black tick marks show the ellipticity and positions of each galaxy in the field. 207
A.2 The angular, G metric. ϕ was calculated as the angle between the the vector joining the true and users predicted position and the vector joining the centre of mass of the system (reference point) and the true position. 208
A.3 The figure shows the score of the top 150 competitors normalised to the score of LENSTOOL for easy direct comparison (where LENSTOOL = 1.0) as a function of the participants final leaderboard rank. The blue points refer to the total score of the competitor and the red the radial part. The scores have been sorted and therefore the points in the radial do not directly correspond to the points in the blue. 210
A.4 Timeline for the improvement of the best scoring algorithm. Initially, a significant amount of progress is made, however towards the end, progress plateaus with few and small incremental improvements. Although typical, this competition saw more more regular improvements than typical machine learning problems. . . 211
A.5 The figure shows the average score of the top 150 competitors radial score as a function of various competition parameters. We see that there is a trend with respect to the mass of the halo, showing that estimates are more uncertain with decreasing mass. Below $10^{14} M_{\odot}$, estimates seem to be extremely varied, and in order to constrain this trend further, we would require more estimates of haloes of that mass. Also the top right panel shows how more SIS haloes were constrained to within $15''$ than NFW. 212
A.6 The red points are the best radial position of each halo for the top 150 competitors. The first panel shows the results of the main halo in each case, and the second two panels, the sub halo. The blue stars in each case represent the winner's (Tim Saliman's) estimated positions. One can clearly see that the points are much more clustered for the main halo. 213
A.7 The Figure shows the radial distance the top three competitors and LENSTOOL estimates are from the true position in arcseconds. The submissions have been binned by mass, and the error bars are the error in the mean of the radial distances in the mass bin. . . . 214
A.8 The score of a random sample of fake entries; 1000 fake submissions with random guesses were scored. This uncertainty on the metric led to less efficient feedback from the leaderboard given to participants. 215

List of Tables

2.1 Cosmological parameters derived from the Planck observations (Planck Collaboration et al., 2013a). 26
2.2 Current constraints on the self-interacting cross-section of dark matter with associated potential problems (Bradač, 2013, Durham Ripples Conference) 43
2.3 Angular Dependence of different scattering mechanisms 49

5.1 Input values and priors used during the reconstruction on the main and sub-halo in the simulations. The values in the square brackets refer to the range, and the dots refer to the different mass scales of the simulations. 111

6.1 Sample of galaxy clusters used in the study. The position in right ascension (RA) and declination (DEC) are given in degrees, followed by the redshift (z), the ACS filter used for the optical imaging, and finally the total exposure time for both the X-ray and the optical. 135
6.2 Mean results from initial analysis using flux 186

A.1 The parameters used for the data sets provided for the "Observing Dark Worlds" competition. 206

1 Introduction for non-specialists

"Men intrinsically do not trust new things that they have not experienced themselves."

1.1 The big bang theory

14 billion years ago the Universe underwent a period of rapid expansion known as inflation. In a fraction of a second it changed from a billion billion billion billion times smaller than the width of a hair to the size we see today. From this moment onwards, the Universe has been getting bigger and expanding at an ever-increasing rate. The end of inflation signalled the beginning of 'cosmology', with the Universe growing and evolving to become the zoo of galaxies and other objects observed today. This evolution has been governed by the various forms of energy in the Universe; photons (small bundles of light), which dominated how objects grew in the early stages of the Universe, matter (e.g. protons, neutrons, dark matter), which dominated the behaviour of structures at intermediate times, and now; an unknown, evocatively named 'dark energy' which dominates the Universe today. In astronomy, Dark energy is a particularly enigmatic problem as it appears to have a strange property; that it has negative pressure, a kind

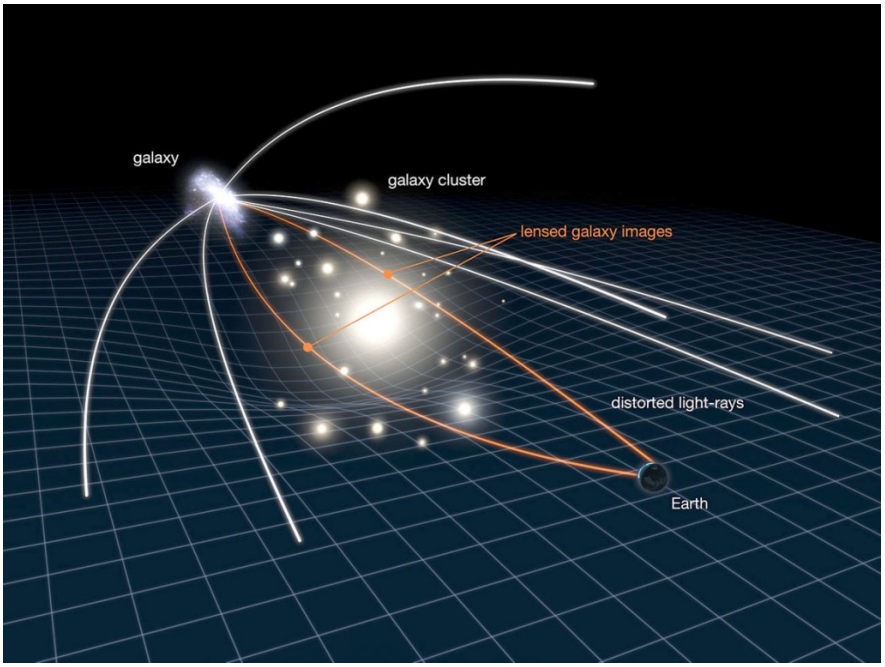

Figure 1.1: How we are able to map out the dark matter in the Universe. The shear mass of dark matter heavily distorts space around the cluster, causing light rays passing close by to be bent. By measuring the apparent deformation of the background galaxies we can infer the distribution of dark matter in the galaxy cluster.

of anti-gravity that is causing the expanding Universe to accelerate. This means that our Universe will ultimately end with all galaxies becoming infinitely far apart and completely unobservable.

1.2 What is dark matter?

Not only is the energy budget of the Universe dominated by some unknown dark energy, but most of the matter seems to be all held up in dark matter. For all the galaxies and stars we can see in the Universe, there is seven times as much dark matter, yet for all this we still do not really know what it is.

What we do know is that dark matter does not interact with light and therefore cannot be seen. It prefers to clump into massive clouds and unlike protons and neutrons, does not collapse to form dark galaxies and dark planets (i.e. if we put on dark matter glasses we would not see a copy-cat dark Universe). Fortunately this amount of dark matter does not go unnoticed and effects the way the Universe

behaves. Its shear mass heavily bends the space around it, like a large weight bending a sheet of rubber. The effect is to cause any object that comes too close to follow the curvature of space, as if rolling a ball near the crest of a hill and seeing it follow the curvature of the hill and fall down.

Similarly, should that ball be rolled fast enough, it wouldn't fall down, but shoot past the hill. However, its path would not be completely unaffected as it will have had its direction slightly altered. If we consider the ball as a photon, then if it travels too close to a large cloud of dark matter, such that it slightly falls down into it, then the path of the photon will be altered. Although we can't see or detect dark matter, we can capitalise on the fact that billions of photons are passing through clouds of dark matter like this all the time and feel the gravitational attraction causing the objects from which they were emitted to be distorted. This is known as gravitational lensing. Since dark matter is dominating the Universe we can use gravitational lensing to trace where the clouds of dark matter are, as if constructing an Ordnance Survey map of the sky. Figure 1.1 shows a diagram of the effect of dark matter with the background galaxy's light being bent by the foreground dark matter.

1.3 Astronomical particle colliders

These clouds of dark matter that prefer to clump can grow to become thousands of times more massive than a single galaxy. This attracts a lot of close by galaxies (as well as forming some of its own) and very hot gas. The result is a huge mixing pot of dark matter, with a sea of hot X-ray emitting gas interspersed with thousands of galaxies, all orbiting the centre of mass. This is known as a galaxy cluster and is the largest known structure in the Universe.

In rare events galaxy clusters can be attracted to other galaxy clusters, resulting in a car crash on an astronomical scale. In the event that two galaxy clusters do collide, their gas, dark matter and galaxies will all behave differently. The galaxies will behave like small bullets that pass by each other completely unaffected. The gas will behave like a liquid such that if the two collide haloes of gas will splash together and either form a single halo, or they will decelerate and become misshapen. What the dark matter does will depend on what dark matter is. If dark matter is collisionless, then it will pass through, like the stars and be

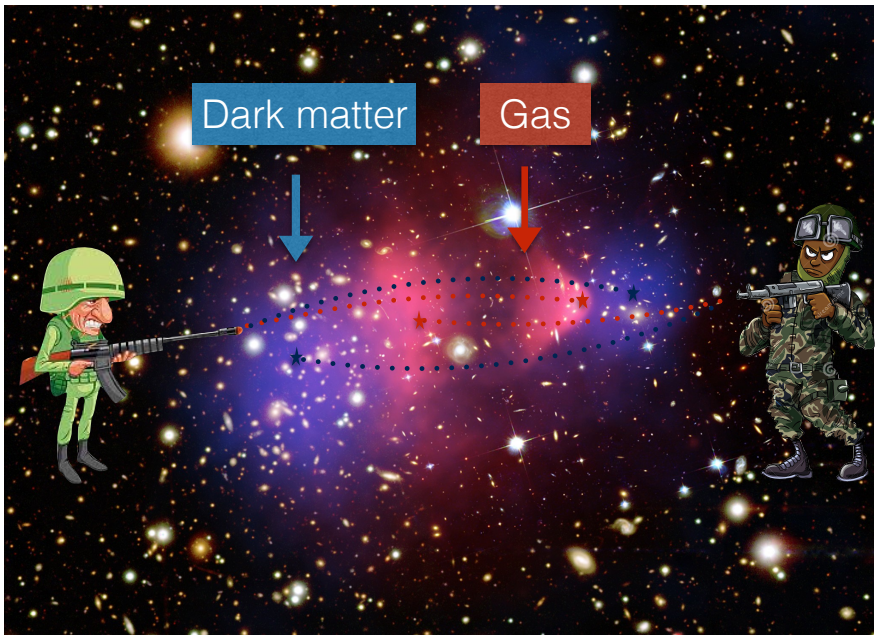

Figure 1.2: Colliding galaxy clusters are ideal laboratories to study the subtle properties of dark matter. Here, two galaxy clusters have passed through one another, causing the gas to separate from its associated dark matter cloud. The dark matter still remains coincident with the collisionless galaxies. By measuring the three different components of a galaxy cluster, I shall study the properties of dark matter in this thesis.

completely unaffected, however if it interacts it will behave differently. We can use gravitational lensing to trace dark matter in these collisions of galaxies clusters and compare this with the distribution of gas and galaxies to make statements on the nature of dark matter in galaxy clusters. It is only this way, in these clouds of dark matter that we test these properties. In this thesis I shall compare the positions of gas, dark matter and galaxies in various clusters in a bid to make further inroads in to the unknown nature of dark matter. Figure 1.2 shows the 'Bullet Cluster', an example of a colliding cluster where the gas (red) as detected in the X-ray, originally associated with the clouds of darks matter (blue), have been stripped and separated during the collision. We observe it here post merger, after they have passed one another. In this thesis I will use these events to directly probe the properties of dark matter.

2 Background Cosmology

"The wise man does at once what the fool does finally."

This introduction will give the reader the essential background information on the principles of cosmology, its constituents and how they influence the observations made. I will introduce the basic cosmological parameter set and their implications for the past, present and ultimately, the fate of the Universe. I will outline the basic cosmological model that has thus far been constrained, reporting benchmark theories and findings that shape the current understanding of the Universe. I will then comment on how future experiments are attempting to test the currently accepted model in hope of new physics beyond the Standard Model.

After an initial outline of background cosmology I shall introduce the concept of dark matter, supporting its theoretical hypothesis with a variety of evidence, originating from a multitude of experiments. I will outline the current models and theories that surround it and how these are tested with both terrestrial and space-based experiments.

Having laid down a phenomalogical basis, I will outline the tools and data that are required to test such theoretical models. I will introduce galaxy clusters, which consist of the largest know densities of dark matter in the Universe; X-ray emitting gas, and its role in testing dark matter and finally I will introduce the

concept of merging clusters and the behaviour of matter during these cosmological train wrecks.

I will conclude by highlighting how the currently favoured cold dark matter model has many successes but also many shortcomings and how discrepancies have led astronomers to suggest newer and more exotic forms of dark matter. I will introduce the concept of self-interacting dark matter and how this may reconcile some of the theoretical inconsistencies, and cover a detailed introduction into the concept of the this paradigm and its observational consequences.

I note here, that this introduction is not designed to be a complete background on the current state of knowledge associated with the Universe, however, this should give the reader sufficient background to understand the motivation for the work that follows it. If the reader is interested in further information beyond what is presented here I would point them towards Peacock (1999), as a more complete overview of cosmological physics. Moreover, I should address my choice of quotes throughout this thesis. I wouldn't say that I am an avid follower of Machiavelli, but many of his quotes spoke to me and seemed to be somewhat appropriate for my work and the last 3.5 years.

2.1 Cosmology and the large scale structure

The Universe is statistically homogeneous and isotropic, that is on large enough scales the Universe is of constant density and the same in all directions. At first this would seem implausible if not impossible as if different parts of the Universe are separated by distances greater than the distance light could have travelled since the beginning of the Universe and could thus not be in causal contact. However, as observed by Layzer (1957) and Shane et al. (1959), the Universe did indeed appear to be homogeneous on large scales. In addition to this cosmological puzzle, in the early 1920's Vesto Slipher observed that galaxies were all apparently redder than they should be, proposing that they were all receding. It was not long after that Edwin Hubble confirmed this by measuring their distances, discovering the Hubble Law, that the recession was proportional to distance (Hubble, 1929). It was with these early discoveries that observational cosmology was born.

2.1.1 Universal geometry

In order to develop a solid understanding of how the dynamics of the Universe behave, it is useful to construct a mathematical basis on which what is observed can be described. The Friedmann Robertson Walker (FRW) metric, which describes a universe that is homogeneous, isotropic and is expanding is given by

$$c^2 d\tau^2 = c^2 dt^2 - R^2(t) \left[dr^2 + S_k^2(r) d\psi^2 \right], \tag{2.1}$$

where $c^2 d\tau^2$ is the proper distance, $R(t)$ is the time dependent scale factor describing the expansion of the Universe, r is the comoving radial distance, ψ is the angular part of this comoving distance and S_k is a function which depends on the geometry of the Universe such that

$$S_k = \begin{cases} \sin\ r & \text{if } k = 1 \\ r & \text{if } k = 0 \\ \sinh\ r & \text{if } k = \text{-}1, \end{cases} \tag{2.2}$$

where k defines the geometry of the Universe with positive k denoting a closed universe, negative k denoting a open universe and $k = 0$ for a flat universe. It is possible to create a dimensionless scale factor, a

$$a = \frac{R(t)}{R_0}, \tag{2.3}$$

where R_0 is the scale factor today and hence $a = 1$ now and the FRW metric is in the form

$$c^2 d\tau^2 = c^2 dt^2 - a^2(t) \left[R_0 dr^2 + S_k^2(r)(d\theta^2 + \sin^2\theta d\phi^2) \right], \tag{2.4}$$

where the angular part has been decomposed into spherical polars and S_k becomes

$$S_K = \begin{cases} R_0 \sin\ r & \text{if } k = 1 \\ R_0 r & \text{if } k = 0 \\ R_0 \sinh\ r & \text{if } k = \text{-}1. \end{cases} \tag{2.5}$$

This metric is extremely useful in understanding how the Universe behaves under certain geometries and also for calculating cosmological distances. Consider an approaching photon, that is travelling on a null geodesic and radially with respect to the observer (such that the angular part of the metric is zero and $c^2 d\tau^2 = 0$), the distance a photon has travelled since the beginning of the Universe is given by

$$R_0 r = c \int_0^{t_0} \frac{dt}{a(t)}, \tag{2.6}$$

where t_0 is the time now, and is known as the particle horizon.

One particularly useful consequence of the FRW metric is its predicted affect on the wavelength of photons travelling through the Universe. Now consider two photons; the first emitted at some time, t_e, which is then observed at some time t_o, and the other being emitted a little bit later at time $t_e + \delta t$, which in turn will be observed at some time $t_o + \delta t$. Since the comoving distance is the same, it is true that

$$\int_{t_e}^{t_o} \frac{dt}{a(t_e)} = \int_{t_e+\lambda_e/c}^{t_o+\lambda_o/c} \frac{dt}{a(t_o)}, \tag{2.7}$$

where the second photon is assumed to be emitted one wavelength later, i.e. $\delta t = \lambda/c$. Hence, it is true that:

$$\int_{t_e}^{t_e+\lambda_o/c} \frac{dt}{a(t_e)} = \int_{t_o}^{t_o+\lambda_o/c} \frac{dt}{a(t_o)}. \tag{2.8}$$

Assuming that this happens over a very short amount of time, such that $a(t)$ is a constant and at time $t_o, a = 1$ it is true that

$$a(t_e) = \frac{\lambda_e}{\lambda_o} = \frac{1}{1+z_e}. \tag{2.9}$$

The result interestingly relates the expansion of the Universe to the change in wavelength of a photon, known as redshift.

2.1.2 The matter dominated universe

The FRW metric is governed by the scale factor a, and hence any cosmological parameters or distances using this metric will depend upon its behaviour. However, how this scale factor changes with cosmological time depends on what is dominating the expansion of the Universe, and therefore within a the make up of the Universe is encoded. It is possible to construct an equation of motion from simple Newtonian dynamics that describes the behaviour of the Universe for various matter components. However, in order to construct a fully relativistic equation of motion of the Universe the Einstein field equations must be solved, which results in the Friedmann equation and is given by

$$\left(\frac{\dot{a}}{a}\right)^2 = \frac{8\pi G\rho(t)}{c^2} - \frac{kc^2}{R_0^2 a(t)^2}, \tag{2.10}$$

where $\rho(t)$ is the energy density of the Universe at time t, the dot denotes a time derivative and G is gravitational constant. This equation nicely shows the relationship between the curvature of the Universe, k and the energy density, reflecting Einstein's theory of general relativity that relates the stress-energy tensor to the curvature of space. Now consider a mean universal density that results in a flat universe, i.e. $k = 0$, this critical density, $\rho_{\rm c}$ is defined as

$$\rho_{\rm c} = \frac{3H_0^2}{8\pi G} \approx 1.88 \times 10^{-26} \Omega h^2 \mathrm{kg/m}^3, \tag{2.11}$$

where $H = \dot{a}/a$, $h = H_0/100\text{km/s/Mpc}$ (H_0 is the Hubble parameter today) and $\Omega = \rho/\rho_c$. Since the energy density is related to the curvature of space time, given a little bit more energy in the Universe ($\rho_\text{c} + \delta\rho$) the Universe would curl up on itself, like a ball, resulting in a closed where distant objects would appear larger than they actually were. In this case, should an observer continue in a straight line they would end up back where they started. In the event there is a small deficit in energy, the Universe would be open, similar to a saddle shape. In such a universe distant objects in the sky will appear smaller than they actually were.

Equation (2.11) now describes how the expansion of the Universe relates to its energy density, however, the energy content of the Universe is made of different types of energy; mass, radiation and a vacuum energy. In order to understand how the scale factor changes with cosmic time, it is necessary to understand how each component of the energy also scales with cosmic time. To begin, it is convenient to consider the Universe as a closed system in thermodynamic equilibrium. Such a system will obey the first law of thermodynamics:

$$dQ = dE + PdV, \tag{2.12}$$

where dQ is the heat added to the system, dE is the change in internal energy and PdV is the work done by the system. Since the total energy, E of the Universe is just $E = \rho V c^2$, which cannot have heat added to it such that $dQ = 0$ and since the volume scales with a^3, such that $dV/V = 3\dot{a}/a$ it is true that

$$\dot{\rho} + 3\frac{\dot{a}}{a}(\rho + P) = 0. \tag{2.13}$$

It is now possible to use the equation of state, $P = w\rho c^2$, to determine how the scale factor scales with different types of matter;

- For non-relativistic matter, $w \approx 0$ and therefore $\rho_m \propto a^{-3}$
- For radiation, $w = 1/3$, such that $\rho_r \propto a^{-4}$
- For a cosmological constant, $w = -1$ and $\dot{\rho} = 0$ hence $\rho =$constant, however, in the event the equation of state for the vacuum energy is unknown, it may be more useful to use the general term for how energy scales with the scale factor, $\rho \propto a^{-3(w+1)}$.

Given how various forms of matter scale with a, and given the Universe is made of matter, radiation and some unknown energy, then equation (2.10) becomes

$$H^2 = H_0^2 \left(\Omega_{\rm m} a^{-3} + \Omega_{\rm r} a^{-4} + \Omega_\Lambda a^{-3(w+1)} - (\Omega - 1) a^{-2} \right), \tag{2.14}$$

where all the dimensionless density parameters here are their values as observed now and $\Omega = \Omega_{\rm m} + \Omega_{\rm r} + \Omega_\Lambda$. Equation (2.14), now has encoded within it, how the expansion of the Universe scales with a universe comprised of various forms of matter. For example, given a flat matter dominated universe ($\Omega = \Omega_{\rm m} = 1$), $a \propto t^{2/3}$, and that using this with equation (2.6), the particle horizon in a matter dominated universe is

$$d_{\rm h} = \frac{2c}{H_0}. \tag{2.15}$$

Since the behaviour of the scale factor depends solely on the content of the Universe, the ultimate fate of the Universe will be governed by the same content. Figure 2.1 shows the how the scale factor (given as the average distance between galaxies on the y-axis) changes with cosmic time for different mass contents in the Universe. For a universe that is matter dominated and closed ($\Omega_{\rm m} = 6$), the expansion rate of the Universe would decelerate, and the separation of galaxies would reduce, resulting in the 'Big Crunch'. For the currently accepted cosmological model, a universe, with $\Omega_{\rm m} = 0.3$ and $\Omega_\Lambda = 0.7$ (Planck Collaboration et al., 2013a), would expect to continue to expand and accelerate until the galaxies becomes infinitely far apart.

2.1.3 Cosmological distances

A key aspect of cosmology is distances, since observations that are based on estimating redshifts requires a method to map between redshift space and proper distance. Encoded in this mapping is how the apparent size of the Universe scales with redshift. In order to calculate the relation between distance and redshift it is useful to go back to equation (2.6). First, by changing the integration variable such that, $dt = da/H(a)a$, and substituting in equation (2.14), and then using

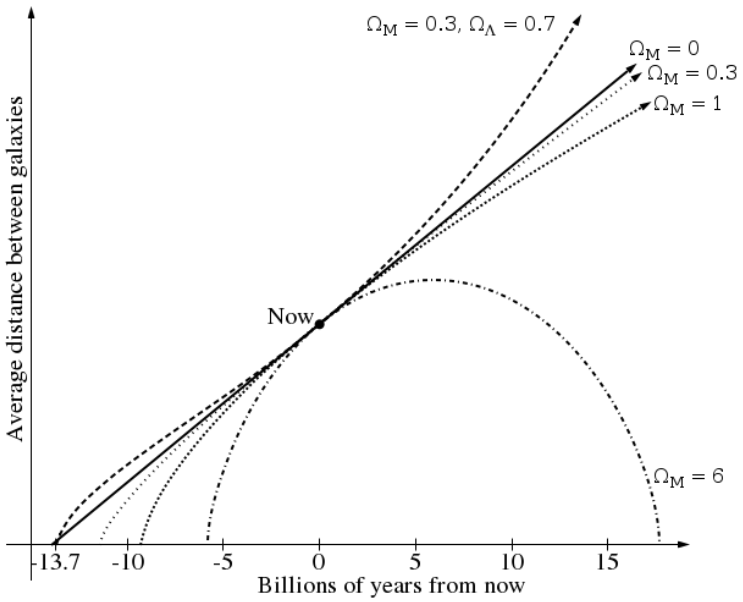

Figure 2.1: Using the Friedmann equation (equation (2.14)) it is possible to determine the affect of cosmological parameters on the age and fate of the Universe. Any total density greater than unity will result in the Universe coming together in 'the Big Crunch', and any open universe will continue to expand at an every increasing rate.

the fact that $a = 1/(1+z)$, the distance redshift relation is given by

$$R_0 dr = \int_0^z \frac{c}{H_0} \left[\Omega_{\rm m}(1+z)^3 + \Omega_{\rm r}(1+z)^4 + \Omega_\Lambda + (1-\Omega)(1+z)^2\right]^{1/2} dz. \quad (2.16)$$

This integral can be either solved numerically or for analytically for each component.

Having constructed an analytical description of the how the Universe grows with time and the relationship between redshift and proper distance, it is appropriate to define two important distances in cosmology; the angular diameter distance, and luminosity distance which is important in studies using supernova. Using the small angle approximation, the size of an object, L, with some angular separation, is just

$$L = aS_k(r)d\psi = \frac{1}{1+z} S_k(r) d\psi = d_{\rm A} d\psi. \quad (2.17)$$

$d_{\rm A}$ is known as the angular diameter distance and is calculated by comparing the expected size of an object to the angular separation in the sky. Figure 2.2 shows the change in angular diameter distance at different redshifts for different cosmologies. In each case a flat universe is shown, with the black solid line showing a vacuum energy dominated, the blue dotted line showing a radiation dominated and the red dashed, a matter dominated universe.

Consider now an object emitting light with some total luminosity L at a distance $S_k(r)$, the photons as they traverse the Universe will not only have their energies redshifted by the expansion of the Universe, reducing the flux by $(1+z)$, but also the rate at which the photons reach the observer is dilated by a factor of $(1+z)$. Therefore flux received by an observer will be

$$f_{\rm obs} = \frac{L}{(1+z)^2 4\pi S_k(r)^2}. \quad (2.18)$$

Using the definition that the luminosity distance, d_L is $f = L/(4\pi d_L^2)$, it is true that

$$d_{\rm L} = (1+z) S_k(r), \quad (2.19)$$

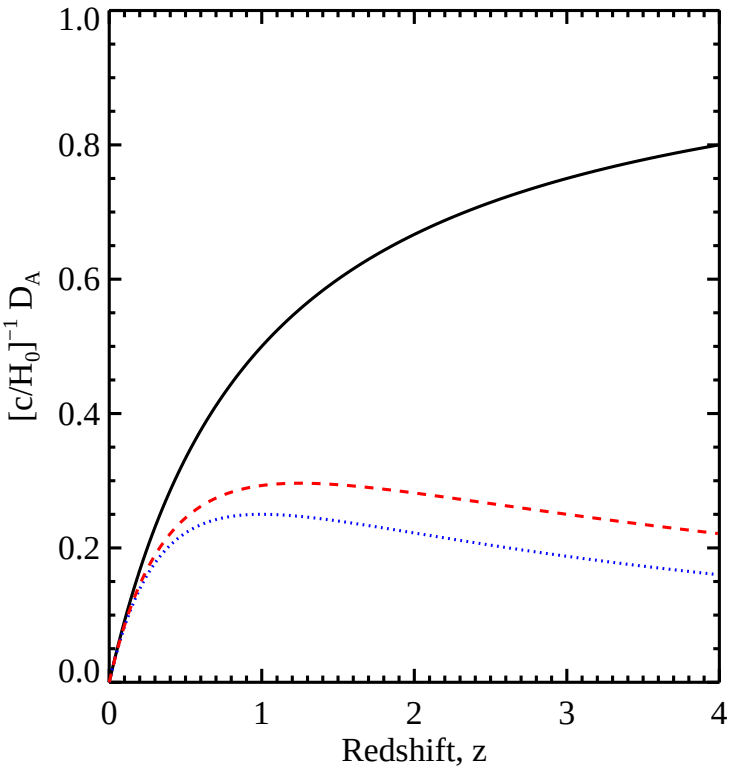

Figure 2.2: The dimensionless proper angular diameter distances for different cosmologies. Since matter will bend the light as it travels through the Universe, the apparent size something is will depend on the matter content of the Universe at that redshift. In each case a flat universe is shown, with the black solid line showing a vacuum energy dominated, the blue dotted line showing a radiation dominated and the red dashed, a matter dominated universe.

and hence

$$d_{\mathrm{L}} = d_{\mathrm{A}}(1+z)^2. \tag{2.20}$$

Equation (2.20) shows how the relationship between a luminosity distance and a distance measured from angular diameters is not a direct one, and that the measurement of cosmological distances should always consider the type of distance that is being studied.

Within the Milky Way galaxy there are a variety of methods to determine distances to stars, however techniques such as parallax become unfeasible when the relative distance from the Earth to the Sun becomes negligible in comparison with the distances that are being measured. The majority of distance measurements are based on either estimating the absolute luminosity of an object assumed to be a standard candle, or using the redshift and converting that into a distance via some assumed cosmological model. It is fortunate that two very close by galaxy clusters can be used to calibrate any distance proxy. The Virgo and Coma clusters respectively are so bright and rich that it is possible to gain extremely accurate measurements of various empirical relations

There are several methods to estimate the absolute luminosity of a galaxy (and hence luminosity distance):

- **Fundamental Plane**: It was found empirically that elliptical galaxies exhibited a tight correlation between their luminosity, L, some characteristic intensity, I_0 at a radius r_0, and the central velocity dispersion σ_v, finding

  $$L \propto I_0^a \sigma_v^b, \tag{2.21}$$

  where $a = -0.7$ and $b = 3$ (Dressler et al., 1987).

- **Faber-Jackson Relation**: A similar empirical intrinsic luminosity estimator for elliptical galaxies, constrained by Faber & Jackson (1976), where they found the relation $L \propto \sigma_v^2$.

- **Tully-Fisher Relation**: This relation was in-fact empirically measured using spiral galaxies. Initially measured by Tully & Fisher (1977), it related the maximum velocity or rotating gas in a spiral to the intrinsic luminosity.

In addition to these empirical estimators of the intrinsic luminosity of a galaxy, there were methods that estimated the intrinsic luminosity assuming some standardised candle, i.e. they were always the same brightness.

- **Cepheid Variables** : Cepheids are stars that have oscillating luminosities. These oscillations are a result of the finite sound speed in the star. For hydrostatic equilibrium the gravitational collapse must balance the pressure, and thus any small contraction will ultimately be pushed back in the time it takes for a pressure wave to traverse the star. Hence, a shorter period would infer a smaller and therefore less luminous star. Empirically these stars have been measured accurately to have a relation $L \propto P^{1.3}$ with very small scatter.

- **Type 1a Supernova** : Type 1a Supernova are a result of a white dwarf accreting mass from a nearby star until it reaches the fundamental Chandrasekhar limit of $1.4M_{\odot}$, when it becomes unstable and explodes. It is assumed to be a standardisable candle since they all share a similar form of light curve (how the intensity of light rises and falls during the event). Using the fact that all light curves were very similar, Phillips (1993) determined an empirical relation between the decay of the light curve since the peak apparent luminosity and the intrinsic peak luminosity, which could be used as a distance estimator.

Known estimators for cosmological distances has led to discoveries that have changed the face of cosmology (e.g. Perlmutter et al., 1998; Riess et al., 1998). Moreover, with an increased understanding of other cosmological parameters, how the Universe became how it is observed today is becoming increasingly clear.

2.1.4 In the beginning

Although the idea of a remanent warm after glow of the big bang permeating the Universe was developed by Gamow (1946), it wasn't until famously discovered by Penzias & Wilson (1965) as an excess in background noise in their radio antenna equating to roughly 3.5K did the Cosmic Microwave Background (CMB) become cemented in cosmological theory. Although first observed almost accidentally, Dicke et al. (1965) simultaneously considered the implications of of a hot dense beginning to the Universe proposing the exact observable that Penzias & Wilson

(1965) detected. They even laid out the rough plans of the construction of the exact horn used by Penzias & Wilson (1965) to detect the CMB.

This benchmark discovery laid to bed recent theories proposing the steady state universe (an esoteric hypothesis predicting a stable universe with no beginning or end (Bondi & Gold, 1948; Hoyle, 1948), requiring the formation of a small amount of matter in order to account for the observed expansion of the Universe). This elegant explanation for the CMB led to the first space-based telescope designed to specifically measure the CMB. Cosmic Background Explorer Satellite (COBE) measured the almost perfect blackbody radiation further lending support to the big bang theory (Mather et al., 1990). However, despite this groundbreaking discovery problems still remained.

The initial observation was that the CMB was inexplicably smooth and isotropic. To within 1 part in 10,000 it was the same temperature over all areas of the sky. Given that the CMB is at a redshift of roughly $z \approx 1000$ then in a matter dominated universe, no areas of the sky that are separated by greater than two degrees *should* be causally connected. However, the *whole sky* is in thermodynamic equilibrium. Further to this, recent measurements of the total cosmological density parameter show that, $\Omega = 1$ to within 1% (Planck Collaboration et al., 2013a). Therefore, given how the scale factor, a scales with time, then at the time of the CMB Ω would have been very close to 1 ($|\Omega - 1| < 0.00006$, assuming that the Universe could not change geometry), presenting problems of fine turning. In addition to these main issues, further problems did exist, ones that could not be solved from within the CMB paradigm.

In order to solve these remaining problems it was postulated that the Universe went through an incredible period of expansion. Lasting less than 10^{38} seconds, the Universe grew by roughly 60 e-foldings (e^{60}), from the quantum level to the size observed today. Initially proposed by Guth (1981) and then later developed by Linde (1983), this expansion quickly smoothed out any observed curvature in the Universe, allowing the Universe to become extremely flat as seen today, and it also allowed distant parts of the sky to be causally connected since at one point they were within the particle horizon.

Until recently, inflation had been a theoretical period of expansion that solved a lot of the problems associated with the observed CMB, however no direct evidence existed. It is theorised that primordial gravitational waves should be

emitted during inflation (Carr, 1980). These waves as predicted by Einstein gravity, would be then stretched and smoothed, until their amplitude became negligible in today's Universe. However, they would have an observable affect on the CMB (Mollerach et al., 2004). Since the gravitational waves at the time of last scattering would stretch and compress primordial plasma they would imprint a pattern on the temperature fluctuations. These patterns can be observed in the polarised B mode power spectrum. That is, they should imprint an effect on the CMB that is similar to the B mode in electrodynamics (e.g. a curl), which when correlated should have a distinct signature at a given scale. The recent BICEP2 experiment in the South Pole detected a 5.9σ detection of the B mode power spectrum at the scales that would indicate the existence of primordial gravitational waves (BICEP2 Collaboration et al., 2014). If correct, this would be the first, direct evidence for the existence of an inflationary era. Moreover, the results favours one of the first inflationary potentials predicting 'chaotic inflation' (Linde, 1983).

2.1.5 Separating the land from the sea

The predicted rapid expansion of the Universe solved many problems associated with cosmology at the time of the discovery of the CMB. One particular success of this theory was that it described how quantum fluctuations in the very early Universe grew to become larger density fluctuations seeding the large scale structure observed today. From this point, just after inflation finished, how these perturbations grow can be calculated analytically. For small perturbations of matter just above the mean background, $\delta = \rho/\bar{\rho} - 1 \ll 1$, and a matter dominated universe with a power law density growth, the density perturbations should grow as $\delta(t) \propto t^{2/3}$.

Linear growth see all structures of different sizes grow independently of their scale, however it is important to consider how growth of structure varies on *different* scales. In order to do so, it is sensible to introduce the power spectrum. This is a proxy for the abundance of structure at different scales and is the Fourier transform of the correlation function and is given by:

$$P(\mathbf{k}) = \langle |\delta_{\mathbf{k}}|^2 \rangle, \tag{2.22}$$

where **k**, is the wavenumber of the Fourier mode. Although in a matter dominated universe $\delta \propto t^{2/3}$, in order to understand the shape of the initial power spectrum, the state and size of the early Universe must be considered. At early times, the Universe was dominated by radiation. As structures grew, particles flew towards the over-densities via gravitational attraction. Perturbations that were larger than the particle horizon could not be pressure supported and therefore grew scale free (assuming a synchronous gauge). However as time continued, the horizon grew, allowing structure to enter the horizon and become radiation pressure supported preventing further collapse. This freezing of growth ended at the epoch of radiation and matter equality, as baryons dominated the behaviour of structure formation. This resulted in a scale dependent suppression of structure below the horizon scale at the time of equality with scales being suppressed by a factor of $f \propto k^{-2}$. For collisionless matter, the structure is further suppressed depending on the free-streaming length of the particle. For collisionless cold dark matter, this suppression is minimal, however for warm or even hot dark matter where the particle had much more energy, structure on small scales is increasingly suppressed, causing a truncation of the initial power spectrum.

2.1.6 Letting the dry land appear

In order to determine the structure of growth in the linear regime, it was assumed that $\delta \ll 1$. As the perturbations grow and become much larger than the background density, the growth will accelerate and this assumption breaks down. Although N-body simulations are used to determine the nature of non-linear structure formation, it is possible to analytically calculate the expected mass function (the number of haloes of a given mass in a given volume) using the Press-Schechter formalism. However this has its drawbacks as it doesn't account for structure within haloes (Peacock & Heavens, 1990; Jedamzik, 1995).

In order to accurately calculate the power spectrum in the non-linear regime it is possible to simulate the positions of collisionless particles. By allowing particles to freely move and only interact under gravity it is possible to recreate the large scale structure observed in the Universe. These simulations have grown significantly in the last few years, with the state-of-the-art reaching particle numbers of 303 billion (Angulo et al., 2012). Such simulations are important since accurate estimations of power spectra are vital for cosmological parameter

estimation.

Galaxy clusters

N-body simulations predict that structure in the Universe forms a web like texture. At the nodes of this cosmic web lie huge haloes of dark matter. These structures are among the largest known objects in the Universe and contain some of the highest densities of dark matter. The huge collection of dark matter results in a massive potential well that distorts the fabric of space-time and dominates the dynamics of the local environment. As a result, it drags and pulls large quantities of baryons into the well instigating the formation of massive galaxies and a sea of ultra-hot ionised gas (mainly hydrogen). The consequence is a energetic mix of galaxies, ionised gas and large quantities of dark matter.

The dynamics, constituents and behaviour of matter in galaxy clusters have been well studied, helping to constrain cosmology and defining cluster scaling relations. Their abundance and mass will depend heavily on how the Universe formed and surveys such as Planck (Planck Collaboration et al., 2011), can use these abundances to estimate the mass content of the Universe. Moreover, the CMB is sensitive to high densities of baryons in the Universe since photons from the surface of last scattering will scatter off electrons within intra-cluster medium (ICM), via inverse Compton scattering. This will cause a shift in the observed CMB spectrum, leaving an imprint (Sunyaev & Zeldovich, 1970). The Sunyaev-Zel'dovich effect (SZ) is independent of redshift and is a relatively new method to study clusters, since prior to Planck they were difficult to resolve. By comparing the observed number of Planck SZ clusters with those calculated in simulations of different cosmological models, it is possible to constrain cosmology. Interestingly, Planck found slightly contentious results from their SZ cluster catalogue, finding a two-sigma tension on their constraint of $\Omega_{\rm m} = 0.29 \pm 0.02$ and constraints of the power spectrum normalisation of $\sigma_8 = 0.75 \pm 0.03$ (Planck Collaboration et al., 2013b). However, in order to account for potential systematics in the X-ray masses, they need to be calibrated with a sample of lensing clusters that overlap the sample. The study by the Planck Collaboration et al. (2013b) was calibrated using an assumed $M_{\rm X}/M_{\rm WL} = 0.8$, derived from simulations. However soon after this was published, it was postulated that they under-estimated their cluster mass calibration and a more accurate calibration of $M_{\rm X}/M_{\rm WL} \sim 0.7$ using

the Weighing the Giants lensing sample (von der Linden et al., 2012), significantly reduced the observed tension (von der Linden et al., 2014).

Complementary to cluster counts, it is possible to use the fraction of gas in clusters to probe cosmology. In the absence of any expulsion mechanisms, the amount of gas (which dominates the baryonic content in clusters) would naively be expected to roughly equal the baryon fraction of the Universe. However, it was realised that this was not entirely true as mechanisms such as AGN and supernova feedback expel gas from the ICM in highly energetic events. Recent simulations with improved models of the hydrodynamics within clusters have derived more accurate and robust estimates of the baryon fraction in clusters (Eke et al., 1998; Kay et al., 2004; Crain et al., 2007; Nagai et al., 2007; Young et al., 2011; Battaglia et al., 2013; Planelles et al., 2013). As a result a recent X-ray study of a sample of galaxy clusters analysing the fraction of gas in a cluster has estimated $\Omega_M = 0.27 \pm 0.04$, the best current constraints from clusters of galaxies (Mantz et al., 2014). Furthermore, by studying the fraction of gas in clusters over a range of redshift it is possible to estimate the dark energy equation of state (Allen et al., 2008; Mantz et al., 2014).

Typical profile of galaxy clusters

The profile of a galaxy cluster has been heavily debated over the previous two decades with observations and simulations varying somewhat on the *expected* shape. Although many profiles have been proposed, (e.g. Sersic (1968) and the Singular Isothermal Sphere (SIS)), it has been found by Navarro et al. (1997, hereafter NFW), that CDM seems to predict that dark matter haloes should follow a $1/r$ relation in the core and a $1/r^3$ in the wings (where r is the radius front the centre of the cluster), more specifically

$$\rho(r) \propto \frac{1}{x\,(1+x)^2}, \qquad \text{where} \qquad x = \frac{r}{r_s}, \tag{2.23}$$

where r_s is the scale radius, which is the radius at which the profile transitions from r^{-1} to r^{-3}, and can be expressed by the NFW concentration parameter, $c = r_{\rm vir}/r_{\rm s}$, where $r_{\rm vir}$ is the virial radius. The relationship between the cluster mass and concentration has been constrained from both simulations and observations, with most studies finding that lower mass haloes are much more

centrally concentrated than larger haloes (e.g. Macciò et al., 2008; King & Mead, 2011; Comerford & Natarajan, 2007; Duffy et al., 2008). Studies to constrain the mass profile of galaxy clusters seem to find that most agree with the NFW profile, with some surprisingly finding very good agreement in the core where baryons should affect the shape (since the NFW profile is based on CDM simulations) (Okabe et al., 2013; Newman et al., 2013; Ettori et al., 2010). While simulations predict that dark matter should follow an NFW profile, the total mass from observations infer that the profile is that of an SIS (Gavazzi et al., 2007; Johnston et al., 2007; Leauthaud et al., 2012).

Although it seems that the total mass (or at least the dark matter) follows an NFW profile, it is thought that the ICM should project a surface intensity in the X-ray according to the β profile (Cavaliere & Fusco-Femiano, 1976)

$$S(r) = S_0 \left[1 + \left(\frac{r}{r_c}\right)^2\right]^{-3\beta/2}, \tag{2.24}$$

where r_c is the core radius and β describes the slope of the profile at large radii (and $\beta \approx 2/3$). Since X-ray emission is caused by Bremmstrahlung radiation, the intensity is proportional to the number density of the electrons, and hence the surface brightness can be related to the density profile of the ICM along the line of sight

$$S_X(r) \propto \int_{-\infty}^{\infty} n_p n_e dl, \tag{2.25}$$

where n_p is the number density of protons and n_e is the number density of electrons, and the integral is carried out along the line of sight. By assuming that the gas is in hydrostatic equilibrium with the dark matter potential and that the DM distribution is spherically symmetric it can be shown that the mass within radius r is

$$\frac{1}{\mu n_p n_e(r)} \frac{d\left[n_e(r) kT(r)\right]}{dr} = -\frac{GM(<r)}{r^2}, \tag{2.26}$$

where μ is the mean molecular weight per Hydrogen atom. It is convention to define the mass, M_{200}, at which the average density of the cluster exceeds two hundred times that of the Universe. Maughan (2007) showed that the X-ray

luminosity is a good mass proxy with low scatter, and recently Israel et al. (2014) found a consistent relation between X-ray and weak lensing mass to $z \approx 0.5$.

2.1.7 Precision cosmology

The initial scale free-linear growth from an initial matter power spectrum, and the subsequent non-linear growth means that small structures form first, and merge to form larger structures later on. It is a prediction of cold dark matter (CDM) N-body simulations that structure forms hierarchically, in a tree like fashion, starting at the trunk and ending up in the leaves (Peebles, 1980; White, 1976; Press & Schechter, 1974). In a purely Gaussian field all the information is contained within two point correlation function and hence its Fourier transform; the power spectrum. In order to make sense of the density field observed, it is usual to constrain the matter power spectrum as this will contain approximately (since the matter field is severely non-Gaussian on the smallest scales) most of the information that describes it. Modern cosmology has been attempting to constrain those properties that describe the matter power spectrum and therefore the Universe. Those cosmological parameters already mentioned previously, such as the matter, radiation and dark energy density parameters, and the Hubble parameter are all important and affect the matter power spectrum on different scales, however there are other important characteristics and parameters that affect it.

Dark energy equation of state

The observed expansion of the Universe and the isotropic and homogeneous CMB has led to the widely accepted theory of the Big Bang. Naively, such a theory would lead to an expected initial acceleration of the Universe followed by a period of deceleration and ultimately collapse as the matter in the Universe looks to pull itself back in. To test this theory it is possible to look for deviations from Hubble's Law.

In the late 20th Century, whilst observing the distances from Supernova, Perlmutter et al. (1998) found such a deviation, yet it turned out that the Universe was actually accelerating, and not slowing as previously expected. Simultaneous work by Riess et al. (1998) confirmed this finding and it was soon accepted that the Universe was in fact accelerating.

This was in-line with other independent work examining the current dynamical state of the Universe. Studies of the total matter content of the Universe showed that $\Omega_{\rm M} < 1$, and since the Universe had been shown to be flat by the CMB, this implied some extra vacuum energy and hence cosmic acceleration. The measurement of $\Omega_{\rm M}$ was carried out in two different methods. The first was using galaxy clustering. By measuring the power spectrum of the galaxies it was possible to estimate the dark matter power spectrum. This spectrum roughly follows a Schechter function, where the turnover is related to the sound horizon at the equality of matter and radiation. By measuring this turnover, it is possible to estimate $\Omega_{\rm M}$, which Percival et al. (2001a) found not to be 1. The second, is that the relative abundance of dark matter to baryons in galaxy clusters was not sufficient to allow $\Omega_{\rm M} = 1$. Since the baryon fraction was well understood from big bang nucleosynthesis (BBN), then the amount of dark matter that existed was not sufficient and that in-fact Fukugita et al. (1998) found that $\Omega_{\rm M} < 0.25$.

The discovery of the accelerating Universe led to the 2011 Nobel Prize in physics and a new era of cosmology. New theories of what could be driving this acceleration were proposed, from cosmological constants, which naturally arise from Einstein's equations, to more exotic scalar fields, also known as dark energy. Even modifications to Einstein's gravity have been proposed, however these suffer from fine tuning as this theory has been stringently tested on solar system scales. Since its cementation into the standard cosmological setup, it has become normal to constrain the dark energy equation of state, w (how energy density relates to pressure), and has been measured to be $w = -1.13 \pm 0.13$ and that the Universe's energy budget is made of $68.6 \pm 2\%$ vacuum energy (Planck Collaboration et al., 2013a).

Spectrum normalisation, σ_8

The spectrum normalisation is an additional and important factor as it defines the amplitude of the matter power spectrum. Its definition is somewhat convoluted, however nominally it is the variance of the linear theory density field when smoothed with some window function in Fourier space, and is given by

$$\sigma^2(R) = \int \triangle^2(k)|W_k|^2 d\ln k, \tag{2.27}$$

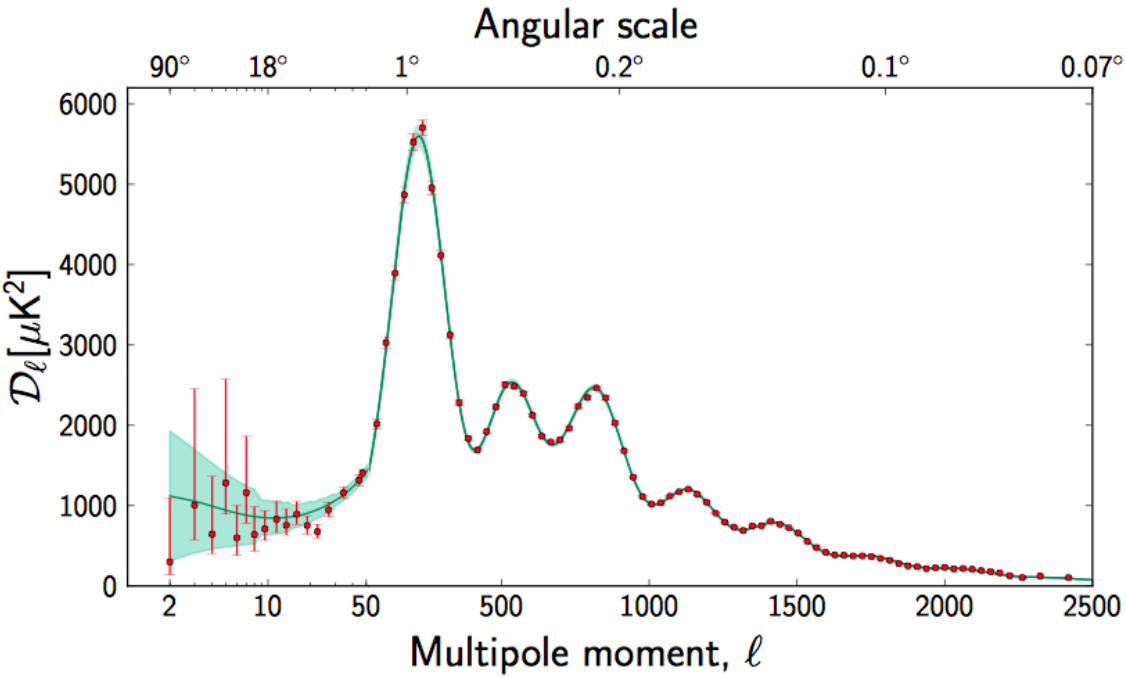

Figure 2.3: Planck Power Spectrum. This show shows the coefficient of each angular multiple measured from the temperature fluctuations of the CMB. The resulting power spectrum can be used to extract cosmological parameters.

where $\triangle^2$ is the linear power for a given scale, k, W_K is the window function. Historically the size of the window function is $8h^{-1}$Mpc.

The state of the art

As a result of late time non-linear growth, the matter density field is severely non-Gaussian with non-trivial coupling between modes, and therefore estimating cosmological parameters from it is very difficult, but possible (e.g. Percival et al., 2001b; Sánchez et al., 2012; Parkinson et al., 2012; de la Torre et al., 2013). Fortunately the surface of last scattering provides us with a snapshot of the Universe at early times when the Universe was extremely Gaussian. It is therefore relatively straight forward to extract cosmological parameters from the *angular power spectrum*, which is the Fourier transform of the temperature fluctuations of the CMB over the full curved sky. Figure 2.3 shows the power spectrum as measured by the Planck space telescope as a function of multipole on the bottom x-axis and angular scale given on the top x-axis.

Table 2.1: Cosmological parameters derived from the Planck observations (Planck Collaboration et al., 2013a).

Parameter	Meaning	Current Best Estimate
Ω_m	Matter density	0.314 ± 0.02
Ω_Λ	Dark energy density	0.686 ± 0.02
Ω_b	Baryon density	0.049 ± 0.00073
H_0	Hubble parameter	67.4 ± 1.4 km s^{-1}Mpc^{-1}
σ_8	Power spectrum normalisation	0.834 ± 0.027
w	Dark energy equation of state	-1.13 ± 0.13
$\sum m_\nu$	Sum of neutrino masses	< 0.23 keV
t_0	Age of the Universe	13.813 ± 0.058Gyr

In order to constrain cosmology using the CMB angular power spectrum it is important to understand how the physics of the early Universe affect the statistics. Since most structures will have formed according the size of the horizon at last scattering, the position of the first peak in the power spectrum will directly probe the horizon at the time of the last scattering. $\theta_H = D_H^{LS}/D_H$, which for a matter dominated Universe is $\theta_H = 1.8\Omega_m^{0.5}$ degrees. Since the horizon at the surface of last scattering is dominated by the total matter density of the Universe, the position of the first peak, can constrain Ω_k.

There have been various different probes of cosmology (e.g. Nuza et al., 2013; Kilbinger et al., 2013; Planck Collaboration et al., 2013a; Riess et al., 2011; Planck Collaboration et al., 2013b), all of which have different degeneracies and systematics. It is important that if probes are combined that all assumptions made and potential systematics are considered, especially in the case of contentious results. Table 2.1 gives the derived parameters from the recent Planck Collaboration et al. (2013a) results. Interestingly, you may notice the discrepancy between the density of baryons and the density of matter in the Universe. This proof for the existence of unobserved mass is just one piece in a long line of evidence for dark matter.

2.2 Dark matter

The existence of a mysterious non-baryonic particle that interacts primarily via gravity and dominates the Universe can seem somewhat perverse. However, several independent lines of evidence for the existence of dark matter have been accumulating now for nearly 100 years and are beyond contention.

It was initially proposed by Zwicky (1933) as a means to explain the discrepancies between the extreme velocity dispersions of galaxies in the Coma cluster and the observed mass. Since this study in the early part of the 20th Century, evidence has continued to grow including independent studies of the velocity of gas rotating in galaxies, which were found to be anonymously high in the outer regions of the galaxy where the light appeared to dissipate. According to Keplerian laws, the velocity of gas is expected to drop off $v \propto r^{-1/2}$, assuming that matter follows light, however studies reported a flat rotation curve, implying a $M \propto r$ relation. Such problems were initially expressed by Oort (1932), yet did not postulate the presence of missing material. Later studies noted similar effects, saying that this could only be explained by either a modification to gravity or the existence of unobserved dark matter (Rubin et al., 1980; Bosma, 1978).

More recently there have been other probes that have independently supported the existence of dark matter. As mentioned, Table 2.1 shows how Planck predicts that the total matter density in the Universe is of order ~ 0.3. However, it is possible to estimate the the baryonic matter density from the CMB using the relative heights of the peaks in the CMB power spectrum, since this is related to the baryon oscillations in the early Universe (Planck Collaboration et al., 2013a), and BBN. BBN refers to the production of the light elements in the early Universe. Since it is impossible to make elements above a certain mass through fusion, it is possible to theoretically estimate the abundance of baryons at the end of the early Universe and hence compare with places where little stellar nulceosynthesis has occurred, for example in dwarf galaxies (e.g Bania et al., 2002; Burles et al., 2001). From these different lines of evidence, baryons only contributes $\sim 13\%$ of this, meaning that there must be another contribution from a non-baryonic component. It seems that dark matter is a necessity in order for structure to grow in the Universe, a fact that is heavily supported by N-body simulations. Moreover, from independent observations it is clear that there is an order of

magnitude discrepancy in the mass of gas in the cluster and the total mass, which cannot be accounted for by the stellar content (e.g. Gonzalez et al., 2013; Giodini et al., 2009a).

More direct evidence from galaxy clusters has originated from studies of colliding and merging clusters. N-body simulations predict that structures in a CDM universe form hierarchically, resulting in merging galaxies and merging galaxy clusters. In the latter scenario, the dynamical differences of dark matter and baryonic are most obvious. During a merger, the haloes of dark matter and gas of the two clusters will merge and interact. If dark matter is collisionless it will pass directly through, seemingly undisturbed, whereas the gas will interact with itself and in some extreme situations shock causing a bow to form in the gas cloud. An example of this was discovered with the merging cluster, 1E0657-55, or more commonly known as the 'Bullet Cluster' (Markevitch et al., 2004; Clowe et al., 2004, 2006; Bradač et al., 2006). Figure 2.4 shows the cluster just after collision. The blue represents the dark matter, and the red denotes the position of the gas. A separation between the dark matter and the gas in both post-merging haloes can clearly be seen . This particular example was one of the first pieces of evidence for dark matter that could not be explained using a modification to gravity (Clowe et al., 2006).

2.2.1 Theories and candidates

The mounting evidence means that dark matter is an undeniable part of the Universe, a part which dominates the gravitational force on scales $\gtrsim$ 1kpc. Consisting of roughly 27% is the energy content of the Universe, exactly what it is still evades us, however studies have been able to shed some light on this dark matter.

2.2.2 Weakly Interacting Massive Particles

A well developed and motivated model is that dark matter is some kind of Weakly Interacting Massive Particle (WIMP). Although previously thought to be a contender, the Massive Compact Halo Object (MACHO), which stated that dark matter was in-fact massive objects that were not sufficiently luminous to be observed, has been ruled out from chemical abundance estimates in white dwarfs

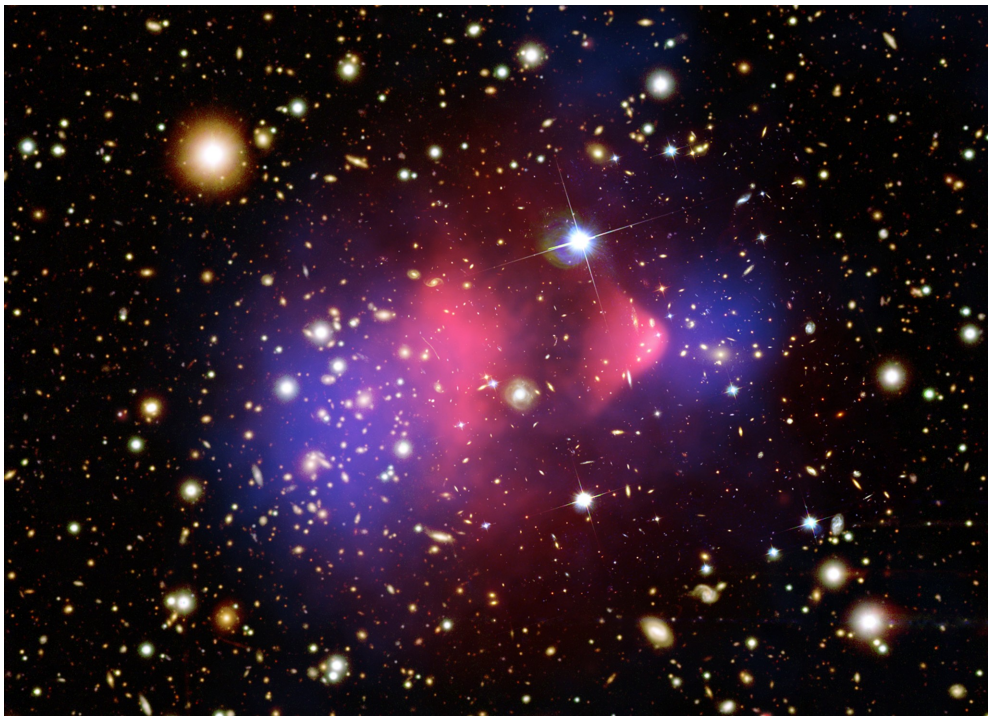

Figure 2.4: The merging cluster 1E0657-55, (Bullet Cluster). This is a typical example of a post-merging galaxy cluster. In the red is the hot X-ray emitting baryonic gas, and in the blue is the dark matter. It can be seen that during the merger the gas is shocked in to a bullet form, and the dark matter has separated from its associated gas. Clowe et al. (2006) find an 8σ offset between gas and an unobservable dark mass.

and comparing to BBN (Fields et al., 2000; Freese et al., 2000).

WIMPs can be considered as any massive particle that interacts via the weak force and are heavily favoured thanks to what has become known as the "WIMP miracle". If dark matter exists as a WIMP, then in order to have survived until this day it must be stable for at least the Hubble time. In early times dark matter particles would annihilate with each other at a rate determined by their annihilation cross-section. Once the expansion rate grew beyond the annihilation cross-section the density would freeze out resulting in the relic density observed today. Figure 2.5 shows how the comoving number density (left y-axis) freezes out as the expansion of the Universe prevents further annihilation.

Using simple approximations from particle physics, the annihilation cross-section that results in a consistent relic density corresponds to a particle with a mass ranging between $m_\chi \sim$ 100GeV - 1TeV, which is the mass scale of weak-sector of the Standard Model. It seems that weakly interacting particles would make very good dark matter candidates.

The temperature of dark matter

Under the assumption that dark matter is some kind of WIMP, its temperature refers to the state of the particle at matter-radiation equality and has a direct effect on the matter power spectrum. The temperature of dark matter is mainly dependent on the mass of the dark matter particle. If it is heavy then it will travel slower and therefore be 'cooler' that lighter dark matter. Neutrinos, the fundamental particle produced during beta decay via the weak interaction are an example of hot dark matter. During the epoch of radiation-matter equality they were highly relativistic, interacting weakly with the light sector. Since they were highly relativistic, they had a large 'free-streaming' length, which is the length a particle can travel before it interacts with another particle. Since neutrinos have mass, then any free streaming will cause suppression of potential wells, resulting in the suppression of power on small scales (Davis et al., 1981). What follows are three main definitions of dark matter and their implications on structure;

- **Cold Dark Matter (CDM)** Non-relativistic at the epoch of matter-radiation equality and is non-realistic now. CDM structures form hierarchically in a bottom-up fashion. Lots of small-scale structure with galaxies and clusters harbouring much substructure.

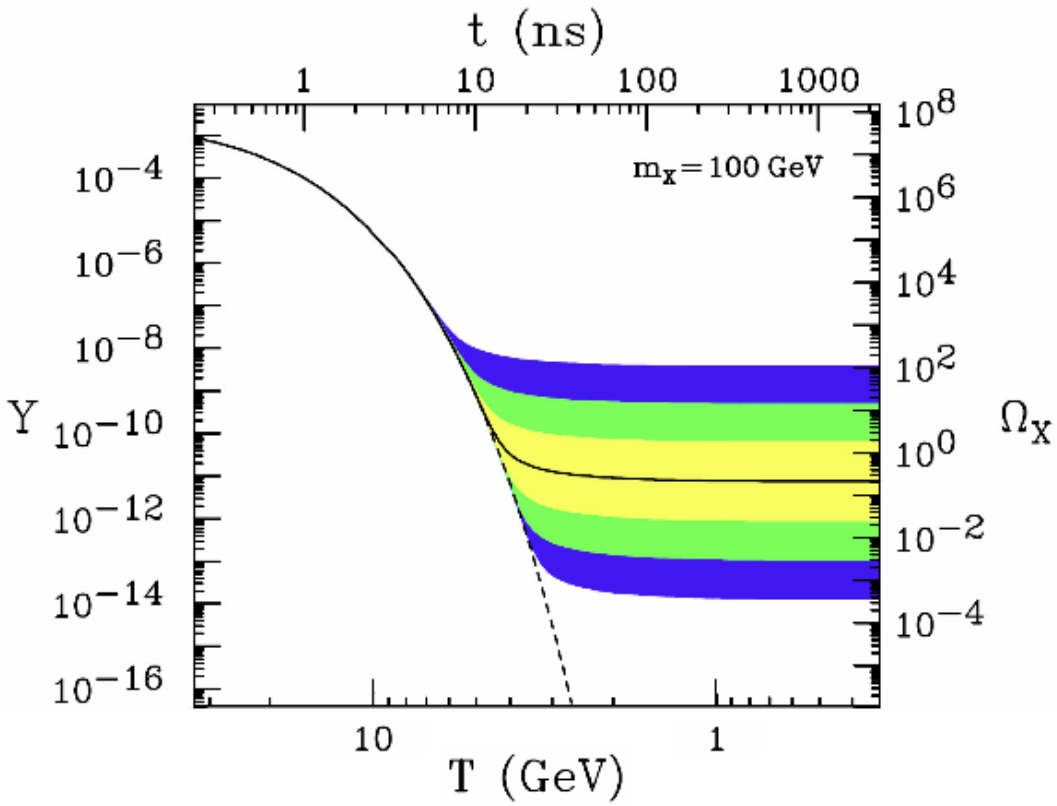

Figure 2.5: The WIMP is a heavily favoured candidate for dark matter. On the left hand y-axis is the comoving number density of dark matter particles, and on the right hand side is the resulting relic density today. These are being shown as a function of temperature of the Universe (bottom) and time (top). At early times, dark matter will have annihilated with itself until the expansion rate of the Universe exceeded the annihilation cross-section causing the number density to freeze out. If the annihilation cross-section was higher it would push the black line and shaded contours down. The black line here shows the annihilation cross-section that returns the correct relic density today with the yellow, green and blue contours representing annihilation cross-sections a factor of 10, 100 and 1000 different. (Feng, 2010)

- **Warm Dark Matter (WDM)** Relativistic at time epoch of matter-radiation however cools, and is non-relativistic now. Since the particles are lighter, they are able to free-stream out of potentials more easily and therefore cause suppression of growth on small scales resulting in less substructure than observed in CDM simulations. Structures still form hierarchically (Viel et al., 2005).

- **Hot Dark Matter (HDM)** Particles are relativistic at early and late times. Structure is heavily smoothed since the free-streaming length of the particle is high and causes structure to form top down with the largest structures forming first. It was found that HDM had a coherence length that was far too large for structure to form, and therefore could not be the main form of dark matter (Davis et al., 1981; White et al., 1983).

Exactly what the temperature dark matter is remains heavily debated. Although pure HDM has already been ruled out by measurements, models of WDM remain consistent with observations and current efforts continue to constrain it (Lovell et al., 2012; King & Merle, 2012; Viel et al., 2005). Moreover, it is possible that dark matter exists in many forms, known as mixed dark matter. For example, a form of hot dark matter exists in neutrinos. These weakly interacting relativistic particles act to smooth out structure, however, as mentioned, these hot particles cannot be the only form, and another component must exist to form the structures observed today.

The Standard Model

Although the temperature of dark matter, which in turn reflects its mass, has broad consequences for the type particle, there are so many dark matter candidates that it is a relatively vague description. Exactly what dark matter is, has yet to be determined with many candidates still potentially viable. Although most models of particle physics predict that dark matter will be an exotic, new particle from a new family, such as supersymmetry, there are candidates that exist under the Standard Model.

In addition to the previously discussed neutrino, the axion is one potential Standard Model particle that could be dark matter. According to quantum chromo dynamics (QCD), strong charge-parity violation could occur, however,

the violating term, θ in the QCD Lagrangian has been constrained to be very small ($< 10^{-9}$), which invites problems of fine tuning. In order to explain this measurement, Peccei & Quinn (1977) proposed that the parameter, θ, was in fact a scalar field and had some symmetry breaking boson known as an axion. This theory was later developed by Weinberg (1978) and has become a leading candidate for dark matter.

Non-standard

I deliberately did not chose the title of this section to say 'supersymmetry'. Originally it was thought that dark matter will most likely be a supersymmetric particle. The theory of supersymmetry is an elegant idea that postulates that all fermions have a supersymmetric boson partners and all bosons have a supersymmetric fermion partner.

Supersymmetry was a highly favoured theory as it predicted the grand unifying of all the forces and it solved the hierarchy problem (why the strength of the forces are so different). This was aesthetically pleasing, and led most to believe it to be true. However the simplest form of supersymmetry predicts that particles should exist at an energy scale currently accessible by particle colliders, and the absence of a detection means that they either did not exist or they were much heavier than originally thought (LUX Collaboration et al., 2013). The lack of any detection of any supersymmetric particle at the Large Hadron Collider (LHC) has forced theorists to either push the symmetry breaking energy scale ever higher, or look to other sources of particles (Beskidt et al., 2012).

Until recently the most favoured supersymmetric particle was the neutralino, which was a combination of the wino, the higgsino, and the bino. Being the lightest of the theorised supersymmetric particles, it was thought this would be stable since it would not be able to break R-parity (a hypothesised conservation law that is required to prevent proton decay). However the expected eigenstates from the minimal supersymmetric model (MSSM) have been ruled out by the recent Large Underground Xenon dark matter experiment (LUX Collaboration et al., 2013), meaning that more exotic forms of this lightest particle are required to match observations.

Modified Gravity

All measurements of dark matter have thus far exploited its gravitational influence. The detection, or the lack thereof, of dark matter has led theorists to postulate that in fact dark matter is just a manifestation of the lack of understanding of gravity (e.g. Milgrom, 1983; Bekenstein & Milgrom, 1984; Bekenstein, 2006). Einstein gravity revolutionised physics by understanding how matter bends and distorts space-time, and it is this curvature that defines the dynamics of objects in the Universe. However until now, this theory has been tested on the local solar system using the Cassini spacecraft (Bertotti et al., 2003), with it passing to an accuracy of 20 parts in a million.

Although an intuitive solution to rotation curves, modified gravity models struggle to predict the observed behaviour of merging clusters such as the Bullet Cluster, where a separated halo of dark matter from gas has been observed (Zhao et al., 2010). In the event that it was modified gravity, the lensing peak would remain with the gas, which dominates over the stellar content, however this is not what is observed (Clowe et al., 2004). In the event that our understanding of gravity breaks down on galaxy scales such that it does explain rotation curves, it could lend support to modified gravity theories attempting to explain the apparent acceleration of the Universe.

2.2.3 Detection

Discovering the ubiquitous particle has become one of the most important problems in modern cosmology. Although it dominates the mass-energy budget of the Universe, it continues to elude us. In a bid to further understand the particle, many experiments have been augmented to try and primarily detect the particle, and also determine its coupling properties.

Particle physics dark matter experiments can be divided into three categories, including those that are trying to directly detect the WIMP wind from the Milky Way as the Earth orbits the Sun, and indirectly detect it via its creation or annihilation. Although subtly different, these two types of experiments are both probing how dark matter couples to Standard Model particles. Figure 2.6 shows the various couplings of dark matter, and those experiments that probe them.

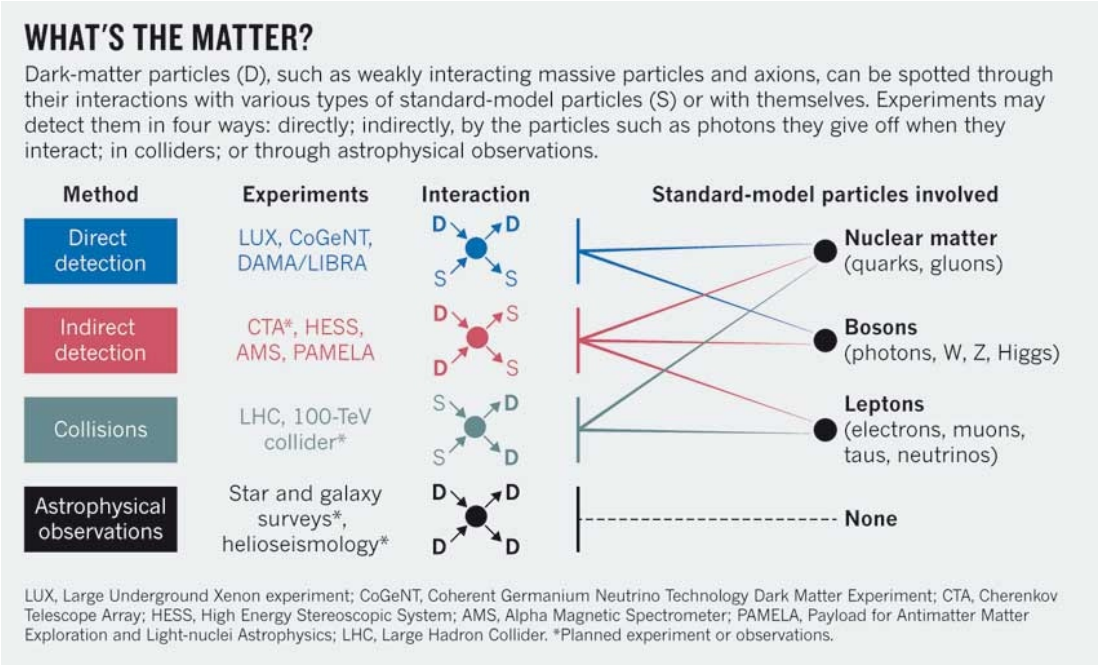

Figure 2.6: A diagram to show the different ways dark matter can couple to standard model particles and to itself. Different terrestrial and space-based experiments are attempting to constrain the standard model coupling, however it is only possible to constrain the self-interaction cross-section via astronomical observations. (Livio & Silk, 2014)

Direct

The basic theory behind direct detection is to take a large volume of a liquid or gas and hope that a dark matter particle will interact with one of the molecules and scatter. The scattering particle will release a photon of a given energy and from this can infer the dark matter particle. The medium used to carry out the test has repercussion for sensitivity and information provided by the test. For example, there are two classes of direct detection experiments; directional and non-directional. That is, experiments that inform the observer of the direction the dark matter particle originated from and those that just inform the observer of an incident. The former is extremely useful since these should correlate with the direction of motion of the Sun orbiting the centre of the Milky Way, however suffer from lack of sensitivity.

The most recent and sensitive experiment was that of LUX which is a large underground Xenon experiment. Harbouring 370kg of liquid Xenon, it is situated 1 mile underground in South Dakota, USA and has the tightest constraints on the properties of dark matter so far (LUX Collaboration et al., 2013). Prior to this, the Xenon100 experiment held the title for most sensitive, with other experiments claiming uncorroborated detections (Aprile et al., 2012).

The most recent DAMA experiment claimed to have observed the seasonal WIMP wind to $\sim 9\sigma$ (Bernabei et al., 2013), with CoGeNT also finding a seasonal variation in their results (Aalseth et al., 2011). Indeed, additional experiments have also claimed detection with the CRESSTII experiment, which looks to observe dark matter scattering off $CaWO_4$ crystals (Angloher et al., 2012), and Cryogenic Dark Matter Search (CDMS) also claiming a detection (CDMS Collaboration et al., 2013). However, none have been corroborated by the two much more sensitive Xenon based experiments. Figure 2.7 shows the Xenon100 and the LUX upper sensitivity limits, and the regimes of claimed detections from other experiments. Although particle physics models of dark matter can explain these discrepancies, it is unlikely that dark matter will be seen in some experiments and not in others.

These direct detection experiments are all non-directional, however experiments such as DRIFT, which is a gaseous detector, allows analysis of the recoil path in the event of a detection and hence the original direction of the dark matter particle. However, though these experiments provide more information into the

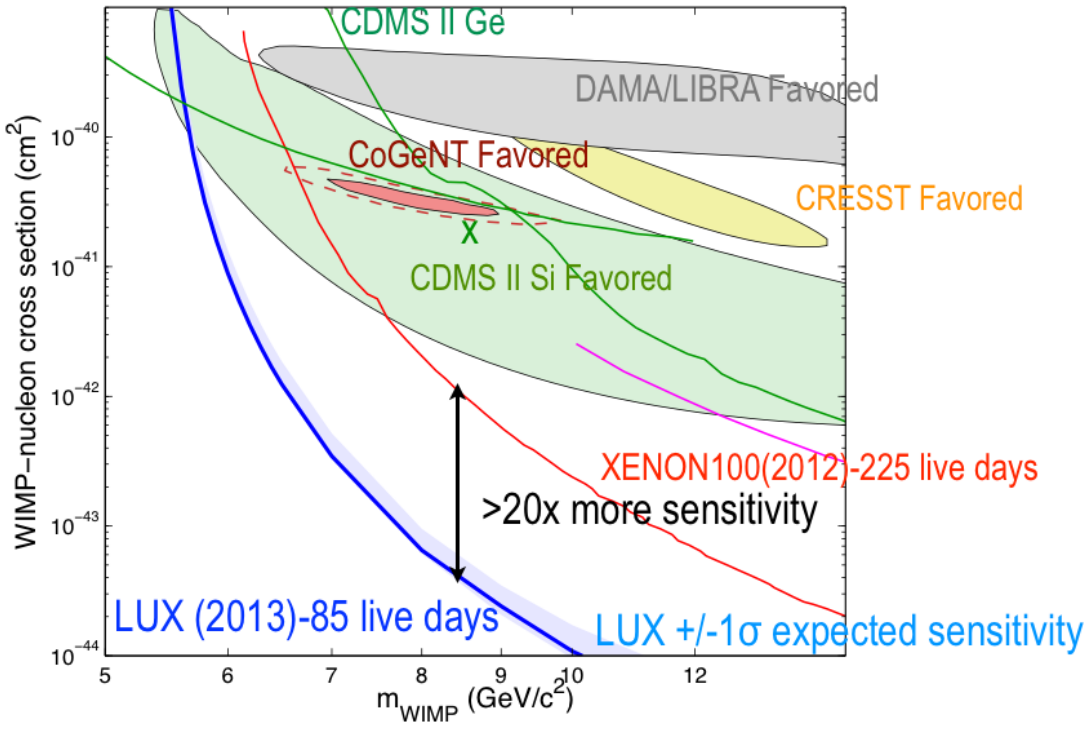

Figure 2.7: A summary of all the current best direct detection experiments, with the lines showing the constraints set by the experiment in the event of a non-detection, and the shaded regions are the parts of the parameter space where the experiment has claimed a detection. Clearly, none of the claimed detection regions overlap, providing further evidence that these are false positives, and not a real detection.

direction of the dark matter particle, the heavy target nucleus means that it is much less sensitive than those in Figure 2.7 (Alner et al., 2005).

Indirect

Naive models of what dark matter is predict that dark matter should have been detected somewhere in the parameter space already explored, however as these detectors continue to argue over claimed detections (and non-detections), it seems that dark matter isn't behaving as originally thought. It is therefore important that other avenues are explored in an attempt to constrain the properties and behaviour of dark matter.

It has been argued that dark matter, should it be a particle, annihilated with itself in the early Universe to produce the relic density observed today. Although this annihilation ceased because the expansion of the Universe caused the number density to drop below a critical threshold, in regions where structure formation has brought together very high densities and relative velocities of dark matter, a similar signal from annihilation dark matter should be detectable. The Fermi-LAT spaced-based telescope is looking for potential signals of annihilating dark matter from the centre of the Galaxy (The Fermi-LAT Collaboration et al., 2013), with recent observations of a spherical excess around the galactic centre inferring the probable signal of annihilating dark matter (Daylan et al., 2014). Also looking for the signal of annihilating dark matter is the Alpha Magnetic Spectrometer (AMS). AMS is a spaced-based mission mounted on the International Space Station and is attempting to extract the dark mater annihilation signal from highly energetic cosmic rays. By estimating the expected background from astrophysical sources, AMS could potentially detect dark matter from an unexpected excess in charged particles from annihilations. Interestingly, they have found tantalising evidence for an excess in positrons at high energies (Aguilar et al., 2013). Unfortunately, this is currently at the very limit of the energy range of the telescope, however they are looking to improve this in order to better understand this excess.

Issues and prospects for dark matter detection

The current lack of any detection of dark matter is somewhat concerning, however the parameter space in which dark matter can reside means that finding it may

not be so easy. Despite theoretical predictions placing dark matter well within the sensitivity of current experiments, the broad range of theoretical models means that predictions are ultimately optimistic. Future, larger direct experiments may shed some light on the matter, however the problem of increasing the experiments yet maintaining sensitivity becomes difficult in large volumes of liquid and gas. Moreover, as the sensitivity of the experiments increase, the background noise from neutrinos rises, providing confusion, which will need to be addressed in the future. Current results seem to point towards space-based experiments as the future for tests of standard model coupling, however with no evidence for physics beyond the standard model at the LHC, it is becoming increasingly difficult to pursue the WIMP paradigm.

2.3 Residual problems with the ΛCDM Universe

Despite the success of the CDM model, inconsistencies remain between simulations and observations. These discrepancies lie in the small-scale structure of the Universe, with simulations predicting far more large galaxy satellites that can produce stars than observed (Boylan-Kolchin et al., 2011; Moore et al., 1999; Klypin et al., 1999) and much cuspier dark matter profiles (Dubinski & Carlberg, 1991; Mateo, 1998) in observed dwarf galaxies. Though these problems lie well within the non-linear regime where baryonic processes are important, there are a few favoured mechanisms to resolve these inconsistencies:

- *Increasingly sophisticated baryonic process.* Our limited knowledge of the feedback loops involved in galaxy and star formation means that it is difficult to robustly simulate and predict the behaviour of baryons in cosmological simulations (Semboloni et al., 2011). It is thought that with increasingly sophisticated simulations, and a better understanding of baryonic processes, these discrepancies will resolve themselves (for a review of the processes see Pontzen & Governato 2014 and references therein).

- *The temperature of dark matter.* The current CDM model predicts large amounts of small-scale structure by decreasing the mass of the dark matter particle such that it had higher energies at earlier times, this small-scale structure can be suppressed. Warm Dark Matter (WDM) models, seem to predict the observed structure in the Universe well and produce less cuspy

profiles than those in CDM simulations (Lovell et al., 2012; King & Merle, 2012; Viel et al., 2005).

- *Self-interacting dark matter.* Current CDM simulations assume that dark matter does not interact with itself. However, it is plausible that in the event that dark matter exists that there are multiple families of particles, or indeed a single eigenstate that mixes with itself (e.g. Berezhiani et al., 1996; Mohapatra et al., 2002; Hodges, 1993; Feng et al., 2009). In the event that dark matter does self-interact, it will cause dark matter haloes to virialise faster, suppressing small-scale structure and produce far cuspier profiles than those in collisionless simulations (Peter et al., 2013; Rocha et al., 2013). In this study I will probe the third of these paradigms, analysing whether or not dark matter is truly collisionless.

2.3.1 Self-Interacting Dark Matter

The self-interacting dark matter (SIDM) paradigm was thought to be ruled out at the beginning the of the 21st Century, when Miralda-Escudé (2002) found that simulations of SIDM predicted far more spherical dark matter haloes than observed. However, consequential simulations with higher resolution showed this not to be true, and in-fact a cross-section of $1\text{cm}^2/\text{g}$ was as consistent with the data as collisionless dark matter (Yoshida et al., 2000; Meneghetti et al., 2001; Peter et al., 2013). Determining whether dark matter truly is collisionless has become vital, since any discovery of self-interaction would open the door to a new regime of particle physics and would dramatically constrain the parameter space for particle physics models.

Measuring SIDM with merging galaxy clusters

Unlike the standard model coupling of dark matter, the self-interaction can only be studied via astronomical observations. As seen in Figure 2.6 there are non standard model particles associated with the self-coupling and that it requires astronomical observations to test it (Livio & Silk, 2014). Initial attempts to constrain the cross-section were made by comparing the observation sphericity of dark matter haloes with simulations with varying values of σ_{DM} (Miralda-Escudé, 2002). Beyond this study, estimates of the cross-section of dark matter were made

using merging galaxy clusters.

The previous section dealt with the cosmology and astrophysics that can be carried out with relaxed galaxy clusters, however, like all structures in the Universe they are in a constant state of accretion and evolution. Just like any structure, clusters formed via the merging of smaller haloes, meaning that rare events can see galaxy clusters (and groups) merge. When they do so, the differential behaviour of each mass component is most evident and they become ideal laboratories to test the properties and behaviour of particles in highly energetic situations.

Merging galaxy clusters have provided some of the most conclusive evidence for the existence of dark matter. Detailed studies by Clowe et al. (2004), and subsequently Clowe et al. (2006) and Bradač et al. (2006), of the Bullet Cluster found direct evidence for a dark matter halo that had become separated during a cluster collision. After spectroscopic follow up of the cluster it became apparent that this merger was highly energetic with each halo exhibiting velocities > 1000km/s, which at the time was difficult to explain with the ΛCDM model. However Shan et al. (2010) highlighted that it was possible to find these events, just that they were very rare.

The Bullet Cluster was a rare event of a merging cluster. Subsequent analysis via simulations predicted that not only was this a particularly high speed merger, but the impact parameter was small, and to first approximation it was a head on collision (Randall et al., 2008). The differing interacting properties of gas and dark matter that resulted in the separation of the two haloes led to further analysis of the cross-section of dark matter (Markevitch et al., 2004). Since this was the first time that anyone had attempted to constrain the interacting properties, they proposed three methods;

- **Scattering depth**: Since the dark matter and gas is seen to separate, they can be qualitatively said to be behaving very differently, and unlike the gas, the dark matter is not acting like a fluid. As a result, the dark matter will have a scattering depth much less than one; $\tau << 1$, and therefore since the scattering depth is dependent on the projected surface density, Σ and the probability of scattering, then Markevitch et al. (2004) state

$$\frac{1}{\Sigma} > \sigma_{\rm DM}/m, \tag{2.28}$$

where $\sigma_{\rm DM}/m$ is the self-interacting cross-section per unit mass of dark matter, and find that $\sigma_{\rm DM}/m < 5{\rm cm}^2/{\rm g}$.

- **Velocity of the substructure** : Markevitch et al. (2004) estimated cross-section by analysing the change in velocity of the dark matter halo. Using the velocity of the group galaxies, they stated that any finite cross-section would result in a deceleration from its free-fall velocity, $v_{\rm ff}$:

$$v - v_{\rm ff} = \frac{\bar{p}}{m}\sigma_{\rm DM}/m\Sigma, \tag{2.29}$$

where they require that because the post-collision velocity is high, the LHS must be $v - v_{\rm ff} < 1000{\rm km/s}$, and they estimate the average momentum lost per collision per unit mass, $\hat{p}/m$ with simple collisional arguments and a dark matter particle mass of $m > 40{\rm GeV}$. From this they gain their loosest constraints of $\sigma_{\rm DM}/m < 7{\rm cm}^2/{\rm g}$.

- **Mass loss and haloes survival** : The final estimate proposed by Markevitch et al. (2004) is based on the hypothesis that during the merger, any interaction cross-section would result in the dark matter haloes losing dark matter via particle evaporation. They show that the expected fraction of particles lost during the collision, χ^{τ_m}, is given by:

$$\chi^{\tau_m} = \sigma_{\rm DM}/m\Sigma \left[1 - 2\left(\frac{v'_{\rm esc}}{v_0}\right)^2\right], \tag{2.30}$$

where the pre-merger escape velocity of the halo is given by $v'_{\rm esc} \approx v_{\rm esc}[1 + (1+f)^{1/2}]/2$, where the sub-halo has reduced in mass by $1+f$, and v_0 is the velocity of the halo (assumed to be constant). Using estimated M/L ratios, they estimate the mass of the haloes before collision getting $1 + f = 0.3$ and hence $\sigma_{\rm DM}/m < 1{\rm cm}^2/{\rm g}$.

Of these techniques, the first method was used by Bradač et al. (2008) to estimate the cross-section of dark matter, getting constraints of $\sigma_{\rm DM}/m < 4{\rm cm}^2/{\rm g}$, Merten et al. (2011) of $\sigma_{\rm DM}/m < 3{\rm cm}^2/{\rm g}$ and Dawson et al. (2012) gaining cross-section of $\sigma_{\rm DM}/m < 7{\rm cm}^2/{\rm g}$. After the first estimates of the cross-section of dark matter, groups attempted to simulate the merging of cluster haloes to constrain the cross-section of dark matter. Randall et al. (2008)

Table 2.2: Current constraints on the self-interacting cross-section of dark matter with associated potential problems (Bradač, 2013, Durham Ripples Conference)

Reference	$\sigma_{\rm DM}/m$ [cm^2/g]	From	Potential Issue
Randall et al. (2008)	< 0.7-1.25	Bullet Cluster	Assumed M/L prior to merger
Gnedin & Ostriker (2001a)	< 0.3	Dark matter (dm) evaporation	Over-prediction Evaporation
Markevitch et al. (2004)	< 1.0	Halo Evaporation	Assumed M/L prior to merger
Dawson et al. (2012)	< 7	dm–gas separation	N/A
Bradač et al. (2008)	< 4	dm–gas separation	N/A
Merten et al. (2009)	< 3	dm–gas separation	N/A

constrained the cross-section of dark matter using simulations of the Bullet Cluster. Assuming that dark matter scatters like hard snooker balls colliding such that when two particles come together in space they scatter elastically and with a completely random direction, Randall et al. (2008) gained constraints of < 0.7cm^2/g, assuming that both haloes had equal M/L ratios prior to the merger. To this day these constraints, are the tightest in the literature. Other constraints have included Gnedin & Ostriker (2001a) who gained constraints of $\sigma_{\rm DM}/m < 0.3$cm^2/g, however they over-predict the amount of evaporation in cluster galaxies. Table 2.3 shows the current constraints of dark matter in the literature.

In addition to those studies mentioned above, all with upper limits, Williams & Saha (2011, hereafter WS11) observed a separation between four dark matter haloes and four large elliptical galaxies in the galaxy cluster A3827. In this study they interpret this offset as a lower limit of a cross-section of dark matter. They modelled the self-interacting dark matter as a linear decelerating term that would cause a slow shift between a collisionless galaxy halo and an interacting (dark matter) halo. Using Newtonian dynamics they related the separation, d,

between dark matter and galaxies to the cross-section via

$$d \approx \frac{GM_{\rm co}M_{\rm dm}\sigma/m}{\pi r^2 s^2}t^2, \tag{2.31}$$

where $M_{\rm co}$ is the mass of the dark matter within the centre of the galaxy, $M_{\rm dm}$ is the dm mass of the halo, s is the size of the galaxy, r is the average distance from the cluster core, and t is the time for in-fall. Assuming radial orbits, a given density profile, point like spatial distribution of stars within the galaxy, assuming that the haloes act as point like particles such that there is no retarding force pulling the haloes back to the dark matter, and the time for in-fall is the Hubble time they find a *lower limit* of the cross-section of dark matter of

$$\sigma/m > 4.5 \times 10^{-7} \left(\frac{t}{10^{10}{\rm yr}}\right)^{-2} {\rm cm}^2{\rm g}^{-2}. \tag{2.32}$$

However it was noted that this value was sensitive to the selection of a very small number of multiple images. A subsequent study of this cluster and two others; A2218 and A1689, they found further offsets between the brightest cluster galaxy (BCG) and the dark matter peak as returned by strong lensing (Mohammed et al., 2014). In this study, they are somewhat more conservative on their interpretation of the offset dark matter stating that it could be line of sight structures, or wobbling of the BCG.

All of the current best constraints on the cross-section of dark matter that are estimated from one cluster are hampered by uncertainties in the impact parameters and the merger history. Re-simulating those mergers, although can reproduce the final observables, still have issues with initial conditions. However, by analysing a sample of clusters, estimates could be combined and averaged out.

2.3.2 Bulleticity

Attempts to constrain the self interaction cross section of dark matter from major galaxy cluster collisions faces two obstacles. First, measuring a separation between the dark matter and baryonic gas requires a merger between clusters of similar masses to be seen at just the right time since the first core passage, and these are rare events (Shan et al., 2010). Secondly, uncertainties in the impact velocity, impact parameter and orientation with respect to the line of

sight severely limit constraints from individual clusters (Randall et al., 2008).

Initially proposed by Massey et al. (2011, hereafter MKN), it was thought that it would be possible to exploit the continually accreting substructure into galaxy clusters as a method to probe the cross-section of dark matter. During in-fall, accreting groups would experience a similar effect to that of the Bullet Cluster, exhibiting a separation between dark matter and gas. Since these in-falling haloes were ubiquitous, it should be possible to make a statistical estimate of the cross-section using a sample of clusters, averaging over all in-fall scenarios and impact parameters. Assuming an isothermal sphere of a given characteristic density ρ_0 at r_0, and a density of the sub-halo, ρ_b, at a distance r from the cluster centre, MKN postulated that the deceleration of a sub-halo due to an interacting dark matter with a coupling, α, (analogous to the Thompson coupling parameter), would be

$$\frac{d^2\mathbf{r}}{dt^2} \approx -\frac{4\pi G\rho_0 r_0^2}{r^2}\left(1-(137\alpha)^2\frac{\rho_0 r_0^2}{\rho_\mathrm{b} r^2}\right)\mathbf{r}, \tag{2.33}$$

where the prefactor $(137\alpha)^2 \approx \sigma/\pi r_\mathrm{b}^2$ for a geometrically thin bullet. As I will show later, this treatment of the dark matter cross-section is not correct, as it models the macroscopic behaviour of an interacting dark matter as a buoyancy force. The separating force used in this method was linear in α^2, from small interactions all the way up to gas dynamics.

Although it is difficult to precisely resolve the positions and masses of individual pieces of small substructure, a statistical "bulleticity" signal can be obtained by averaging the measurements from many clusters. The bulleticity vector $\boldsymbol{b}$ is the offset between substructure's total mass (where dark matter dominates) and baryonic components in the plane of the sky

$$\boldsymbol{b} \equiv b_r\hat{\boldsymbol{e}}_r + b_t\hat{\boldsymbol{e}}_t, \tag{2.34}$$

where $\hat{\boldsymbol{e}}_r$ and $\hat{\boldsymbol{e}}_t$ are unit vectors in the radial and tangential directions with respect to the cluster centre.

Hydrodynamical simulations show that, despite complex and interacting processes, the net effect of cluster gastrophysics is a force on the substructure gas similar to a simple buoyancy that produces an offset $\langle b_r\rangle > 0$. The simulations also show that, with a sufficiently large sample and no preferred

in-fall handedness, $\langle b_t \rangle \equiv 0$. However, such a requirement is relatively easy to satisfy and does not necessarily mean that all systematics have been tested for, and although is a good sanity check, further tests should be carried out. Checking that measurements of this are consistent with zero will be a useful test for residual systematics.

MKN showed that for a ΛCDM paradigm with collisionless dark matter, the expected radial offset between baryonic and dark components of substructure is $\sim 10'', 3.5''$ and $2''$ at a redshift $z = 0.1, 0.3, 0.6$ respectively at a radial of distance of $0.15r_{500}$ (the radius at which the density is 500 times that the of the Universal mean density), which increased towards to the centre of the cluster. Therefore the measurement of an offset relies upon an ability to measure the position of substructure components with minimal bias near to the core. Statistical errors will be gradually beaten down by averaging many measured offsets. However any systematic bias in the centroid of either component would propagate into constraints on the interaction cross-section.

2.3.3 The differential cross-section

It is clear from each previous study associated with the cross-section, that how one deals with the dark matter scattering is not clear. In the observable sector of the Universe there are many types of scattering that can occur, each with different dependency on the scattering angle. To analyse this it is convenient to begin with the *differential cross-section*, which is the probability that a particle will scatter in a particular direction, then the total cross-section of a particle will be integral over the whole solid angle, Ω:

$$\sigma = \oint d\Omega \frac{d\sigma}{d\Omega}. \tag{2.35}$$

Most simulations have used a scattering mechanism that is independent of the scattering angle (e.g. Randall et al., 2008; Kochanek & White, 2000), however Kahlhoefer et al. (2014, hereafter K13) noted that in the case where there is a light mediator exchanged during the scattering, there will be some dependency on the angle, with the majority of the scatterings occurring transverse to the impact angle. K13 carried out an in-depth study into the observable effects of interacting dark matter in known interacting systems. They note that because the mass of a

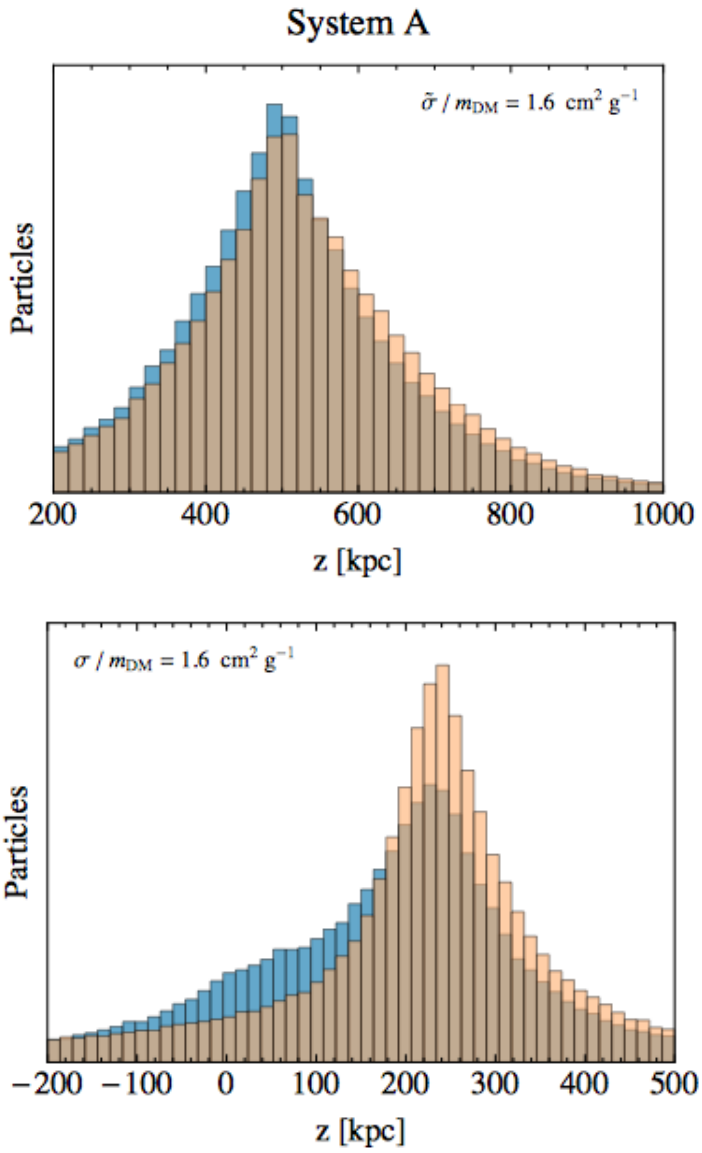

Figure 2.8: The effect of two different scattering mechanisms on the distribution of dark matter. Each panel shows the same merging system, A520, with the blue showing the resulting distribution of interacting dark matter and the orange showing the resulting galaxy particle distribution (assumed collisionless). The top panel shows the 1D distribution of dark matter particles for a scattering mechanism that occurs rarely with large amounts of momentum exchange. The bottom panel shows the resulting 1D distribution of dark matter in the event it interacts often with small amounts of momentum exchange.

dark matter particle is unknown, there will always be a degeneracy between $\sigma_{\rm DM}$ and the mass of the particle. However the degeneracy can be broken by analysing the different observable consequences of the two regimes;

- **Few interactions with large momentum exchange** : KS13 found that scatterings that had no angular dependence resulted in few interactions and large momentum exchange. This would result in particle evaporation during a merger, which may falsely be observed as a separation between dark matter and galaxies. However, as the top panel of Figure 2.8 shows, the distribution of dark matter particles (blue) after a merger remains coincident with the collisionless galaxy particles (orange) and hence they find no evidence for a separation between dark matter and galaxies.

- **Many interactions with small momentum exchange** : The amount of momentum exchanged during these types of interactions is heavily constrained by the Bullet Cluster since the amount of mass loss is thought to be only a factor of ~ 0.3. In the event that dark matter has an angular dependency (see Table 2.3), then the scatterings will occur in the direction of the collision and they will happen often. Since they occur regularly the amount of momentum exchanged will be small, resulting in a redistribution of dark matter particles. As the bottom panel of Figure 2.8 shows, the distribution of dark matter particles post merger (blue) does shift, with many of the particles trailing the galaxies (orange), however the peak of each distribution does remain coincident.

The results from K13, were important since it was clear that different scattering mechanisms resulted in different observables, and therefore observations of dark matter-galaxy separation would be constraining a different $\sigma_{\rm DM}$ than if they were estimating $\sigma_{\rm DM}$ from the mass loss during a merger. Although the study here by K13 was the first in-depth study of dark matter scatterings, these were numerical simulations and future detailed simulations should be carried out to examine the extent of these results, and if there truly is no mean halo separation.

2.3.4 Scientific aims of this thesis

The cold dark matter paradigm has clearly many successes, but also important flaws that must be resolved in order to fully understand dark matter and its role

Table 2.3: Angular Dependence of different scattering mechanisms

Type	Angular Dependence
Hard-sphere	$\frac{\mathrm{d}\sigma}{\mathrm{d}\Omega} \propto R^2$
Thompson	$\frac{\mathrm{d}\sigma}{\mathrm{d}\Omega} \propto 1 - \cos^2\phi$
Rutherford	$\frac{\mathrm{d}\sigma}{\mathrm{d}\Omega} \propto \csc^4(\phi/2)$

in structure formation in the Universe. To this end, the aim of this thesis is to critically analyse the self-interacting dark matter paradigm, both theoretically and observationally. Specifically I aim to

- Develop an improved theoretical model of dark matter self-interactions during substructure in-fall and show how this can be used to directly constrain the cross-section of dark matter from observations without the need for simulations
- To develop a weak lensing and X-ray data analysis pipeline that can be used for an inhomongenous sample of galaxy clusters
- Predict the impact of systematics on the measurements of the cross-section of dark matter
- To constrain the cross-section of dark matter from a sample of galaxy clusters.

Outline of this thesis

This thesis is organised as follows: I will initially outline the theory of gravitational lensing in Chapter 3. Following the MKN hypothesis that dark matter should separate during in-fall as well as during major mergers, in Chapter 4 I will develop a new method to estimate the cross-section of dark matter. In this chapter I will also re-iterate the importance of understanding how the observable relates to the underlying scattering mechanism. In Chapter 5 I will analyse the prospects of measuring dark matter substructure in galaxy clusters, making the most stringent test of weak lensing in galaxy clusters to date. In doing so I will identify the impact of weak lensing systematic on the measurement of σ_{DM}. In Chapter 6 I will develop a new pipeline specifically to measure the cross-section

of dark matter, and will observationally constrain SIDM from an inhomongenous sample of galaxy clusters. In Chapter 7 I will conclude and propose work for the future.

3 Gravitational Lensing

"Never was anything great achieved without danger."

As first suggested by Newton, photons, just like matter, feel the gravitational pull of other bodies in close proximity. The result is that as light traverses the Universe, its path or geodesic, is distorted resulting in the apparent deformation and magnification of the emitting object. Although predicting a similar effect, Einstein's theory of relativity hypothesised that the deformation would be twice that of Newtonian distortion. In May 1919, after careful measurement of the position of objects just behind the sun during an eclipse, Dyson et al. (1920) showed that in fact Einstein and his theory of relativity were correct. It took almost 60 years after this measurement for astronomers to make the first detection of cosmological gravitational lensing with Walsh et al. (1979) discovering the first gravitational lensed quasar, 0957+561, bringing lensing to the forefront of cosmology.

For a full review please see Bartelmann & Schneider (2001); Massey et al. (2010); Refregier (2003); Hoekstra & Jain (2008). Einstein gravity predicts that for a point mass, the angle that a photon will be deflected by $\hat{\boldsymbol{\alpha}}$, is given by

$$\hat{\boldsymbol{\alpha}} = \frac{4GM}{c^2 \boldsymbol{\xi}}, \tag{3.1}$$

where c is the speed of light, M is the mass of the deflecting lens and ξ is the impact parameter (or how close the photon is to the point mass at closest approach). For an extended halo made of many small elements of mass, $dm = \rho(\boldsymbol{r})dV$, then the deflection angle for a photon will be the summed total of the many small deflections due to the mass elements at position $\boldsymbol{\xi}'$ and the photon position $\boldsymbol{\xi}$

$$\begin{aligned}\hat{\boldsymbol{\alpha}}(\boldsymbol{\xi}) &= \frac{4G}{c^2}\sum dm\frac{\boldsymbol{\xi}-\boldsymbol{\xi}'}{|\boldsymbol{\xi}-\boldsymbol{\xi}'|^2},\\ &= \frac{4G}{c^2}\int d^2\xi\int dr'\rho(r)\frac{\boldsymbol{\xi}-\boldsymbol{\xi}'}{|\boldsymbol{\xi}-\boldsymbol{\xi}'|^2},\end{aligned} \tag{3.2}$$

where the second integration is from where the photon was emitted to where it was observed, and hence the integration of the density along the line of sight is just the projected surface mass density, $\Sigma(\boldsymbol{\xi}')$

$$\hat{\boldsymbol{\alpha}}(\boldsymbol{\xi}) = \frac{4G}{c^2}\int d^2\xi\ \Sigma(\boldsymbol{\xi}')\frac{\boldsymbol{\xi}-\boldsymbol{\xi}'}{|\boldsymbol{\xi}-\boldsymbol{\xi}'|^2}. \tag{3.3}$$

Since this does not differentiate between what matter is causing the distortion, gravitational lensing traces the total mass distribution; light and dark.

3.1 The basics of gravitational lensing

Gravitational lensing can be considered a geometrical mapping from a source plane, where the photon began, to the image plane, where it is observed. This is simply described by the lens equation, which simply shows how the coordinate in the source plane, $\boldsymbol{\beta}$ is deflected by some angle $\boldsymbol{\alpha}$ to give a new coordinate $\boldsymbol{\theta}$, i.e.

$$\boldsymbol{\beta} = \boldsymbol{\theta} - \hat{\boldsymbol{\alpha}}. \tag{3.4}$$

Since this is an angular separation on the sky, rather than equation (3.3), which defines the deflection angle in terms of the proper separation between a point mass and the photon, it is useful to use the scaled deflection angle which is simply $\boldsymbol{\alpha} = \frac{D_{\rm ls}}{D_{\rm s}}\hat{\boldsymbol{\alpha}}$, where $D_{\rm ls}$ is the distance from the lens to the source, $D_{\rm l}$ is the distance from the observer to the lens and $D_{\rm s}$ is the distance from the observer to the source, making $\boldsymbol{\xi} = D_{\rm l}\boldsymbol{\theta}$, where $\boldsymbol{\theta}$ is the angular separation on the sky (and

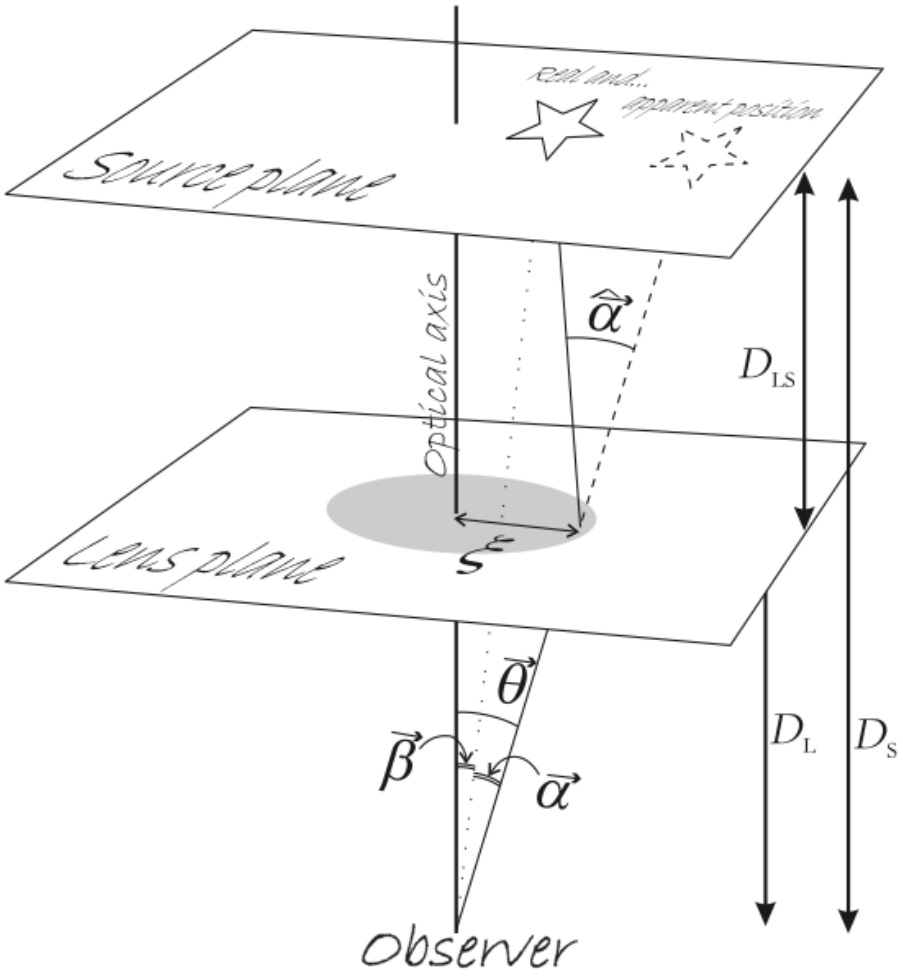

Figure 3.1: Typical geometry of a gravitational lens.

hence all distances are angular diameter distances). Figure 3.1 shows the lensing framework. It is also convenient to now define the dimensionless convergence, κ as

$$\kappa = \frac{\Sigma}{\Sigma_{cr}} \quad \text{where} \quad \Sigma_{cr} = \frac{c^2}{4\pi G}\frac{D_\mathrm{s}}{D_\mathrm{l} D_\mathrm{ls}}, \tag{3.5}$$

then the deflection angle (equation (4.1)) in terms of the angular separation of the photon from the lens is

$$\boldsymbol{\alpha}(\boldsymbol{\theta}) = \frac{1}{\pi}\int d^2\boldsymbol{\theta}'\kappa(\boldsymbol{\theta}')\frac{\boldsymbol{\theta}-\boldsymbol{\theta}'}{|\boldsymbol{\theta}-\boldsymbol{\theta}'|^2}. \tag{3.6}$$

According to Einstein gravity, the deflection of a photon is related to the gradient of the potential via

$$\boldsymbol{\alpha} = \nabla\psi, \tag{3.7}$$

where ψ is the 2 dimensional lensing potential and is given by integrating the three dimensional potential, Φ, along the line of sight

$$\psi = \frac{D_\mathrm{ls}}{D_\mathrm{l} D_\mathrm{s}}\frac{2}{c^2}\int \Phi(D_\mathrm{l}, \boldsymbol{\theta}, z)dz, \tag{3.8}$$

we can related the convergence (surface density) to the distorting potential using equations (3.6) and (3.7) via

$$\psi = \frac{1}{\pi}\int \kappa(\boldsymbol{\theta}) \ln|\boldsymbol{\theta}-\boldsymbol{\theta}'|d^2\boldsymbol{\theta}'. \tag{3.9}$$

Inverting this equation, it is given that the dimensionless surface density κ is simply a combination of the second derivatives of the lensing potential given by

$$\kappa(\boldsymbol{\theta}) = \frac{1}{2}\left(\psi_{11}+\psi_{22}\right) = \frac{1}{2}\nabla^2\psi, \tag{3.10}$$

where the subscripts of ψ refer to the derivative of the lensing potential in orthogonal directions of the sky. In fact the derivative of equation (3.4) shows how the change in the source plane changes with the mapping to the image plane,

and using equation (3.3), it follows that

$$\frac{\partial \boldsymbol{\beta}}{\partial \boldsymbol{\theta}} = \delta_{ij} - \frac{\partial^2 \psi}{\partial \boldsymbol{\theta}_i \partial \boldsymbol{\theta}_j}. \tag{3.11}$$

The resulting mapping matrix gives the Jacobian matrix, A which defines how an object is transformed (in the weak limit) during lensing in terms of these second derivatives (where assuming weak lensing means stopping at higher order terms and ignoring linear terms that can't be measured for galaxies)

$$A = \begin{pmatrix} 1-\psi_{11} & -\psi_{12} \\ -\psi_{21} & 1-\psi_{22} \end{pmatrix} = \begin{pmatrix} 1-\kappa & 0 \\ 0 & 1-\kappa \end{pmatrix} + \begin{pmatrix} -\gamma_1 & -\gamma_2 \\ -\gamma_2 & \gamma_1 \end{pmatrix}, \tag{3.12}$$

where positive (negative) γ_1 corresponds to a stretching along the x (and y) axis, and positive (negative) γ_2 corresponds to a stretching along the 45° (135°). The first part of A containing κ corresponds to a magnification (or demagnification) and the second part corresponds to a shear as shown in Figure 3.1, with

$$\gamma_1 = \frac{1}{2}\left(\psi_{11} - \psi_{22}\right) \qquad \gamma_2 = \psi_{21}. \tag{3.13}$$

As light moves past over densities within the Universe the effect is a tangential shear, $\gamma_{\rm t}$, given by

$$\gamma_{\rm t} = -\left(\gamma_1 \cos(2\phi) + \gamma_2 \sin(2\phi)\right) \quad \text{and} \quad \gamma_\times = -\gamma_1 \sin(2\phi) + \gamma_2 \cos(2\phi), \tag{3.14}$$

where ϕ is the position angle of the galaxy with respect to the centre of the deflecting potential, and the cross-shear, $\gamma_\times$, gives the error in the tangential shear estimate.

This matrix also highlights a particularly important aspect of gravitational lensing, which is that that there is a fundamental degeneracy between the shear and the the convergence, and only the reduced shear can be directly observed, which is given by

$$g = \frac{\gamma}{1-\kappa}, \tag{3.15}$$

where the complex notation of γ and g has been used, whereby $\boldsymbol{\gamma} = |\gamma| e^{-i2\boldsymbol{\theta}}$, with

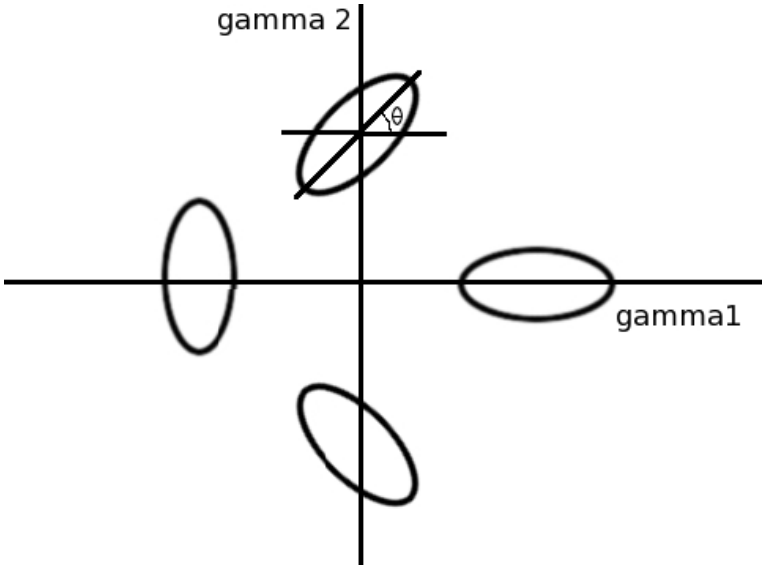

Figure 3.2: The effect of gravitational shear, γ on a circularly symmetric galaxy. A positive (negative) γ_1 corresponds to a stretching along the x (and y) axis, and positive (negative) γ_2 corresponds to a stretching along the 45° (135°).

$\boldsymbol{\theta}$ defining the angle of the galaxy from the the positive x-axis.

According to Liouville's theorem, lensing conserves surface brightness, such that the number of photons does not change, they just move around so the image becomes distorted. Therefore, the magnification, μ, of an object can be defined as

$$\mu = \frac{\text{image area}}{\text{source area}} = \frac{\delta\boldsymbol{\theta}^2}{\delta\boldsymbol{\beta}^2} = \frac{1}{(1-\kappa)^2 - |\gamma|^2} \approx 1 + 2\kappa. \tag{3.16}$$

3.2 Observing gravitational lensing

Gravitational lensing has become a key tool in the continuing effort to understand the Universe. Its independence from any assumptions on the dynamical state of structure, free from unknown galaxy bias, tracing the underlying matter power spectrum, and with the increased resolution and sensitivity of ground and space-based telescopes, has now resulted in the first constraints from the gravitational lensing by the large scale structure, or 'cosmic shear' (e.g. Wittman et al., 2000; Bacon et al., 2000; Van Waerbeke et al., 2000; Kaiser et al., 2000; Kilbinger et al., 2013; Massey et al., 2007b). In order to fully exploit the benefits of gravitational

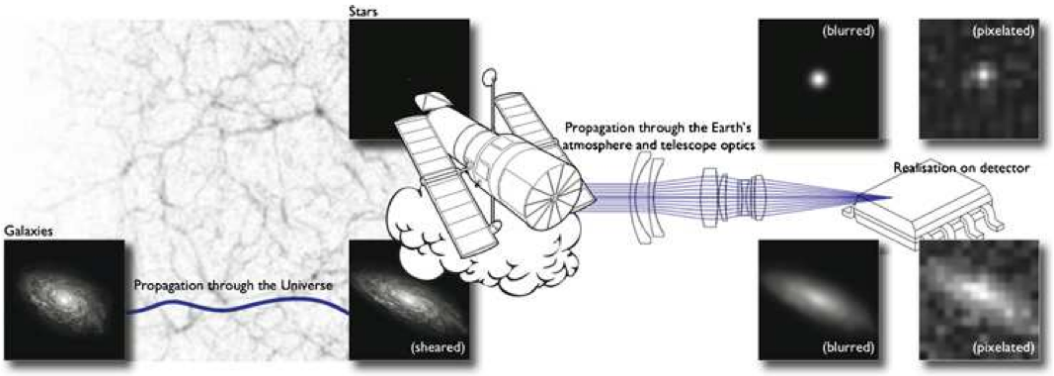

Figure 3.3: The main effects on a galaxy image as it traverses the Universe. The initial galaxy, with some intrinsic ellipticity is sheared, the galaxy is then blurred by the point spread function of the telescope due to either abnormalities in the optics or the atmosphere, and then the image is pixelised and made noisy (Kitching et al., 2010). The aim is to reverse the observed effects to measure the initial shearing.

lensing the shapes of galaxies need to be measured to sub-percent accuracy (e.g Amara & Refregier, 2006; Laureijs et al., 2011), with many methods existing to measure the shape of galaxies and hence their gravitational shear.

Unfortunately this is difficult as photons from distant galaxies are affected by many different processes. Figure 3.3 shows how the image of a galaxy is changed at different stages. The galaxy begins, not as a circular image but it has some intrinsic ellipticity, $\chi^{(s)}$, it is then sheared by the matter that permeates the Universe. It then enters the atmosphere and the telescope where they both imprint a point spread function (PSF) on the image. This reflects the different refractive indices of the atmosphere and the abnormalities that exist in the telescope. Finally the photons hit the camera and are pixelised with some added noise $\sigma_{\rm shape}$, to the get the final image. The aim is to reverse these effects such that the shear can be estimated.

The most common forms of shape measurement are either model fitting realistic galaxy profiles to an image and and estimate a ellipticity via some best fit parameters (e.g. Miller et al., 2007; Zuntz et al., 2013) or contracting the image down to statistics known as moments (e.g. Kaiser et al., 1995; Rhodes et al., 2000). For the purposes of this thesis I will concentrate on the latter as this is used later on.

Moments based

The distribution of light intensity in an image can be decomposed into normalised 'image moments' given by

$$Q_{ij} = \frac{\int (x - x_0)^i (y - y_0)^j I(x, y) w(x, y) dx dy}{\int I(x, y) w(x, y) dx dy}, \tag{3.17}$$

where the amount of flux at x and y is given by $I(x, y)$, i and j give the moment of order $i + j$, the weight function, w causes the integral to converge in the wings and is usually Gaussian with a width from the initial estimate of the size of the galaxy, and the centre of the isophote (x_0, y_0) is given by setting the first order moment to zero. Using this the complex ellipticity, $\epsilon = \epsilon_1 + i\epsilon_2$ of a galaxy using the second and fourth order moments can be described by

$$\begin{aligned} \epsilon &= \frac{Q_{11} - Q_{22} + 2iQ_{12}}{Q_{11} + Q_{22}} \\ &= \frac{a^2 - b^2}{a^2 + b^2} e^{-2i\boldsymbol{\theta}}, \end{aligned} \tag{3.18}$$

where the ellipticity has also been expressed as a combination of its major (a) and minor (b) axes, $\boldsymbol{\theta}$ is the position angle the galaxy makes with the x-axis, and the size of a galaxy is normally, $d = \sqrt{(Q_{11} + Q_{22})/2}$.

Having constructed a mathematical description of the ellipticity of a galaxy via its moments, Q, it is possible to calculate how these transform under the Jacobian, A, via the matrix multiplication, AQA^T. This will determine how the intrinsic moments of a galaxy, and hence the ellipticity, map from the source plane, $\epsilon^{(s)}$ to the ellipticity in the image plane, ϵ

$$\epsilon^{(s)} = \frac{\epsilon - 2g + g^2 \epsilon^\star}{1 + |g|^2 - 2\Re(g\epsilon^\star)}, \tag{3.19}$$

where the star denotes the complex conjugate (Bartelmann & Schneider, 2001). In the weak lensing limit, such that g is very small, this simply becomes, $\epsilon^{(s)} = \epsilon - 2\gamma$. Unfortunately, the intrinsic ellipticity is unknown, and hence so is the shear. However, the intrinsic ellipticity of individual galaxies is not required, all that is, is that the assumption that all galaxies are randomly orientated such that $\langle \epsilon^{(s)} \rangle = 0$ needs to hold. By Taylor expanding each component of observed

ellipticity, ϵ_i to first order only, it is possible to exploit this assumption

$$\epsilon_i = \epsilon_i^{(s)} + \frac{\partial \epsilon_i^{(s)}}{\partial \gamma_j}\gamma_j + ... \,, \tag{3.20}$$

where the coefficient of the second term is the shear susceptibility tensor, or P_{ij}, which is diagonal if the isophote has a well defined centre. Assuming that this tensor is diagonal such that it is reduced this to a scalar, $P_{\rm sh}$ and dividing through by $P_{\rm sh}$, then using the fact that all galaxies are randomly orientated and averaging over many galaxies (and hence removing the first term of equation (3.20)), it is possible to construct a noisy estimator of the shear

$$\langle \tilde{\gamma_i} \rangle = \langle \frac{\epsilon_i}{P_{\rm sh}} \rangle = \langle \gamma_i \rangle + \langle \epsilon_i^{(s)} \rangle = \langle \gamma_i \rangle, \tag{3.21}$$

where

$$P_{\rm sh} \approx \frac{\partial \epsilon_i^{(s)}}{\partial \gamma_j} \qquad \text{and} \qquad \epsilon_i = \frac{a-b}{a+b} e^{i2\theta} \tag{3.22}$$

Equation (3.21) shows that with an estimation of $P_{\rm sh}$, an estimate of the shear of an individual galaxy can be obtained with the uncertainty defined by the width of the intrinsic ellipticity distribution, σ_ϵ.

In addition to the intrinsic shape of galaxies, the shape measurement also suffers from effects caused by the telescope and the atmosphere that imprints as PSF,

$$\epsilon^{(T)} = \epsilon + P_{sm*}\epsilon_*, \tag{3.23}$$

where the total ellipticity, $\epsilon^{(T)}$ is the observed ellipticity plus a combination of the star ellipticity and a smearing susceptibility. Here it is assumed that the star's ellipticity, ϵ_*, is a clean estimate of the PSF, since theoretically a star is a delta function and therefore, the convolution of a PSF imprints only the PSF. This acts to complicate equation (3.21)

$$\tilde{\gamma} = (P^\gamma)^{-1} \left(\epsilon - \frac{P_{\rm sm}}{P_{\rm sm*}} \epsilon_* \right), \tag{3.24}$$

where $P^\gamma = P_{\rm sh} - P_{\rm sm}(P_{\rm sm*})^{-1} P_{sh*}$. This relation will hold if the source is smeared

isotropically.

This standard method to measure moments and correct for PSF was outlined by Kaiser et al. (1995, hereafter KSB) and corrects ellipticities, however a method laid out by Rhodes et al. (2000, hereafter RRG) developed a technique that corrected for the PSF using the raw moments. RRG highlighted that the KSB method had some shortcomings, specifically that the second order moments of the PSF depended heavily on the weight used, with this even more so for PSFs with broad wings such as some space-based telescopes. Therefore, this method was designed for space-based observations, and hence the analytical correction to the moments in this technique are only valid when the PSF is much smaller than the galaxy (which is not true for ground-based techniques).

3.3 Dark matter mass mapping

Gravitational lensing is caused by the mass along the radial path of a photon distorting its null geodesics as the travel through the Universe. It is possible to use this phenomenon to map out the total matter in the Universe, projected onto a 2D surface. Dark matter mapping is a slight misnomer since as mentioned, gravitational lensing probes *all* the matter along the line of sight, however in a Universe that is dominated by dark matter, to first order, this is what lensing is doing.

It has become common place to map out the dark matter in the Universe on both small and large scales, however the methods to do so are varied. Since the background galaxies are being sheared by the same deflecting potentials, their shapes will become correlated. Figure 3.4 shows the distorting effect of foreground structure on distant galaxies (Jain et al., 2000). Each tick mark represents the ellipticity of a galaxy in a 1° field caused by the integrated mass along the line of sight. In this ray-tracing simulation, galaxies are assumed to have no intrinsic ellipticity such that any observed ellipticity is caused by the shearing effect of the foreground structure shown in white. The correlated tangential shear can be clearly seen around the large over-densities. These correlated shapes can be used to map out the distribution of dark matter in the observed Universe, whilst extracting cosmological parameters.

Large scale maps, such as those in Figure 3.4 (and larger), have been used

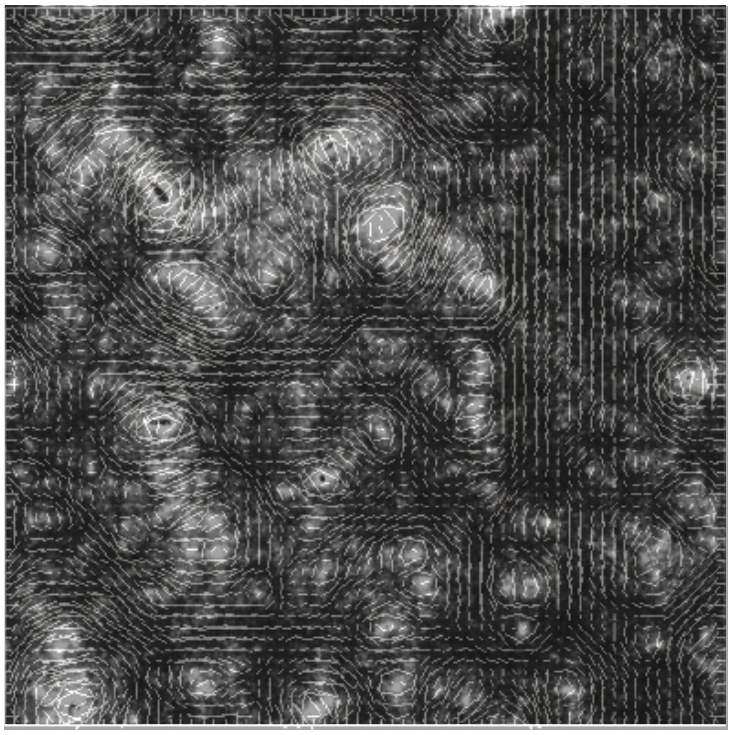

Figure 3.4: The results of a ray tracing simulation. Each tick mark represents the ellipticity of a galaxy caused by the background over density (white diffuse clouds). The correlated shapes of galaxies can be clearly seen at the over densities of matter. These correlated shapes can be used to map out the dark matter on large scales, extracting cosmological parameters, and on small to test the nature of dark matter (Jain et al., 2000).

mainly to show qualitatively that the kind of structure seen in simulations does resemble what is observed in the Universe (Van Waerbeke et al., 2013; Massey et al., 2007b; Schrabback et al., 2010). However, they have also been used directly for cosmology via convergence peak counts. Peak counting relies on the hypothesis that there should be a certain number and distribution of mass peaks in the Universe given a certain cosmological model. By comparing the number and mass of haloes observed to those calculate in simulations the best fitting cosmological model can be constrained (Hamana et al., 2004)

Dark matter mapping on the galaxy cluster scale has also become a rich source of science (e.g. Postman et al., 2012). The density of matter in galaxy clusters results in a lensing signal that is extremely strong, ranging from weak regime in the outer wings to strong lensing in the core, where arcs and multiple images of distorted distant galaxies are often observed. The first detection of such strong lensing arcs was in the Abell cluster A370 (Lynds & Petrosian, 1986; Soucail et al., 1988). Methods to model and reconstruct the dark matter in galaxy clusters are varied, with some using a direct inversion of the shear to the convergence, and others that fit analytical models of dark matter haloes to the data. Here I will outline the basics of these methods.

3.3.1 Direct inversion : Kaiser and Squires

Equation (3.12) relates the observables, κ and γ, to the lensing potential ψ. Therefore, since the two effects are caused by the same underlying potential, κ can be directly related to γ (Kaiser & Squires, 1993, hereafter KS93). Rewriting equation (3.10) as $\kappa = \frac{1}{2}\nabla^2\Psi$, it has already been shown that

$$\gamma_i = D_i\psi \qquad \text{where} \qquad D_i = \begin{pmatrix} \partial^2/\partial\theta_1\theta_1 - \partial^2/\partial\theta_2\theta_2 \\ 2\partial^2/\partial\theta_1\theta_2 \end{pmatrix}. \tag{3.25}$$

Take the Fourier transform of each of these the potential Ψ can be eliminated from the equation to get

$$\tilde{\gamma}_i = \chi_i\tilde{\kappa}, \qquad \text{where} \qquad \chi_i = \frac{1}{k^2}\begin{pmatrix} k_1^2 - k_2^2 \\ 2k_1k_2 \end{pmatrix} \tag{3.26}$$

where k is the wavenumber and is $k = \sqrt{k_1^2 + k_2^2}$ and tildes represent the Fourier transform. Therefore the dimensionless surface density can be related directly to the observed shear. However, this method uses Fourier transforms which assumes periodic boundaries, which isn't true in the case of a finite field, and hence this breaks down at the edges, returning spurious effects. Since the above calculation is simply a convolution the transformation can be carried out directly in real space using the convolution theorem, finding that

$$\kappa = \frac{2}{\pi} \int d^2\boldsymbol{\theta}' \frac{\chi_i(\theta_i' - \boldsymbol{\theta}_i)}{(\boldsymbol{\theta}_i' - \boldsymbol{\theta}_i)^2} \gamma_i(\boldsymbol{\theta}'). \tag{3.27}$$

This method assumes a continuous shear field, and therefore in practice, where there are point estimators of the field, a window function that smooths between galaxies is required, and hence the resolution of a mass map from this technique (and any technique) is limited by the separation of galaxies and the smoothing kernel used. Moreover, the integration is from minus infinity to infinity, and therefore in the event of a finite field, this method will also suffer from edge effects.

3.3.2 Aperture mass

Although a non-parametric inversion, KS93 has problems convolving the shear field, resulting in spurious peaks of convergence. Another non-parametric method that avoids any convolution is the aperture mass statistics, $M_{\rm AP}$. This sums the tangential shear, $\gamma_{\rm t}$ within some radius, centred around a given point and smoothed with some window function, Q,

$$M_{\rm AP} = \int_0^R d^2\boldsymbol{\theta} Q(\boldsymbol{\theta}, \theta) \gamma_t(\boldsymbol{\theta}), \tag{3.28}$$

and is the expected signal that lensing imprints on a galaxy (Schneider & Bartelmann, 1997). The perpendicular measurement, which uses $\gamma_\times$ instead of $\gamma_{\rm t}$ in equation (3.28), gives an estimate of the error in the mass within the aperture.

Model Fitting : LENSTOOL

It is possible to reconstruct the dark matter in a cluster by fitting analytical profiles of dark matter haloes directly to the data. Wright & Brainerd (2000) and

Lasky & Fluke (2009) both set out the equation expressing the lensing signal that a dark matter halo would imprint on a galaxy at a projected position within that halo for various density profiles. For example, the signal for a particular galaxy at a distance, $\boldsymbol{\theta}$ from the centre of a singular isothermal sphere (SIS) would be:

$$|\gamma| = \frac{\theta_{\rm E}}{2\theta}, \tag{3.29}$$

where $\boldsymbol{\theta}_{\rm E}$ is the Einstein radius and is given by the constant velocity dispersion, σ within the halo (which defines an SIS) and the critical surface density, $\boldsymbol{\theta}_{\rm E} = G\,\Sigma_{\rm cr}/\sigma^2$. Also, for an SIS profile, the shear and the convergence are equal. Since this work mainly uses the NFW profile, here we report the analytical equations for the convergence, $\kappa = \Sigma/\Sigma_{\rm c}$, and shear, γ,

$$\Sigma_{NFW}(x) = \begin{cases} \frac{2r_s\delta_c\rho_c}{x^2-1}\left[1 - \text{arctanh}\sqrt{\frac{1-x}{1+x}}\right] & x < 1 \\ \frac{2r_s\delta_c\rho_c}{3} & x = 1 \\ \frac{2r_s\delta_c\rho_c}{x^2-1}\left[1 - \arctan\sqrt{\frac{x-1}{1+x}}\right] & x > 1, \end{cases} \tag{3.30}$$

and

$$\Sigma_{\rm c} = \frac{c^2}{4\pi G}\frac{D_s}{D_d D_{ds}}, \tag{3.31}$$

$$\gamma_{NFW}(x) = \begin{cases} \frac{r_s\delta_c\rho_c}{\Sigma_c} f_<(x) & x < 1 \\ \frac{2r_s\delta_c\rho_c}{\Sigma_c}\left[\frac{10}{3} + 4\ln\left(\frac{1}{2}\right)\right] & x = 1 \\ \frac{2r_s\delta_c\rho_c}{\Sigma_c} f_>(x) & x > 1, \end{cases} \tag{3.32}$$

$$\begin{aligned} f_<(x) = \; & \frac{8\text{arctanh}\sqrt{(1-x)(1+x)}}{x^2\sqrt{1-x^2}} + \frac{4}{x^2}\ln\left(\frac{x}{2}\right) \\ & -\frac{2}{(x^2-1)} + \frac{4\text{arctanh}\sqrt{(1-x)/(1+x)}}{(x^2-1)(1-x^2)^{1/2}}, \end{aligned} \tag{3.33}$$

$$\begin{aligned} f_>(x) = \; & \frac{8\text{arctanh}\sqrt{(x-1)(1+x)}}{x^2\sqrt{x^2-1}} + \frac{4}{x^2}\ln\left(\frac{x}{2}\right) \\ & -\frac{2}{(x^2-1)} + \frac{4\text{arctanh}\sqrt{(1-x)/(1+x)}}{(x^2-1)^{3/2}}, \end{aligned} \tag{3.34}$$

and $x = r/r_s$. δ_c is the characteristic over density of a halo and is a function of the concentration parameter and ρ_c is the critical density. Thus by placing down multiple haloes of different mass and assuming that to first order $\gamma_{tot} = \gamma_{\rm mainhalo} + \gamma_{\rm subhalo_1} + \gamma_{\rm subhalo_2} + \cdots + \gamma_{\rm subhalo_n}$ an analytical model of a cluster can be created.

By proposing various combinations of parameters for the chosen density profile and determining the resulting shear signal, it would be possible to compute the best fitting parameters via some quality factor. However how the sampler explores this parameter space and compares the shear is dependent on the mass reconstruction method. Here I will discuss one particular method : LENSTOOL (Jullo et al., 2007). I choose this particular method and explain in detail how it works as it will become clear later that it is a vital part of this thesis. This is because model fitting is a convenient and direct approach when only a few parameters are needed, with marginalisation over every other parameter.

LENSTOOL is a publicly available strong and weak lensing reconstruction method that fits analytical fits of dark matter haloes to the data and then returns the posterior likelihoods of the multidimensional parameter space. LENSTOOL can use a variety of different density profiles to fit, and then samples using Monte Carlo Markov Chain, with slice sampling.

The basis of LENSTOOL is in Bayes's theorem that states that the probability of a particular set of parameters, $\boldsymbol{\theta} = \{\theta_1, \theta_2 ...\}$, given some data D is

$$p(\boldsymbol{\theta}|D) = \frac{p(D|\boldsymbol{\theta})p(\boldsymbol{\theta})}{p(D)}, \tag{3.35}$$

where

- $p(\boldsymbol{\theta}|D)$ is the posterior (the probability of the shear given the set of parameters for a dark matter halo)
- $p(D|\boldsymbol{\theta})$ is the likelihood (the probability the shear given the set of dark matter parameters)
- $p(\boldsymbol{\theta})$ is the prior belief in the data (i.e. dark matter haloes will have a mass ranging between $M = [0 - 10^{16} M_{\odot}]$)
- $p(D)$ is the evidence (that it is intact a NFW with the defined parameters)

To calculate the likelihood of a given set of dark matter halo parameters, LENSTOOL converts the observed semi major and minor axes into ellipticities, ϵ and then maps these back to the source plane via equation (3.19) using the proposed dark matter halo parameters. The resulting ellipticities in the source plane should reflect the intrinsic (assumed) Gaussian distribution of galaxy ellipticities with a mean of zero and variance, σ_ϵ. Therefore the likelihood is defined as

$$p(D|\boldsymbol{\theta}) = \frac{1}{(2\pi\sigma^2)^{N/2}} e^{-\chi^2/2}. \quad \text{where} \quad \chi^2 = \sum_{i=1}^{N} \frac{(e_i^{(s)})^2}{\sigma_i^2}, \tag{3.36}$$

where the sum is over N galaxies and the total error in the ellipticity, σ, is the sum of the intrinsic ellipticity and the shape measurement error added in quadrature, i.e. $\sigma = \sqrt{\sigma_\epsilon^2 + \sigma_{\text{shape}}^2}$. Since the variance of ellipticity, σ_ϵ can be estimated, the final best fitting model should have a χ^2/number of degrees of freedom (dof) should be approximately equal one.

This quality factor can now determine how well a given set of parameters fits the data, and can hence systematically search to find the best fitting parameters. One method to test the parameters is to just move through the defined parameter range, with a constant increment. This grid based sampling technique is computationally expensive, with the number of calculations = N^D, where N is the number of samples and D is the number of parameters (dimensions). For a given NFW halo, with 6 parameters (position, mass, concentration, ellipticity and angle), and $\sim$ 1000 samples, this will amount to an unfeasible 10^{18} calculations. It is possible to be more sophisticated and use a Monte Carlo Markov Chain method.

Monte Carlo Markov Chains (MCMC) are simply semi-random walks through a parameter space with a tendency to move towards regions of higher probability. The benefit is that computational time is not wasted sampling areas of the parameters space that are very unlikely, however the negative is that maximum likelihood metropolis hastings MCMC are sensitive to local maxima in the likelihood surface. There are methods to mitigate getting stuck in local regions of high likelihood such as having numerous chains, all beginning in different parts of the parameter space and seeing if they evolve to the same point. Alternatively, it is useful to have an adaptive step length between chosen parameters which

depends on the likelihood at that position, such that if the likelihood is low then it can have a larger step to the next proposed parameter set (i.e. slice sampling).

The way that LENSTOOL samples the posterior is that it has an initial burn-in phase where it calculates the posterior using a slightly adapted Bayes theorem

$$p(\boldsymbol{\theta}|D) = p(D|\boldsymbol{\theta})^{\lambda} p(\boldsymbol{\theta}), \tag{3.37}$$

where λ is some scaling factor that places more or less importance for a given likelihood. On the initial burn-in, λ will be 0, placing all the weight on the prior, and then over time it will place increasing emphasis on the likelihood, until it reaches 1, when the prior is irrelevant and the weight is on the likelihood and the burn-in phase is finished.

After this point, how LENSTOOL samples depends on the user. It has two modes, denoted 'Inverse 3' and 'Inverse 4' in the LENSTOOL package:

- **Inverse 3** : The first mode is the full posterior mode, where λ remains at 1 meaning that although the sampler prefers to sample more likely regions, it still probes and samples the outer regions of the posterior surface

- **Inverse 4** : The second mode continues to increase λ post burn-in, placing further weight on high regions of likelihood, causing the sampler to quickly converge on the most likely region and return the best fitting parameters within the given priors.

The first is useful to estimate the width of the posterior and hence the uncertainties in parameter estimates, and the latter is useful for returning a point estimator of the maximum likelihood that *should* not be biased.

There are other types of reconstruction methods that use a mix of the two parametric and non-parametric, for example Merten et al. (2009) have an adaptive grid method that attempts to reconstruct the potential. However, which method is used depends on the intended science. As I will highlight later, the parametric method of LENSTOOL lends itself to this study. Figure 3.5 shows the comparison of the non-parametric KS93 direct inversion, and the parametric LENSTOOL for the Bullet Cluster. The top panel shows the lines of constant estimated convergence from Clowe et al. (2006), and the blue contours in the bottom panel show the integrated mass density in units of $10^8 M_{\odot}/\text{arcsecond}^2$ for the best fitting model as return by LENSTOOL. Although the two agree with the two main haloes

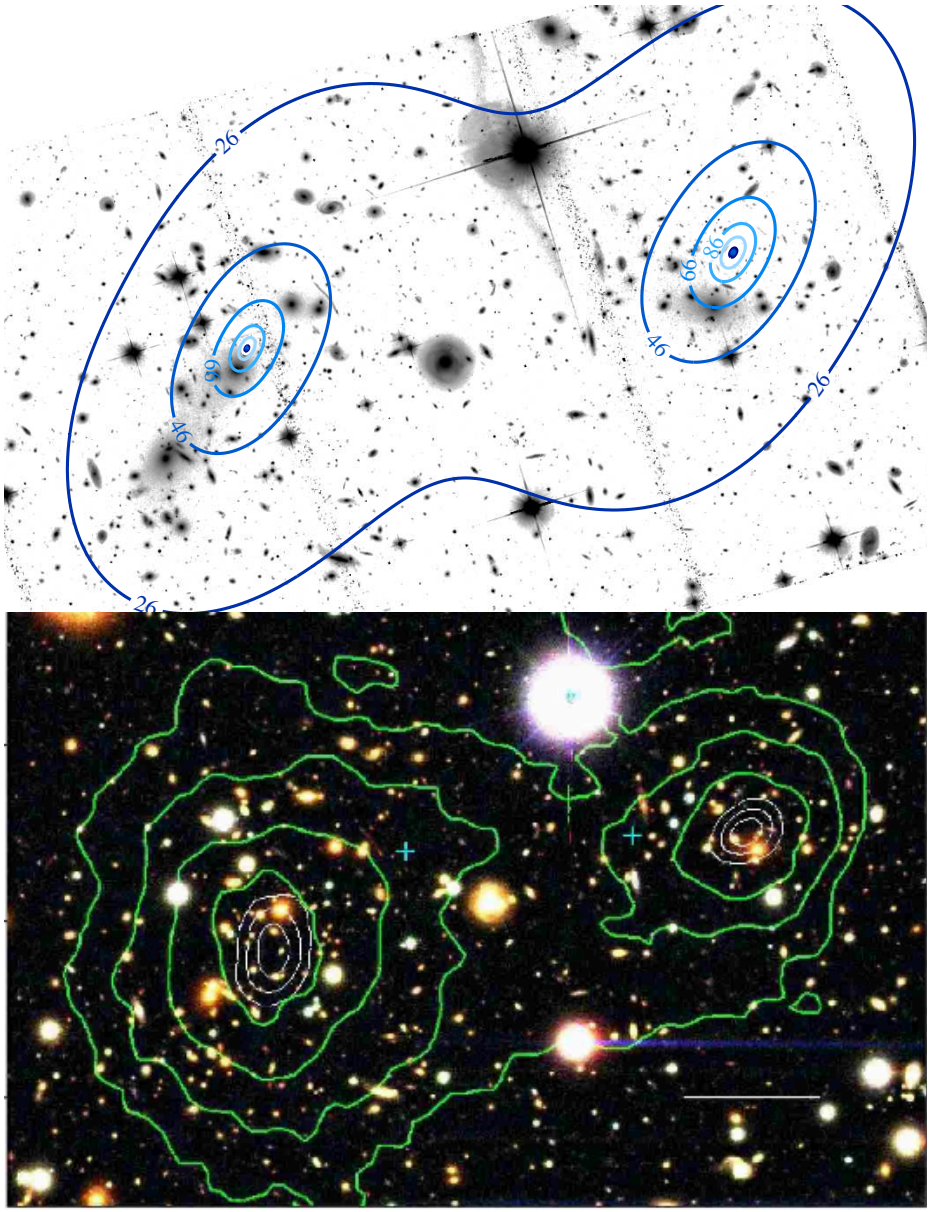

Figure 3.5: Two methods to reconstruct the dark matter in the galaxy cluster 1E0657-55 (the Bullet Cluster). The top panel shows, in blue, the best fitting model as returned by LENSTOOL in units of projected mass density ($10^8 M_\odot$/arcsecond^2) and the lower panel, in green, is the result of the direct inversion (non-parametric) using the Kaiser Squires formalism, in units of dimensionless convergence from Clowe et al. (2006) (the white is the one, two and 3 σ contour regions of their best fitting position. It can be seen that although both methods return similar mass distributions, the Kaiser-Squires method is not a parametric fit. The white bar in the bottom panel represents 200kpc and both panels have the same scale.

in the east and west of the field, the KS93 shows excess convergence outside the field showing issues with the Fourier transform used during the inversion, however it is free from assumptions of the halo profile.

One advantage of the non-parametric method is that is a simple search tool for new galaxy clusters in large datasets, not previously discovered (Wittman et al., 2001). Having said this, Marshall et al. (2002) showed that it is possible to determine the unknown number of haloes in a field by using maximum entropy arguments and the Bayes evidence. From this, they showed how to reconstruct the full information in a cluster in a purely Bayesian framework. Further to this, non-parametric mass profile estimates are very useful for calibrating X-ray masses that assume hydrostatic equilibrium and non-thermal pressure (e.g. von der Linden et al., 2014; Maughan, 2005; Zhang et al., 2007a,b).

Using clusters as telescopes

The high dense environments of galaxy clusters have provided astronomers with important insights in to the formation of the Universe and how it evolves over time. Harbouring the largest densities of total mass in the Universe, they heavily distort distant galaxies. As shown in this chapter, this distortion not only shears galaxies, but also magnifies the galaxy via κ (equation (3.16)). This means that distant galaxies and other astrophysical objects that are below the flux limit of the telescope become observable, and objects that were born in the very early universe can be studied. A recent survey specifically observing large clusters in attempt to study distant Supernova called the Cluster Lensing And Supernova survey with Hubble (CLASH) has attempted to dually study merging clusters as well as observe distant objects (Postman et al., 2012; Whalen et al., 2013).

Although a very useful tool for studying distant objects, the science is heavily dependent on the mass model used as the object needs to mapped correctly back to the original source plane. Many models have been constructed using a combination of strong and weak lensing and spectroscopy in order to reduce the effects of these systematics (e.g. Coe et al., 2012; Medezinski et al., 2013).

4 On the cross-section of dark matter

"There is nothing more difficult to take in hand, more perilous to conduct, or more uncertain in its success, than to take the lead in the introduction of a new order of things."

4.1 Dark matter in minor mergers

A decade ago, self-interacting DM was thought to be ruled out by negative results on tests for sphericity (Miralda-Escudé, 2002), cores (Yoshida et al., 2000; Meneghetti et al., 2001), and sub-halo evaporation (Gnedin & Ostriker, 2001b) in galaxy clusters. However, recent high resolution simulations show that self-interactions produce much more triaxial inner haloes (Peter et al., 2013), smaller cores (Rocha et al., 2013; Vogelsberger et al., 2012), and less evaporation than previously thought. A self-interaction cross-section per particle mass, $\sigma/m \approx 1$ cm^2/g remains as consistent with observations as non-interacting CDM.

The largest bound structures in the Universe are galaxy clusters which are collections of several thousands of galaxies, each surrounded by vast ($> 10^{14} M_\odot$) quantities of DM and mainly ionised hydrogen gas. The highly-successful cold

dark matter model of structure formation predicts that galaxy clusters grow hierarchically, by continually accreting smaller groups of galaxies and occasionally colliding. Such minor and major merging events offer a unique laboratory in which to investigate the particle physics of DM. Compared to terrestrial colliders, the energy per particle during a merger is small (a factor of 10^{-6} less than that at LHC), but the cumulative number density of dark matter particles is enormous with collisions involving up to $\sim 10^{70}$ particles per major merging event (assuming $m = 10$ GeV dark matter particles).

It is possible to map the locations of all components of a galaxy cluster. Intracluster gas in galaxy clusters emits bremstrahlung radiation, which is visible at X-ray wavelengths (Felten et al., 1966; Sarazin, 1988; Arnaud, 2005), whilst the DM component can be mapped via gravitational lensing (Kaiser, 1984; Bartelmann & Schneider, 2001; Refregier, 2003; Hoekstra & Jain, 2008; Massey et al., 2010). Several studies of individual clusters have constrained $\sigma_{\rm DM}/m$ by observing the separation of DM from gas in the aftermath of a collision leading to constraints on the total interaction cross-section per unit mass of DM: 1ES 0657-558 (Clowe et al., 2004, 2006; Bradač et al., 2006; Markevitch et al., 2004); MACSJ0025.4-1222 (Bradač et al., 2008); A520 (Mahdavi et al., 2007; Clowe et al., 2012; Jee et al., 2012); A2744 (Merten et al., 2011); DLSCL J0916.2+2951 (Dawson et al., 2012). Each cluster constitutes three components: the member galaxies, the intracluster baryonic gas, and the DM halo. The components' different interaction cross-sections make them behave differently during the collision. Galaxies act as collisionless test particles, passing through the collision unimpeded (except via gravity). The large cross-section of baryonic gas makes it lag behind the galaxies. Non-interacting DM should remain with the galaxies, and interacting dark matter should lie between the galaxies and the gas (tending to the position of the gas as $\sigma_{\rm DM}$ tends to the effective cross section of Hydrogen).

Kahlhoefer et al. (2014, hereafter K13) studied various self-interacting models and their implications for the behaviour of merging dark matter haloes. They showed that the same value for the cross-section of dark matter could result in different observable effects depending on the type of scattering that was occurring. They found that by studying the behaviour of dark matter during mergers it is possible to not only constrain the self-interaction cross-section, but also place

constraints on the type of dark matter scattering.

In order for a self-interacting dark matter halo to separate in the described fashion the overall particle velocity distribution needs to shift. This can only occur if dark matter particles self-interact often, albeit weakly, allowing particle momentum redistribution and transfer of momentum from the in-falling halo to the overall halo. Also, the amount of momentum exchanged must be small in order to satisfy constraints from studies of the Bullet Cluster (Markevitch et al., 2004). Such scattering models are necessarily angularly dependent, with the majority of scattering occurring parallel to the direction of motion. This is not the case for hard-sphere interactions which have isotropic scattering (e.g. Randall et al., 2008). Finally, in order for such a cross-section to be observable, it must be velocity *independent* resulting in a halo drag $\propto v^2$. This work, will therefore test the hypothesis that dark matter interacts often with small momentum exchange, and that the interactions are velocity independent.

Whether the interaction cross-section is velocity independent remains to be seen. However, such an assumption will lead to a estimation of the cross-section at the mean velocity of merging. The reason why the dependance is the square of the velocity is because you have two multiplicative factors. The first is that the particles are hitting with an increased momentum and therefore have a higher force impacted on the halo, and secondly the higher velocity means that the halo is sweeping through more background density and hence has yet further force applied to the halo. These two factors result in a velocity squared drag term on the halo.

Unfortunately, major merger events, observed shortly after first core passage for maximal observed separation of components, are rare in the Universe (Shan et al., 2010; Watson et al., 2013). Constraints on $\sigma_{\rm DM}$ from a small number of systems are fundamentally limited by their unknown impact velocity, impact parameter and angle with respect to the line of sight (Markevitch et al., 2004; Randall et al., 2008).

As suggested by Massey et al. (2011, hereafter MKN), the separation between galaxies, gas and DM can also be measured in minor mergers. The displacement of gas and dark matter from galaxies is likely to be much smaller than in major mergers. However, minor merger events are the dominant growth mechanism for large-scale structure in the Universe, and most clusters are accreting a piece of

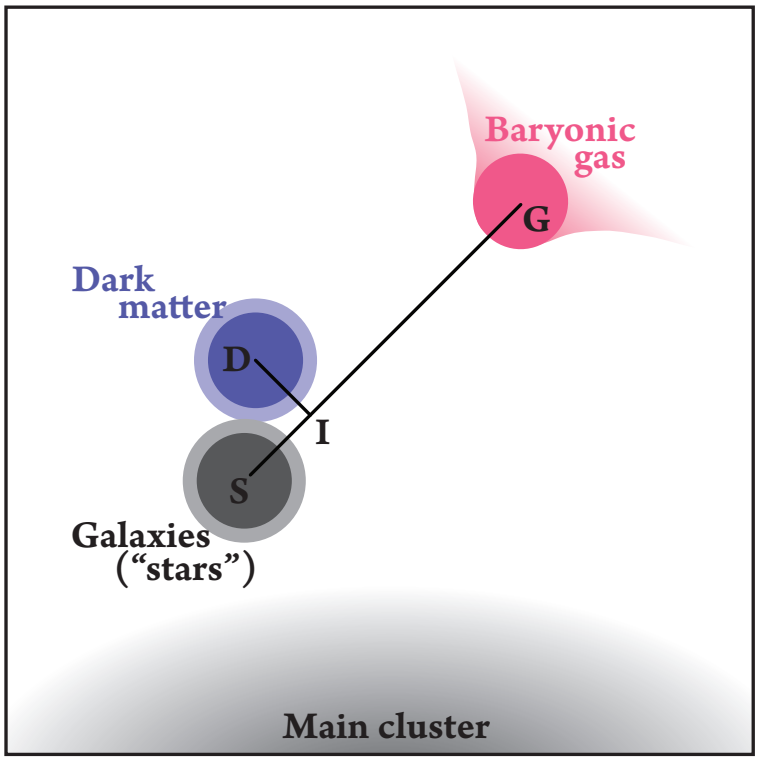

Figure 4.1: Cartoon illustrating how I propose to use all three components of in-falling substructure. The vector from galaxies to gas defines an (approximate) direction of infall. Dark matter should lie some fraction along this vector, depending upon its interaction cross section. The observed positions will be noisy, so in practice I will measure the parallel and perpendicular vectors from galaxies to dark matter. If $\sigma_{\rm DM}= 0$, these should both average to zero. Throughout this chapter I adopt shorthand subscript notation G for gas, D for dark matter, I for the intersection point closest to the dark matter in the direction towards the gas, and S ("stars") for galaxies.

substructure around ∼10% of their total mass at any time (e.g. Powell et al., 2009). Analysis of a sufficiently large observed sample of minor mergers should yield much tighter constrains on $\sigma_{\rm DM}/m$ than a small number of major mergers, while automatically averaging over systematic uncertainty in orbital parameters. The statistically averaged offset stacked over many pairs of DM and gas sub-haloes was coined "bulleticity", and can be obtained from potentially hundreds of thousands of clusters across the sky.

Using hydrodynamical simulations of ordinary clusters, MKN found that substructures' DM and gas components become separated during infall by $|\boldsymbol{b}| \simeq 10''$ (18 h^{-1} kpc) at $z = 0.1$. Observing such small separations requires high precision DM astrometry. This is easily achievable using strong gravitational lensing. Indeed, Williams & Saha (2011, hereafter WS11) discovered a ∼3″ offset between the DM *and the sub-halo galaxies* in A3827 (at $z = 0.1$) that implies a tantalising first detection of weakly interacting DM. However, a statistical bulleticity measurement relies upon measurements from a very large sample of clusters, and strong lensing of substructure is rare. We will therefore address using weak gravitational lensing to constrain the positions of substructure in the following chapter. Using a parametric mass map reconstruction and marginalising over "nuisance" parameters that here include cluster mass and concentration, I achieved a precision on the position of simulated clusters' main- and sub-haloes of better than 1″.

The main limitation of the MKN technique is that substructures are observed both falling into the cluster and heading out. DM lies closer to the cluster centre than gas during infall, but the situation is reversed after core passage. Since most observable substructures at high redshift are still falling in to a cluster, MKN suggested separating the offsets into radial and tangential components. In principle, this permits a statistically robust measurement of the radial separation b_r, in which DM is closer to the cluster centre than the gas. It also permits a simultaneous null test, because symmetry requires the mean signal of the tangential separation b_t to also be zero. Unfortunately, MKN found in simulations that the radial bulleticity signal is an order of magnitude smaller than the absolute bulleticity at $z = 0.6$, and it becomes vanishingly small at $z = 0$. Measuring this signal would be observationally challenging, and interpreting it may rely upon accurate cosmological simulations that specify the merger history.

Extending the idea laid out by MKN in this chapter I develop a statistical technique for measuring $\sigma_{\rm DM}/m$ from a large sample of major and minor mergers. Building on the earlier idea of averaging over many collision scenarios, this new method breaks previous degeneracies by using the galaxy component to define the motion of the sub-halo, and the ratio of the distances from the DM and gas component to the galaxy component to remove uncertainties in the projection orientation to the line of sight. By using the distance from the gas to the galaxies I will be able to calibrate any finite offset between the DM and the galaxies resulting in a cross-section measured directly from data

This chapter is organised as follows. In Section 4.2 I develop an analytic model of substructure infall into a cluster, which I can use to develop qualitative understanding of the effects of DM interactions, and to quantitatively interpret future observations. In Section 4.3 I apply the method on mock data from full hydrodynamical simulations of galaxy clusters embedded in the standard cosmological model. In Section 4.4 I estimate expected constraints on various parameters from realistic data. We discuss the results and conclude in Section 4.5.

4.2 Methodology

Here I present a new method to constrain $\sigma_{\rm DM}/m$ from minor mergers. We exploit the fact that each piece of substructure contains *three* components (galaxies, gas and dark matter), from which *two* 2D offsets can be measured independently. By measuring the ratio of the observed offset between the galaxies and dark matter and the offset between the galaxies and the X-ray gas, one can consider a parameter which is independent of any projection degeneracies. In order to interpret this parameter for a measurement of $\sigma_{\rm DM}/m$, I derive an analytical prescription of sub-halo infall including all relevant forces such as; the cluster potential, the DM sub-halo potential, drag on the gas, DM interactions and the resultant drag on a DM halo and buoyancy.

As illustrated in Figure 4.1, I incorporate all information of the sub-halo system into the analysis. Compared to MKN, the two extra pieces of information define (i) a new preferred direction and (ii) a calibrated scale length. We shall probe the cross-section through the offset between the galaxies and DM, but

interpret it in terms of the offset between the galaxies and the gas. Throughout this chapter I adopt shorthand subscript notation G for gas, D for dark matter, I for the intersection point closest to the dark matter in the direction towards the gas, and S (stars) for galaxies.

4.2.1 Calibrating $\sigma_{\rm DM}/m$ with relative distances

We assume that substructure member galaxies act as collisionless test particles during infall, acted upon by only the force of gravity. We also assume that the main extra force acting on the baryonic gas is a drag force from the intracluster medium (ICM), which gradually separates it from the galaxies. Crucially, this offset defines a unique displacement vector $\boldsymbol{d}_{\rm SG} = \overline{SG}$ that is antiparallel to the direction of motion, whether the substructure is falling into or emerging out of the cluster. We propose measuring the position of the dark matter with respect to this direction.

The observed position of DM will depend upon its interaction cross-section. If $\sigma_{\rm DM} = 0$, the collisionless DM will remain with the galaxies. If $\sigma_{\rm DM} > 0$, forces on the DM will be exerted in the same direction[1] as those on the gas, and it will move some fraction $\boldsymbol{d}_{\rm SI}$ ($\overline{SI}$ in Figure 4.1) along the vector. Using the galaxies to define the direction of motion ensures that this should remain positive even if the substructure has already passed through the main cluster, thus preserving the signal rather than averaging most of it away. Furthermore, symmetry again provides a null test. Regardless of the origin and nature of the forces, a lack of preference for apparently clockwise or anticlockwise mergers still demands that the mean observed perpendicular offset of dark matter from the infall direction, $\langle \boldsymbol{d}_{\rm DI} \rangle$, ($\overline{DI}$ in Figure 4.1) must be consistent with zero.

We propose calibrating the observed offset of substructure DM against the offset of substructure gas, whose properties are assumed to be well known and

[1]The substructure's DM could potentially interact with both the cluster ICM (DM-baryon interactions) and the cluster DM (DM-DM interactions). These cluster components will have slightly different physical extent. If DM-baryon interactions dominate, the substructure DM will experience a force in the same direction and at the same time as the substructure gas. If DM-DM interactions dominate, the force could start acting earlier and in a slightly different direction, but I shall neglect this for now.

understood. We form the ratio

$$\beta \equiv \frac{|\boldsymbol{d}_{\rm SD}|}{|\boldsymbol{d}_{\rm SG}|} = \frac{d_{\rm SD}}{d_{\rm SG}}. \tag{4.1}$$

The cross-section of dark matter should be measurable from

$$\beta_{\parallel} \equiv \frac{d_{\rm SI}}{d_{\rm SG}}, \tag{4.2}$$

where I choose a Greek rather than Roman letter to denote the dimensionless quantity. The simultaneous null test for systematics can be measured through

$$\beta_{\perp} \equiv \frac{d_{\rm DI}}{d_{\rm SG}}, \tag{4.3}$$

which should be consistent with zero in a large sample. Any deviation from this should reflect the statistical error in the positional estimates of DM.

Introducing a ratio has advantages and disadvantages. The great advantage of taking this ratio, is that every individual measurement is now invariant to changes in the orientation of the merger with respect to the line of sight. If the merger is viewed in the plane of the sky, all the apparent angular distances will be large, and the signal-to-noise ratio will be maximised. If the merger occurs close to the line of sight, the apparent angular distances in both the numerator and denominator will shrink equally: the signal will remain the same, but will be measured with more noise. This makes it possible to combine the observed values of $\langle\beta_{\parallel}\rangle$ and $\langle\beta_{\perp}\rangle$ from a large sample of bullets via a simple weighted mean. One disadvantage is that noise on both a numerator and denominator can lead to non-Gaussian or even biased error distributions, which I will need to treat with care.

4.2.2 A physical model of dark matter and gas infall

The accretion of substructure onto a cluster is a complex process that requires sophisticated hydrodynamical simulations to model completely. However, I can build an approximate analytic model that will aid understanding and should be sufficiently accurate to interpret an initial detection of β. Notably, I shall add sufficient complexity to deal with many of the known limitations of previous work. However, like previous work we make assumptions. We assume that neither the

dark matter, galaxies or gas experience dynamical friction. We also assume that the dark matter and the galaxies are equally retarded by the gas as it separates. In the event that the dark matter is an extended halo this doesn't hold, however this is a second order effect which will not be considered.

Let us first explicitly define the forces acting on the three components, galaxies, gas, DM, of substructure falling into a cluster. Following MKN, I assume the distribution of mass in the cluster is a singular isothermal sphere with characteristic density ρ_0 at radius r_0, although as we will see, the precise form does not matter. In addition to gravitational attraction towards the cluster, the gas will feel a drag force, $\boldsymbol{D}_{\rm G}$, and the DM a drag force, $\boldsymbol{D}_{\rm D}$, plus gas and DM will feel a buoyancy, $\boldsymbol{B}_{\rm G}$ and $\boldsymbol{B}_{\rm D}$ respectively, due to particle-particle interactions within the ICM. There is also a gravitational attraction of the galaxies and gas towards the substructure's dominant DM component, $\boldsymbol{G}_{\rm SD}$ and $\boldsymbol{G}_{\rm GD}$. I neglect the gravitational influence of the other, less massive components. In the reference frame of the cluster the equations of motion for the substructure galaxies, gas and dark matter, are respectively,

$$\frac{{\rm d}^2\boldsymbol{r}_{\rm S}}{{\rm dt}^2} = -\frac{4\pi G\rho_0 r_0^2}{r_{\rm S}^2}\boldsymbol{r}_{\rm S} + \frac{\boldsymbol{G}_{\rm SD}}{M_{\rm S}}, \tag{4.4}$$

$$\frac{{\rm d}^2\boldsymbol{r}_{\rm G}}{{\rm d}t^2} = -\frac{4\pi G\rho_0 r_0^2}{r_{\rm G}^2}\boldsymbol{r}_{\rm G} + \frac{\boldsymbol{D}_{\rm G}}{M_{\rm G}} + \frac{\boldsymbol{B}_{\rm G}}{M_{\rm G}} + \frac{\boldsymbol{G}_{\rm GD}}{M_{\rm G}} \tag{4.5}$$

$$\frac{{\rm d}^2\boldsymbol{r}_{\rm D}}{{\rm d}t^2} = -\frac{4\pi G\rho_0 r_0^2}{r_{\rm D}^2}\boldsymbol{r}_{\rm D} + \frac{\boldsymbol{D}_{\rm D}}{M_{\rm D}} + \frac{\boldsymbol{B}_{\rm D}}{M_{\rm D}}, \tag{4.6}$$

where M_S, M_G, M_D are the masses of the galaxy, gas and DM component respectively.

Drag forces

The macroscopic behaviour of the substructure gas is determined by its macroscopic, hydrodynamic properties. As the substructure's gas component moves through the cluster ICM, it experiences turbulent drag (Thacker et al., 2000). The drag force on the gas obeys the drag equation (Frisch, 1995),

$$\boldsymbol{D}_{\rm G} = -\frac{1}{2}C_{\rm G}A_{\rm G}\rho_{\rm G}^{\rm ICM}v_{\rm G}^2\hat{\boldsymbol{v}}_{\rm G}, \tag{4.7}$$

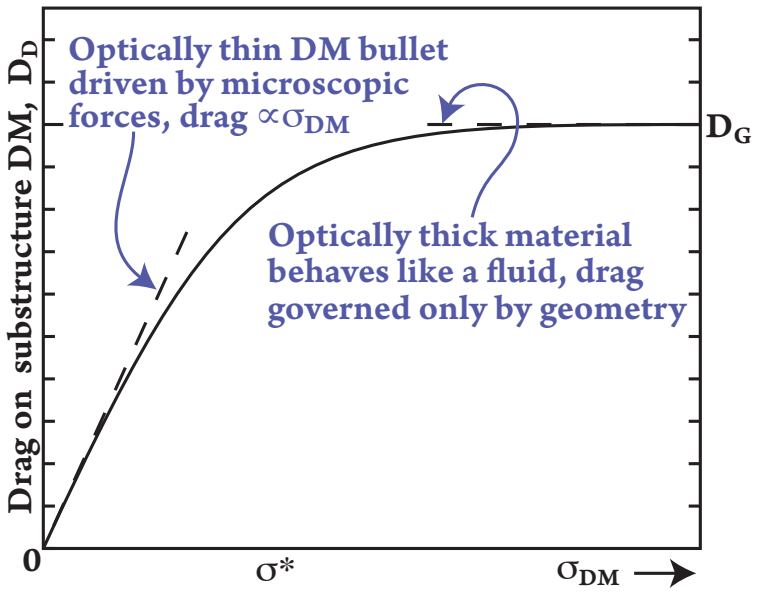

Figure 4.2: Generic behaviour of drag force acting on dark matter substructure, as a function of interaction cross-section. We propose an interpolation function between the two well-understood extremes based on optical depth. This function is essential to calibrate the observed behaviour of the DM against the behaviour of the gas.

where $\rho_{\rm G}^{\rm ICM}$ is the density of gas in the ICM, $\boldsymbol{v}_{\rm G}$ is the infall velocity of the substructure gas (with $\hat{\boldsymbol{v}}_{\mathbf{G}}$ denoting the unit vector in the direction of the velocity), $A_{\rm G}$ is its cross-sectional areas and $C_{\rm G}$ is the coefficient of drag, which is determined by its geometry.

If the DM has a low interaction cross-section per unit mass (with respect to the in-falling gas), its macroscopic behaviour is instead determined by its microscopic properties (high cross-sections have been ruled out since scattering would result in evaporation and disruption of haloes which hasn't been observed). The regime of dark matter scattering, which I model here is a velocity independent one, with small momentum exchange. KT13 considered such scattering, and found that the resulting interactions were frequent with a small momentum transfer in each case, resulting in an effective drag on a halo given by

$$\boldsymbol{D}_{\rm D} = -\frac{1}{4}\left(\frac{\sigma_{\rm DM}}{m}\right)\rho_{\rm D}^{\rm ICM} M_{\rm D} v_{\rm D}^2 \hat{\boldsymbol{v}}_{\rm D}, \tag{4.8}$$

where $\rho_{\rm D}^{\rm ICM}$ is the density of DM in the ICM, $\boldsymbol{v}_{\rm D} = {\rm d}\boldsymbol{r}_{\rm D}/{\rm d}t$ is the velocity of

the substructure DM, $\hat{\boldsymbol{v}}_{\mathbf{D}}$ denotes the unit vector in the direction of the velocity, $M_{\rm D}$ is its mass, and $\sigma_{\rm DM}/m$ is the momentum transfer cross-section of the dark matter. K13 have shown that there are plausible models of SIDM which satisfy this assumption, for example interaction via a dark mediator. However, they also point out that there are particle physics models of dark matter which could result in evaporation of sub-haloes or particle redistribution and does not result in an effective drag force. I should therefore note that the model will probe specific types of anisotropic scattering due to long range forces, and not the "hard-sphere" SIDM with isotropic scattering that most simulators are currently modelling. In other words this observable has the potential to probe a *different* kind of SIDM. These models of SIDM would include those that mediate the interaction via a massive boson, analogous to the W or Z boson, such that the interaction is over a short distance. Such hard sphere models have been preferentially simulated due to the trivial computation, (e.g. Randall et al., 2008), however future simulations will need to simulate both in order to fully understand SIDM.

Above some threshold the drag properties of a halo will be entirely dependent on the macroscopic properties of the halo itself, and not the microscopic particle properties. Our self-calibrating method is based around a comparison of the forces acting on DM with those acting on the galaxies and the gas. We therefore need to model the drag on particles anywhere between these extremes. Equations (4.7) and (4.8) provide boundary conditions: for low cross-sections, the drag force is proportional to $\sigma_{\rm DM}/m$ but, above some threshold, the force depends only on geometry of the DM substructure. This suggests an analogue of optical depth. The coincidence that the drag is proportional to the square of velocity in both extremes is useful; we assume that this holds throughout the transition (neglecting any phase in which the flow is laminar, and obeys Stokes' law), and that the DM drag force is more generally

$$\boldsymbol{D}_{\rm D} = -\frac{1}{2} C_{\rm D} A_{\rm D} \rho_{\rm D}^{\rm ICM} \left(1 - {\rm e}^{-\sigma_{\rm DM}/\sigma^\star}\right) v_{\rm D}^2 \hat{\boldsymbol{v}}_{\rm D}, \tag{4.9}$$

where geometric quantities for the DM are analogous to those for the gas, and

$$\frac{\sigma_{\rm DM}}{\sigma^\star} = \frac{1}{2\,C_{\rm D}} \frac{\sigma_{\rm DM}/m}{A_{\rm D}/M_{\rm D}}. \tag{4.10}$$

This can be interpreted as an optical depth

$$\tau \equiv \frac{3\sigma_{\rm DM}}{\sigma^\star} \approx n\,\sigma_{\rm DM} s_{\rm D}, \tag{4.11}$$

when $C_{\rm D} \approx 1/2$, and the substructure has a characteristic scale $s_{\rm D}$ for which its cross-sectional area $A_{\rm D} = \pi s_{\rm D}^2$, $n = M_{\rm D}/(mV_{\rm D})$ is the DM particle density in the substructure with a volume $V_{\rm D} = 4\pi s_{\rm D}^3/3$. Figure 4.2 diagrammatically shows the knowledge of the two extremes between the low cross-section of the dark matter and the highly interacting gas and how I interpolate between the two regimes. I see that this relationship between the two regimes is essential in order to calibrate the observed behaviour of the DM to that of the gas.

Equation (4.9) recovers equation (4.8) in the optically thin limit ($\tau << 1$), and is the DM analogue to equation (4.7) if it is optically thick. The transition in behaviour occurs when the cross-section reaches a critical value $\sigma_{\rm DM} \simeq \sigma^\star/3$ (i.e. $\tau \simeq 1$) where, from equation (4.10),

$$\frac{\sigma^\star}{m} \approx \frac{2\,C_{\rm D} A_{\rm D}}{M_{\rm D}} \approx \frac{\pi s_{\rm D}^2}{M_{\rm D}} \tag{4.12}$$

$$\approx 14.1 \left(\frac{s_{\rm D}}{100\ h^{-1}{\rm kpc}}\right)^2 \left(\frac{M_{\rm D}}{10^{13} h^{-1} M_\odot}\right)^{-1} {\rm cm}^2/{\rm g}\ . \tag{4.13}$$

The implications are that many small haloes will be required in order to assess the cross-section of haloes. However, I note here that the numbers used as naive numbers, and do not take into account that smaller haloes are more compact that larger ones, which will improve the sensitivity.

Buoyancy force

It was thought that the overriding effect of SIDM would be analogous to a buoyancy force acting on the dark matter. As haloes in-fall, the dark matter within the cluster will act to push the dark matter and gas out. MKN analysed this effect and modelled DM substructure with mean density $\rho_{\rm D}$, moving in an ICM distributed as a singular isothermal sphere, with density ρ_0 at radius r_0, will experience a *buoyancy* (MKN)

$$\boldsymbol{B}_{\rm D} = \frac{4GM_{\rm D}\rho_0^2 r_0^4}{\rho_{\rm D} s_{\rm D}^2} \frac{\boldsymbol{r}_{\rm D}}{r_{\rm D}^4} \sigma_{\rm DM}^2. \tag{4.14}$$

This acts in the radial direction, anti-parallel to the infall velocity, complicating the analysis. Full hydrodynamical simulations will be essential to characterise its effect.

However, the buoyancy of DM and gas fall off rapidly, as $\propto 1/r^3$. Such forces should be negligible outside the cluster core, furthermore, the drag according to equation (4.8) on the dark matter is $\propto \boldsymbol{v}^2$, and therefore will always dominate and hence, I assume

$$\boldsymbol{B}_{\rm D} \approx \boldsymbol{B}_{\rm G} \approx \boldsymbol{0}. \tag{4.15}$$

In MKN buoyancy was assumed to be the dominant force, but in-fact the $1/r^3$ term means that it can be neglected.

Mutual gravitational attraction of extended substructure components

The gravitational attraction of the substructure's DM acts on the gas and member galaxies to keep them bound. WS11 commented that this force might be important if the substructure components are physically extended, but do not include it in their analysis. For small separations of galaxies and dark matter, I find that it can be the most important effect.

To qualitatively understand the effect of gravitational attraction between substructure components, let us explore a simple model. We assume the mass in each component follows a profile

$$\rho(r) = \frac{\rho_0}{(1 + (r/r_{\rm core})^2)^{3\eta/2}}, \tag{4.16}$$

where $\eta = 2/3$, $r_{\rm core} = 60$kpc for the DM, $r_{\rm core} = 10$kpc for the galaxies and gas, and the density of the gas halo is lower by the ratio of the baryon density to the total matter density, $\rho_0^{\rm Gas} = (\Omega_b/\Omega_m)\rho_0^{\rm DM} \approx 0.13\rho_0^{\rm DM}$ (Planck Collaboration et al., 2013a). I model the galaxies as a delta-function and determine the force on an extended body inside a DM potential by convolving its density profile, given by equation (4.16), with the force on a point particle in the potential. As illustrated in Figure 4.3, the force has three distinct regimes;

1. With a small separation ($\lesssim 30$ kpc in this example) between two still-overlapping components, the restoring force increases linearly with separa-

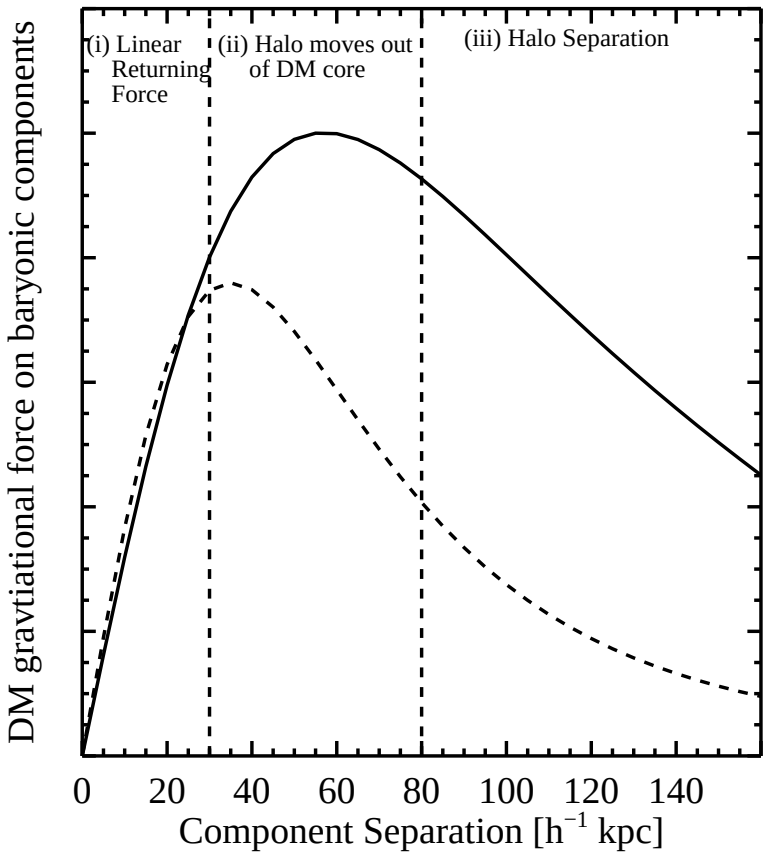

Figure 4.3: The gravitational force that an extended dark matter halo has on an extended gas halo (solid line) and galaxies (dashed line), as a function of their separation. In this particular case, I model the force on substructure gas (solid line) and stars (dashed line) due to substructure DM, using representative component sizes discussed in the text. The dashed vertical lines delineate the regimes set out in the text.

tion.

2. At intermediate separations ($\sim$ 30–80 kpc), when the components are in each others' wings, the force peaks then decreases.

3. At large separations ($\gtrsim$ 80 kpc), the two components have separated and the force is $\propto 1/r^2$.

The typically 18 h^{-1} kpc separations of collisionless DM and X-ray gas found by MKN suggest that most in-falling substructure occupies the first regime, in which the substructure's three components physically overlap. Indeed, once gas (and later perhaps DM) begins to spill out of the local potential well of the substructure's DM, they will rapidly become stripped due to tidal forces and, if they are moving fast enough near the cluster core, ram pressure. We therefore assume that bullets *in which all three components are observed* must necessarily be and have always been in the first regime.

We have described above how substructure gas experiences drag from the ICM, causing it to separate from the DM; now gravity from the (dominant) DM will act to pull it back. The gravitational returning force increases linearly with distance from the DM in this regime, so I can model this force as

$$\boldsymbol{G}_{\rm GD} = k_{\rm GD} M_{\rm G} \boldsymbol{d}_{\rm GD} = k_{\rm GD} M_{\rm G} \left(\boldsymbol{d}_{\rm SD} - \boldsymbol{d}_{\rm SG} \right), \tag{4.17}$$

where k_{GD} is the gradient of the linear returning force. Any drag on the DM will begin to separate it from the galaxies. A similar gravitational restoring force will act on the galaxies,

$$\boldsymbol{G}_{\rm SD} = k_{\rm SD} M_{\rm S} \boldsymbol{d}_{\rm SD}, \tag{4.18}$$

where k_{SD} is the gradient of the force opposing their separation.

We assume that the displacements of substructure components from the galaxies are antiparallel to the direction of their infall. This is automatically satisfied if the offset is caused by the drag force. If buoyancy is non-negligible, or the direction of infall has changed, the offsets will temporarily display some residual component perpendicular to the direction of motion, i.e. finite $|\beta_\perp|$. Symmetry ensures that $\langle \beta_\perp \rangle = 0$, but $\beta_\parallel$ may be temporarily lowered.

We have assumed that the displaced gas component will have no affect on the position of either the dark matter or galaxies. Indeed, in the limit that they are point particles, the gravitational attraction of the gas on its counterparts will be equal. However, since they are not, the gas may act to pull the DM more than the galaxies and result in a displacement even in the case of collisionless dark matter. I assume that this effect is zero, but may need addressing in future experiments.

4.2.3 Instantaneous quasi-equilibrium

We shall now consider the relative motions of the DM (D) and gas (G) components to the non-interacting galaxies (S). Any measurement of bulleticity requires observations of all three substructure components. As discussed in Section 4.2.2, if the substructure ever passed very close to the cluster core, the very steep gravitational potential there would overwhelm the local substructure potential. Substructure gas would spill out and, unbound, would be rapidly dispersed into the ICM. Such a disrupted system would thus not be observed, and not enter the sample. For substructure well away from the core

$$\boldsymbol{r}_{\rm S} \approx \boldsymbol{r}_{\rm G} \approx \boldsymbol{r}_{\rm D} \gg \boldsymbol{d}_{\rm SG}. \tag{4.19}$$

In this limit, and moving into the galaxy frame of reference I find

$$\begin{aligned}\frac{{\rm d}^2\boldsymbol{r}_{\rm G}}{{\rm d}t^2} - \frac{{\rm d}^2\boldsymbol{r}_{\rm S}}{{\rm d}t^2} &\approx \frac{\boldsymbol{D}_{\rm G}}{M_{\rm G}} + \frac{\boldsymbol{B}_{\rm G}}{M_{\rm G}} + \frac{\boldsymbol{G}_{\rm GD}}{M_{\rm G}} - \frac{\boldsymbol{G}_{\rm SD}}{M_{\rm S}} &(4.20)\\ &\approx -\frac{C_{\rm G}A_{\rm G}\rho_{\rm G}^{\rm ICM}v_{\rm G}^2}{2M_{\rm G}}\hat{\boldsymbol{v}}_{\rm G} + k_{\rm GD}d_{\rm SG}\hat{\boldsymbol{v}}_{\rm G} \\ &\qquad + (k_{\rm SD} - k_{\rm GD})d_{\rm SD}\hat{\boldsymbol{v}}_{\rm D} &(4.21)\end{aligned}$$

and

$$\begin{aligned}\frac{{\rm d}^2\boldsymbol{r}_{\rm D}}{{\rm d}t^2} - \frac{{\rm d}^2\boldsymbol{r}_{\rm S}}{{\rm d}t^2} &\approx \frac{\boldsymbol{D}_{\rm D}}{M_{\rm D}} + \frac{\boldsymbol{B}_{\rm D}}{M_{\rm D}} - \frac{\boldsymbol{G}_{\rm SD}}{M_{\rm S}} &(4.22)\\ &\approx -\frac{C_{\rm D}A_{\rm D}\rho_{\rm D}^{\rm ICM}v_{\rm D}^2}{2M_{\rm D}}\left(1 - {\rm e}^{-\sigma_{\rm DM}/\sigma^\star}\right)\hat{\boldsymbol{v}}_{\rm D} \\ &\qquad + k_{\rm SD}d_{\rm SD}\hat{\boldsymbol{v}}_{\rm D}\ . &(4.23)\end{aligned}$$

While the substructure passes through the outskirts of the cluster, drag separates the gas, then the DM, from the galaxies. However, the gravitational attraction

of the DM acts to pull the components back together. If it wasn't for this restoring force, the gas halo would separate and dissipate very quickly. Since the gravitational returning force increases linearly with separation, both the gas and galaxies will separate from the dark matter until the restoring force balances the drag and the components reach quasi-equilibrium. Analogous to an adiabatic process, the time the system takes to reach equilibrium is much less than the dynamical timescale of the in-falling sub-halo. Therefore quasi-equilibrium occurs before the halo falls in further.

As the substructure accelerates towards the cluster, or moves through denser ICM, the drag will increase. The components separate further, but the gravitational returning force again increases until it balances the drag force, and the system establishes a new quasi-equilibrium.

Evidence for this equilibrium state can be seen in Figure 4.4, a simulated example of a sub-halo in-falling into a cluster, with the red representing the gas, the blue the dark matter and the white the galaxies. I see that whilst the peaks are separated the gas has not been stripped. Moreover, the study by MKN found a peak separation of up to $\sim 18h^{-1}$kpc, providing more evidence to show this force must balance with the restoring force. While in this quasi-equilibrium state, the components' accelerations and velocities are equal

$$\frac{\mathrm{d}^2\boldsymbol{r}_\mathrm{S}}{\mathrm{d}t^2} = \frac{\mathrm{d}^2\boldsymbol{r}_\mathrm{G}}{\mathrm{d}t^2} = \frac{\mathrm{d}^2\boldsymbol{r}_\mathrm{D}}{\mathrm{d}t^2}, \tag{4.24}$$

and

$$\boldsymbol{v}_\mathrm{S} = \boldsymbol{v}_\mathrm{G} = \boldsymbol{v}_\mathrm{D}. \tag{4.25}$$

This requires

$$\frac{\mathrm{d}^2\boldsymbol{r}_\mathrm{G}}{\mathrm{d}t^2} - \frac{\mathrm{d}^2\boldsymbol{r}_\mathrm{S}}{\mathrm{d}t^2} = 4\pi G\rho_0 r_0^2 \left(\frac{r_\mathrm{G} - r_\mathrm{S}}{r_\mathrm{G} r_\mathrm{S}}\right) \approx 0. \tag{4.26}$$

Note that in this model I assume that haloes retain their shape and separate. K13 found when simulating major mergers the resulting distribution of galaxy particles post-collision is in-fact asymmetric and the peaks stay coincident. However, here I am considering smaller sub-haloes in an on-going process, where particles reach a temporary equilibrium rather than a completed pass of a

secondary halo in which the particles have already begun to relax. Moreover, the aim of this work is to be able interpret the weak lensing observable, which is sensitive to the mean mass distribution in a system, as a cross-section. In this sense the haloes will be separated as apposed to the K13 treatment which was carried out in the context of strong lensing which probes the peak of the mass distribution. Under these dynamic conditions, equation (4.21) yields

$$d_{\mathrm{SG}} = \frac{C_{\mathrm{G}} A_{\mathrm{G}} \rho_{\mathrm{G}}^{\mathrm{ICM}} v_{\mathrm{S}}^2}{2 M_{\mathrm{G}} k_{\mathrm{GD}}} - \frac{(k_{\mathrm{SD}} - k_{\mathrm{GD}})}{k_{\mathrm{GD}}} d_{\mathrm{SD}} \tag{4.27}$$

and equation (4.23) reduces to

$$d_{\mathrm{SD}} = \frac{C_{\mathrm{D}} A_{\mathrm{D}} \rho_{\mathrm{D}}^{\mathrm{ICM}} v_{\mathrm{S}}^2}{2 M_{\mathrm{D}} k_{\mathrm{SD}}} \left(1 - \mathrm{e}^{-\sigma/\sigma^\star}\right). \tag{4.28}$$

We shall assume that the baryon fraction

$$f_b \equiv \frac{\Omega_b}{\Omega_m} = \frac{\rho_{\mathrm{G}}^{\mathrm{ICM}}}{\rho_{\mathrm{D}}^{\mathrm{ICM}} + \rho_{\mathrm{G}}^{\mathrm{ICM}}} \tag{4.29}$$

is roughly constant throughout the system. This implies

$$\frac{\rho_{\mathrm{D}}^{\mathrm{ICM}}}{\rho_{\mathrm{G}}^{\mathrm{ICM}}} \approx \frac{M_{\mathrm{D}}}{M_{\mathrm{G}}} = \frac{1 - f_b}{f_b}. \tag{4.30}$$

This approximation may not be quite accurate if the baryon faction depends on the radius from the cluster centre, however, all that we require is that that the baryon fraction, $\Omega_{\mathrm{B}}/\Omega_{\mathrm{M}}$ is greater than the gas fraction in the cluster. This assumption will result in a conservative upper limit on the cross-section of dark matter. We shall also assume geometric similarity so the drag coefficients coincide

$$C_{\mathrm{D}} \approx C_{\mathrm{G}}, \tag{4.31}$$

as do the areas

$$A_{\mathrm{D}} \approx A_{\mathrm{G}}, \tag{4.32}$$

and

$$k_{\mathrm{GD}} \approx k_{\mathrm{SD}}. \tag{4.33}$$

Although the former approximation may not be strictly true, it will result in a conservative estimate of an upper limit of the cross-section of dark matter since the dark matter will remain spherical, whereas the gas will strip and therefore reduce its drag coefficient. The latter is reasonable because the values of k are mainly driven by the inner slope of the same DM potential. However, the values are also perturbed by the distribution of mass in the gas and galaxies, so it may be necessary to model for future surveys, when averaging over many thousands of clusters allow a high-precision measurement.

Taking the ratio of equations (4.27) and (4.28), I find

$$\beta \equiv \frac{d_{\mathrm{SD}}}{d_{\mathrm{SG}}} \approx 1 - \mathrm{e}^{-\sigma_{\mathrm{DM}}/\sigma^\star}. \tag{4.34}$$

Hence I find that the proposed quantity is independent of the substructure infall velocity and the time since the infall began.

Recall from equation (4.13) that $\sigma^\star$ strictly depends upon the size and mass of each piece of substructure. When I come to compute and interpret a mean value $\langle\beta\rangle$, it might be necessary to measure these properties and weight measurements from each piece of substructure appropriately, or to constrain and statistically marginalise over a distribution of $s_{\mathrm{D}}^2/M_{\mathrm{D}}$ with global nuisance parameters. This may be necessary for future, high-precision measurements using many thousands of clusters. To interpret the first observations of this effect, it should be sufficiently accurate to assume a mean value $\langle s_{\mathrm{D}}^2/M_{\mathrm{D}}\rangle \sim 4.5\,\mathrm{cm}^2/\mathrm{g}$.

4.3 Applying the method to simulations

4.3.1 Hydrodynamical simulations of clusters

To check the feasibility of measuring σ_{DM}/m in real astronomical data, we need to apply the method in a controlled environment, using hydrodynamical simulations of galaxy clusters. These simulations use non-interacting DM with $\sigma_{\mathrm{DM}} = 0$, so they will be useful only to predict the typical level of signal-to-noise ratio for

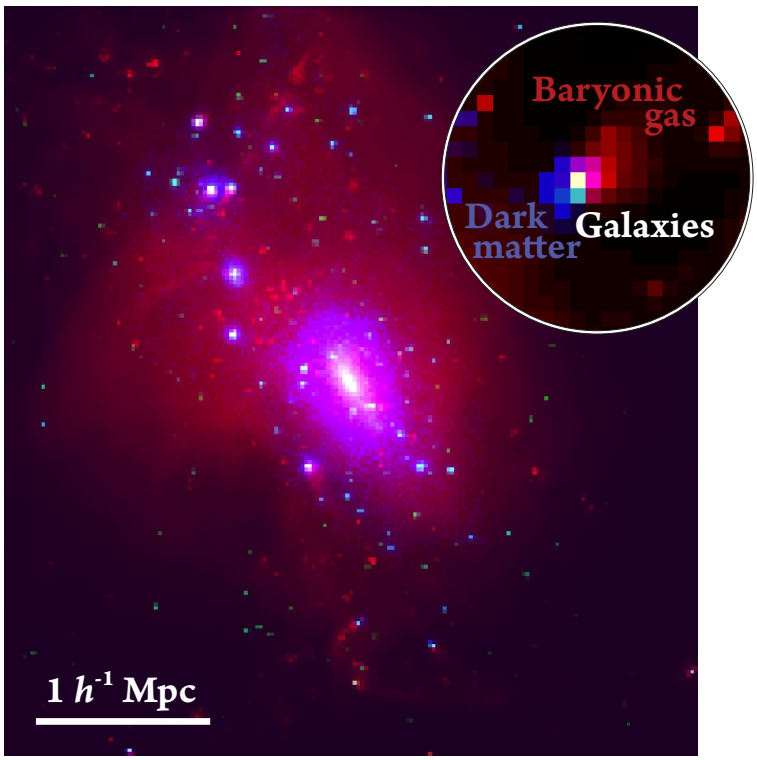

Figure 4.4: Hydrodynamical simulation of a galaxy cluster growing through minor mergers. The inset zooms into one piece of in-falling substructure. Blue shows the projected distribution of dark matter, red shows the standard model baryonic gas, and white shows galaxies. In this simulation, the dark matter is non-interacting, and therefore is expected to lie in the same place as the galaxies. However, there is a clear separation between in-falling substructure's galaxies and baryonic gas.

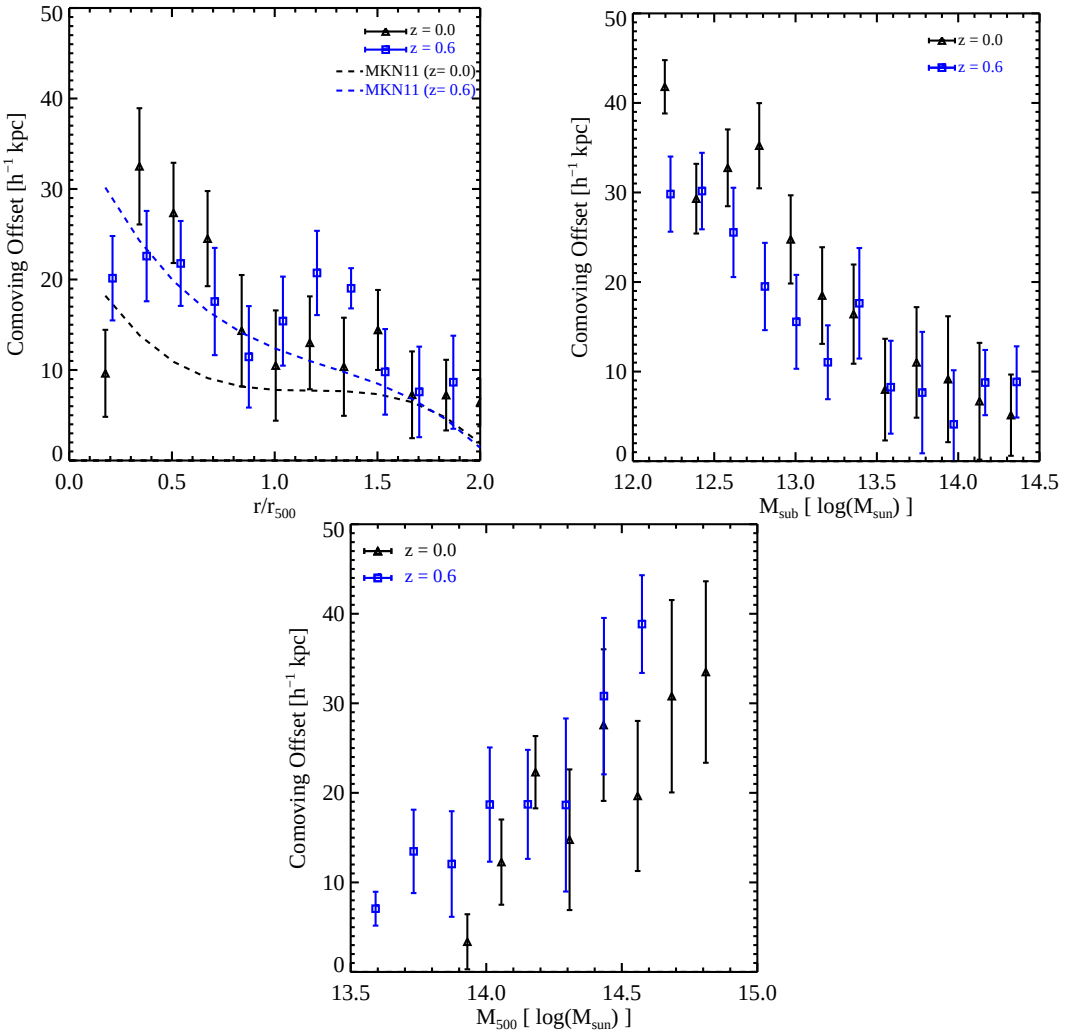

Figure 4.5: Projected offsets d_{SG} between galaxies and gas in substructure around 30 clusters in hydrodynamical simulations that include the effects of gas cooling, star formation, supernova feedback and AGN feedback. In each case the black points are the results from clusters at a redshift of 0 and the blue points are from haloes at a redshift of 0.6. The left panel shows the offset as a function of the projected distance from the cluster in units of r_{500}, the radius inside which the density is 500 times greater than the mean density in the Universe. The dashed lines show earlier predictions from MKN. The centre panel shows the offset as a function of the mass of the sub-halo (see equation 4.35). The right panel shows the offset as a function of its parent cluster mass, M_{500}, the total mass inside a sphere of radius r_{500}. Each point shows the weighted mean of offsets within that particular radial or mass bin, with the error bars representing the one-sigma error.

observations.

We study 30 galaxy clusters, extracted from a large ($[500h^{-1}\mathrm{Mpc}]^3$) dark matter only simulation, run as part of the Virgo Consortium's Millennium Gas project (Pike et al. in preparation). These were re-simulated using Gadget 2 (Springel, 2005), where the gas dynamics is modelled using the Smoothed Particle Hydrodynamics (SPH) method. The WMAP 7 cosmology was adopted (Larson et al., 2011) with $\Omega_\mathrm{m} = 0.272$, $\Omega_\Lambda = 0.728$, $\Omega_\mathrm{b} = 0.0455$, $h = 0.704$ and $\sigma_8 = 0.81$. Clusters were selected by defining 5 bins equidistant in $\log(M_{200})$, between $10^{14}h^{-1}M_\odot$ and $10^{15}h^{-}1M_\odot$, and drawing 6 objects at random from within each bin. The mass resolution was chosen to keep the number of particles constant ($\sim 10^6$) within r_{200}, such that the dynamic range of cluster substructure was similar across the mass range. Furthermore the spatial resolution ranged between $3 - 8h^{-1}$ comoving kpc and $9 - 15h^{-1}$ comoving kpc for redshifts z=0.6 and z=0 respectively. The gravitational softening length (held fixed in physical co-ordinates at $z < 3$) was set to $\epsilon = 6h^{-1}$kpc for the most massive haloes, decreasing to $3h^{-1}$kpc for the least massive objects.

Radiative cooling (assuming zero metallicity gas), star formation and feedback from stars and active galactic nuclei (AGN) were implemented, as described in Newton & Kay (2013). Including AGN feedback is particularly important for avoiding a cooling catastrophe and broadly reproducing the observed cluster scaling relations at low redshift. The prescription used for the simulations follows that set out by (Booth & Schaye, 2009). Black hole seeds were inserted at a redshift of 5.2, where a gas particle was converted in each subhalo or friends-of-friends (FOF) group with $M_{200} > 3 \times 10^{10}h^{-1}M_\odot$, where M_{200} is the mass within the radius at which the mean density is 200 times greater than the mean density in the Universe. Each black hole had an initial mass of $10^5h^{-1}M_\odot$ and could subsequently grow via mergers with other black holes or accretion of gas using a modified version of the Bondi Hoyle formula. The available energy for feedback was proportional to the mass accreted onto the black hole, with an overall heating efficiency of 1.5 per cent. Gas particles were heated to a fixed temperature (varying from 10^8K in the lowest mass clusters to $10^{8.5}$K in the most massive systems) when the required amount of energy was available.

For each of the 30 clusters, I constructed projected 2D maps of the density of the dark matter, the stellar material and the hot ($T > 10^6$K) X-ray emitting

gas along the z-axis. For the analysis I observed the clusters at two snapshots; one at a redshift $z = 0.6$ and the other at redshift zero. At these redshifts, the 30 clusters have M_{500} masses spanning the range $10^{13.5}$ – $10^{14.7} M_{\odot}$, with a mean mass $2.6 \times 10^{14} M_{\odot}$ and $1.1 \times 10^{14} M_{\odot}$ at $z = 0$ and $z = 0.6$ respectively, where M_{500} is the mass within the radius at which the mean density is 500 times greater than the mean density in the Universe. Fig. 4.4 shows the density field from one of the simulated clusters at $z = 0.6$. Here, the distribution of DM is shown in blue, the hot gas in red and the stellar material (galaxies and intracluster light) in white. The inset shows a zoomed view of a typical piece of subtructure where the DM and gas are clearly separated.

We use the public code *Wavdetect*, from CIAO TOOLS (Fruscione et al., 2006) to identify peaks in the DM, gas and stellar density maps. With the better peak detection algorithm than MKN, and a better model for AGN physics, I am now able to include substructure anywhere near a cluster, including the inner core ($r < 0.3\ r_{500}$). The substructure masses span the range $10^{12.0}$– $10^{14.4} \mathrm{M}_{\odot}$ with a mean mass $8.6 \times 10^{12} \mathrm{M}_{\odot}$ and $6.3 \times 10^{12} \mathrm{M}_{\odot}$ at redshifts $z = 0$ and $z = 0.6$. I find, on average, 10 substructures per cluster, with a mean value of $\langle M_{\rm sub}/M_{\rm cl} \rangle = 0.03$. We match adjacent gas, DM and stellar mass peaks, recording the positions and the standard errors returned by *Wavdetect*. For now, I complete this process without noise, but I shall repeat it in the presence of realistic observational noise in Section 4.4. comoving coordinates.

4.3.2 Component offsets in noise-free simulations

The mean offset between substructures' galaxies and baryonic gas is shown in Figure 4.5, as a function of various cluster properties. Position estimates from low-mass peaks are noisy, so I use inverse variance error estimates to compute a weighted mean. The black (blue) points show the offset around clusters at redshift $z = 0$ ($z = 0.6$).

The left panel of Figure 4.5 shows the offset between substructure components (in units of h^{-1}kpc), as a function of projected distance from the cluster in units of r_{500}. The dashed lines show the results of MKN as reference. At a redshift 0.6, I recover a similar $\sim 20 h^{-1}$kpc offset, but I find no statistically significant redshift dependence. We find that the offset drops at small projected radii. This is probably because substructures really passing through the core are disrupted and

dispersed. We therefore preferentially see substructure at large 3D radii, whose positions have been projected near the centre of the cluster. Their separations align nearly with the line of sight, so their projected separations appear small.

The middle panel of Figure 4.5 shows the offset as a function of the substructure mass. To estimate the substructure mass, I used the ratio of the total mass signal detected by *Wavdetect* near the substructure ($S_{\rm sub}$) and main cluster ($S_{\rm cl}$), i.e.

$$M_{\rm sub} = \frac{S_{\rm sub}}{S_{\rm cl}} M_{\rm cl}, \tag{4.35}$$

where $M_{\rm cluster}$ is the mass of the main cluster M_{500}. The decreased offset for massive substructures is consistent with the analytical model. The larger gravitational returning force will bind the stars and gas closer to the DM throughout infall.

The right panel of Figure 4.5 shows the offset as a function of the parent cluster mass. The increased offset near massive clusters is also consistent with the analytic model. More massive clusters have a higher density ICM, so the drag (and buoyancy) forces that drive the offsets will be increased.

We next look at the offset between substructures' galaxies and DM. In real data I expect this offset to reflect the interaction cross-section of DM, and any detected offset will imply a non-zero $\sigma_{\rm DM}/m$. The DM used for these simulations is collisionless, so I expect the offset to be consistent with zero. The offset between galaxies and the DM intersection point is shown in Figure 4.6. The position of the DM is indeed consistent with that of the member galaxies at both redshifts. Since there is also no significant gradient towards low mass substructure, I am confident that there is no residual bias in the simulations or subsequent analysis.

The transverse distance between the DM position and the intersection point, $d_{\rm DI}$, reflects the error in the estimated position of the DM, and should therefore be unbiased and consistent with zero. Figure 4.7 shows the offset between the DM and the intersection point as a function of the mass of the sub-halo. We see that the offset is consistent with zero in all cases, even at lower signal peaks. I am therefore confident there is no residual bias in the simulations or analysis.

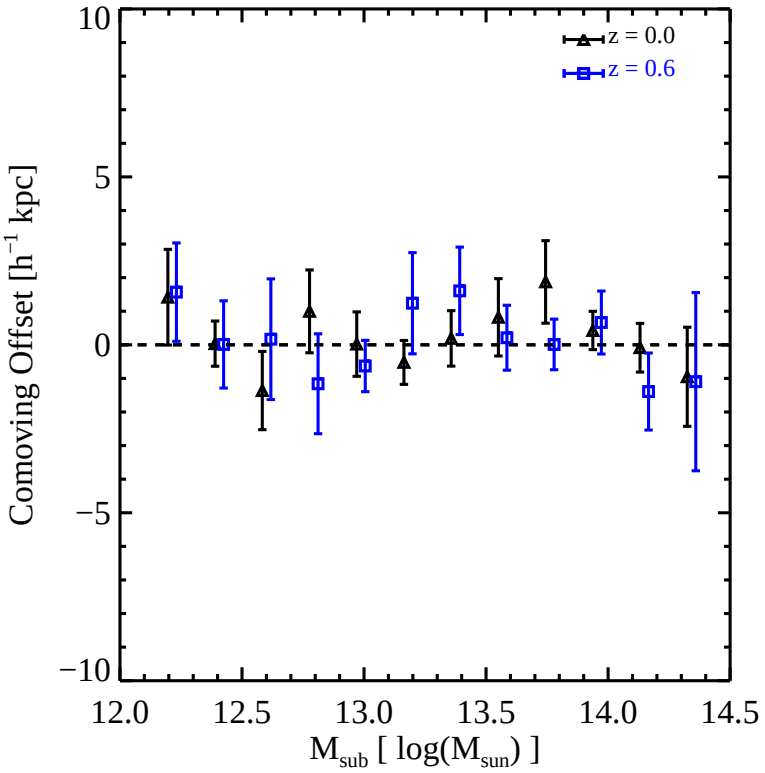

Figure 4.6: Projected offsets between substructure galaxies and the intersection point with DM in the direction towards the gas (SI) for $z = 0$ and $z = 0.6$. In real data, this distance will probe the finite cross-section of DM. Since the simulations explicitly use collisionless DM, I expect these offsets to be consistent with zero. Each point shows the weighted mean of offsets within that particular mass bin, with the error bars representing the one sigma error.

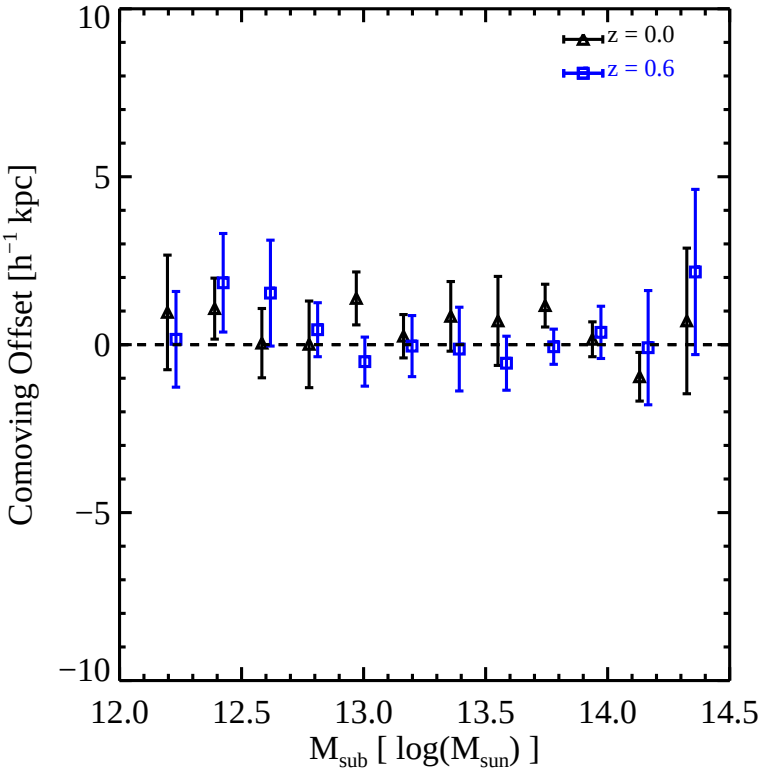

Figure 4.7: Projected, transverse offsets between DM and the intersection point (DI) for $z = 0$ and $z = 0.6$, which tests for potential systematics. Under the assumption that over an ensemble average there is no preferred in-fall direction and there is no systematic bias in the positional estimates of DM, this parameter should be consistent with zero. Each point shows the weighted mean of offsets within that particular mass bin, with the error bars representing the one-sigma error.

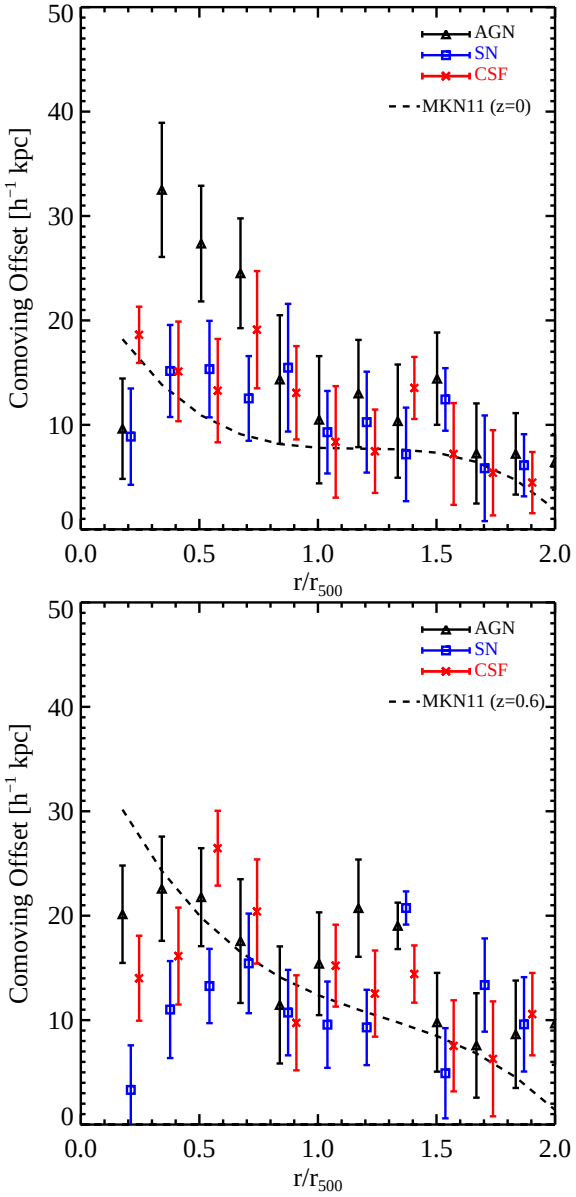

Figure 4.8: The observed offsets in substructure components appear broadly robust to astrophysical processes. The panels show the projected offsets $d_{\rm GI}$ between gas and dark matter (in the direction towards the galaxies) in substructure around 30 simulated clusters at $z = 0$ (left) and $z = 0.6$ (right), assuming different models of baryonic physics. Dashed lines show earlier predictions from MKN, for reference and ease of comparison.

4.3.3 Robustness to astrophysical effects

I find the offsets between substructure components at $z = 0$ consistent with those reported by MKN. Interestingly, I find little evolution with redshift, which was found by MKN, with discrepant offsets by $z = 0.6$.

We follow this interesting result and analyse the simulations. The simulations used in this chapter, as in MKN, modelled the cooling of gas, star formation and supernova feedback but also included feedback from AGN. AGN have a prominent effect throughout the cluster environment that may change the dynamics and properties of the in-falling sub-haloes.

In order to ensure that the redshift discrepancy is not due to the addition of AGN, I test the effects of astrophysical processes on substructure offsets and repeat the analysis on a range of simulations. Figure 4.8 shows the offset between substructure gas and DM at $z = 0.6$ (left) and $z = 0$ (right) in simulations with varying degrees of baryonic physics;

1. Cooling and star formation only (CSF, red points in Figure 4.8).

2. Cooling, star formation and supernova feedback (SN, blue points in Figure 4.8).

3. Cooling, star formation, supernova and active galactic nuclei feedback (AGN, black points in Figure 4.8).

The offset signal remains measurable in all cases, but I find differences near the cluster core and especially at low redshift. This is presumably due to the injection of outward energy by AGN into even the substructure gas, and will be more evident at lower redshift since feedback is proportional to the square the black holes mass which is increasing with cosmic time. The simulations without AGN feedback (blue points) are more consistent with the MKN simulations of similar physics. We therefore conclude that the small discrepancy between the amplitude of the offsets reported in this chapter and MKN are potentially due to different prescriptions of baryonic physics. However this does not account for the lack of observed redshift dependance. Indeed, the discrepancies could be attributed to how different codes simulate baryonic physics. In MKN, the code used to simulate the bayonic gas physics in the cluster was an adaptive mesh refinement code (AMR), whereas the code used for the simulations in this work

was based on smooth particle hydrodynamics (SPH). It is commonly understood that AMR and SPH differ in the way they calculate the physics of hydrodynamical bodies in clusters. These differences are most evident in the apparent stability of gaseous haloes. AMR structures are more likely to disrupt and disperse that SPH gas haloes Agertz et al. (2007). This could mean that any in-falling gas halo that separates from its bound DM sub-halo may disperse before exhibits a large separation from its DM host. On the other hand, SPH is known to form much more stable structures, which may mean that haloes can become significantly more separated before it disrupts and becomes part of the ICM. These differences could contribute to the discrepancies in displacements between the work in MKN and this study. I note that although there are differences between the two studies, the true underlying nature of the simulations and resulting implications for cluster dynamics are beyond the scope of this work.

4.3.4 Total matter vs. dark matter systematic bias?

We shall advocate using gravitational lensing to map the distribution of DM. However, gravitational lensing probes the *total mass* along a line of sight (see reviews by Bartelmann & Schneider 2001; Refregier 2003; Massey et al. 2010). The total mass is dominated by DM, but roughly 15% is in the baryonic gas at an offset location. In their analysis of the Bullet Cluster, Clowe et al. (2006) fitted the distribution of mass due to the X-ray emitting gas, and subtracted that from the lensing measurement of total mass in order to define a dark matter - gas offset. In principle, it would be possible to do the same in minor mergers, although the much lower S/N may cause practical difficulties.

In order to test such a systematic I convert the projected density fields of the cosmological simulations used in section 4.3 into 30 gravitational lensing maps via the formalism in Kaiser & Squires (1993), which demonstrates how the lensing signal is related to the projected surface density via a convolution. I limit the mock observations to the field of view of the *Hubble Space Telescope* (HST) Advanced Camera for Surveys, and assume a density of 80 galaxies arcmin^{-2}, as expected from a two-orbit exposure using the F814W band. I then scatter the background galaxies randomly on the sky, and interpolate the shear field to their positions, assuming they are all $z_{\rm source} = 1$. From these shear maps I conservatively select the two most massive DM haloes and reconstruct the

expected position (with *no noise in the ellipticity of the galaxy*), for two cases; one with the total matter in the simulation and one with the dark matter only. Then using LENSTOOL (Jullo et al., 2007), I reconstruct the DM positions with flat priors centred on the distribution of galaxies, making sure this prior includes the position of the gas halo. I test the effect of including the full matter distribution by calculating the resultant $\beta_{\|}$ using equation (4.2) for the two cases.

As Figure 4.9 shows, the false assumption that lensing measures only DM does indeed introduce a bias, mimicking the effect of a small interaction cross-section – but at the very low level of $\Delta\beta_{\|} \sim 0.005$. This is an order of magnitude below the statistical accuracy that will be possible with existing data (see next Section), so I shall neglect the effect for now. When the method is applied to future, very large surveys, and probes $\beta_{\|} < 0.05$, I suggest that the algorithm should be extended to simultaneously fit the DM and gas mass.

4.4 Prospects for measuring signal with realistic noise

By using the location of substructure galaxies as a proxy for the direction of in-fall, one can retain the $\sim 20h^{-1}$kpc absolute offset between DM and gas seen by MKN. To estimate this *signal* as accurately as possible, I have so far exploited noise-free simulations, and used many substructures per cluster, (using the well-known ΛCDM tendency to produce more satellite haloes than observed in data, (e.g. Springel et al., 2008)). To estimate a realistic *signal-to-noise*, and the prospects for constraining $\sigma_{\rm DM}/m$, I shall now add observational noise reflecting existing datasets to the shear fields used in section 4.3.4.

Once again, identifying only the two most massive sub-haloes in each of the sample of 30 clusters, I then consider the expected noise on the positions of each of their components.

4.4.1 Signal as a function of cluster redshift

Our simulations show no redshift dependence in the various substructure component offsets, in units of physical comoving separation (Figure 4.5). However, the apparent *angular* offsets, and the amount of a cluster visible in

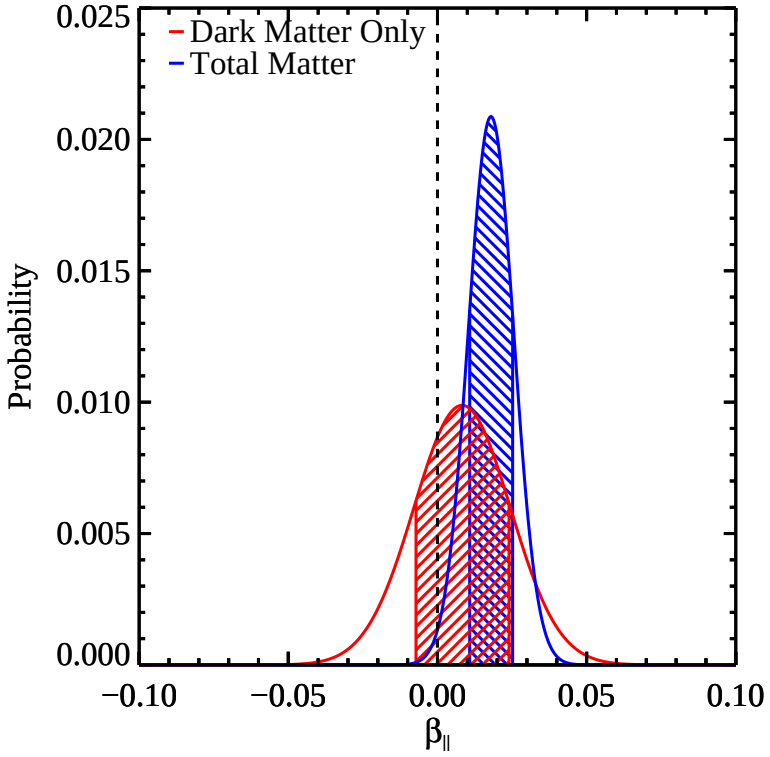

Figure 4.9: Bias induced in measurements of $\beta_{\|}$ by assuming that gravitational lensing measures only DM (blue, diagonally down hatching), rather that the total mass (red, diagonally up hatching). This is *an order of magnitude below* the expected statistical precision for 30 clusters. We can only detect this systematic effect in the *noise-free* simulations – note the change of scale on the horizontal-axis is compared to Figure 4.10. Only in very large, future surveys, will it be necessary to simultaneously fit (and subtract) the mass in the other substructure components.

a telescope's field of view, will depend upon the distance to the cluster (its gravitational lensing signal also depends on the distance). We could rely upon this lack of evolution. However, to compare measurements from clusters at different redshifts in a controlled way, we take the mass snapshot of each cluster at $z = 0$, and rescale it as if it were at $z_{\rm lens} = 0.2$, 0.4 and 0.6. In each case, I assume all 30 clusters are at the same redshift; in reality, a sample will include clusters from a range of redshifts.

I impose an source galaxy intrinsic ellipticity distribution with $\sigma_\epsilon = 0.3$ (Leauthaud et al., 2007a). Here I am primarily interested in the potential for error from the complex morphologies of the simulated substructure and will address systematics later in the thesis. For those haloes that exist at a redshift of z=0.6,

however lie outside of the field of view (FOV) at a redshift of z=0, I discard these and select the next largest sub-halo in the FOV.

4.4.2 Noise in X-ray and Galaxy observations

We note that the noise in the positions of the member galaxies should be sub-dominant to the error in the position of the dark matter. The error in the gas haloes however, should be reasonably well-estimated from the simulations. In the case of isolated sub-haloes in observational X-ray data, positions can be extremely well constrained. The dominant error in the positions of gas haloes will arise from estimating the distribution of non spherical, amorphous haloes that have uncertain merger histories. Such effects are simulated via the hydrodynamics of the simulation and are included in the positional estimates from the peak finder however to reflect expected shot noise I introduce additional noise into the X-ray halo positions.

4.4.3 Expected statistical precision

After measuring the position of all the substructure components, I measure $\beta_{\parallel}$ (see equation 4.2) for each bullet. We model the probability distribution function (PDF) of this as a Gaussian centered on the best-fit value and a width corresponding to the measurement error. Figure 4.10 shows the stacked PDF of $\langle\beta_{\parallel}\rangle$ at three different redshifts.

All of the estimates of $\beta_{\parallel}$ are consistent with zero, as expected for simulations of non-interacting DM (Figure 4.10). Constraints are tightest for clusters at low redshift, where the angular separation of components is larger, and the gravitational lensing signal is stronger. For clusters at $z = 0.2$, the two-tailed 68% confidence limit on $\langle\beta_{\parallel}\rangle$ is ± 0.15, implying that I will be able to make a $\sim 6\sigma$ detection of an offset between DM and baryonic gas in data.

To estimate the constraints on $\sigma_{\rm DM}/m$, I propagate the PDFs of $\langle\beta_{\parallel}\rangle$ through equation (4.9). For the purposes of this exercise, I assume that $\sigma^{\star}/m = 4.5\pi\,{\rm cm}^2{\rm g}^{-1}$. The expected constraints from clusters at the three redshifts are shown in Figure 4.11.

We find that a conservative sample size of ~ 60 sub-haloes should constrain $\sigma_{\rm DM}/m$ to less that $1\,{\rm cm}^2/{\rm g}^{-1}$ at the 68% confidence level (or within those errors

if the DM really is collisional). We note that although the simulations here are of CDM only, and not SIDM, the error bars gained are not expected to alter in the presence of interacting dark matter since they reflect the expected scatter when fitting profiles to amorphous haloes of dark matter. I am therefore confident that such constraints can be made in the presence of observational data. In the current regime, this is limited only by $\sqrt{n}$ statistics of the number of pieces of observed substructure. This is extremely encouraging for future detections which will have access to orders of magnitude greater numbers of galaxy clusters.

4.5 Conclusions

We have presented a new method to probe the interaction cross-section of dark matter ($\sigma_{\rm DM}/m$). By measuring the relative distance that a dark matter sub-halo lies from its galactic component with respect to the distance the baryonic gas lies from the same galactic component, I have derived a new parameter β, which is independent of any line of sight projections. In order to interpret this parameter β as a cross-section I have developed an approximate analytic model for substructure infall, considering all the major forces acting on the three components. In particular, I model the DM interactions based on the type of frequent, velocity independent interactions, outlined in K13, with particles exchanging small amounts of momentum, resulting in a overall drag force on the halo. This regime means that the interpretation is unique in probing types of DM scattering similar to that of Rutherford scattering, in which the differential cross-section is highly anisotropic.

We show, in the limit that the cross-section of DM is small, that the ratio, β, of the distance between an in-falling dark matter (DM) halo and member galaxies and in-falling gas halo and member galaxies scales linearly with the optical depth of the DM-halo. In the regime that the cross-section becomes comparable with baryonic gas and the halo becomes optically thick I postulate the scaling of $\sigma_{\rm DM}/m$ to larger values. We predict that this scaling follows the general equation for the attenuation of momentum from scattering particles through a medium. This interpretation satisfies the conditions that requires this scaling to be linear in the low limit and tend to some value determined by the macroscopic properties of the halo. We parameterise this transition regime with $\sigma^{\star}$ and find

that $\sigma^\star = \pi s_{\rm D}^2/M_{\rm D}$ where s and M are the size and mass of the DM halo and is analogous to a sub-halo with an optical depth of unity.

The specific improvement of the method over previous work is to use the position of substructure member galaxies to define the direction of infall. This removes the dominant uncertainties in previous merging cluster estimates of $\sigma_{\rm DM}/m$, due to the unknown orientation with respect to the line of sight, and the time of infall. It also defines a preferred direction in each cluster in which to optimally search for a signal (and a perpendicular direction to use as a systematics test). We have applied the method to hydrodynamical simulations of galaxy cluster formation. The expected offset of $\sim 20h^{-1}\,$kpc is an order of magnitude larger than without the preferred direction, and should be readily observable with existing archival data. We find that one should be able to detect an offset between collisionless DM and gas at $\sim 6\sigma$, and measure $\sigma_{\rm DM}/m$ with 68% confidence limits of $\pm 1.0\,{\rm cm}^2{\rm g}^{-1}$.

Our analytic model should be sufficient to look for and interpret measurements of $\sigma_{\rm DM}/m$ from existing archival data. However, the main benefit of statistically exploiting minor mergers rather than a few major mergers, is that there is an almost limitless number of them all over the sky. These will be observed in the next decade by surveys such as Euclid[1] (Laureijs et al., 2011) and WFIRST AFTA (Spergel et al., 2013) which will observe > 1000 clusters resulting in potential statistical errors of $< 0.1{\rm cm}^2{\rm g}^{-1}$. In order to understand the physics of substructure in-fall and the separation of mass components, at the level of accuracy required to interpret those data, I will require accurate simulations of minor mergers with DM of varying cross-sections.

[1] http://www.euclid-ec.org

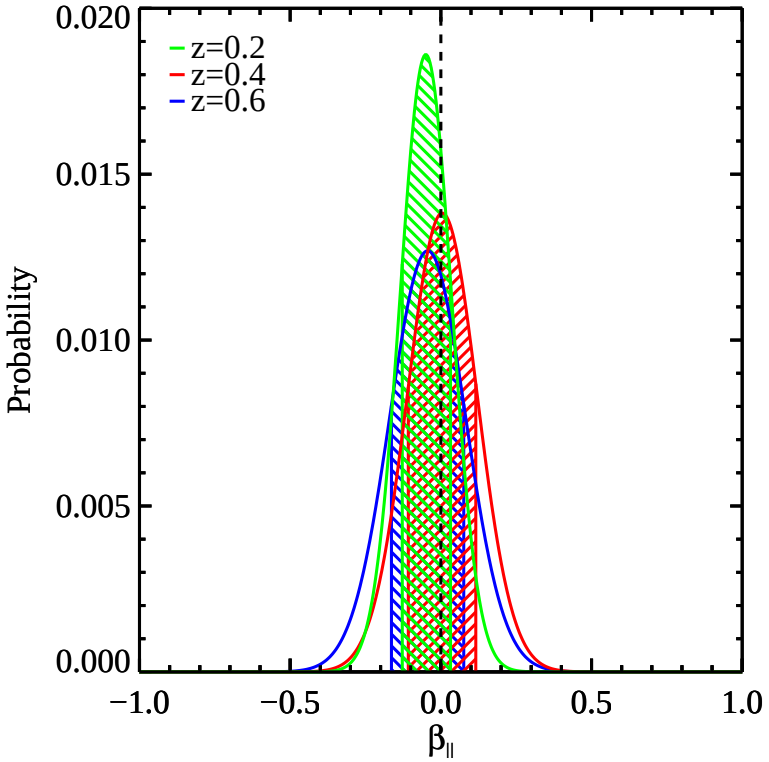

Figure 4.10: Potential constraints on $\beta_{\parallel}$ from a sample of 60 minor mergers in the presence of realistic observational noise. Hatched regions show the integrated 68% confidence limits. The different colours show expected constraints if the clusters were all at redshift $z_{\rm lens} = 0.2$, 0.4 or 0.6, where the tall Gaussian with diagonally down hatching is $z = 0.2$, the middle peak with diagonally upward hatching is $z = 0.4$, and the smallest peak with diagonally downward hatching is $z = 0.6$. We have explicitly removed all redshift-dependence of the physical signal; the changing errors here are due to the apparent angular size and the lensing geometry at different distances from the observer. All the distributions are consistent with zero, as expected from the collisionless dark matter used in the simulations.

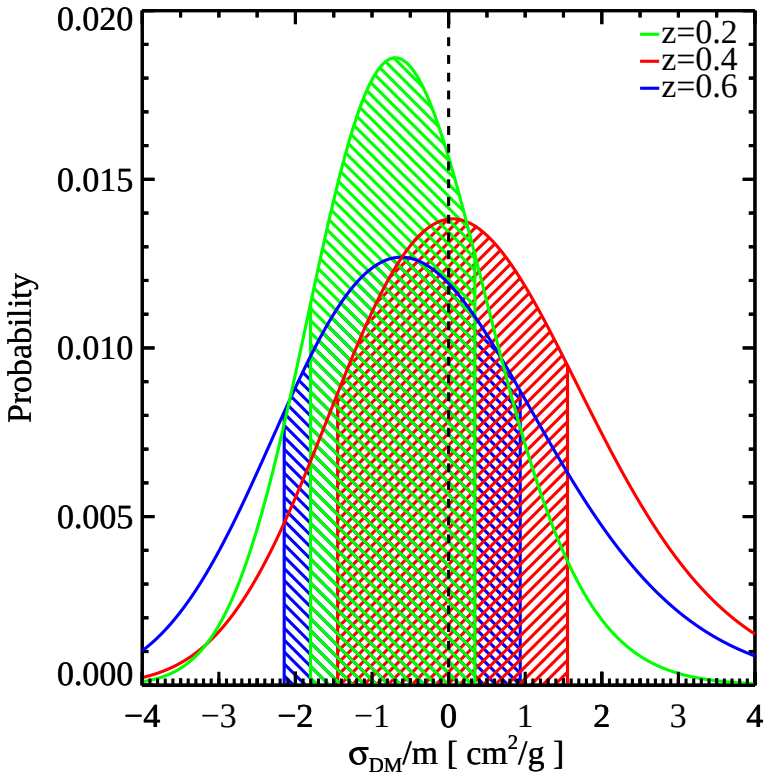

Figure 4.11: Potential constraints on the self-interaction cross-section of DM $\sigma_{\rm DM}/m$ from a sample of 60 minor mergers in the presence of realistic observational noise. Hatched regions show the integrated 68% confidence limits, where the tall Gaussian with diagonally down hatching is $z = 0.2$, the middle peak with diagonally upward hatching is $z = 0.4$, and the smallest peak with diagonally downward hatching is $z = 0.6$.. This is a propagation of Figure 4.10 using equation 4.9, assuming $\sigma^\star/m = 4.5\pi\,{\rm cm}^2{\rm g}^{-1}$. For clusters at redshift $z = 0.2$ the constraints are much tighter implying potentially a limit of $< 1{\rm cm}^2{\rm g}^{-1}$ to 68% confidence.

5 Accuracy of sub-halo positions in galaxy clusters

"I'm not interested in the preserving the status quo; I want to overthrow it."

5.1 Dark matter astrometry

Massey et al. (2011, hereafter MKN) showed that a collisionless dark matter sub-halo should separate from it's associate gas halo during accretion due to its differing interaction properties. When averaged over many haloes and in-falling scenarios, this effect was found to be $\sim 10'', 3.5''$ and $2''$ at a redshift $z = 0.1, 0.3, 0.6$ respectively at a radial of distance of $0.15r_{500}$, which increased towards to the centre of the cluster. Therefore the measurement of an offset relies upon an ability to measure the position of substructure components with minimal bias near to the core. Statistical errors will be gradually beaten down by averaging many measured offsets. However any systematic bias in the centroid of either component will propagate into constraints on the interaction cross-section.

The spatial resolution of the X-ray space telescope Chandra is sub-arcsecond, whereas any weak lensing map will be limited by the finite density of resolved galaxies to $\sim 10''$ with the deepest, highest resolution data (e.g. Massey et al., 2007b) . Although the accuracy in which one can define the X-ray peak will depend on the distribution of gas the dark matter peak will be affected by a

similar problem. Therefore it is possible to assume that the error in the X-ray peak position is subdominant to that of dark matter, and study in detail the reliability of weak lensing centroid estimates only. We will also quantify the precision of weak lensing centroiding, to estimate the sample size required to detect bulleticity.

In this work I assess the precision and accuracy of weak gravitational lensing measurements of the *position* of mass peaks. This differs from the many studies that have assessed the precision and accuracy of measurement of the *mass* of mass peaks. We investigate whether it will be possible to detect small offsets in position on the sky between the baryonic and DM density peaks of cluster substructures (Massey et al., 2011, hereafter MKN). We imagine detecting these in-falling galaxy groups, and measuring their barycenters, from their X-ray (or optical) emission, and comparing with the positions of mass density peaks reconstructed by analysis of weakly lensed background objects in the vicinity. Such analyses have been carried out in individual interacting clusters using flexible exploratory mapping techniques by (e.g. Clowe et al., 2004; Markevitch et al., 2004); here I consider measuring offsets – "bulleticities" – in many different clusters, and combining the results in a statistical measurement of the interaction cross-section (MKN). In particular, I am interested in using analytically simulated data to answer the following questions:

- To what precision can I measure the offset in a single in-falling substructure?
- Can I identify a point estimator whose simple combination over a sample will provide a measurement of sub-halo position with minimal bias?
- What are the dominant sources of residual bias in this estimate?
- How large a sample of observed clusters am I likely to need to be able to detect an offset between dark matter and baryonic as predicted by MKN?
- What further investigation might be needed to prove the utility of this technique for probing DM interaction cross-sections?

This chapter is organised as follows. In Section 5.2 I present an end-to-end simulation pipeline in which I start with a known mass distribution, simulate HST lensing data, then use LENSTOOL to reconstruct the mass distribution. In Section 5.3 I describe the results and in Section 5.6 I conclude.

5.2 Methodology

5.2.1 Simulated shear fields

In order to examine the exact behaviour of weak lensing as a positional estimate of dark matter I need initial experiments in carefully controlled environments. This includes having mass distributions with well defined correct answers rather than cosmological simulations. We therefore create simulated shear fields containing DM haloes of known position, mass and ellipticity. For typical clusters, an empirical relation (Macciò et al., 2008) suggests that the concentration of an NFW halo is related to the mass via,

$$\log\langle c\rangle = 0.830 - 0.098 \log\left(M_{\rm vir}/\left[10^{12}h^{-1}M_{\odot}\right]\right), \tag{5.1}$$

where $M_{\rm vir}$ is the virial mass and the dimensionless hubble parameter, $h = H_0/100{\rm Mpc/km/s}$.

Using multiple NFW haloes, I construct a cluster system with in-falling galaxy group(s). As shown in Figure 5.1, the baseline configuration includes a main halo in the centre of the field of view plus a sub-halo 49″ to the north. Substructure typically contains $\sim 10\%$ of the mass of a system (e.g. Cohn, 2012), we fix the mass of the sub-halo to be always 10% that of the parent halo (with a concentration parameter given by equation 5.1). In the event there is more that one halo in the field, the shears will simply add, such that $\gamma_{\rm total} = \gamma_{\rm main\ halo} + \gamma_{\rm sub-halo_1} + \gamma_{\rm sub-halo_2} + \cdots + \gamma_{\rm sub-halo_n}$.

In order to get high signal to noise imaging of cluster cores I manufacture simulated Hubble Space Telescope (HST) weak lensing measurements of the cluster system. In a $200'' \times 200''$ field of view, shear measurements are simulated from 80 (randomly placed) galaxies per square arc minute, as could be obtained from a full 1-orbit exposure in the F814W band with the Advanced Camera for Surveys (ACS). In a typical Hubble archive the redshift of a cluster varies between 0 and 1. I choose a conservative redshift of 0.6, at which the bulleticity signal is small but potentially detectable. For each cluster configuration and mass, I generate 100 noise realisations.

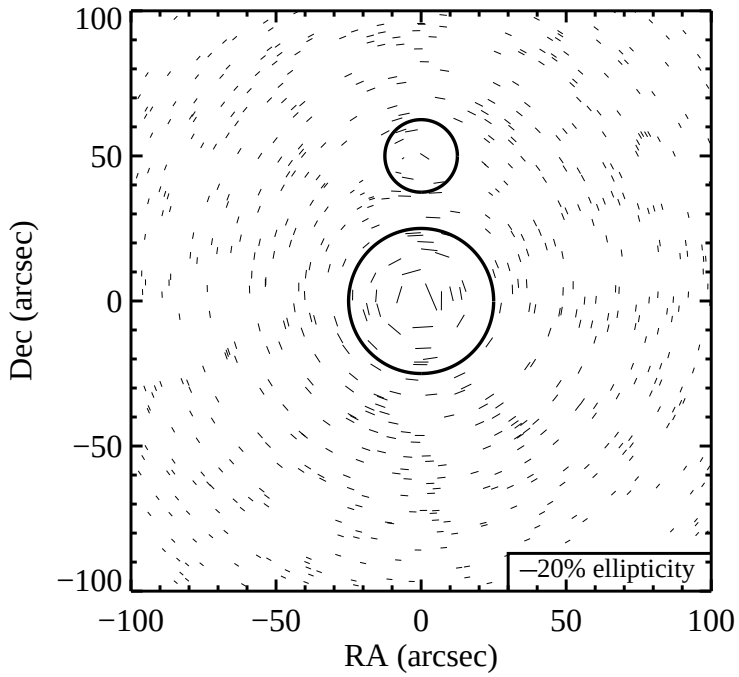

Figure 5.1: The reduced shear signal of a simulated cluster with a NFW profile. The main halo has a M_{200} of $8 \times 10^{14} M_{\odot}$ and is positioned at (0,0) and the sub-halo, $8 \times 10^{13} M_{\odot}$, is positioned at (0,49). The field of view represents that of a Hubble Space telescope Advanced Camera for Surveys with a typical density of galaxies of 80/square arc minute. The circles are a guide for where they are placed and have no physical significance.

Intrinsic galaxy morphologies

The basic challenge with weak lensing measurements is that galaxies are not inherently circular – indeed, the ellipticity of a typical galaxy is an order of magnitude larger than the shear. Chance alignments of galaxies can mimic a coherent gravitational lensing signal and introduce noise into the mass reconstruction. In individual clusters, such noise can cause centroid shifts of $\sim 10''$, but this should average away as long as the noise has no preferred direction over a sample of clusters. Leauthaud et al. (2007) state that galaxies typically have a intrinsic ellipticity distribution with a mean of zero and an width, $e_{\rm int}$ of 0.3. This can be expressed as a complex number by $e_{\rm int} = |e_{\rm int}| \exp(2i\theta)$, where θ, is the angle of the galaxy. I can then transform the galaxy from the source plane to the image plane using the prescribed treatment to derive the expected shear on a galaxy with some random intrinsic ellipticity.

Elliptical Mass Distributions

Galaxy clusters are often not spherically symmetric (Jetzer et al., 2002). Misidentifying the shape of a halo can introduce spurious detections of substructure along the major axis, or shift the apparent position of real substructure. It is therefore important to check whether elliptical haloes affect the centroid estimate of both the cluster and the sub-halo. We have run simulations with both a spherical and an elliptical main halo. In elliptical cases, the ellipticity of the main potential was fixed at 0.2 (where ellipticity = $[a^2 - b^2]/[a^2 + b^2]$). To span a range of possible scenarios, the major axis is aligned at 0°, 45° or 90° from the positive x-axis (in the latter case, this points towards the sub-halo).

It was considered that force fitting a circularly symmetric fit to an elliptical main halo could potentially bias the position however the signal to noise of the sub-halo would mean that constraining the ellipticity would not be possible. Moreover DM would interact only gravitationally, and therefore I expect any in-falling halo to retain its radial symmetry, thus in all cases the sub-halo is kept circular.

Table 5.1: Input values and priors used during the reconstruction on the main and sub-halo in the simulations. The values in the square brackets refer to the range, and the dots refer to the different mass scales of the simulations.

	Input Value	Prior	Type
Main Position (arcseconds)	(0,0)	30 on (0,0)	Gaussian
Sub 1 Position (arcseconds)	(0,49)	25″ on (0,49)	Flat Circle
Sub 2 Position (arcseconds)	(49,49),(49,0),(0,-49)	25″ Radius	Flat Circle
Main Halo Mass ($M_\odot$)	$(1, 1.5 \ldots 7.5, 8) \times 10^{14}$	$[0.5, 49] \times 10^{14}$	Flat
Sub Halo Mass ($M_\odot$)	$(1, 1.5 \ldots 7.5, 8) \times 10^{13}$	$[0.5, 49] \times 10^{13}$	Flat
Main Halo Concentration	Mass:Conc Rel	$[1, 10]$	Flat
Sub Halo Concentration	Mass:Conc Rel	$[1, 10]$	Flat
Mass Priors	$M_{main} > M_{sub}$	$M_{main} > M_{sub}$	Heavy Side

Imperfect shape measurement

Achieving sub-percent accuracy in the measurement of galaxies' apparent shapes is an ongoing challenge Heymans et al. (2006); Massey et al. (2007a); Bridle et al. (2010); Kitching et al. (2012a); Mandelbaum et al. (2013); Kitching et al. (2012b). Even with a *space*-based telescope, the point spread function (PSF) varies across the field of view and can change over time (Rhodes et al., 2000). If the PSF is not accurately modelled or the image effectively deconvolved, it can be spuriously imprinted upon the shear measurements. Image noise and pixelation further impede the measurement of small, faint galaxy shapes.

We do not consider multiplicative shear measurement biases here, since they bias only the recovered mass estimates, and not the positions. We do, however, consider additive shear measurement biases, which will affect the inferred mass clump positions. The PSF normally has a preferred direction with respect to the telescope, but the location of substructure and the angle of orientation at which the cluster is imaged will vary from cluster to cluster. In each realisation of a simulated catalogue, I add a constant spurious signal c_i to each component of shear, drawn from a Gaussian distribution with mean 0 and standard deviation 0.01 (which is split into shear components so that it is in a random direction).

Finally, I model the pixelation noise by adding an additional stochastic component to each shear measurement, drawn from a Gaussian distribution with mean 0 and width 0.01 again split into components, although this is effectively degenerate with (and subdominant to) the intrinsic ellipticity. Thus the observed shears become

$$e_i^{\rm tot} = e_i^{(\rm I)} + c_i + \sigma_i^N. \tag{5.2}$$

Although many algorithms linearise the lensing potential, which doesn't hold in regimes of $g > 0.1$, the bias introduced by this assumption can be considered a multiplicative factor to the shear and in fact would not have an affect on the position of the sub-halo (Melchior & Viola, 2012)

Galaxy redshift distribution

A statistical measurement of bulleticity will require a large sample of galaxy clusters, and multicolour imaging may not be available for them all. The distortion experienced by each galaxy image depends upon the lensing geometry. With only monochromatic imaging, it can even be impossible to tell whether galaxies are behind a cluster (and therefore lensed) or in front of it (and therefore undistorted). Allowing foreground galaxies in the galaxy catalogue will dilute the inferred shear signal. We introduce a source galaxy redshift distribution

$$p(z) \propto z^2 \exp\left[-\left(\frac{z}{z^\star}\right)^{1.5}\right], \tag{5.3}$$

where $z^\star = z_{\rm med}/1.1412$ and $z_{\rm med} = 1.0$ (Taylor et al., 2007). We apply this uniformly across the field of view. We assume I know exactly the redshift of the cluster (0.6) and for the purposes of measuring the position I do not concern ourself with $\Sigma_{\rm crit}$ and the total mass.

A further problem with having only monochromatic imaging is that it will be impossible to distinguish between background sources and cluster members. Although the effect of this would be further dilution of the signal, since the members will be correlated with the density profile of the cluster the dilution will also be correlated. It is therefore possible for the position of the halo to be biased if these galaxies are included in the reconstruction. Therefore, a simple

distribution of member galaxies is placed over the cluster such that they follow the NFW profile. The number of member galaxies is then increased and to study the affect the member galaxies may have.

Multiple substructures

In the paradigm of hierarchical structure formation, clusters grow through multiple mergers, so multiple sub-haloes may be physically close to a cluster at a given time. The presence of multiple sub-haloes will complicate the shear field and thus make it harder to estimate the positions of each. It is therefore important to be confident that if sub-haloes are close together in real space their signals do not cause a bias in any direction. A set of realisations were run where a second sub-halo was introduced into the field. The first sub-halo remained at (0,49) arcseconds from the main halo; to span a range of possible configurations, the second halo was placed at three different positions (49,49), (-49,0) and (0,-49) arcseconds from the main halo.

Potential line of sight contamination

Independent large scale structure at different redshifts may happen to lie along the line of sight to the cluster, and be misinterpreted as substructure (Hoekstra, 2001; Spinelli et al., 2012). As unassociated galaxy groups will not be falling into the cluster, they will not exhibit any systematic offset between DM and gas, and their inclusion will spuriously dilute the measured bulleticity. Since substructure will be initially identified via X-ray imaging, I can estimate the number of coincidentally aligned structures by considering the density of X-ray luminous groups in unpointed observations.

In the 1.64 square degree COSMOS survey (Scoville et al., 2007), Finoguenov et al. (2007) found 206 X-ray groups with masses 10^{13}–$10^{14} M_{\odot} h_{72}^{-1}$, which matches the mass range considered in this work. Leauthaud et al. (2010) tried to detect all of these groups via weak lensing from 1-orbit HST imaging. About a quarter of the groups are detected at greater than the 2σ detection threshold. Scaling this down to the $200'' \times 200''$ ACS field of view, I expect a contaminant of around 1 spurious peak for every 20 clusters. This $\sim 5\%$ dilution should be considered in a second larger survey (e.g. HSC, DES, Euclid), and could be reduced if (even coarse) photometric redshifts were available for some galaxies.

Substructure as a function of distance from the cluster centre and mass ratio

The basis simulation is set up such that the distance the sub-halo is from the centre of the cluster and the mass fraction between the main halo and the sub-halo is held constant. Although the values used for the simulations are that of a typical cluster these will not be constant in the case of real data and therefore the radial distance and the mass fraction are both independently varied.

5.2.2 Mass reconstruction

Many algorithms have been developed to reconstruct the mass, concentration and position of massive ($> 10^{14} M_{\odot}$) haloes from observations of weak (and strong) gravitational lensing (Bradač et al., 2005; Cacciato et al., 2006; Diego et al., 2007; Merten et al., 2009). However, testing of these has generally focussed on the mass and concentration parameters, positional accuracy has not yet been pushed to the low $\sim 10^{13} M_{\odot}$ mass regime.

To determine the viability of bulleticity measurements, weak lensing reconstructions must be tested in scenarios that reflect the environments in which it will be used. The main requirement for bulleticity is an accurate estimate of the sub-halo and main halo positions with minimal bias.

We will use the publicly available LENSTOOL since this uses analytical NFW haloes, reporting single point estimators of the position of a dark matter halo, and hence is particular ideal for this study. For a review of LENSTOOL, please see Section 3.3.2.

We note here that since the chi-squared is calculated in the source plane, the reconstruction can be affected by the way LENSTOOL converts from the source plane to the image plane. The input parameters for LENSTOOL are the semi major axis a, the semi minor axis, b, and the angle of the galaxy with respect to the image x-axis. These ellipse descriptors not only define the ellipticity of the galaxy but also the size. It has been shown in Schmidt et al. (2012) that measuring the sizes of a galaxies is difficult and also ambiguous in how one defines it therefore I would like to avoid using this parameter. We therefore decide to use *option 7* in LENSTOOL[1], which transforms the ellpiticity parameters of the galaxy in the

[1]We also tested *option 6* which takes a,b and the angle and transforms them directly to the source plane via equation a matrix operation of the image moments, however this requires full

image plane removing any information on the size of galaxy. The ellipticity $e^{(I)}$ is then transformed into the source plane via in the equation (3.19). From this the chi-squared is calculated. Since LENSTOOL calculates the source ellipticity in this way I assign some nominal value to the size of the galaxy in the simulations.

Weak lensing mass reconstructions inevitably have limited resolution, as the shear field is sampled only at the positions of a finite number of background galaxies. Fortunately, all that is required to get a robust measurement of bulleticity, is unbiased centroid measurements. Where available, strong lensing dramatically tightens the resolution of mass maps – but to rely on strong lensing would unacceptably reduce the number of clusters that I could use.

Since bulleticity measurements will always require overlapping X-ray observations, I will use them to inject information into the reconstruction as a Bayesian prior. By assuming that each X-ray peak has an associated group of galaxies, and that the maximum signal for bulleticity is $\sim 10''$ at a redshift of 0.1 (MKN), it is only necessary to consider mass peaks within a small area around the substructure and main cluster only, ignoring the rest of the field of view. So if the X-ray suggests a two body configuration then this is the model that is used.

Table 5.1 shows the positions and masses of the clumps simulated with the associated priors used.

Estimation of sub-halo position

In order to understand LENSTOOL and its behaviour in the weak lensing limit for a two halo system, I tested it on noise free simulations where the galaxies were inherently circular and the only effect was gravitational shear. Since Lenstool is a maximum likelihood algorithm in the case of zero noise the chi-squared calculation becomes undefined, so therefore I set the variance of ellipticity in LENSTOOL to a very small value (0.01).

Figure 5.4 shows the full posteriors for the positions of the main and sub-halo. The positions from the sampler have been binned with the maximum likelihoods shown as solid lines and the true values as dotted. The top panels show radial and tangential position of the main halo and the lower panels show the radial and tangential positions of the sub-halo. It is clear that in the situation where there

knowledge of the size of the galaxy in order to obtain correct a, b and angle parameters. Failure to do so will cause a bias in the parameter estimation hence why I used *option 7*. Incidentally I found no increase in error by using *option 7*.

is no noise and the exact profile is given to lenstool the maximum likelihood is centred on the true position with extremely small variance.

5.3 Results

The expected offset between dark and baryonic components is $\sim 2''$ ($\sim 3.5''$) at a redshift of 0.6 (0.3) at a radial of distance of $0.15r_{500}$ and therefore any bias needs to be subdominant in comparison. The redshift distribution of clusters in the COSMOS field (Finoguenov et al. 2007) suggest that I expect a similar number of clusters at a redshift of 0.3 to 0.6, therefore the measurement of an offset can tolerate $\sim 0.5''$ bias in the reconstruction in order to measure a bulleticity signal to $\sim 3\sigma$ significance detection.

In an attempt to understand the behaviour of LENSTOOL, initial simple simulations were run and then an increasing number of contaminants and complexities were introduced. Unless stated otherwise, each panel in each figure shows δ: the maximum likelihood radial position minus the true position for a given mass and simulation configuration, weighted averaged over 100 realisations for a given mass scale and then averaged over each configuration shown in the cartoon inset of the plot, i.e.

$$\delta_{\rm halo}(m) = \langle \langle r_{\rm Meas}(m) - r_{\rm True} \rangle_{100} \rangle_{\rm config}, \tag{5.4}$$

and the error for the given configuration is just given by the error in the mean. Furthermore the main halo is always 10 times more massive than the sub-halo (and appropriate concentrations given by equation 5.1).

We carried out four initial tests in the simplest two body case: one with a circular main halo and three with elliptical main haloes at different angles. Each test contained a simple background galaxy Gaussian intrinsic distribution and was run 100 times with different noise realisations. I then fitted two lines of best fit to the data to determine any significant bias in the positional estimates. One was a constant offset and the other a mass dependent one. For the sub halo I found that the reduced chi-square for a mass dependent line was 1.34, whereas for a constant offset I found a reduced chi-square of 1.25. Thus I found no significant evidence for a mass dependent bias and therefore fitted a constant offset.

Each configuration showed in the cartoon inset of Figure 5.5 exhibited no

Figure 5.2: Main halo positional estimates

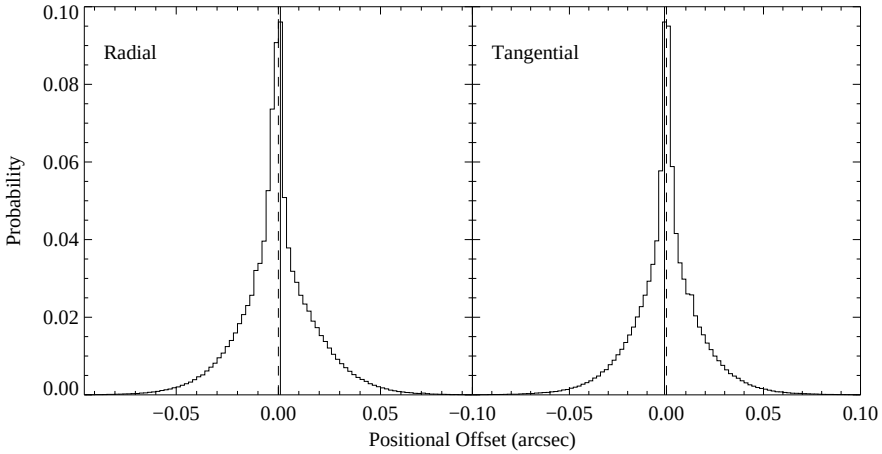

Figure 5.3: Sub-halo positional estimates

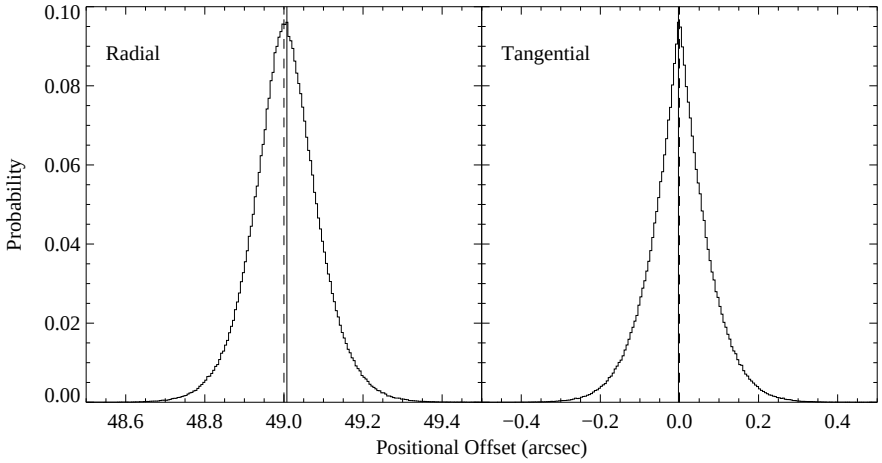

Figure 5.4: The likelihood surface for the main (top) and sub (bottom) halo positions in the case of zero noise (gravitational shear only). The binned histograms show the true posteriors and their maximum likelihoods as the solid line. The dotted line is the true position. The left hand panels are the position in the radial direction and the right hand panels are tangential direction. In the case of no noise the likelihood surface derived from LENSTOOL exhibits no bias around the maximum likelihood.

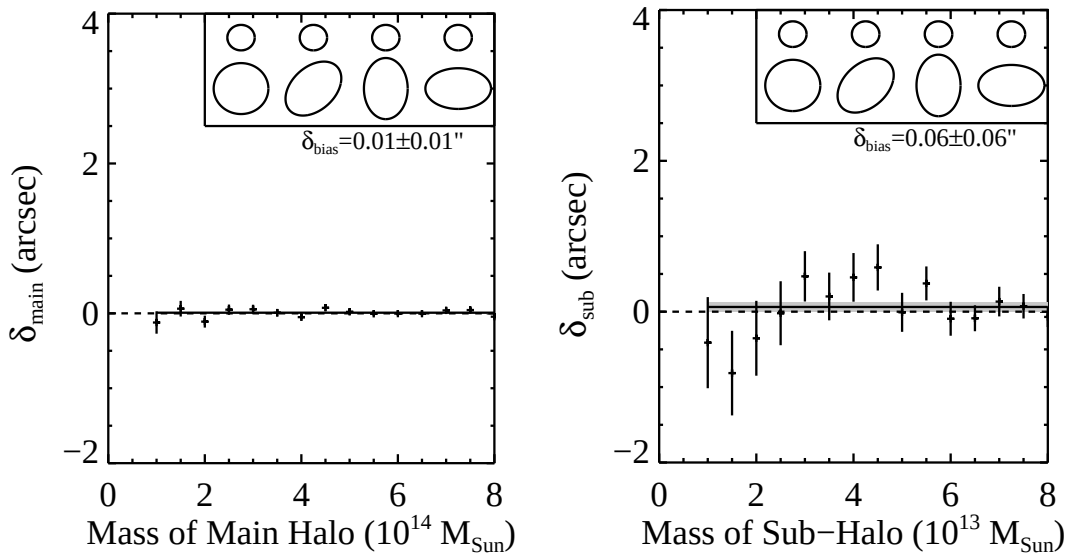

Figure 5.5: **Intrinsic ellipticities only**: The left and right hand panel show the positional estimates of the main and sub-halo respectively. In this initial test the background galaxies only contained a Gaussian intrinsic ellipticity distribution. The mass of the respective haloes are shown, in all cases the sub-halo was 10 times less massive than the main halo. (So results at $8 \times 10^{14} M_{\odot}$ main halo in the left hand panel are from the same simulation as those shown at $8 \times 10^{13} M_{\odot}$ in the right hand panel). A variety of configurations were tested with the cartoon inset showing the setup in each case. For each configuration, 100 noise realisations were run at the mass scale, the position of each halo estimated and then averaged over the all configurations. (so each point reflects 400 averaged simulations).

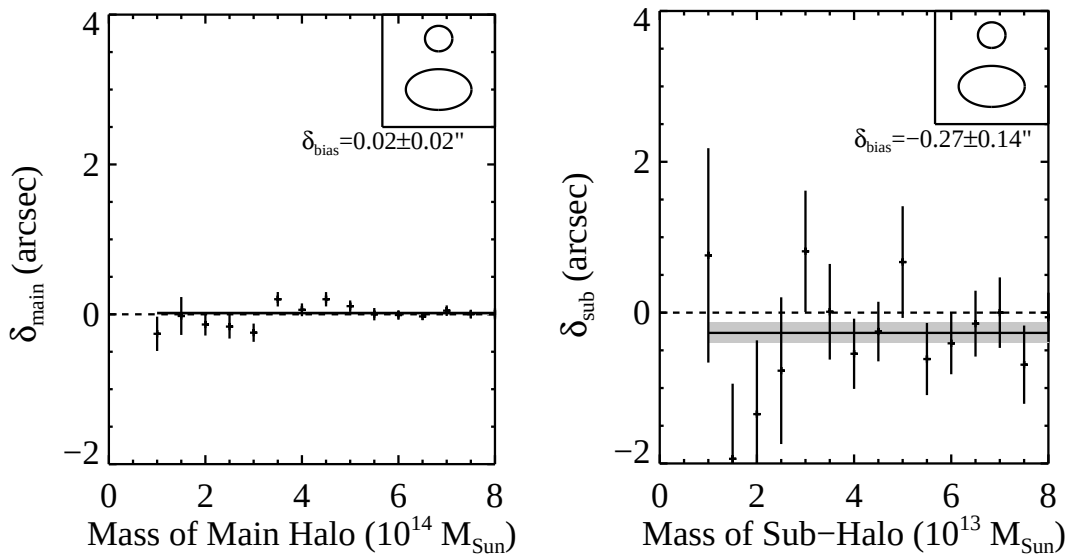

Figure 5.6: **Intrinsic ellipticities and shape measurement bias**: The left and right hand panel are the positional estimates of the main and sub-halo respectively. In each case the mass is given and the main halo is 10 times more massive than the sub-halo. The main halo is elliptical and the background galaxies have shape measurement bias and intrinsic ellipticities. In this case 100 realisations were run and the average position at each mass scale calculated.

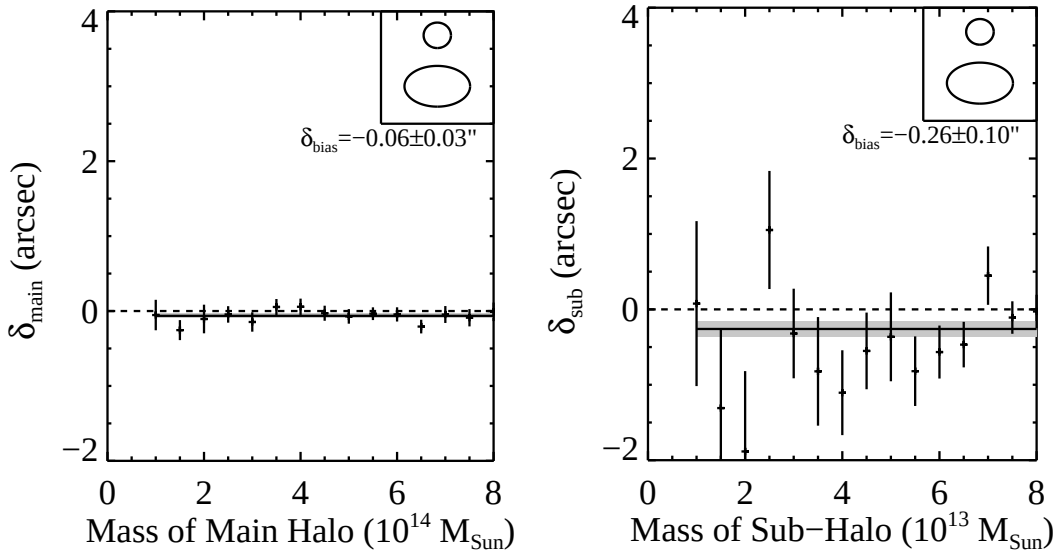

Figure 5.7: **Intrinsic ellipticities, shape measurement bias and source galaxy redshift distribution**: The left and right hand panel are the positional estimates of the main and sub-halo respectively. In each case the mass is given and the main halo is 10 times more massive than the sub-halo. The main halo is elliptical and the background galaxies have shape measurement bias, a distribution in their redshift and intrinsic ellipticities. In this case 100 realisations were run and the average position at each mass scale calculated.

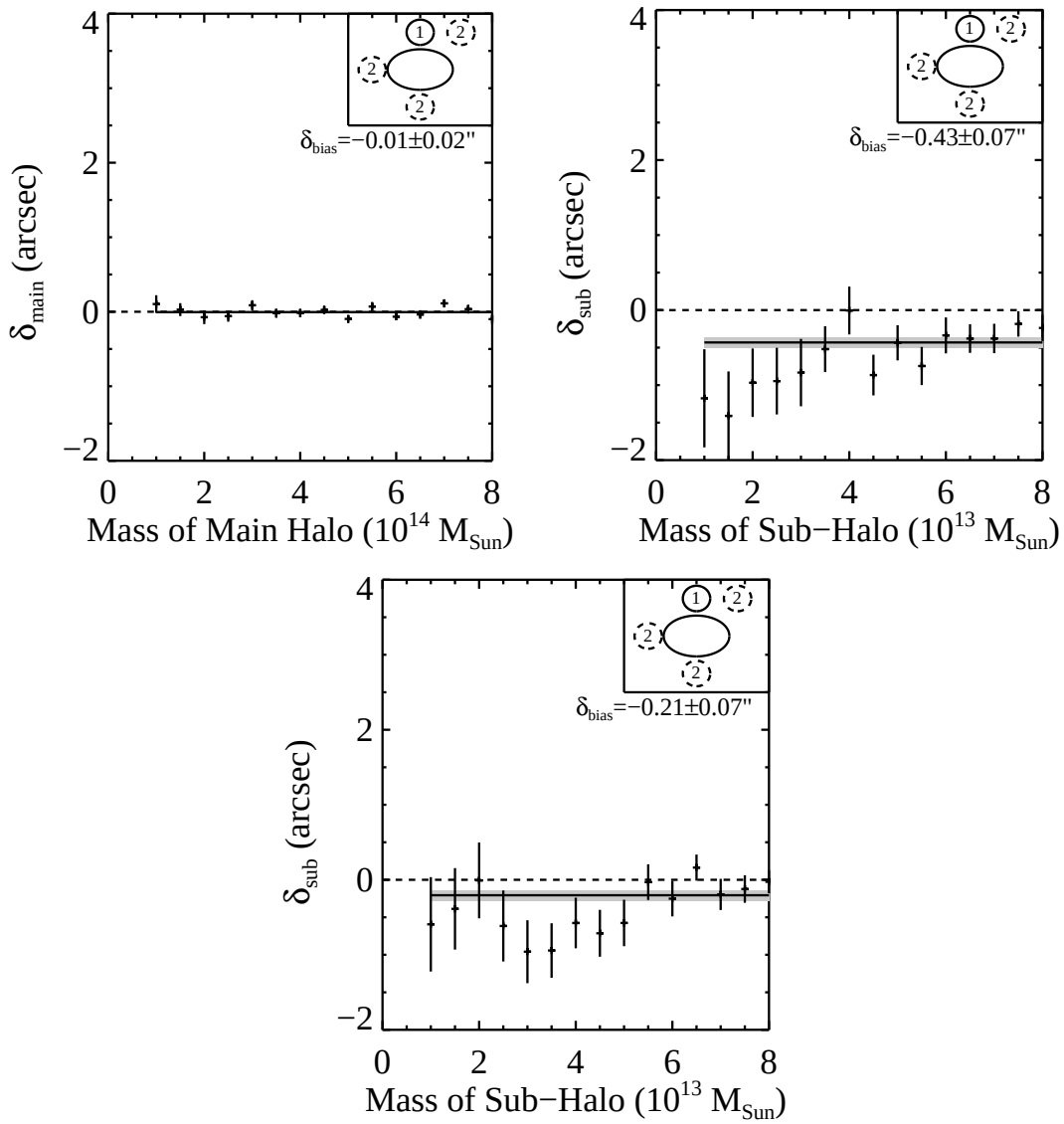

Figure 5.8: **Dual sub-halo simulation, with intrinsic ellipticities, shear measurement bias and source galaxy redshift distribution**: The top left panel shows the positional estimates of the main halo, the top right the estimates of *sub-halo 1* and the bottom panel gives the estimates of *sub-halo 2*. The masses of the haloes are given. In each case the sub-haloes are 10 times smaller in mass (so they are equal size) than the main halo. The background galaxies have intrinsic ellipticities, shape measurement bias and a redshift distribution. The plots show 3 different configurations (given by the dashed circles). In each case *sub-halo 1* is kept in the same place as shown in the cartoon inset, and for each of the 3 scenarios *sub-halo 2* is positioned as shown. In each scenario 100 noise realisations are run and the positions averaged over all configurations and noise realisations.

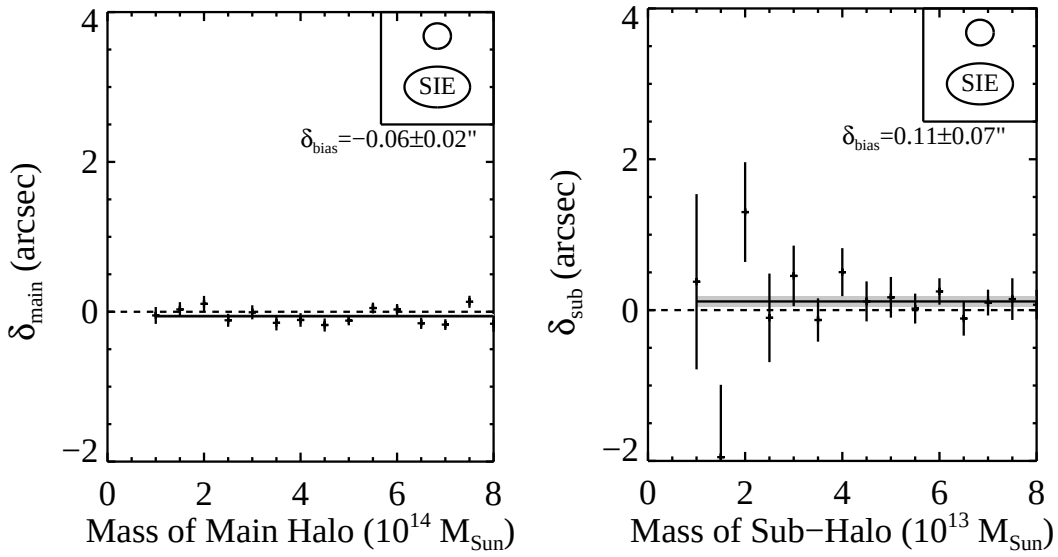

Figure 5.9: **Simulated SIE haloes, with intrinsic ellipticities, source galaxy redshift distribution and shape measurement bias**: The left hand panel and right hand panel show the main and sub-halo positional estimates respectively. In this scenario a SIE profile is simulated and NFW fitted imitating profile misidentification in real data. The main halo is always 10 times larger than the sub-halo, and the source galaxies have shape measurement bias, intrinsic ellipticities and a redshift distribution. 100 noise realisations were run and the average position estimated in each case.

bias and therefore in order to better constrain the error on positional estimates I compiled the results into Figure 5.5 giving the combined results from the initial tests.

It was found that LENSTOOL was robust to a basic level of noise so I introduced further sources of contaminants. The left and right hand panel of Figure 5.6 shows δ for the main and sub-halo respectively when shape measurement bias is introduced. The left hand panel of Figure 5.6 seems to show that the the shape measurement bias has no affect on the positional estimate of the main halo, however the sub-halo in the right hand panel of Figure 5.6, seems to be slightly biased in the negative radial direction (towards the main halo). The cause of this will be the preferred direction of each galaxy. The level of the bias is of order 0.01, which is a similar level to the expected signal from a dark matter sub-halo. Because each galaxy has a preferred direction it will mean that the preferred fit of the halo will not be the correct one, causing a bias in the position. This bias of $0.27 \pm 0.14''$ is well within the tolerated level.

Gravitational lensing is a geometrical effect and hence the signal is dependent on the distance the galaxy is from the halo. To this effect, LENSTOOL requires knowledge of the source galaxy redshift, something that will not be know in the data (and shall be approximated to one). I therefore introduce a redshift distribution into to source galaxies and test the approximation that their redshifts are 1. Figure 5.7 shows the results when such a distribution is introduced. Both panels in Figure 5.7 has no significant evidence for an increase in bias due a source galaxy redshift approximation from that of Figure 5.6.

Using the same signal contaminants as Figure 5.7 (intrinsic ellipticities, source redshift and shape measurement bias), I introduce a second sub-halo, complicating the geometrical setup of the simulations. I ran three different scenarios; in each case the main halo was at the centre of the field and sub-halo 1 was kept at the position previously simulated. The new, second sub halo was placed at three different locations as shown in the cartoon inset. The positions were chosen to test the extremes of every possible case (since it is impossible to run the infinite number of configurations). These included a configuration where the two haloes were close by one another, on opposite sides of the cluster and at right angles to one another. For each sub halo 2 position 100 noise realisations were run. In all cases the main halo was 10 times more massive than the sub-

haloes, and the sub-haloes were equal size. I found that there was no preferred bias dependent on the position of the second sub-halo and so averaged these simulations together in order to better constrain the bias and error bars. Figure 5.8 shows hat the bias introduced by the source galaxy distribution is evident in the two body system. The more complicated geometrical setup seems to have no affect on the overall bias.

Figure 5.9 is a test into the model dependancy of the reconstruction method. Although NFW profiles have been extensively studied with both simulated and empirical data, the inclusion of baryons have shown that profiles depart from the assumed NFW (Duffy et al., 2010). Therefore in order to understand what the affect of this is, Figure 5.9 shows the positional accuracy of the main and sub-halo in the case where a singular isothermal ellipsoid is simulated and using LENSTOOL a NFW is fitted. The left hand panel of Figure 5.9 shows that the sub halo has an insignificant positive bias, seemingly in contradiction to previous results.

This unbiased nature is due to the fact that the central core of an SIS is extremely peaked. An NFW has a much flatter profile in the core and therefore may introduce more uncertainty in the peak position. One effect of introducing an SIS is that the scatter seems to be much larger and at smaller masses the positional estimates become unreliable. In the event that the number density of galaxies reduce and hence a lower signal to noise, the profile position may be biased due to the mis-modelling of the wings of each cluster, however this bias here seems to be sub-statistical.

5.3.1 Accuracy as a function of distance from the cluster and mass fraction

The top two panels in Figure 5.10 show the results if the halo masses are kept constant ($8\times10^{14}M_{\odot}$) at a redshift of 0.6 with an ellipticity of 0.2, positional angle of 180°, shape measurement bias and a background galaxy redshift distribution, and the sub-halo is moved from close to the cluster outwards and (second two panels) the mass fraction is increased ($^{M_{\rm sub}}/_{M_{\rm main}}$).

The fitted lines shows over what mass interval the mass independent-bias remains, until the chi-square of the line becomes greater than one standard deviation from the expected value. Both panels in Figure 5.10 shows that the

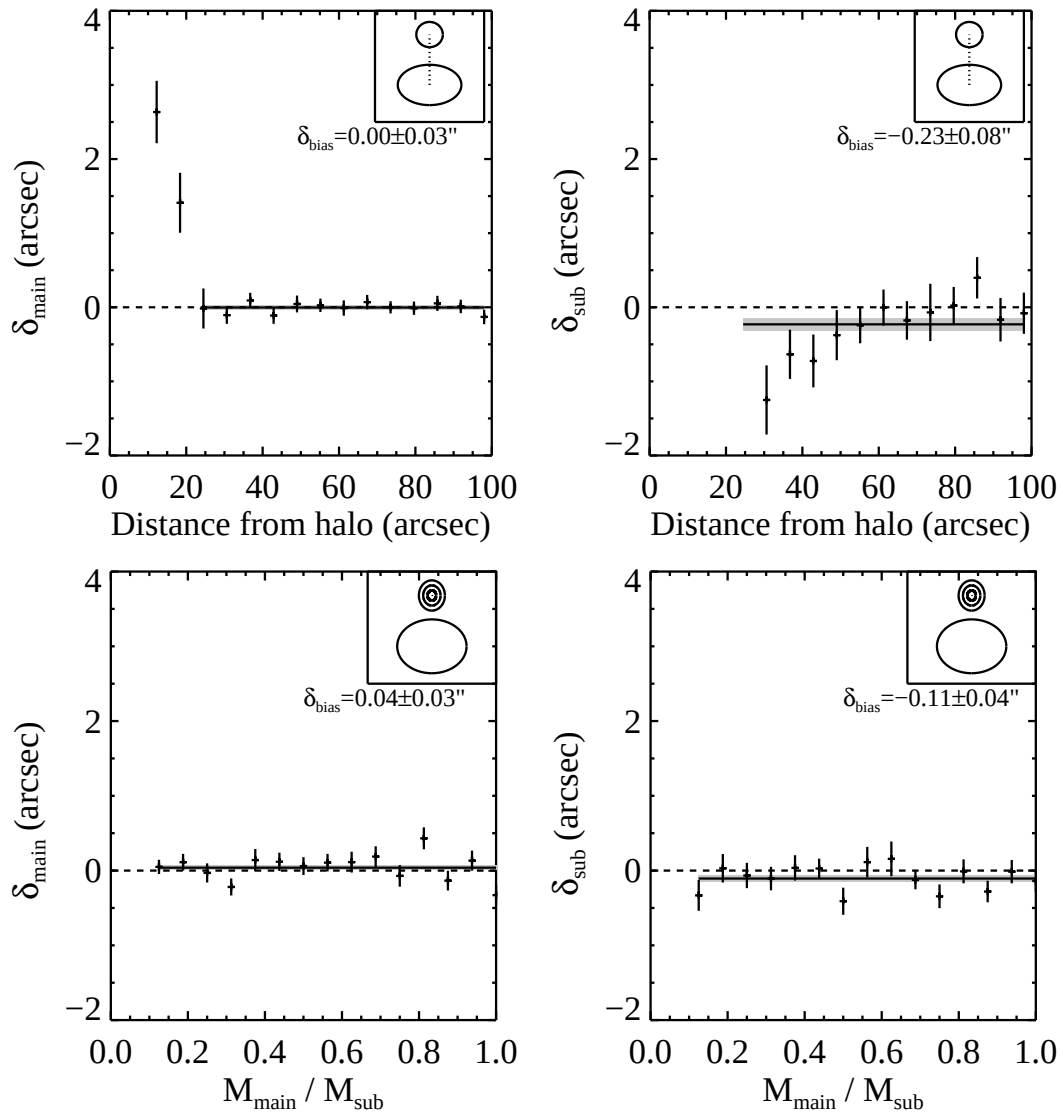

Figure 5.10: **Weak lensing accuracy as a function of the radial position from the cluster and mass fraction** ($^{M_{\rm sub}}/_{M_{\rm main}}$). In each case the background galaxies have intrinsic ellipticities, redshift distribution and shape measurement bias. The first two panels (main and sub-halo respectively) show an $8 \times 10^{13} M_{\odot}$ cluster (with associated 10 times large parent halo), simulated at various distances from the main halo. The catastrophic failure at $< 30''$ is due to the sub-halo position overlapping with the parent halo. The second two panels show the positional estimates of a main halo of 8×10^{14} and sub-halo with an increasing sub-halo mass (decreasing ratio). It is shown that the bias is mass fraction independent and is robust to minor mergers as well as substructure infall.

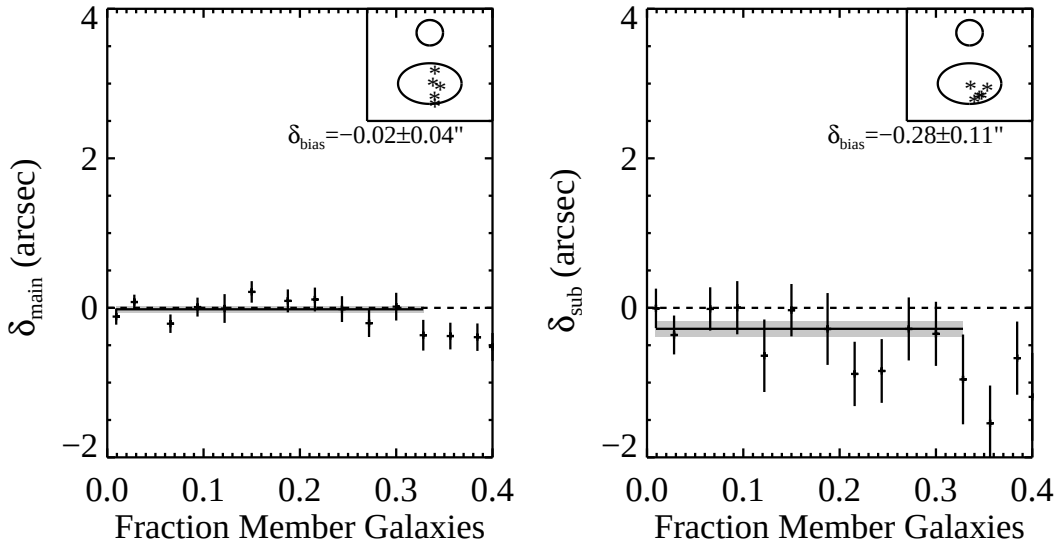

Figure 5.11: Main (top) and Sub (bottom panel) position as function of cluster member contamination expressed as a percentage of the total background galaxy number.

fit breaks down at low radii ($< 30''$). This value coincides with the size of the prior around the sub-halo and shows that the sampler cannot de-merge the two haloes. Both of the lower panels in Figure 5.10 show that the bias is independent of mass ratio, and even in the case where the two haloes are of equivalent size the bias remains negligible. This is promising as it shows the reconstruction should be reliable even in the case of a minor merger and not just substructure infall.

5.3.2 Cluster member inclusion

Figure 5.11 show the results from including member galaxies into the reconstruction. The fraction of background galaxies is calculated by summing the total number of member galaxies in the field of view and dividing by the number of background galaxies. It can be seen that the reconstruction is reliable up to $\sim 30\%$ of the background galaxies, at which the position of the sub and main halo become unreliable. Given a background density of 80 per sq. arc minute, which is significantly less found by Hoekstra et al. (2011), I can conclude from these plots that I not worried about inclusion of these member galaxies.

5.4 Precision of lenstool

Throughout this investigation I have consistently found that by averaging many clusters together one can measure the position of DM haloes accurately to within $\sim 0.3''$. Understanding how precisely I can measure these offsets informs us how many offsets will need to be measured in order to make a statistically significant detection.

The error bars derived from LENSTOOL give a rough estimate of the number of sub-haloes that are required to robustly measure a significant offset between dark matter and gas. I decide to use the error bars from Figure 5.7 to derive the precision. These were the error bars in the case of all signal contaminants. I found no evidence for additional uncertainty due to member galaxies at the expected level, and therefore have not factored these into the errors.

Dietrich et al. (2012) find that cosmic shear can offset the position of weak lensing peaks of order 5kpc ($0.7''$ at a $z = 0.6$). I expect such a contaminant to average out to zero but have a contribution to the overall error and precision. We therefore add this contaminant in quadrature to the error bars given in and calculate for a given size of clusters of a given mass with a given mass sub-halo for a cluster at redshift $z = 0.6$. Figure 5.12 shows between $\sim 20-50$ measured offsets are required in order to have statistically significant detection. In this scenario there is also shape measurement bias and a source galaxy redshift distribution.

Since typical clusters each have conservatively 1 in-falling group of galaxies containing $\sim$ 10% of their mass, this suggests between $20 \sim 50$ clusters are needed. This is feasible within the current HST and Chandra archive. Furthermore, any strong lensing detections would tighten the constraints on the mass and concentration of the main halo can be more tightly constrained, and will lead to a better measurement of the offset. It is would be trivial to include a strong lensing model in to LENSTOOL, however relative weighting of the constraints provided is an issue which will be addressed in future work.

Although basing predicted sample sizes on controlled environments such as those studied here, the results give us optimism to carry out the measurement in real data.

In the case of definite peaks and well defined profiles I expect a sample of between $20 \sim 50$ to be sufficient in order to measure a significant offset. I use

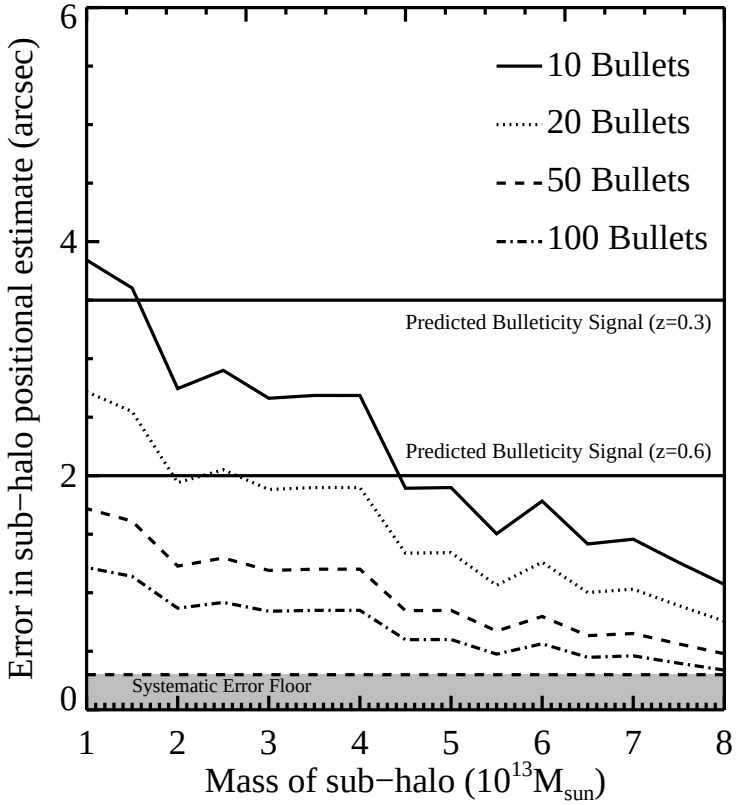

Figure 5.12: 1 The error in the mean position for various sample sizes. In order to detect an overall offset between baryonic and dark matter the error in the mean of the sample size needs to be less than the expected signal. For clusters at redshift $z = 0.6$, the bulleticity is $\sim 2''$, and for a redshift $z = 0.3$ this increases to $3.5''$. A sample of ~ 50 offsets should yield a significant detection of bulleticity, and LENSTOOL can measure these offsets with subdominant systematic bias.

this sample size as a confirmation that one should be able to make a detection using the current Hubble archive. I expect the true sample size to be larger than this and using hydrodynamical simulations, a more accurate sample size can be determined. Such tests are beyond the scope of this work and will be carried out in conjunction with the data.

5.5 Discussion

Through carefully controlled experiments, it was found that the likelihood surfaces for the reconstructed sub-halo positions are symmetric around the true

value in the regime of infinite signal to noise. In the presence of trivial noise contaminants the estimated positions are also not biased, however adding shape measurement bias seems to introduce a small bias of order $\sim 0.3''$ in the sub-halo.

In order to better constrain the errors and any bias in position I averaged each mass scale over each single sub-halo configuration, and dual halo configuration. It was found that the positional bias in all cases is independent of mass and configuration. For a single halo configuration the only cause of bias was due to imperfect shape measurement. The observed offset of $0.27 \pm 0.14''$ is well within the tolerated level. This bias was seen throughout the simulation using NFW profiles, including the dual sub halo configurations. In the case of an SIS profile, I found that the positional estimate no longer observed a bias, which was due to the peaky nature of the central core, however the errors become unacceptably large below $1.5 \times 10^{13} M_{\odot}$.

In all of the simulations I do not find strong evidence for a positional bias of greater than $0.5''$. Importantly, this performance is sufficient to enable a detection of the theoretically expected $\sim 2.0''$ ($\sim 3.5''$) offset between substructure's dark matter and gas as it falls into massive clusters at a redshift of 0.6 (0.3) (Massey et al., 2011).

Initial work using the HST archive will aim to measure the average displacement between dark matter and both gas and stars, that could provide evidence for self interacting dark matter. This displacement can then be calibrated with simulations of interacting dark matter to estimate its cross section.

With a sample of clusters already available in the HST archive, averaging the measured offset of many pieces of substructure will provide sufficiently accurate dark matter centroiding to detect an offset. Future space missions (e.g. Euclid[1] (Laureijs et al., 2011)) will increase the sample of available clusters by many orders of magnitude. However fully exploiting such data would require improved mass reconstruction techniques (for a detailed discussion on algorithm development specifically for mass reconstruction see Appendix A).

Furthermore, in the quasi-weak lensing regime considered here, flexion, the third derivative of the lensing potential, becomes important. As the gradient of the tidal field it is more sensitive to small-scale structure, similar to that investigated here (Bacon et al., 2006). The positional information in this higher

[1] http://www.euclid-ec.org

order process could therefore provide significantly improved offset measurements. Unfortunately, flexion remains extremely difficult to measure and it fundamental properties such as the intrinsic flexion distribution and accuracy requirements are still yet to be determined (Viola et al., 2012). Future algorithms could potentially exploit this extra information however this is currently not possible.

5.6 Conclusions

Measuring the separation of dark matter and baryonic gas in groups of in-falling galaxies requires accurate astrometry. In the introduction I proposed five primary questions,

- To what precision can I measure the offset in a single in-falling substructure?
- Can I identify a point estimator whose simple combination over a sample will provide a measurement of sub-halo position with minimal bias?
- What are the dominant sources of residual bias in this estimate?
- How large a sample of observed clusters are I likely to need to be able to detect an offset between dark matter and baryonic as predicted by MKN?
- What further investigation might be needed to prove the utility of this technique for probing DM interaction cross-sections?

In reference to these, I find that

- The public LENSTOOL software can measure the position of individual $1.5 \times 10^{13} M_{\odot}$ peaks with $\sim 0.3''$ systematic bias, as long as they are at least $\sim 30''$ from the cluster centre. Any sub-haloes detected above this threshold will be real and only biased to $\sim 0.3''$.
- The maximum likelihood value of the 2 dimensional position likelihood surface is found to be the best point source estimator, being negligibly biased in the noise free case compared to the mean value estimator.
- The dominant source of bias is caused by a preferred direction to the shape of galaxies introduced by an biased shape measurement algorithm.

- Since typical clusters each have on average 1 in-falling groups of galaxies containing $\sim$ 10% of their mass, between $20 - 50$ clusters are needed to detect an offset between dark and baryonic matter.
- The method will need to be tested on full hydrodynamical simulations (containing a more complex distribution of mass) in parallel with real data to show that the displacement obtained from data is reliable.

This work gives us confidence to pursue offsets as a technique in the measurement of the DM cross-section.

6 Constraints on the self-interaction cross-section of dark matter

"Where the willingness is great, the difficulties cannot be great."

6.1 Constraining the cross-section of dark matter with 28 galaxy clusters

In this thesis I have tested the accuracy and precision of weak gravitational lensing as a method to constrain the positions of sub-haloes in galaxy clusters. In order to utilise substructure to constrain the self-interaction cross-section of dark matter I have also developed a new method which uses minor mergers. In this chapter I will analyse the relative position of dark matter with respect to the associated galaxies and the position of gas with respect to galaxies, to test whether dark matter scatters often, with little momentum exchange and is velocity independent. I will use a sample of minor and major mergers in order to average over many merging scenarios and gain a robust estimate. Having gained an estimate of the ratio between the separation of galaxies and dark matter and galaxies and gas, I will make the first estimate of the cross-section of dark matter from an ensemble of galaxy clusters. In addition to this I will make the first analysis of a set of new merging systems that have not been previously studied. In doing so, I will present

to the community potential systems that can be followed up in the future and studied.

This chapter is organised as follows. In Section 6.2 I outline the data utilised in the study and the data reduction process in Section 6.3. In Section 6.4 will present the analysis of the sample of merging galaxy clusters, along with the constraints for the cross-section of dark matter. In Section 6.5 I discuss the findings in the context of the broader cosmological model and make the conclusions in Section 6.6 .

6.2 Data

I utilise existing images from the *Hubble Space Telescope* (HST) taken by the Advanced Camera for Surveys (ACS) and Chandra X-ray Observatory archives. I choose HST specifically since I require deep imaging of the core of clusters where potential separations between baryons and dark matter will be most evident. Where possible I used the HST F814W filter, however where there are significantly more exposures in a different filter I use these. In the event that there is no F814W data I use the filter that has the largest number of exposures, and never use any filter below a wavelength of 606nm, since below this the number density of background galaxies drops too low for a satisfactory lensing signal. In a bid to exploit the full availability of data I do not discriminate against orientation or epoch, and hence have a inhomogeneous data set from various observation runs, for which I detail how I cope with in Section 6.3. In order to verify the shape measurement pipeline I analyse various clusters in different bands to ensure a consistent result, however in the analysis I only use one filter. In both the optical and X-ray case, I download raw files and associated calibration files and re-reduce using the pipeline.

The cluster sample is chosen specifically to include those that show significant structure, or recent merging activity in the X-ray. Amongst those known already in the literature ($\sim$ 16 clusters) I use an additional $\sim$ 14 clusters to make a full initial sample of 30 unrelaxed merging clusters. These additional clusters were identified by eye using a large sample of reduced X-ray cluster [1] and then follow up work to identify if that cluster had optical HST coverage.

[1] www.roe.ac.uk/ert/chandraclusters

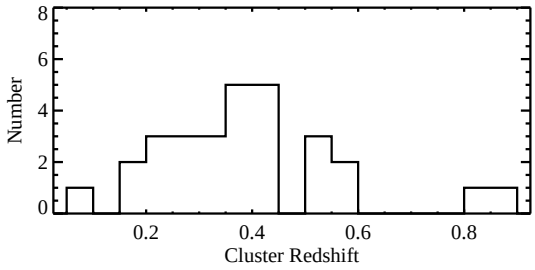

Figure 6.1: The redshift distribution of the clusters used in this work.

Although I attempt to use only low redshift clusters where any observed angular separation will be largest, I note that higher redshift clusters will also provide some signal. Figure 6.1 shows the redshift distribution of the cluster sample used for this work. As it can be seen the majority of the clusters lie at $z < 0.6$, with two clusters lying between $0.8 < z < 0.9$. Table 6.1 shows a more detailed description of the cluster sample used including redshift and exposure time in the optical and X-ray.

6.3 Method

Here I detail the pipeline used to reduce both the optical and X-ray data. In all cases I begin from raw data files in order to produce the highest quality final data product.

6.3.1 X-ray analysis technique

I use the publicly available *CIAO* tools *version 4.5* to reduce and smooth the Chandra data. For each observation I first reprocess the raw event 1 files using the *CIAO repro* tool and make a first pass at removing point sources using *celldetect*. I then filter each event file for any potential spurious events such as solar flares by clipping the table at the 4σ around the mean energy level and combine them using the *merge_obs* script from *CIAO* tools. This script combines the events in to a single exposure map corrected flux image and produce exposure maps for each observation and a combined exposure map. I then pass this image through *Wavdetect* to smooth the image. In order to determine the position of the haloes I use SExtractor on the smoothed images (see Section 6.3.4).

Table 6.1: Sample of galaxy clusters used in the study. The position in right ascension (RA) and declination (DEC) are given in degrees, followed by the redshift (z), the ACS filter used for the optical imaging, and finally the total exposure time for both the X-ray and the optical.

Cluster	RA (deg)	DEC (deg)	z	ACS Filter	ACS (s)	Chandra (ks)
1E0657	104.612	-55.9477	0.2960	F814W, F775W	15094.0	603.2
A1758	203.194	50.5426	0.2792	F814W	10000.0	224.0
A2163	243.937	-6.14690	0.2792	F814W	10000.0	224.0
A2744	3.58210	-30.3898	0.3080	F814W	11980.0	134.4
A370	39.9627	-1.58000	0.3730	F814W	3840.00	103.0
A3827	330.480	-59.9536	0.0990	F814W	5224.00	47.3
A520	73.5395	2.93110	0.2020	F814W	18320.0	546.9
A781	140.149	30.4927	0.2980	F814W	1620.00	49.8
DLSCLJ0916	139.046	29.8450	0.5343	F814W	9894.00	41.4
El Gordo	15.7277	-49.2560	0.8700	F814W	1916.00	361.6
MACSJ0025	6.37460	-12.3818	0.5843	F814W	4200.00	169.6
MACSJ0152	28.1473	-28.8944	0.3410	F606W	1200.00	20.1
MACSJ0358	59.7174	-29.9320	0.4280	F814W	4620.00	66.1
MACSJ0416	64.0392	-24.0735	0.4200	F814W	4037.00	18.6
MACSJ0417	64.3926	-11.9111	0.4430	F814W	1910.00	96.9
MACSJ0553	88.3494	-33.7117	0.4070	F814W	4572.00	89.5
MACSJ0717	109.389	37.7528	0.5458	F814W	8893.00	84.1
MACSJ0911	137.793	17.7775	0.5049	F814W	6743.00	46.9
MACSJ1006	151.730	32.0198	0.3590	F814W	1440.00	13.3
MACSJ1226	186.694	21.8673	0.3700	F814W	5520.00	155.2
MACSJ1354	208.635	77.2528	0.3967	F814W	1200.00	35.7
MACSJ1731	262.913	22.8660	0.3890	F814W	1440.00	22.4
MACSJ2243	340.837	-9.58910	0.4470	F606W	1200.00	22.0
MS1054	164.245	-3.62000	0.8260	F606W	8100.00	92.2
RXCJ0105	16.4096	-24.6801	0.2300	F606W	1200.00	22.2
RXCJ0638	99.6953	-53.9735	0.1658	F606W	1200.00	21.8
RXJ1000	150.132	44.1491	0.1540	F606W	1200.00	20.8
SPTCL2332	352.959	-50.8642	0.5707	F606W	7680.00	39.9
ZWCL1234	189.045	28.9929	0.2214	F814W	27632.0	52.9
ZWCL1358	209.951	62.5163	0.3290	F850LP	13692.0	64.9

The Chandra PSF and *Wavdetect*

Wavdetect is a wavelet smoothing algorithm that uses a mexican hat filter of a given scale to smooth the data. It uses the given size of the Chandra PSF at each position in the field to calculate the estimate original size of a source. However, since I am using combined multiple observations of the same cluster, the PSF model will be not a simple function. It is known that the Chandra PSF grows large at the wings (Gilmour et al., 2009), and therefore needs to be considered carefully when constructing the PSF map which is passed in to *Wavdetect*. To do this I construct a PSF map using *mkpsfmap* for each individual exposure at an effective energy of 1keV and then combined each PSF model weighting them by their respective exposure map. Figure 6.2 shows an example of the PSF map used for A520. This is particularly important during this stage as it allows *Wavdetect* to determine between a point source (a source on scales of a pixels or two) and a broader, dispersed sub-halo

Once the observations have been reduced into a single flux image with an associated PSF model, I initially pass it through *Wavdetect* using the smallest scales; $1, 2$ pixels. This acts to further remove point sources. I remove those sources found at these scales from the flux image and then pass the image through *Wavdetect* one last time using scales $4, 8, 16, 32$ pixels. The actual scales used varied slightly depending on the cluster; in some cases smaller scales, such as 4 and 8, were not used since these haloes were much broader, and only added noise to the smoothed map. Once this was complete I checked the image for further point sources by eye.

6.3.2 Weak Lensing Analysis

As before, I will use the distortion of photons by foreground structures to map out the dark matter distribution in the galaxy clusters. To construct the images I acquire the raw data files and reprocessed them. Initially I treat the images for charge transfer inefficient (CTI), using the method laid out in Massey (2010). I then pass these images through the publicly available *Calacs*, which calibrates the images and produces FLT files. I then tweak these images using the *tweakReg* tool and then drizzle them together to create a mosaiced stacked image. As described in Rhodes et al. (2007) I use a final drizzle pixel scale of $0.03''$ and a pixel fraction

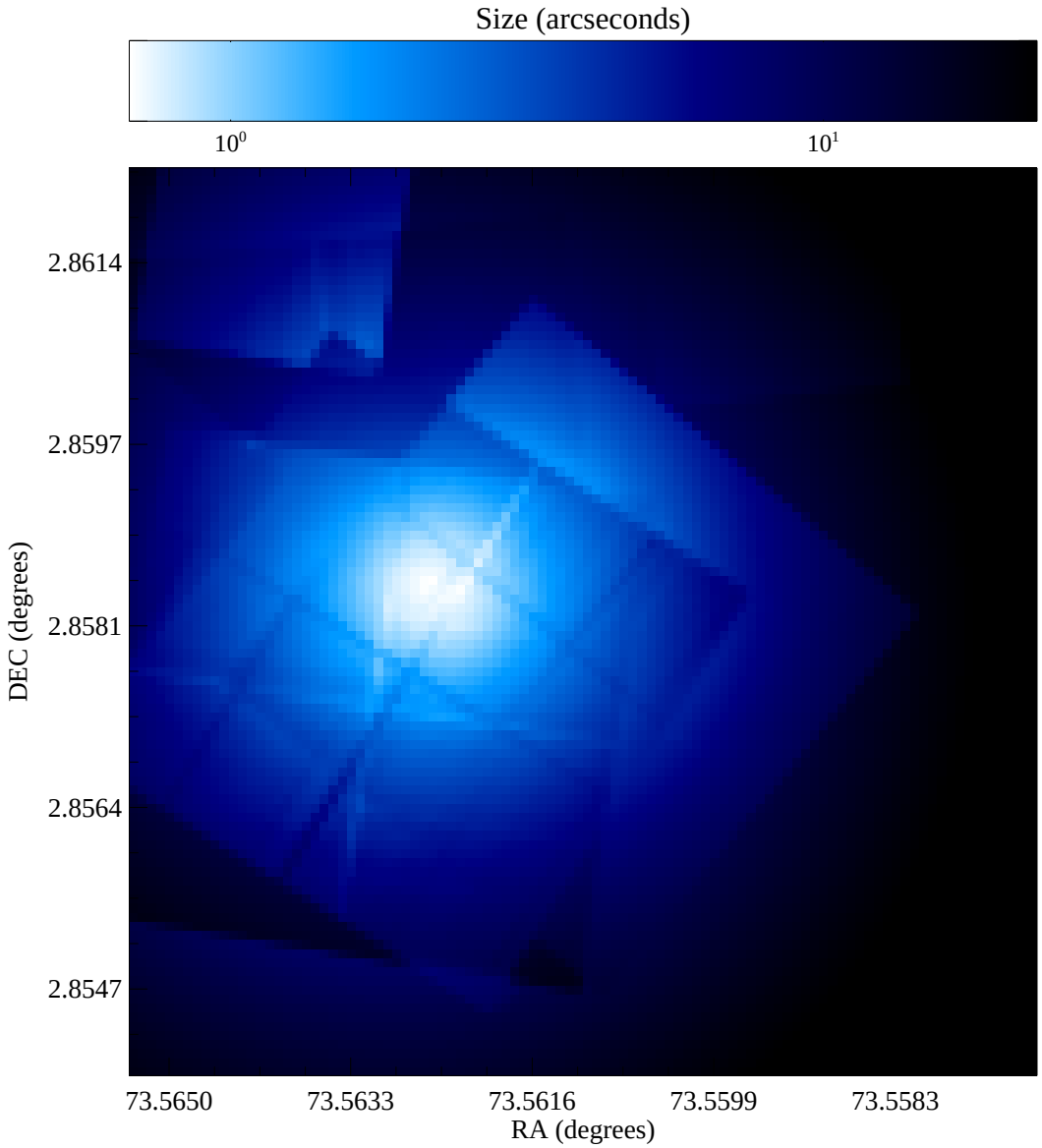

Figure 6.2: An example PSF model that is implemented at the *Wavdetect* stage. The image shows a combined exposure map weighted PSF map stacked for the various observations of the cluster A520.

of 0.8. In the process I also produce drizzled images of each individual exposure for use during PSF estimation.

In order to fully exploit the Hubble archive I developed the weak lensing pipeline such that it could be used for any filter, in any orientation. This means that shape measurement has to be treated carefully. I use the RRG method (Rhodes et al., 2000), measuring the image weighted second and fourth order moments (see Section 3.2 for more) and construct the shear estimator;

$$\langle \epsilon_i \rangle = G\gamma_i, \tag{6.1}$$

where G is the shear susceptibility, and is an empirical factor dependent on the flux of the object. By simply taking the inverse of this equation I can calculate the estimated shear on an individual galaxy. Using the calibrated and measured value of G from Leauthaud et al. (2007b), I can estimate the final shear. Moreover, the shape measurement is calibrated on simulations of galaxies using STEP like simulations (Heymans et al., 2006; Massey et al., 2007a), correcting shear measurements with a multplicative bias of $\langle m \rangle = 20.1 \times 10^{-2}$ and an additive bias of $\langle c \rangle = 23.3 \times 10^{-4}$ (Leauthaud et al., 2007b).

Estimating the PSF in a mosaiced image

In order to determine the positions of groups of dark matter haloes in clusters, I need to estimate the shear extremely precisely. This requires precise handling of the Hubble PSF, which the RRG pipeline corrects for. In the case of COSMOS, the images were aligned such that the x-y axis of the chip was always in the same axis as the physical coordinates. This allowed simple handling of the PSF. In the Hubble archive, many of the images were at various orientations and mosaiced different, such that the PSF, similar to Chandra, was not a smooth function over the field. For example, consider a galaxy that, in one image is near the centre, but in a different observation, is at the edge of the chip where the PSF degrades sharply, it soon becomes clear that the combined PSF is not a smooth function. To handle this I adapted the RRG method.

I first make a star-galaxy cut by using SExtractor to locate objects in the drizzled image and then identify the stars using a mixture of magnitude – size diagrams and magnitude – μ_{max} (the maximum flux in a single pixel in the source). I make the cuts and then measured the second and fourth order moments

of the stars in *each* exposure. Using Tiny Tim for the given HST filter, I compare the star ellipticities with those in each PSF model for all focus positions. Having found the best fitting focus position and the associated model, I then interpolate the PSF model to the position of the galaxies that lay within the exposure. Figure 6.3 shows the distribution of focus positions over the sample of clusters. Each colour represents the best fitting focus position for each observation of a single cluster. As it can be seen, there is a clear tendency for HST to be at a focus position of $-2\mu m$.

Once I have estimated PSF at the position of the galaxy I rotate the moments into the reference frame of the drizzle mosaiced image through an angle ϕ, via

$$\begin{aligned}\mu'_{jk} = &\sum_{r=0}^{j}\sum_{s=0}^{k}(-1)^{k-s}\binom{j}{r}\binom{k}{s}(\cos\phi)^{j-r+s} \\ &\times\ (\sin\phi)^{k+r-s}(\mu_{j+k-r-s,r+s})\end{aligned} \tag{6.2}$$

where μ' is the rotated moments of μ, which is of the same order $N = j + k$ (Teague, 1980). Iterating over every exposure, I sum the contributing moments to each galaxy depending on its relative position in the image and then found the average moment in the reference frame of the drizzled image. Using this 'average' PSF, I correct the galaxy to determine the correct image moments and hence the shear. Figure 6.4 shows the estimated PSF model for the cluster MACSJ0416.

Final shear catalogues

In order to construct homogeneous final catalogues, I make various cuts. In the case of those images that have greater than 2 stacked exposures, I only accept shear estimates on those galaxies with greater than or equal to three exposures covering them. For those images with only two stacked exposures I place the threshold at two exposures (throwing away those galaxies that have only 1 exposure covering it). This acts to remove those galaxies at the edges of the field and the centre, along the chip boundaries where it is particular noisy. I also make a signal-to-noise cut, (as returned by SExtractor) of 4.4 (Leauthaud et al., 2007b). I mask the images for saturated stars and I also mask out very large galaxies (plus any smaller galaxies that may lie in the wings of the larger ones and have distorted isophotes), and any galaxy that is less than $\sim 0.1''$. Figure 6.5

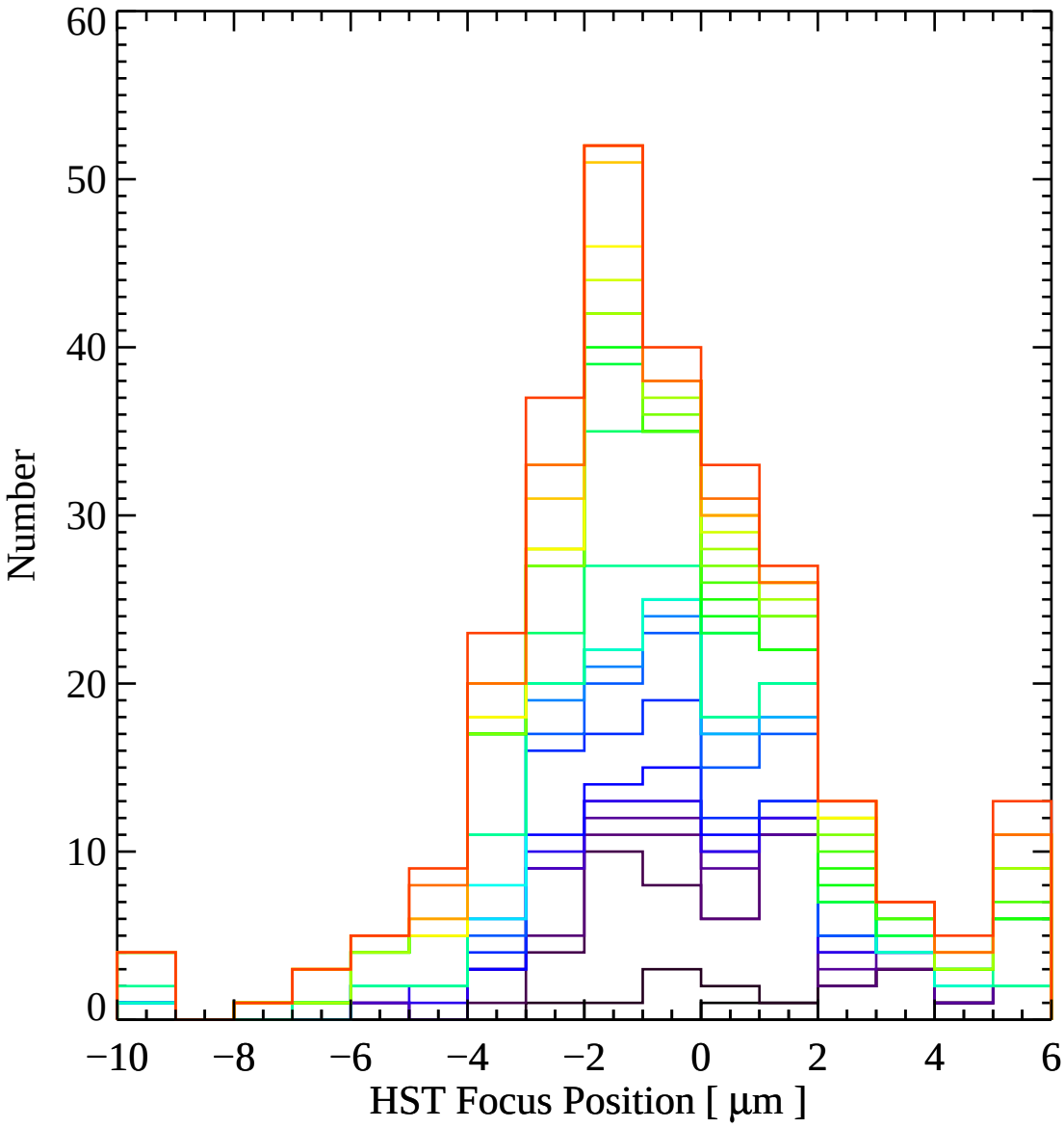

Figure 6.3: The distribution of best fitting focus positions for the acquired HST observations. Each colour represents the distribution of best fitting focus positions for each cluster over the various observations. To determine the best fitting focus position the ellipticity of the stars was compared to that of the Tiny Tim model for the given filter.

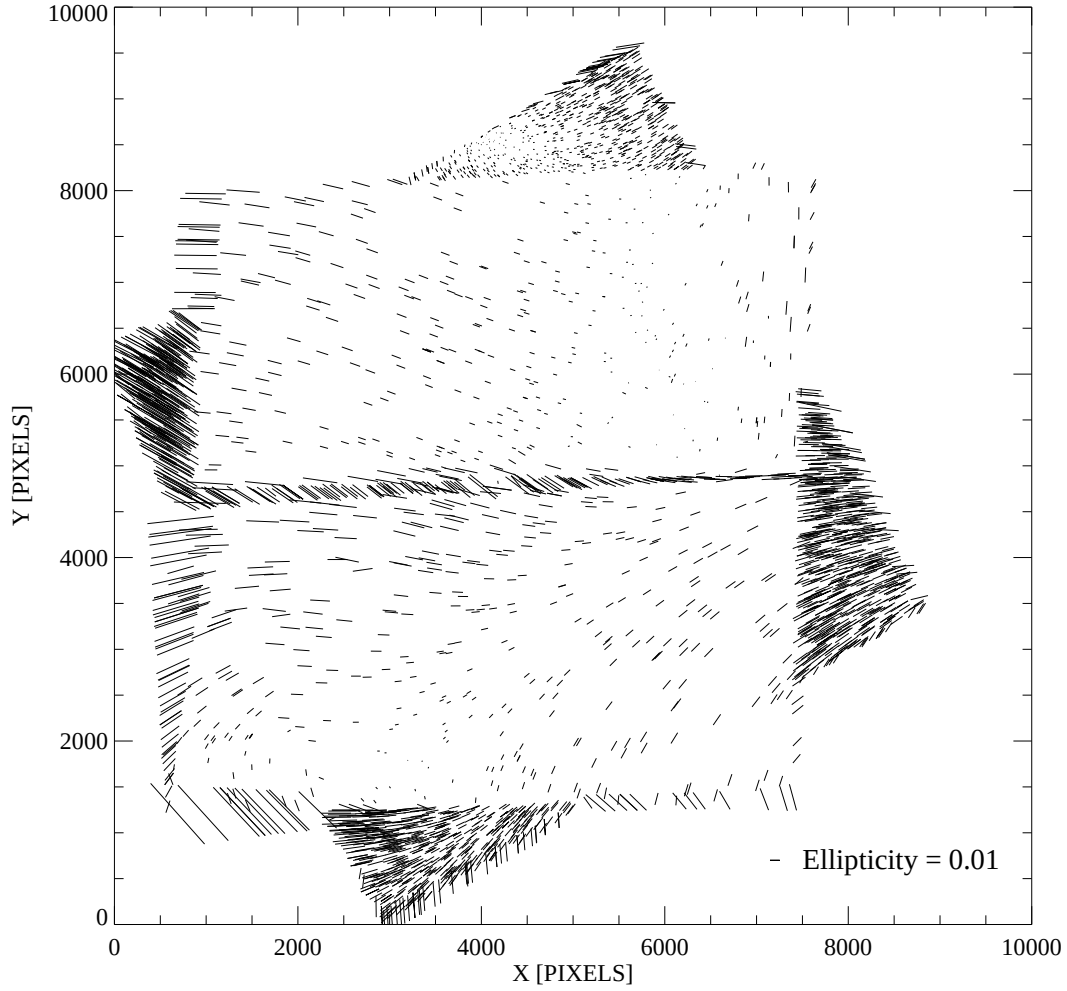

Figure 6.4: An example of the PSF model for the cluster MACSJ0416. Each mark shows the position of an object returned by SExtractor. Not all of these objects are galaxies and have sufficient exposures, therefore many of the objects will not be in the final shear catalogue. Each tick mark shows the ellipticity of the PSF at that position in the field. Many more objects are found in the edges since there are less exposures and hence higher noise.

shows the comparison of two final shear catalogues for the cluster A3827. The top panel shows the comparison of γ_1 between the independent estimates using the F814W and F606W band, and the bottom panel shows the comparison of γ_2 between the same bands. As expected there is some scatter between the two estimates (albeit very small), however most importantly there is no bias.

6.3.3 Mass reconstruction

As before I use the publicly available LENSTOOL (Jullo et al., 2007) to reconstruct the positions of matter in the galaxy clusters as it provides point estimators for the positions of dark matter haloes. In order to get the best fitting position I use *Inverse 4* option which allowed the sampler to fall down the hill of likelihood and report the maximum likelihood parameters. To avoid local maxima, LENSTOOL uses ten simultaneous sampling chains. I also run option *Inverse 3* such that its step size never becomes to small and its continues probe the entire posterior surface. This way it I estimate the width of the posterior surface and hence the uncertainty on the estimate. In order to gain estimates of the positions of dark matter haloes I use the estimate for the maximum likelihood and the error bars from the second, full posterior method. I find that the average error in the final lensing peaks were $\sigma_{\rm WL} \approx 11'' \approx 60$kpc (at a $z_{\rm eff} = 0.4$).

Since LENSTOOL requires a predetermined number of haloes I used the gas and galaxy distribution as additional information in making this decision. I decide to use a NFW density profile when fitting the haloes (hereafter NFW, Navarro et al. 1997). However, it is possible to know the correct number of bodies by comparing the Bayes evidence for each combination of haloes (Marshall et al., 2002). However, in a sample size this large such an approach is computationally unfeasible. Any specific map making choices and decisions made on the number of haloes is given in the individual cluster descriptions.

6.3.4 Galaxy Distribution

Many different tracers exist for the galaxy distribution. I have to be particularly careful since any chosen one may have repercussions for the results and estimates of the cross-section of dark matter. George et al. (2012) found that the best estimator of the bottom of the dark matter potential is the BGG within the scale

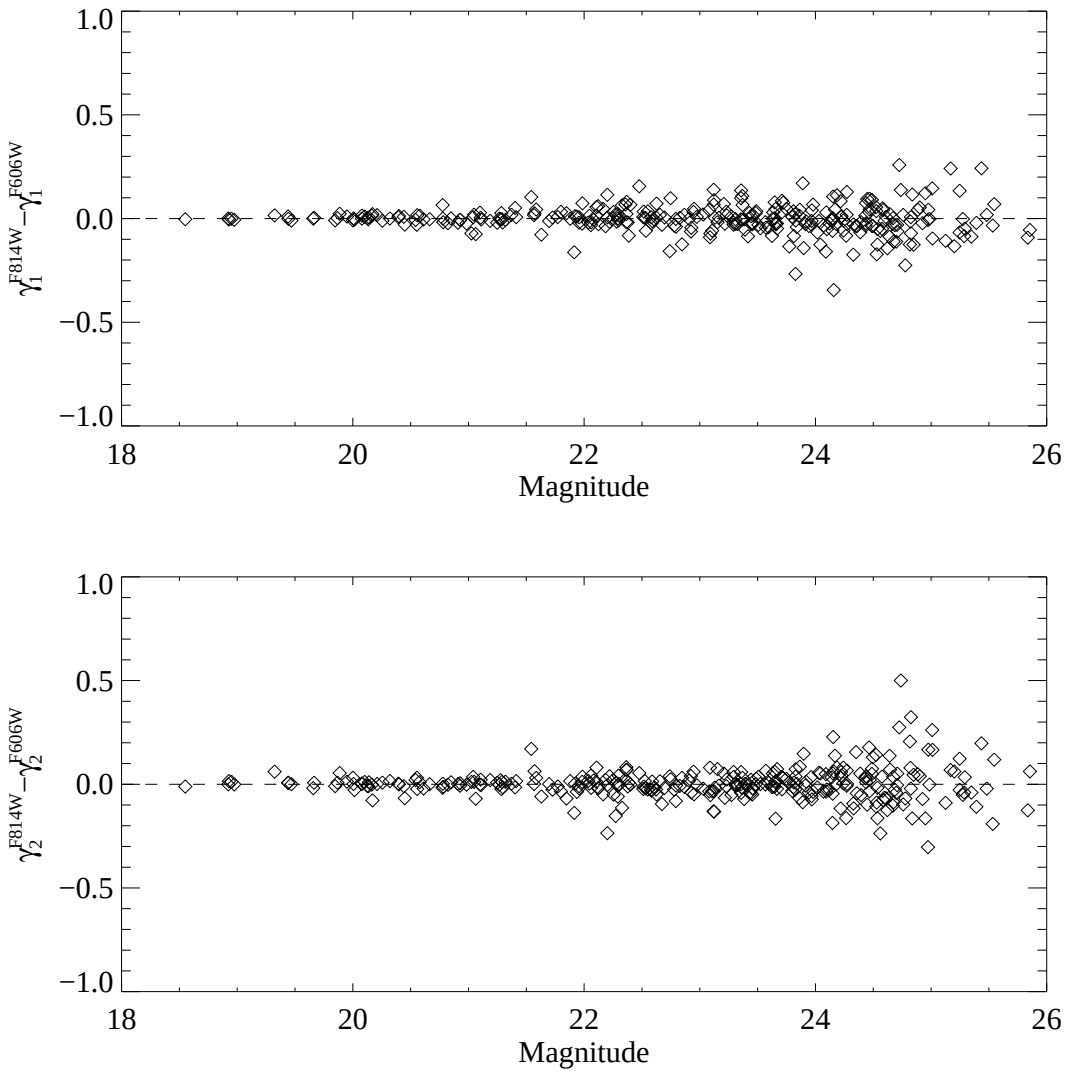

Figure 6.5: A comparison between the measured shears for the cluster A3827 in the F814W and the F606W ACS filter.

radius of the X-ray gas. This was identified by studying the lensing signal around each of these points, however these were relaxed, isolated groups, for which they expected no intrinsic offset between dark matter and galaxies. In this study, this is the exact signal I am attempting to constrain, and therefore do not necessarily want the galaxy proxy that gives the bottom of the potential.

In order to carry out a comprehensive study I use three different proxies of the galaxy distribution; number density, the Brightest Group Galaxy (BGG) and the flux weighted galaxy density. In a bid to homogenise the data set, I abandon all colour information and accept that any foreground (and background) galaxies will merely add Poisson noise to the various estimates (albeit in different magnitudes). This will result in added variance to the estimates, however, most importantly, no systematic bias. Any cut in colour may impose a bias, which I would avoid, even if it is at the cost of precision.

I estimate the number density of galaxies by passing the galaxy catalogue used for the shear analysis through *Wavdetect*, used in the X-ray analysis. In this case, however I use much larger scales (32, 64) as the sampling is much less (between $30 - 80$ galaxies/arcmin^2 as apposed to the thousands of photons detected by Chandra). To create flux smoothed maps, I mask out all stars in the image as identified during the shape measurement process and then smooth the mosaiced HST image using *Wavdetect* on scales of 32 and 64. Finally I identify the BGG by finding the brightest galaxy within the prior used for the dark matter reconstruction.

Using sextractor to estimate the positions of haloes

In each case where I have smoothed data with *Wavdetect* (i.e. the X-ray gas, the number density and the flux weighted density of galaxies), I have had to estimate the position of haloes. In order to estimate their positions I used SExtractor on the *Wavdetect* smoothed images. SExtractor calculates the bary-center from the first order moments of the profile, which means that it an intensity weighted mean of the centre of the isophote, resulting in the peak density contour not always coinciding with the position of the centre of the estimated isophote.

Although a very good positional estimator, SExtractor does not return the uncertainties in the positional error of the isophotes. In order to determine the error in the positions of each of the components, I iteratively re-smoothed the

maps using different scales and re-extracted the haloes. I then found the variance in the position of the halo from the various iterations,. For each case I iterated 4 times (since it is computationally expensive). For the X-ray maps I each iteration used scales; (2, 6, 14, 30), (4, 12, 28), (6, 10, 18, 34) and (8, 12, 20, 36) pixels. For the galaxy maps, I used scales (2, 6, 14, 30), (4, 12, 28), (6, 10, 18, 34) and (8, 12, 20, 36) pixels. I found that the average error for the gas peaks was $\sigma_{\rm XR} \approx 5'' \approx 20$kpc (at a $z_{\rm eff} = 0.4$) and the galaxy peaks had an average error of $\sigma_{\rm GAL} \approx 1'' \approx 5$kpc (at a $z_{\rm eff} = 0.4$) .

Iterative dark matter reconstruction

The method used to reconstruct each system is unique to this study. During the analysis I will use the galaxies as the central co-ordinate system for each combined system of dark matter, gas and galaxies, and hence the priors for the dark matter must not asymmetrically cut off this co-ordinate system in any particular direction. I therefore initially reconstruct the dark matter with priors that incorporate the gas and any group galaxies that obviously exist nearby. Once I have this first iteration of a map, I identify and associate gas, dark matter and galaxies in to systems of three mass components. I see that in this case, the dark matter will be biased towards to gas, and therefore I must reconstruct the dark matter a second time with the prior centred on the galaxy position of choice (and hence have to reconstruct the dark matter three times, each time with the prior placed over the position of the flux weighted, number density and BGG galaxy proxy). This way I null any bias imposed by the choice of prior.

6.4 Results

I adopt the same nomenclature as earlier in this thesis to define the mass component offsets. I begin by defining the centre of the coordinate system, which is the position of the galaxy estimator, with the positive x-axis defined by the vector joining the galaxies to the gas. From here I define the following observables as used in the previous section. Figure 6.6 shows diagrammatically the different vectors that I measure for each system. The position of the dark matter with respect to the galaxies defines the sign of the various vectors. This Figure shows the sign of the vectors in the event that dark matter should lie in four different

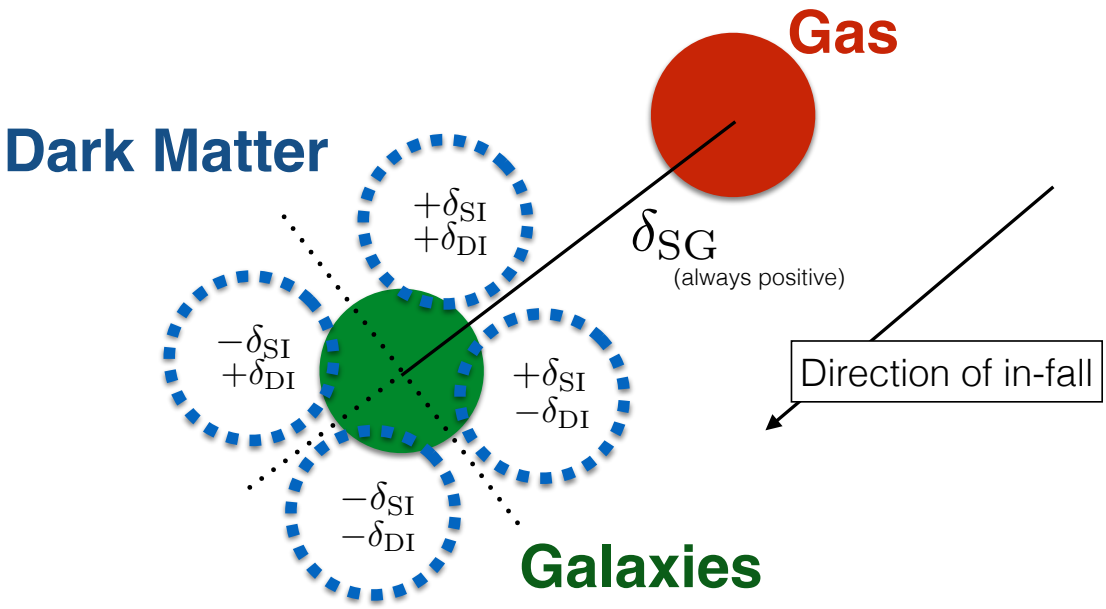

Figure 6.6: Illustration of how I propose to use all three components of in-falling substructure, with the sign of each vector shown with the potential centroid of the measured dark matter. The vector, δ_{SG}, from galaxies (green) to gas (red) defines our coordinate system and the assumed direction of infall. This is always positive. Theoretically, dark matter should lie some fraction along this vector, depending upon its interaction cross section. However, the observed position will be noisy, so in practice I will measure the parallel, δ_{SI}, and perpendicular, δ_{DI}, vectors from galaxies to dark matter (blue). In the event that for an individual system I measure the dark matter position to be in front of the galaxies and be above the vector, δ_{SG}, then δ_{SI} will be negative and δ_{DI} shall be positive. The diagram shows how the sign for each of these vectors change with each potential position of dark matter.

quadrants. With reference to this Figure, we define the following vectors:

- $\delta_{\rm SG}$: The separation between the galaxies (S) and the gas (G) (which by definition is always positive)
- Intersection point (I) : The closest point along the vector, **SG**, to the dark matter position (D)
- $\delta_{\rm SI}$: The separation between the galaxies and the intersection point
- $\delta_{\rm DI}$: The separation between the dark matter and the intersection point
- $\delta_{\rm GI}$: The separation between the gas position and the intersection point

6.4.1 Individual Cluster Analysis

Here I present the results from the analysis of 30 galaxy clusters. Although I have not used every cluster and halo in the final analysis, I include it here as they are still merging and interesting clusters that need to be raised for further study. With reference to this Figure, in each case the following Figures show:

- The first Figure presents the optical HST, drizzled image and its associated masks represented as green boxes
- The second Figure shows the same field of view as Figure 1, but it presents the density contours from the best fitting dark matter density profile (in blue and in units of integrated projected mass density ($10^8 M_\odot$ / arcsecond^2), the wavelet smoothed X-ray image (the heat map and in units of photons/cm^2/s) and finally the flux weighted galaxy distribution(the green contours and in units of 1/10 counts/s). The black lines provides the reader with information about the ACS chip boundaries and field of view and the black triangles show the configuration of the selected halo system used for the analysis.
- In the case where I have used the halo in the final sample I also present a diagram of the offsets between the three mass components ($\delta_{\rm SI}$ in blue and $\delta_{\rm SG}$ in red).

As a guide to how the reconstruction was carried out, I present here the steps taken to reconstruct the cluster A370. Initially I smoothed the gas map and the galaxy map. I then looked to reconstruct the dark matter where resolved gas (X-ray) haloes existed. This reconstruction had a flat prior that included any close by galaxy haloes according to the smoothed map. Once the dark matter has been reconstructed, I assembled a system of three haloes, the galaxies, dark matter and gas. Once I had constructed the system, I repositioned the dark matter prior on top of the galaxy halo and re-reconstructed the dark matter to gain an estimate of its final position. From this system I then measured the three vectors.

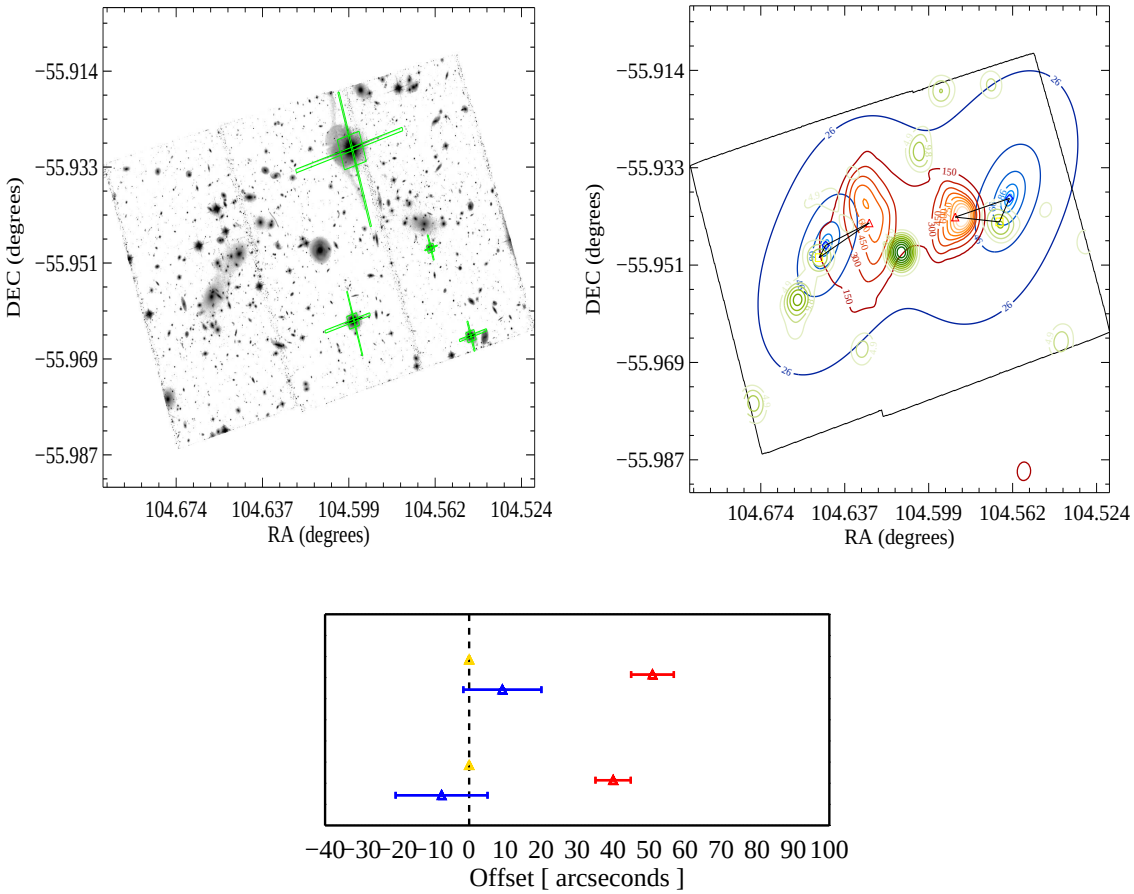

Figure 6.7: 1E0657

1E0657

The cluster 1E0657-55 or more commonly known as the Bullet Cluster was considered the smoking gun for dark matter. Many studies have now confirmed a significant offset between dark matter and gas (Markevitch et al. (2004); Clowe et al. (2004); Bradač et al. (2006)). Considered to a be cluster post-merger, the nature of the gas shock intimates that it is a merger that has a very small impact parameter (Randall et al., 2008). Here I find a significant offset once again, providing more evidence for the existence of a separation. Interestingly the easterly group of galaxies is bimodal, which may be a consequence of the merger, or simply a foreground structure.

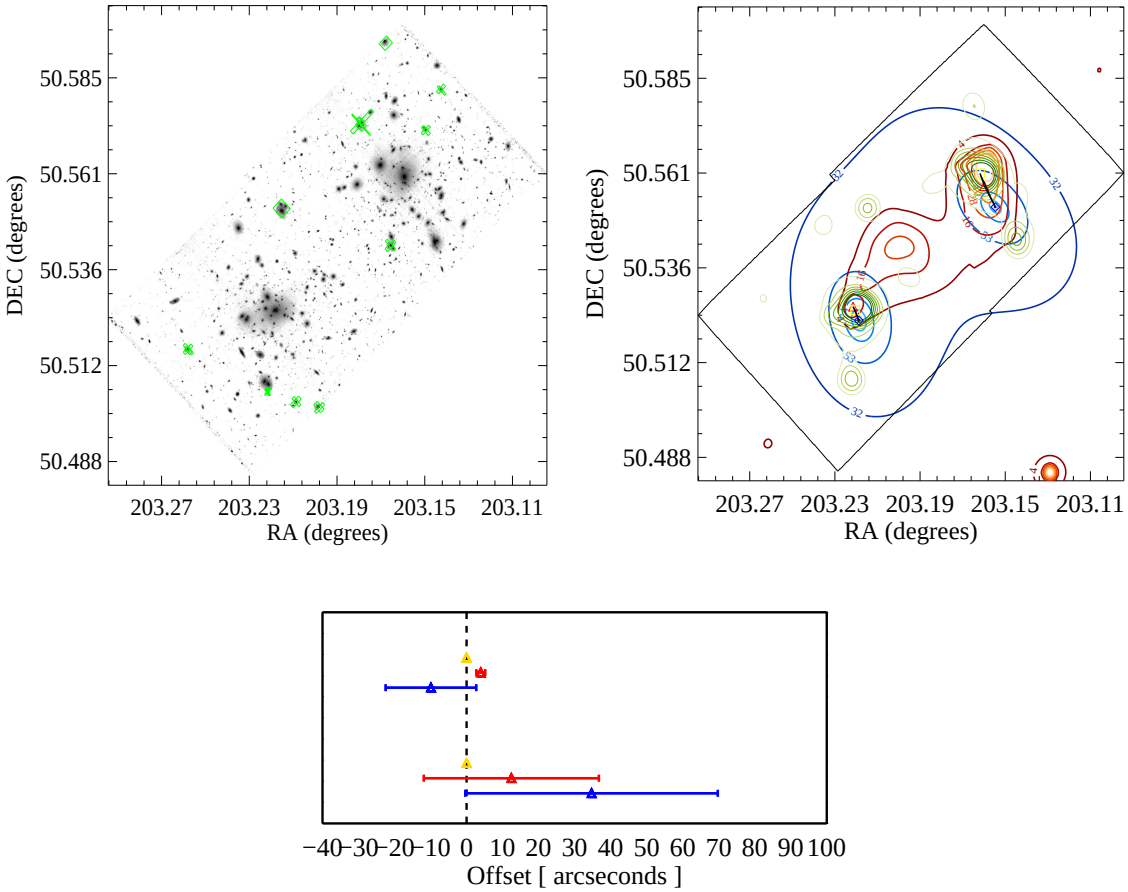

Figure 6.8: A1758

A1758

A1758 seems to have more that one part to the merging system. The gas intimates that during the merger the cluster either fragmented into a secondary halo, or there were three originally. The dark matter peak seemingly coincides with the galaxy peak rendering more support for the existence of a central halo. It is clear that the north and south peak are more massive than the central peak, and therefore postulate that originally this was a two body merger, however the complex nature of it resulted in three distinct bodies.

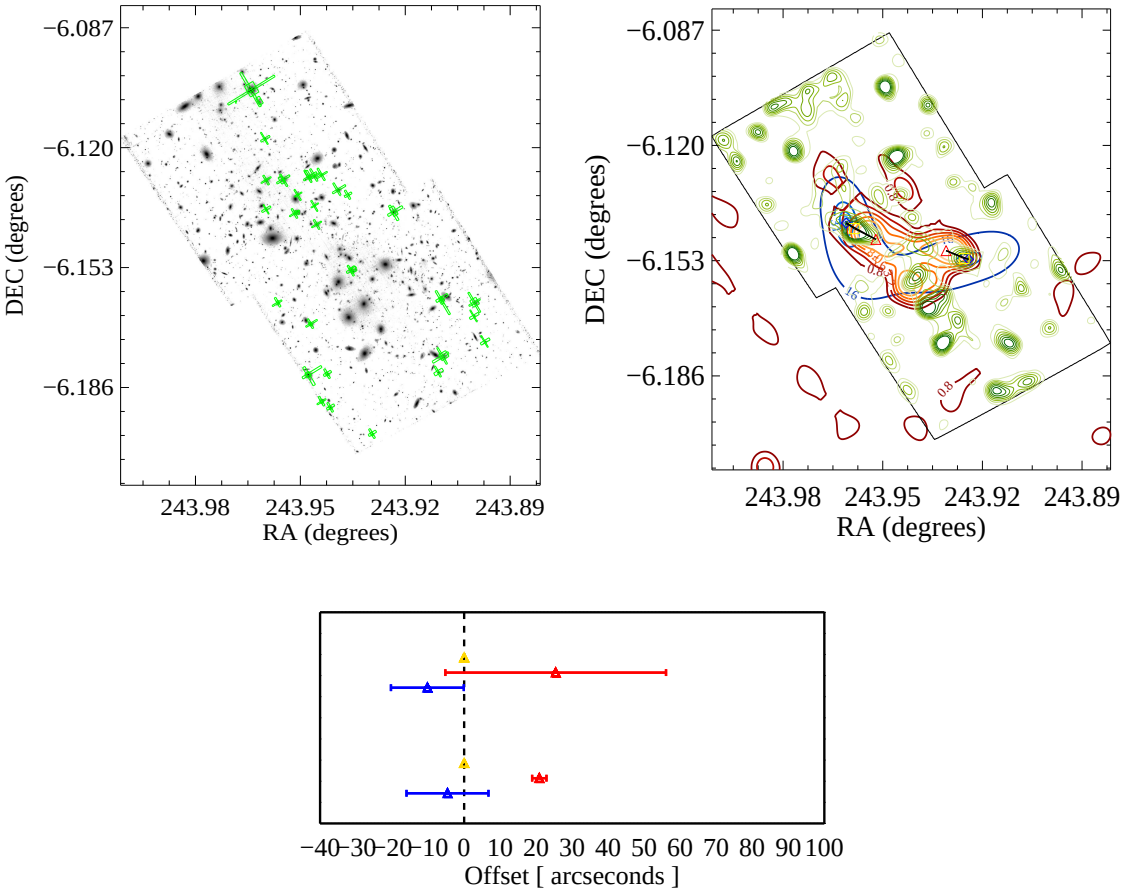

Figure 6.9: A2163

A2163

A2163 is an interesting cluster as the X-ray seems to intimate a multi-modal distribution of mass in the system, which is in a complex state of merging. Bourdin et al. (2011) carried out a detailed study of the system in the X-ray and find that the south-west peak is currently passing through the north eastern peak. In attempt to reconstruct the entire system I fit 5 bodies to this system including those haloes that are separated from the main structure (north and north east) however I find no evidence for haloes here. Moreover, the addition southern peak shows no evidence for dark matter either. I therefore reconstruct a 2 body merging scenario, and assume that the additional X-ray features a complexity of the merger that I can not resolve.

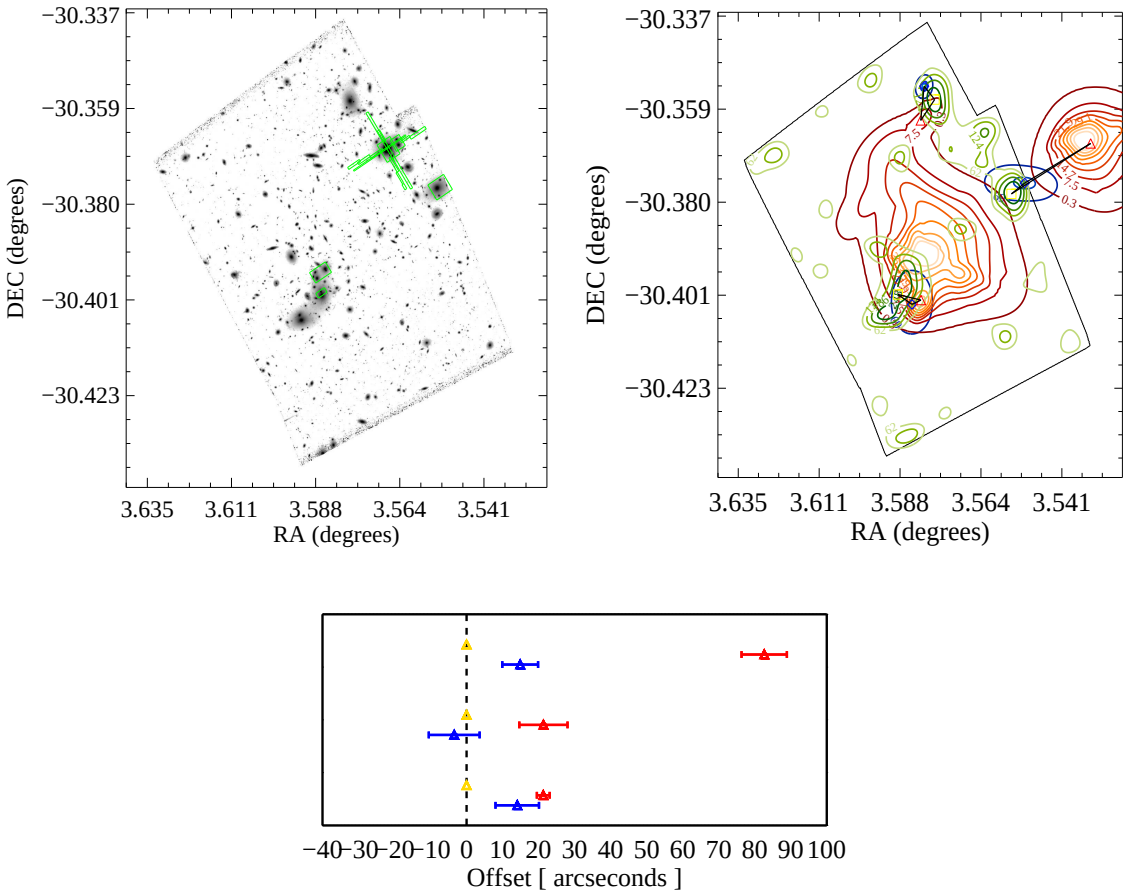

Figure 6.10: A2744

A2744

A2744 is a particular difficult merging system. The Northern, Southern and Westerly peaks suggest a non-trivial merging scenario. It is not clear that the gas peak, several hundred kilo-parsecs offset from the westerly peak are connected, moreover, the position of the lensing peak outside the field of view suggests some extra dark matter that exists outside the field. Merten et al. (2011) suggest that there exists two haloes at this position, either side of this halo. However since I do not have access to this I can only describe this with one halo, which may be finding the average position between the two.

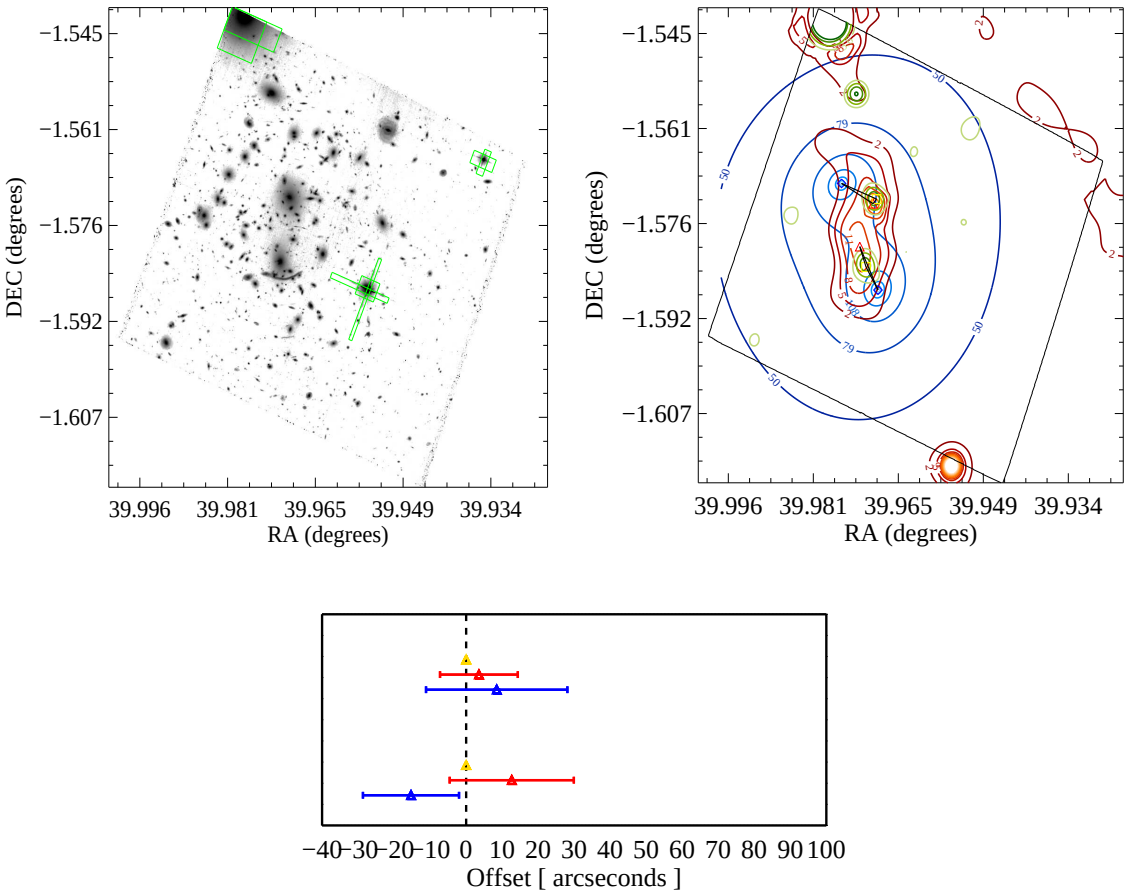

Figure 6.11: A370

A370

A370 was one of the first lensing systems to be discovered with its giant arc clearly encircling the Southerly giant galaxy. The X-ray gas distribution seems to show a bimodal distribution, this along with the obvious double brightest cluster galaxy suggest merging activity. I find evidence for two peaks, however with the lack of strong lensing information I suffer from lack of precision.

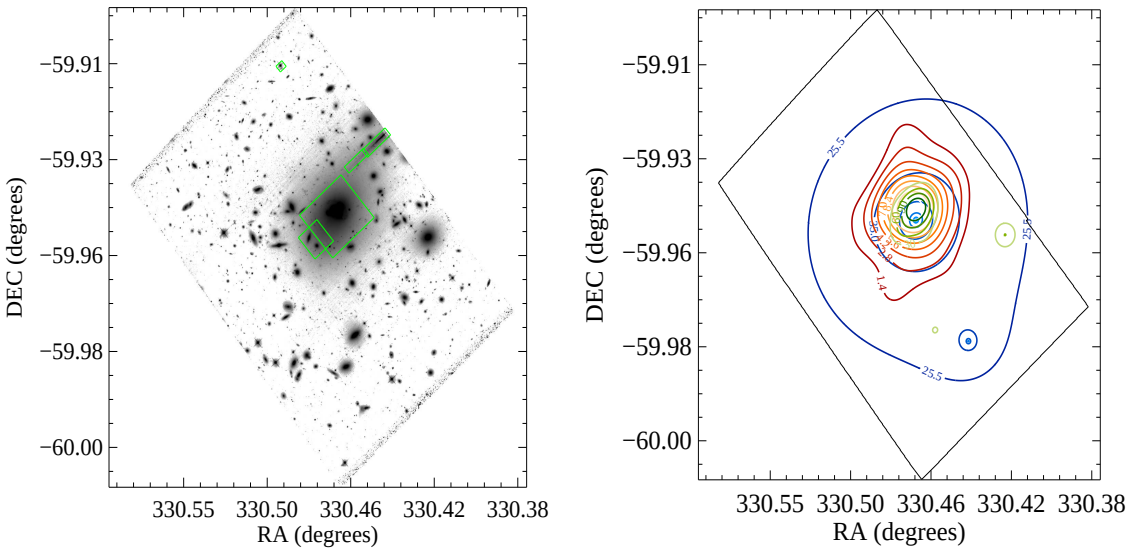

Figure 6.12: A3827

A3827

A3827 was initially studied by Williams & Saha (2011) where they found an offset between dark matter and galaxies in the central core. Known as the Cannibal cluster, the central region is complicated, consisting of many sub haloes. I find low evidence for the existence of a southerly peak from the X-ray despite the strong evidence for a dark matter peak from the lensing and an associated galaxy peak. Since the low signal to noise of the X-ray makes it impossible to resolve the region as a separate sub halo, I do not use this system in the final sample.

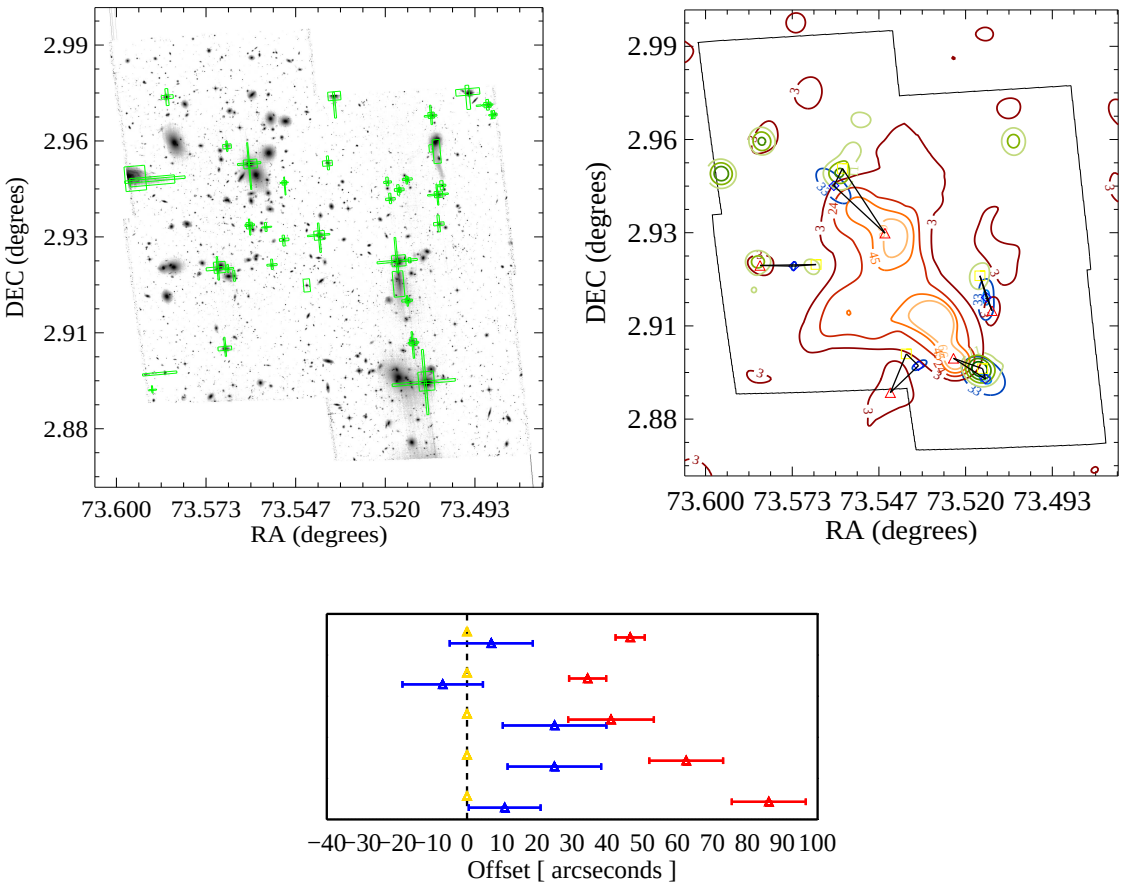

Figure 6.13: A520

A520

The merging history of A520, or the Train Wreck cluster has been highly disputed. The initial study postulated the existence of a dark core between the north and south gas peak (Mahdavi et al., 2007). However later studies found no such core (Clowe et al., 2012; Jee et al., 2012). A clearly complicated merger I attempt to reconstruct the positions of haloes as freely as possible. An initial reconstruction placed priors and haloes over each of the observed gas peaks. That is southern, central, easterly, south eastern and westerly peak. Having run the reconstruction I find no evidence for peaks in the central of easterly gas region. I therefore adjust the priors roughly placing them over the clear galaxy peaks. That is the southern, eastern, western, south western and north peaks. For all regions I find significant evidence for the existence of dark matter at these positions. This supports the claim that no dark matter core exists in A520.

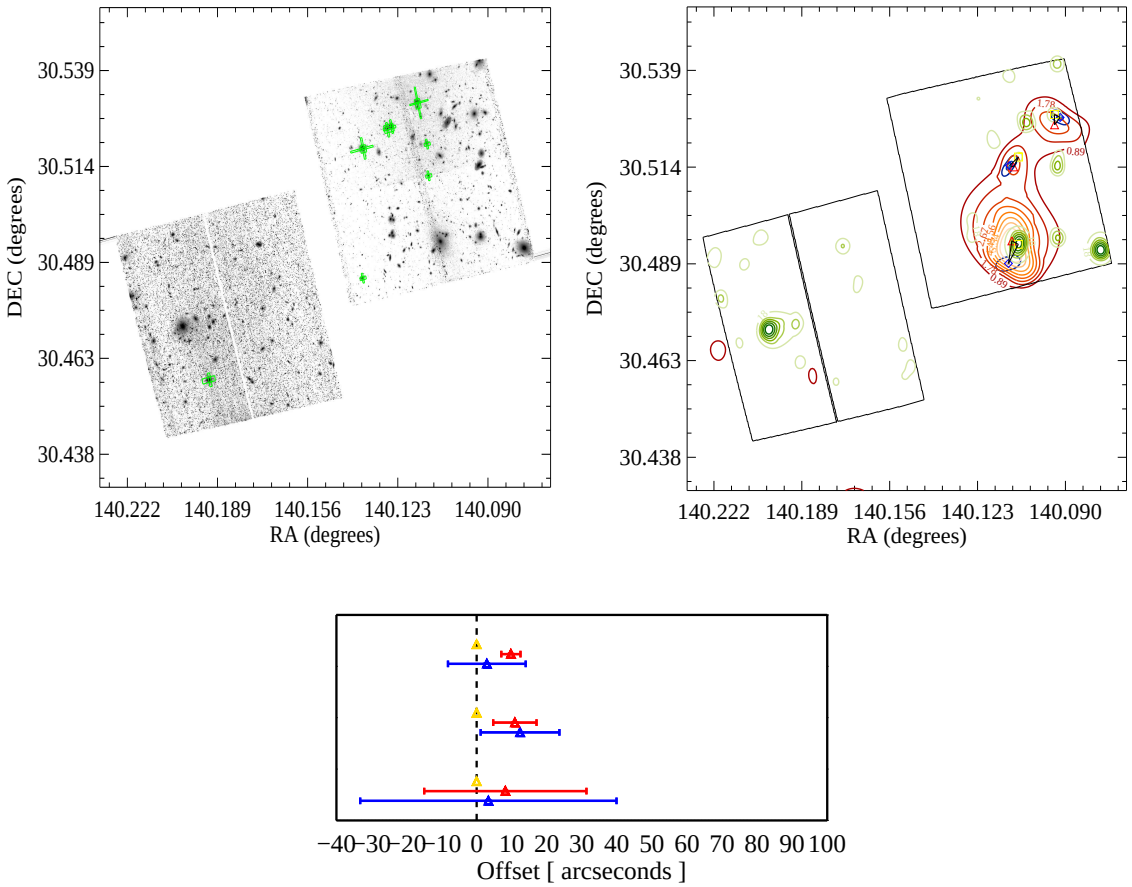

Figure 6.14: A781

A781

A781 is divided into two parts as shown in Figure 6.14. It can clearly be seen in the optical that a large group of galaxies exist in the south easterly field, and the north western field has a multitude of galaxy haloes. As unveiled in the X-ray, the north westerly field exhibits a complicated system with three clear gas peaks. The southern field, however, exhibits no such peak. This maybe due to very low X-ray emission, however I note that the southern field coincidentally aligned with the chip separation in the ACIS CCD. Concentrating on the northern field, I reconstruct the position of three dark matter haloes as suggested by the X-ray. I considered the existence of a halo to the east or south of the northern peak by extending the prior, however the peak remained coincident with the northern gas peak and closest galaxy peak. Moreover, I find evidence for the existence of a central peak, and therefore conclude that this is a three halo system.

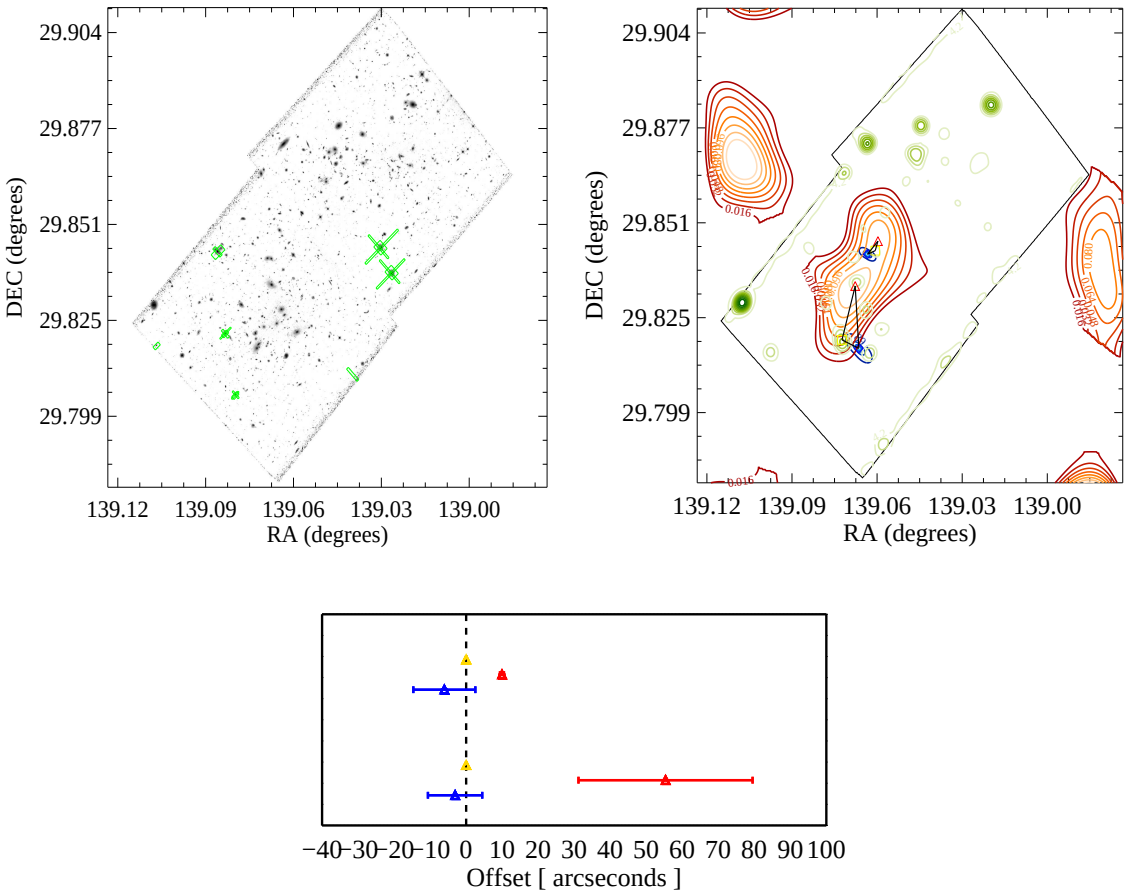

Figure 6.15: DLSCLJ0916

DLSCLJ0916

DLSCLJ0916, or the musket ball cluster is an extremely faint merging system. With very low signal to noise in the X-ray, there is clear evidence for the case of a merger with a strong lensing signal. I postulate that the merger has stripped the clusters of a large amount of cool gas, and hence why it is a faint system. The southern peak is well constrained and shows a clear offset with gas, however the easterly peak is slightly more complicated. It is not clear whether the observed gas peak is associated with the central dark matter peak as shown in Figure 6.4.1, or it is associated with the distant galaxy group seen in the north east of the field. In order to construct an estimator from these two peaks I use a consistent association of the closest peaks.

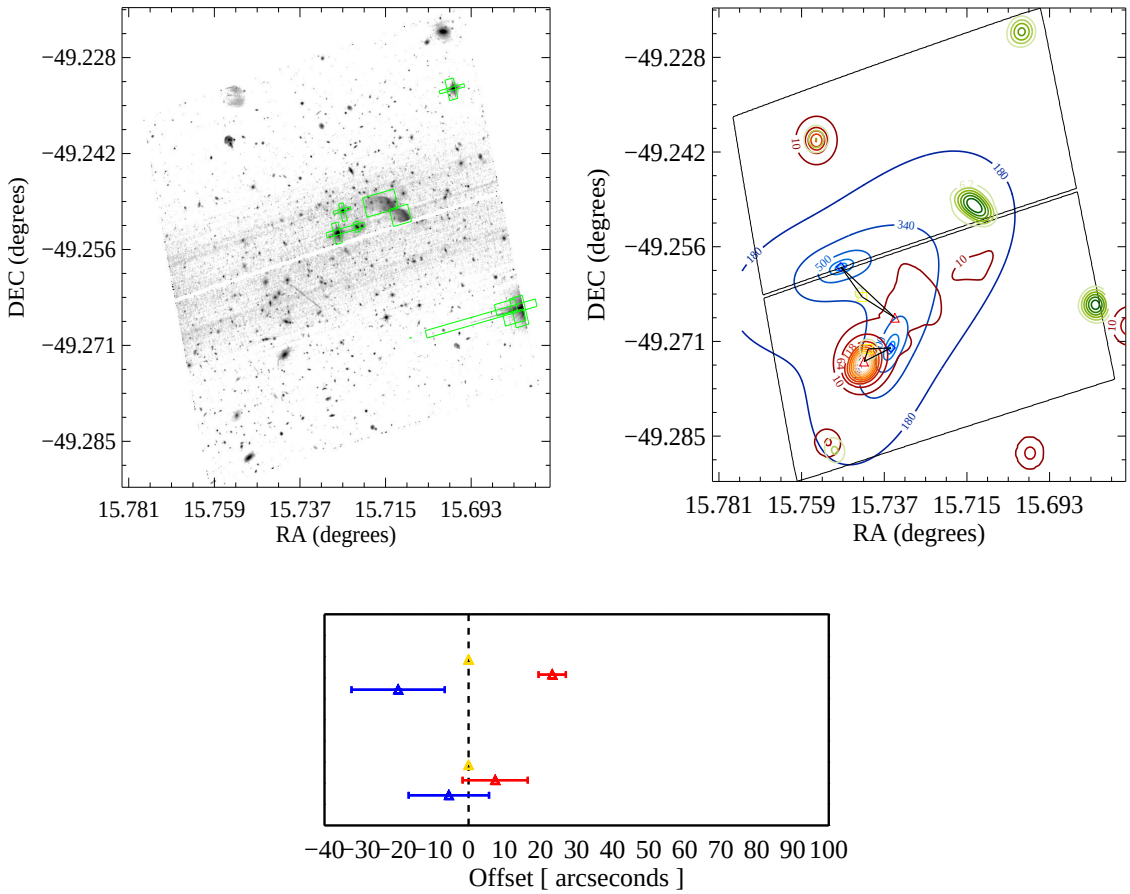

Figure 6.16: El Gordo

El Gordo

El Gordo is the largest and most luminous merging cluster currently known. At a very high redshift, it is disputed whether such large objects should exist so early in the Universe. Exhibiting a merging history, although very far away, the size of the merger means that I still have the ability to include it in the study. Figure 6.4.1 shows significant X-ray emission lagging behind the main halo. I place a large prior for the second halo since it is unclear exactly where this should be. I find evidence that it coincides with the galaxy peak to the north of the main halo, intimating an unusual merger. However I do note here that estimates of galaxy positions will be highly uncertain due to many foreground structures in between $z = 0$ and $z = 0.89$.

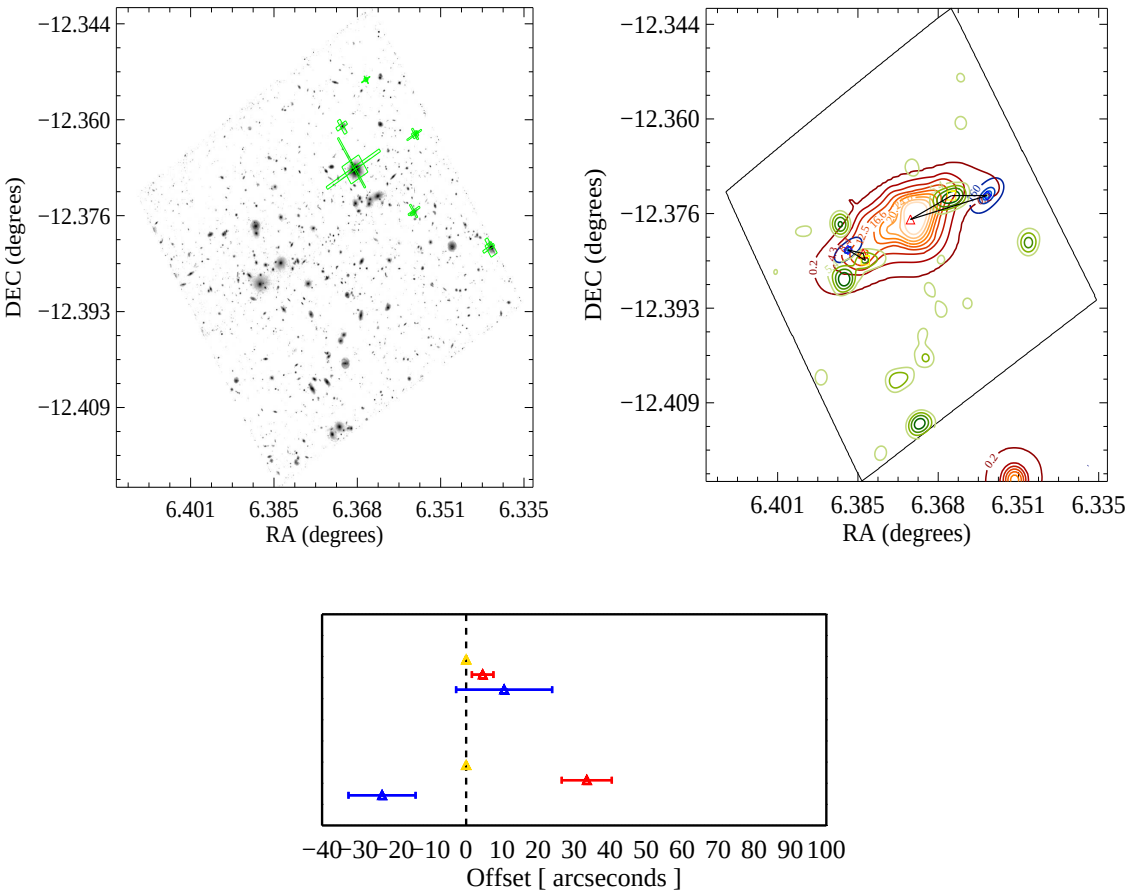

Figure 6.17: MACSJ0025

MACSJ0025

MACSJ0025 or more commonly known as the Baby Bullet Cluster, was found not long after the Bullet Cluster (Bradač et al., 2008). Although not appearing to exhibit separated haloes, when smoothed it is possible to find small-scale structure in the core. This allows me to extract two gas haloes that can be attributed to each of the passing dark matter haloes and galaxy groups. I find significant peaks for both the east and westerly ends of the gas halo, supporting evidence for a merging galaxy cluster.

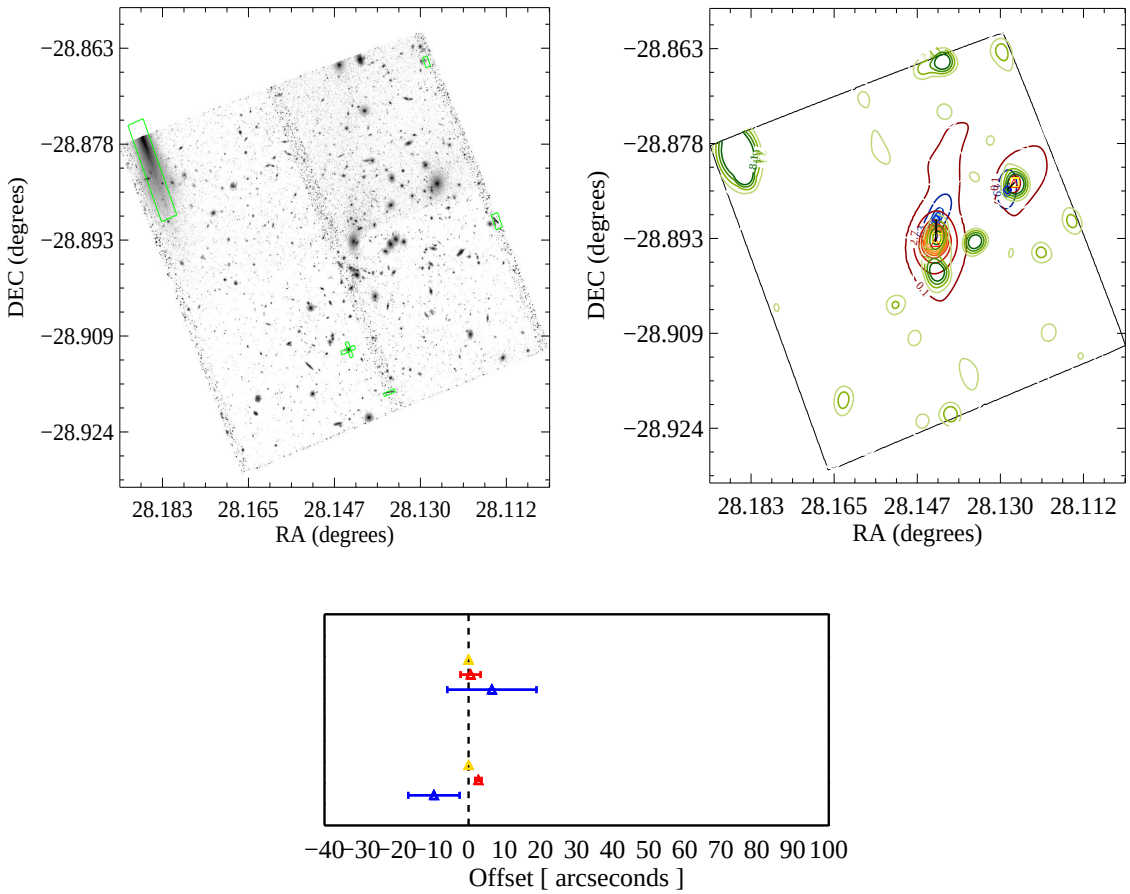

Figure 6.18: MACSJ0152

MACSJ0152

MACSJ0152 is a classic example of a galaxy cluster with substructure. The main halo exhibits excess x-ray to the north of the halo suggesting some non virial activity, with a second sub-halo to the north west seemingly accreting onto the galaxy cluster. I find a significant dark matter peak that is slightly offset from the galaxy peak, however this is not significant.

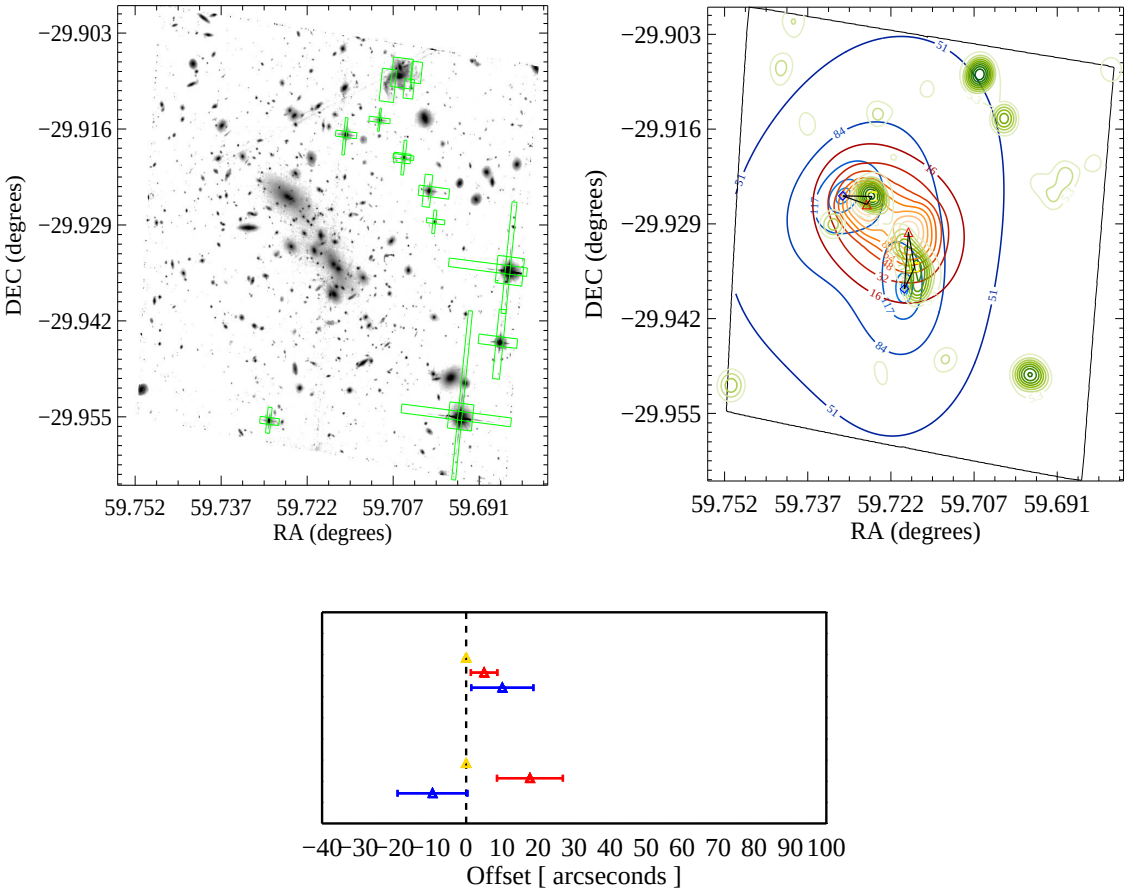

Figure 6.19: MACSJ0358

MACSJ0358

MACSJ0358 is a typical example of a merging system. I observe two significant gas peaks, both containing large galaxies. I see that the southern galaxy distribution is slightly offset from the gas intimating that I am observing it post merger. I note that the southern dark matter peak prefers the central part and does not coincide with the galaxy peak. I conclude that this may be a result of the poor resolution of weak lensing. In the event I have no strong lensing information it is difficult to discern between two haloes and one. However, I do find evidence for two peaks.

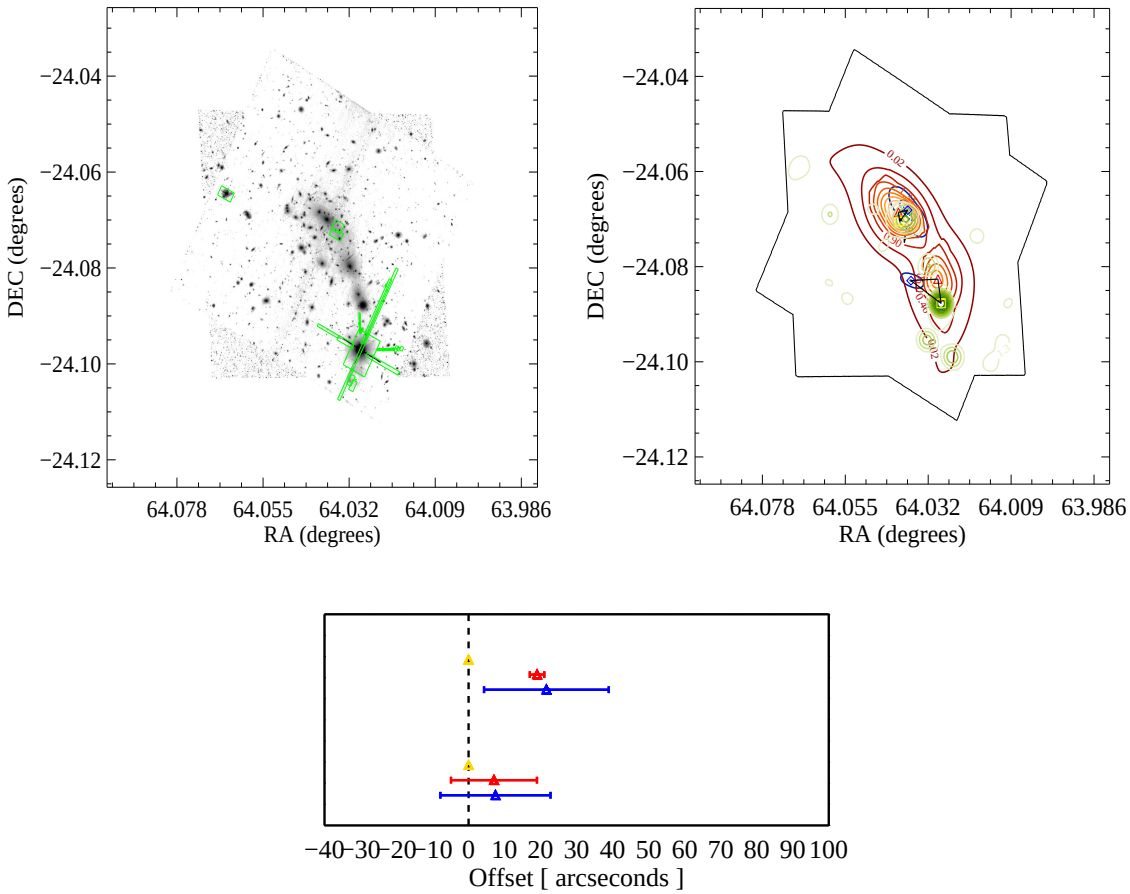

Figure 6.20: MACSJ0416

MACSJ0416

MACSJ0416, a large merging cluster at a redshift of $z = 0.42$ exhibits clear bimodality in the X-ray gas peak. Although seemingly a large BGG for each of the haloes, the lensing reconstruction suggests excess mass to the east of the system. This maybe an artefact of the large mask in the southern region of the field caused by the large star.

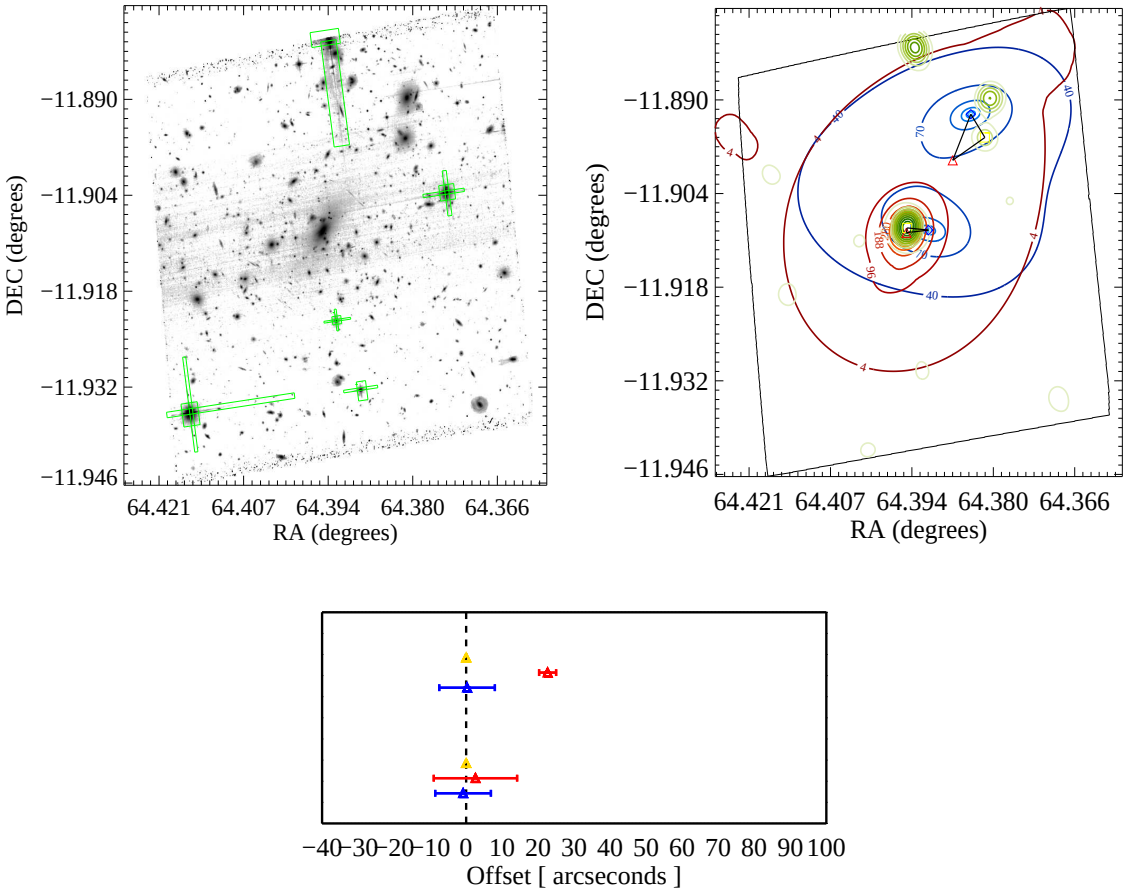

Figure 6.21: MACSJ0417

MACSJ0417

The cluster MACSJ0417 shows clear X-ray gas excess in the north-west region of the field. In this region lie a group of large galaxies that appear to be associated with this gas excess. The dark matter reconstruction supports evidence for the existence of a sub-group in the north-west as I find a significant dark matter peak. I postulate that this system is in a state of accretion. I see in this reconstruction I have assigned the galaxies of the sub-peak to the westerly galaxy and not the northern. This was because there were two haloes very close and it is unclear clear which peak I should use, so I assign the closest one to the dark matter halo.

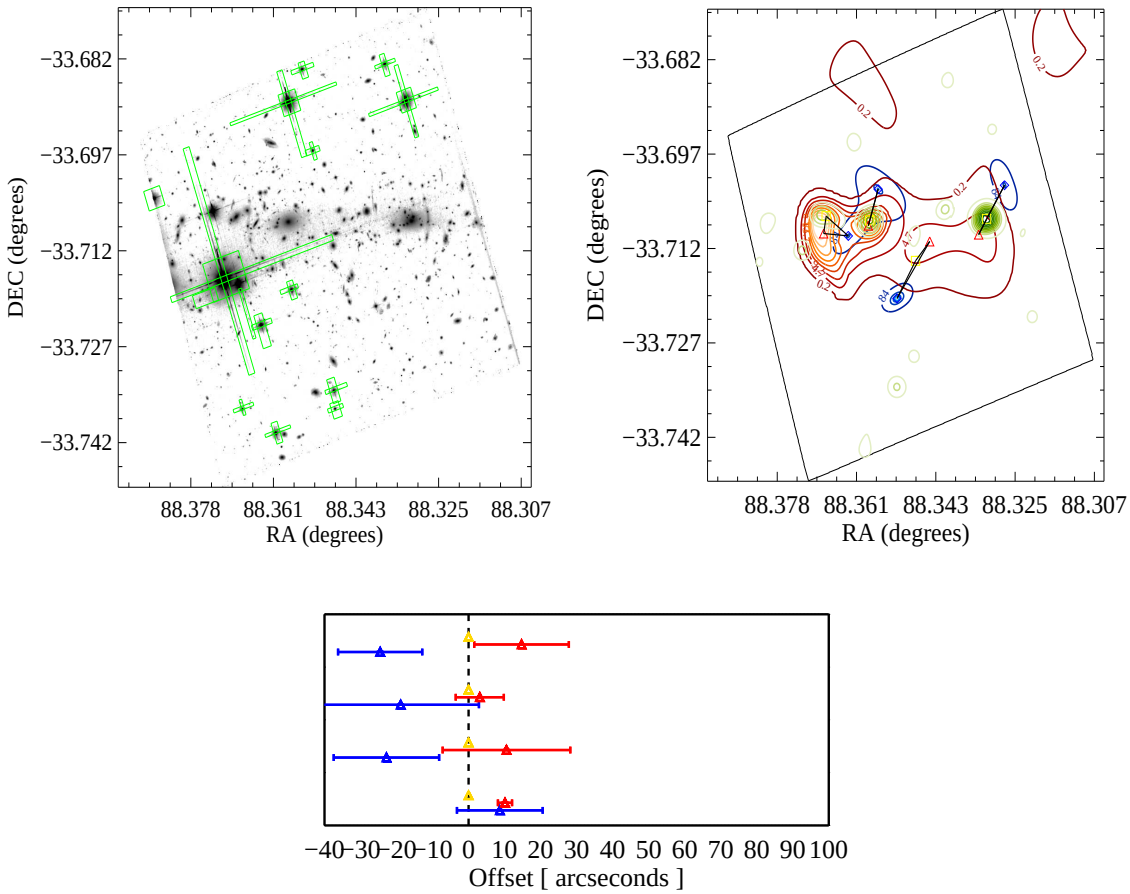

Figure 6.22: MACSJ0553

MACSJ0553

The distribution of X-ray emitting gas in MACSJ0553 is complicated, seemingly having had a recent non-trivial merger. The optical image suggests three main systems belonging to the three large cluster galaxies, with some region to the east of the most the most westerly peak not harbouring a giant galaxy. Although there seems to be no large galaxy associated with each peak, I find evidence for the existence of these haloes.

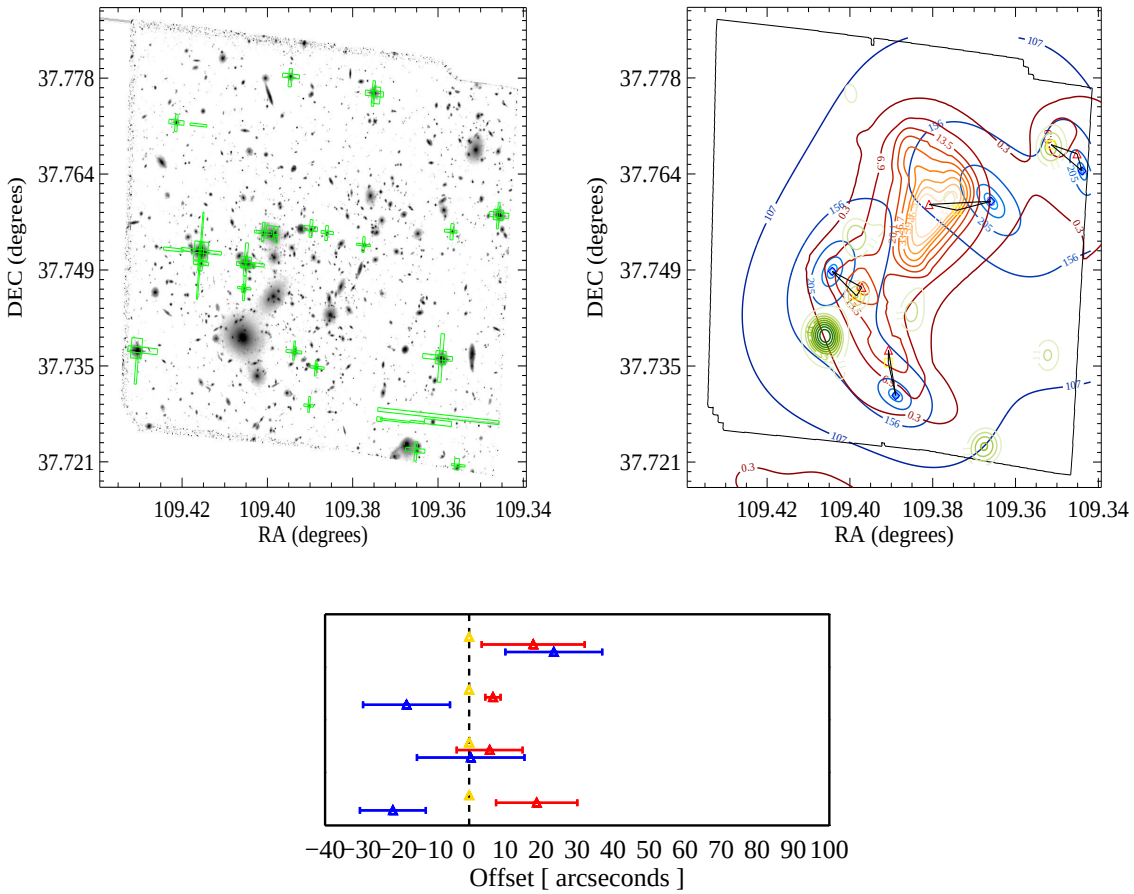

Figure 6.23: MACSJ0717

MACSJ0717

Similar to MACSJ0553, MACSJ0717 has a complicated distribution of gas, with four resolved haloes. I find that the two south easterly peaks and the north westerly peak are well constrained, however the dark matter peak of the central gas halo is unconstrained, which should be considered when observing the large offset from both the galaxies and the gas. Interestingly the north westerly peak is well constrained, and very significant, however exhibits a large offset from its associated galaxies and gas. The presence of the masked star in this region may well be biasing the estimate, plus the estimate is very close to edge of the field.

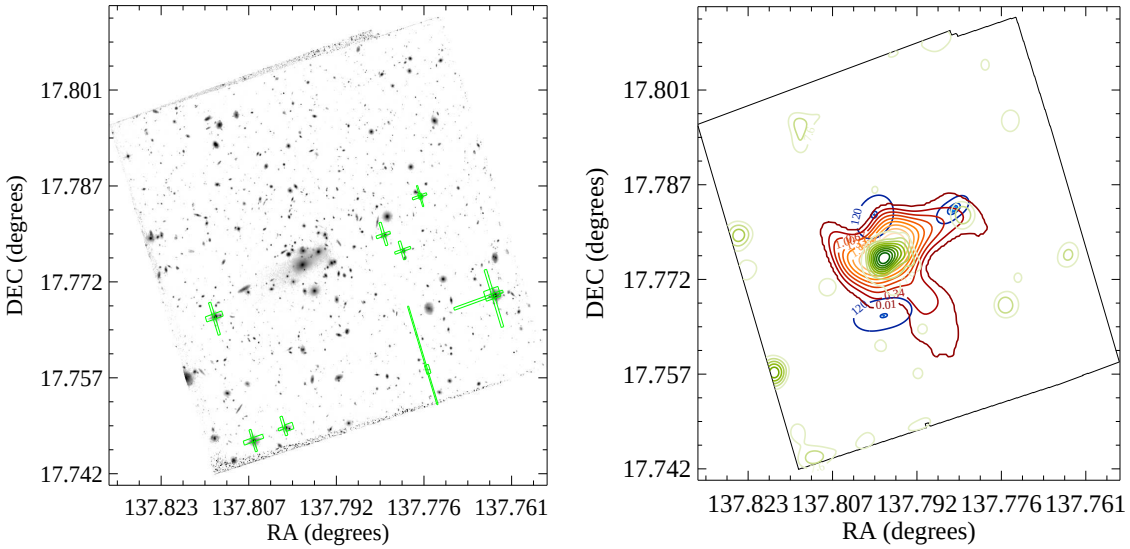

Figure 6.24: MACSJ0911

MACSJ0911

The gas distribution in MACSJ0911 is very interesting with excess towards both the west and the south of the halo. The coincident excess in galaxy flux and number density in these positions indicates that I am observing this cluster sometime after a major merger, where the gas has been stripped from its associated cluster potential. Although this halo exhibits strong evidence for a merging system, I cannot resolve separate haloes for each group and therefore cannot include this system in the sample.

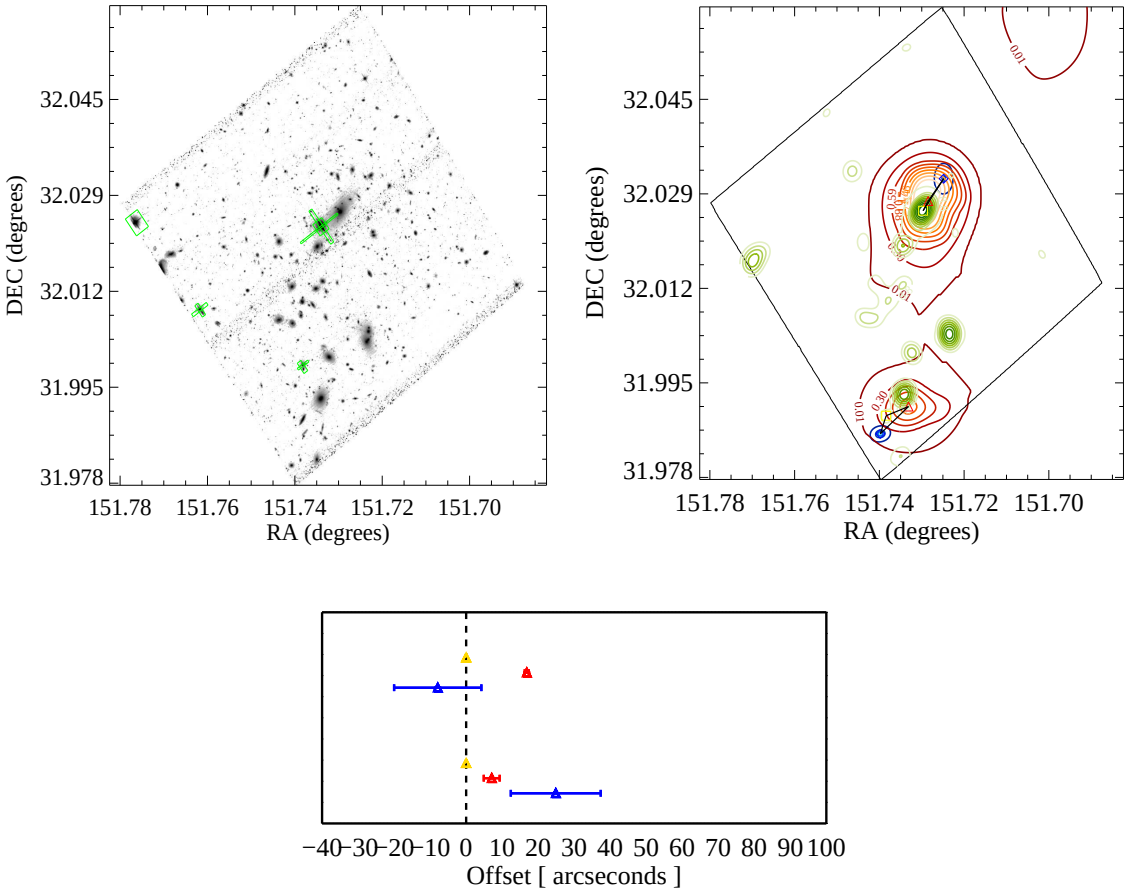

Figure 6.25: MACSJ1006

MACSJ1006

MACSJ1006 is another classically accreting system that has a sub-halo to the south appearing the fall onto the main galaxy cluster. This southerly system has a faint broad X-ray signal typical of a large group, with the dark matter peak offset from the galaxies and gas. Being close to the edge of the field, this offset is not significant, however the gas is clearly still bound, and is a good example of sub-halo in-fall.

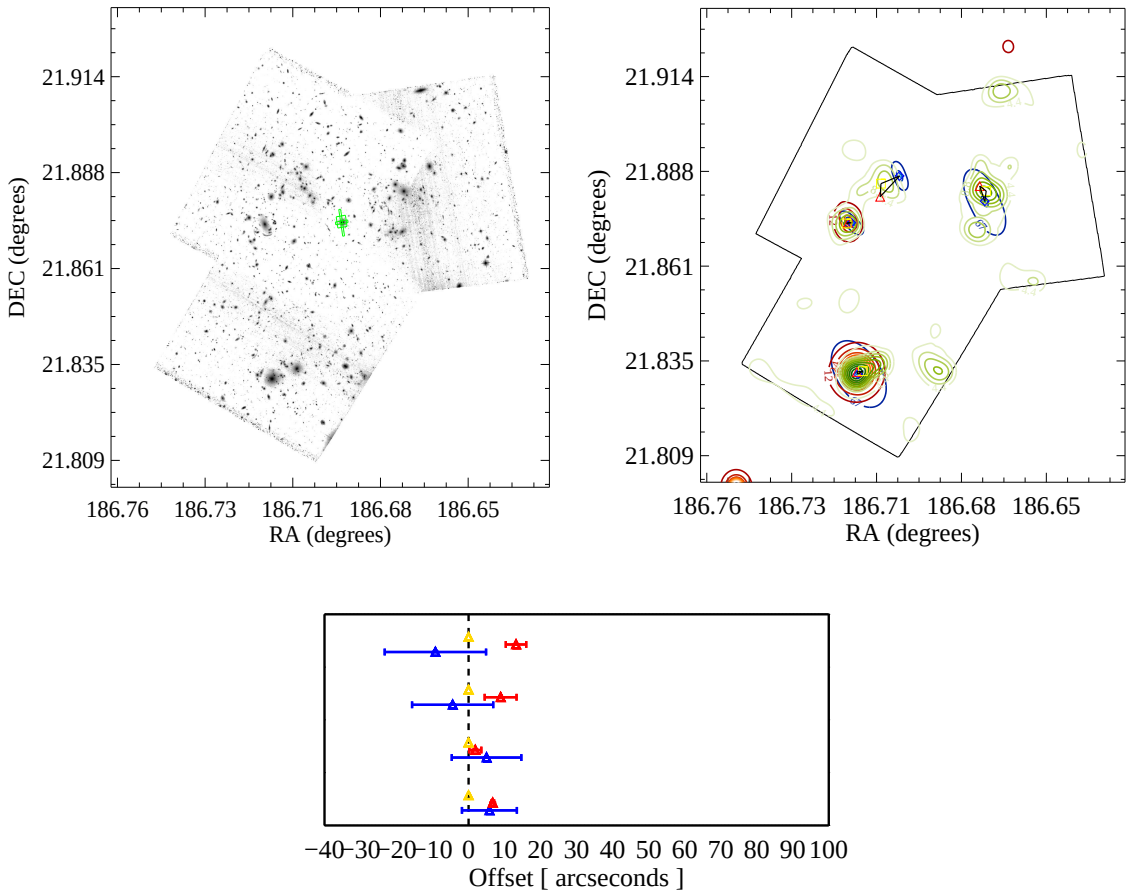

Figure 6.26: MACSJ1226

MACSJ1226

MACSJ1226 is a large system, composed of three large haloes, and one smaller one. The southern and north west haloes are seemingly relaxed, however, under the assumption that are all coincident in real space (i.e. they have the same redshift) they should be experiencing 'bullet' like effects. The north easterly peak, also shows similar relaxation, however has a small peak to its north-west, where there is a large over-density of galaxies, gas and the lensing signal is well constrained. In this particular system, the gas is clearly not relaxed, exhibiting non-virial behaviour, and the dark matter peak is offset slightly from the haloes, albeit within statistical error.

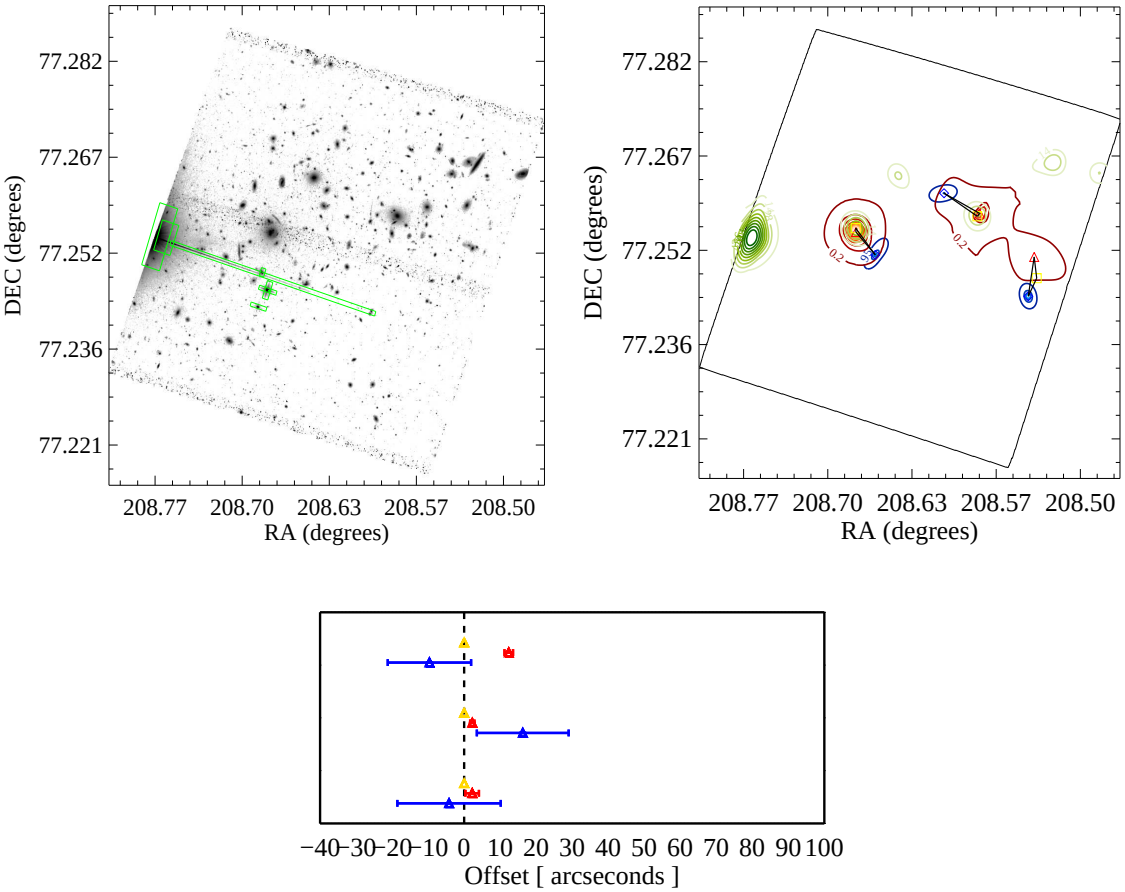

Figure 6.27: MACSJ1354

MACSJ1354

The galaxy cluster MACSJ1354 appears to be a three body system, with one apparently circularly symmetric halo and two that are in a state of merging. Of these three haloes, two are well constrained, and the third, the central of the three, has a large uncertainty in the position of dark matter. The main halo appears to have its associated dark matter offset from the baryonic component, this maybe due to the large mask to the West of this peak.

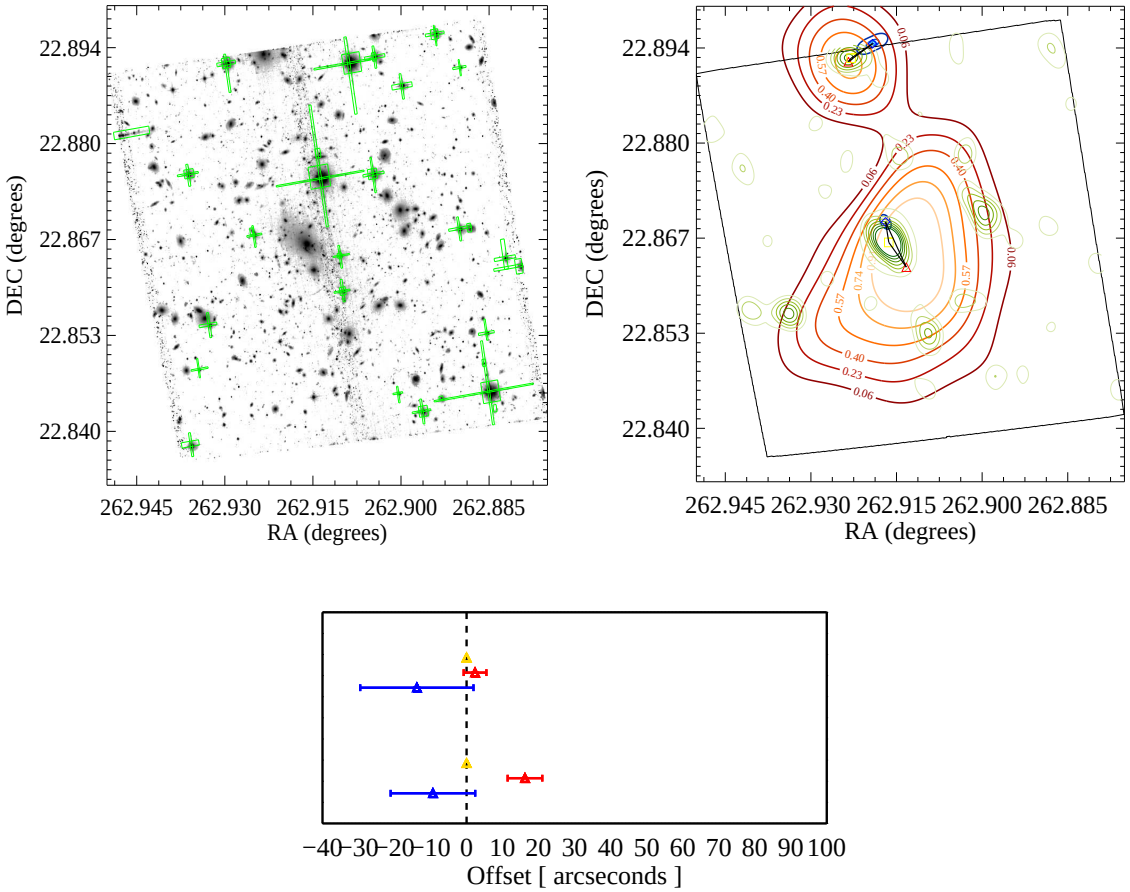

Figure 6.28: MACSJ1731

MACSJ1731

Cluster MACSJ1731 shows clear evidence for two large groups in a state of merging. It isn't clear the direction of motion of the group, however the dark matter halo is well constrained. This field is heavily masked and the dark matter halo is close to the edge of the field, both of which could be biasing the halo position slightly. Interestingly the main halo has its galaxies offset from the bary-center of the gas. This is also true with the dark matter center. Moreover, there appears to be slight elongation in the gas distribution towards to the west of the cluster where a large group of galaxies exist. This slight evidence that this cluster has seen another merger prior to the northerly peak accreting.

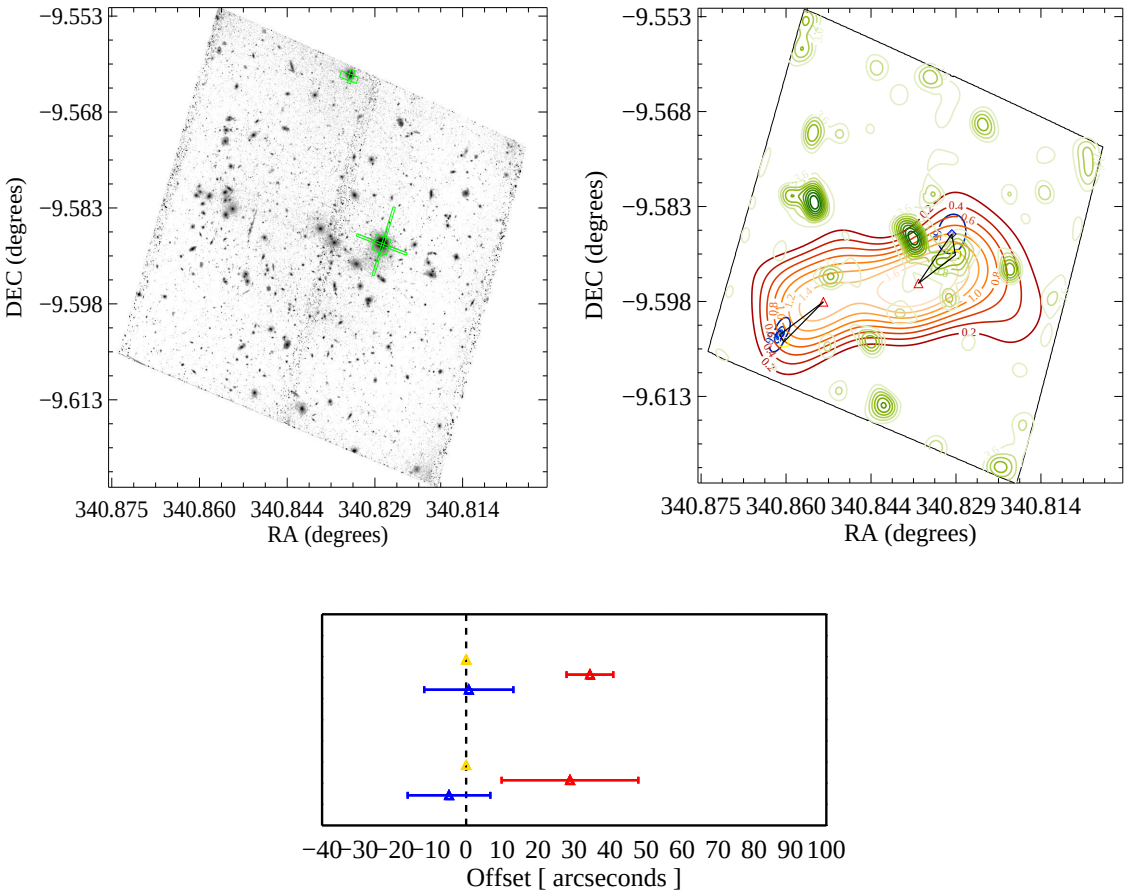

Figure 6.29: MACSJ2243

MACSJ2243

The gas distribution of MACSJ2243 is highly elliptical, with the primary centroid centred over the member galaxies to the west of the field, close the star mask. The history of this is somewhat uncertain. Although the cluster appears to be highly elliptical, the presence of a large group of galaxies in the north can be clear seen, however harbour no observed baryonic gas. This maybe because it is too hot and there cannot be observed by Chandra, or during its merger with the main halo it has had its gas stripped and this has been accreted on to the main halo in the west. In order to keep the method consistent, I conlcude that the easterly peak is small and associated the closest galaxies to this halo and constrain a dark matter halo which prefers to position itself to the south of the gas halo.

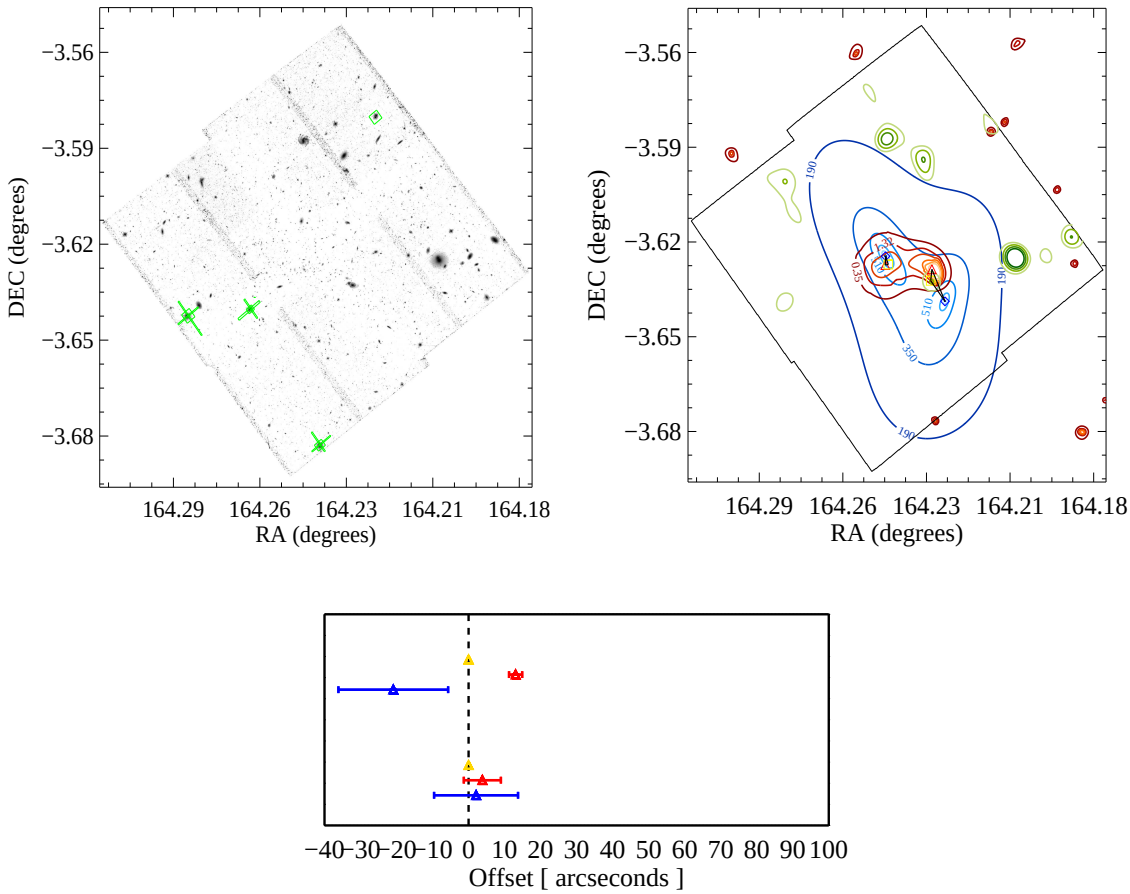

Figure 6.30: MS1054

MS1054

MS1054 is a classic merging system at a very high redshift ($z = 0.86$, second in the sample to El Gordo). Due to the high redshift it is difficult to estimate the distribution of galaxies, especially for the flux weighted as it will be dominated by foreground galaxies. However I include it in the sample due to the size of the cluster. The apparent offset between galaxies and the gas distribution, and the slightly shocked front of the westerly halo suggests that this system is being observed post-merger. I therefore would expect the dark matter to also leading the gas. I find that the dark matter in both cases are roughly where I expect, however have large uncertainties due to the high redshift nature of the cluster.

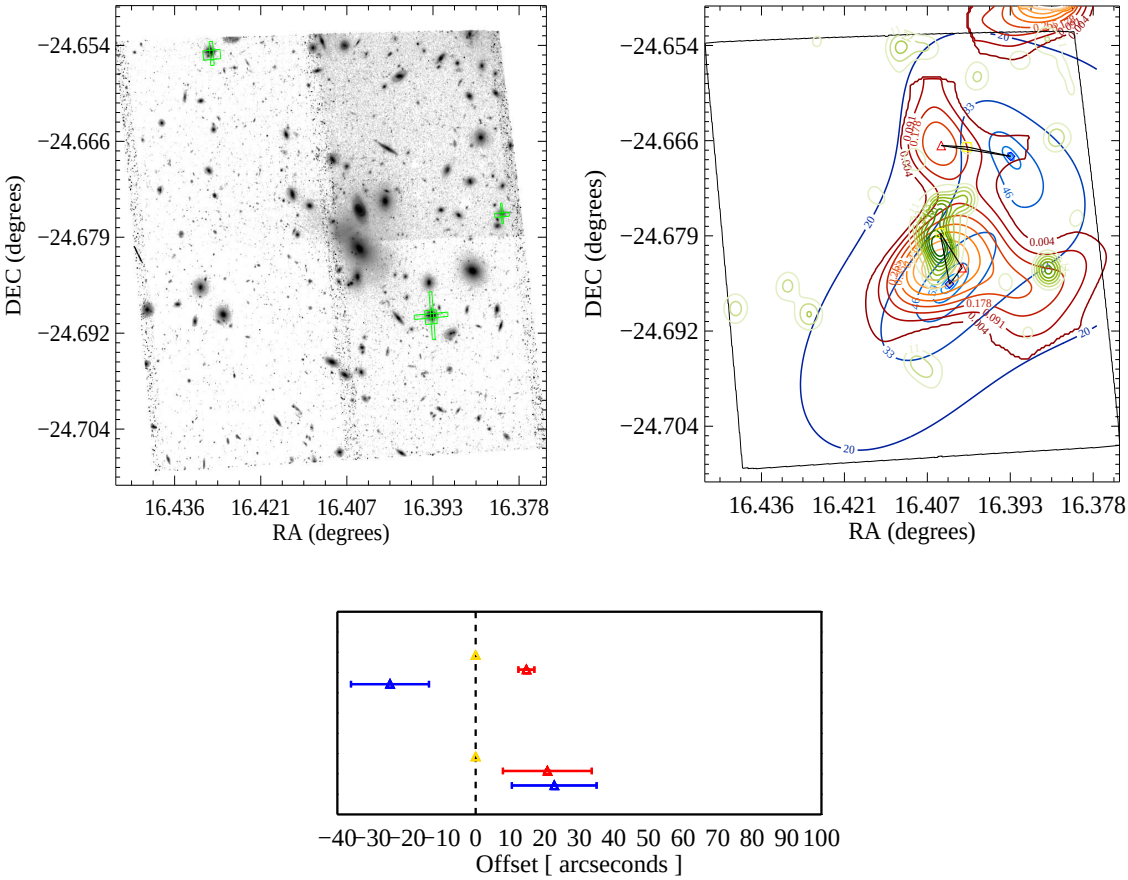

Figure 6.31: RXCJ0105

RXCJ0105

RXCJ0105 harbours a complex gas distribution, consisting of 3 haloes within the field of HST, and a second system to the north, implying some previous merging history that should be considered when interpreting this system. The edges of the northern system can be seen in the very north of Figure 6.31. The southern system covered by HST has three main regions, the central halo that consists of three large bright galaxies. The northern peak is resolved, however interestingly doesn't have any galaxies or dark matter associated with this region. I include this halo in the reconstruction and I find that the dark matter is coincident with the galaxy group to the west of this region. The large excess extending to the west of the main halo does seemingly harbour a group of galaxies, and the dark matter halo is well constrained. However, it is impossible to resolve a gas halo from the distribution, and thus I cannot include this halo in the sample.

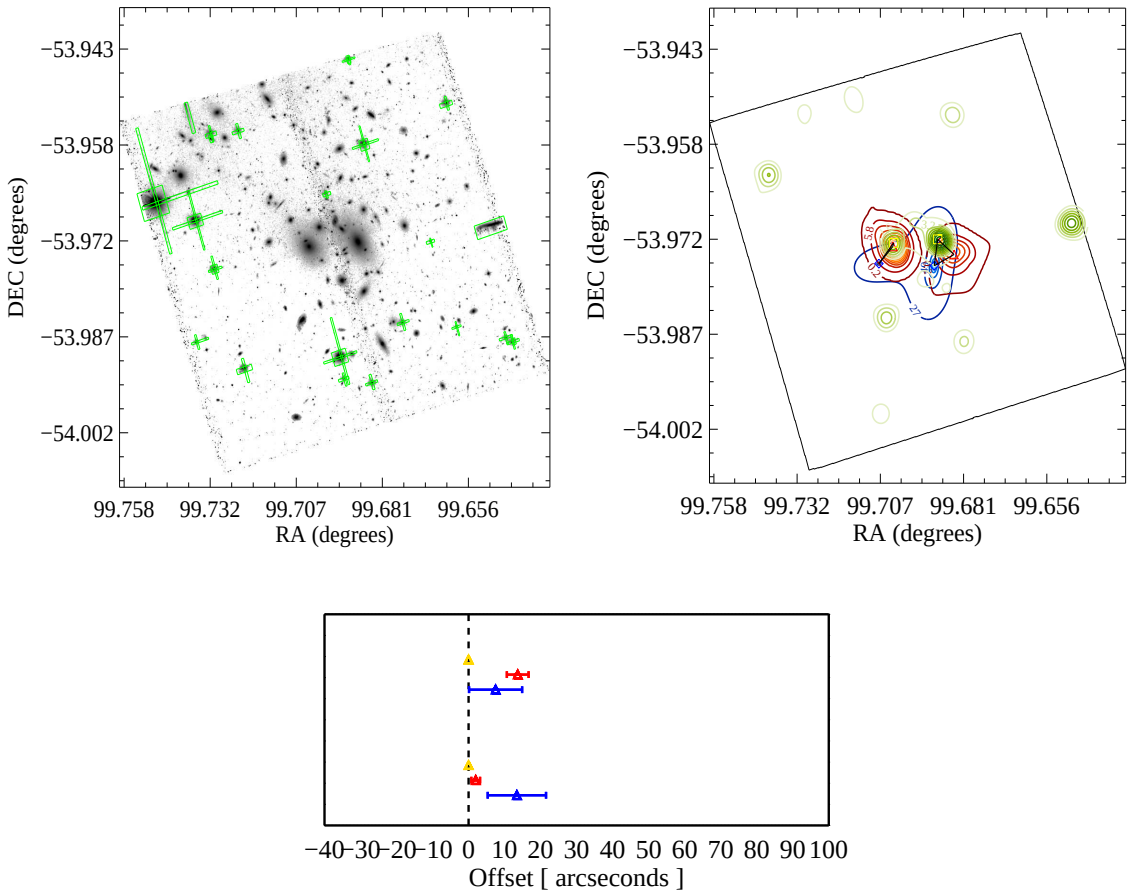

Figure 6.32: RXCJ0638

RXCJ0638

RXCJ0638 has a clear separation between two gas peaks, both of which have an associated large bright galaxy. This suggests that they are in in the process of merging, about to collide. I fit this system with two haloes, and find that both are constrained, however are forced away from one another. This could be systematic of the fact that weak lensing does not reconstruct the central core very well, or the system is in-fact one dark matter halo. The latter scenario is improbable since in order for a merger to produce a dark core, it would require a very high cross-section of dark matter (Kahlhoefer et al., 2014).

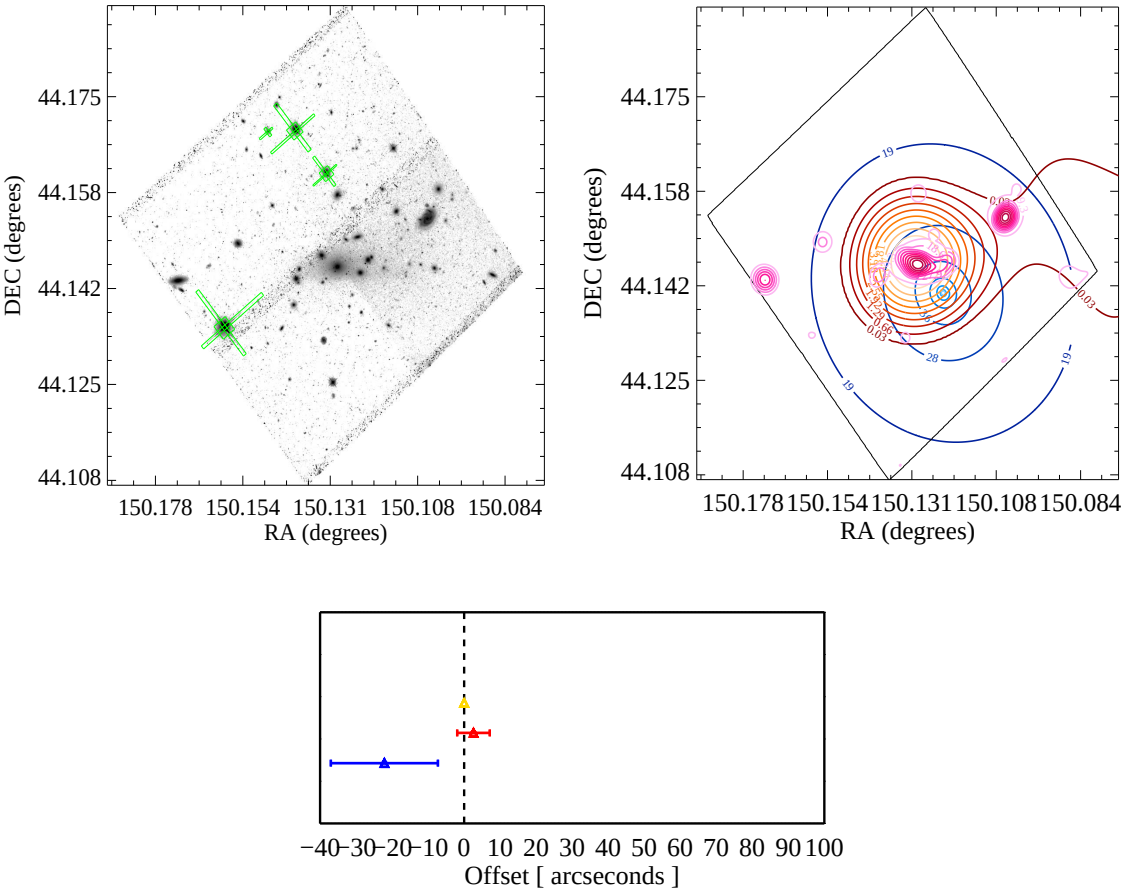

Figure 6.33: RXJ1000

RXJ1000

The Reflex cluster, RXJ1000 appears to have its associated gas halo aligned with the galaxies, suggesting dynamic equilibrium, however, the excess X-ray gas in the West of the region also suggests a previous merging event. Furthermore, the shape of the gas halo supports the hypothesis that this passed through a less dense cloud at some earlier time. The coincident gas and galaxy haloes could be either post-merger relaxation or a line of sight projection effect, and the halo is in-fact coming in or out of the page. Moreover the galaxy distribution appears to trail off towards to the secondary halo. This could be coincidence or caused by tidal striping during the merger.

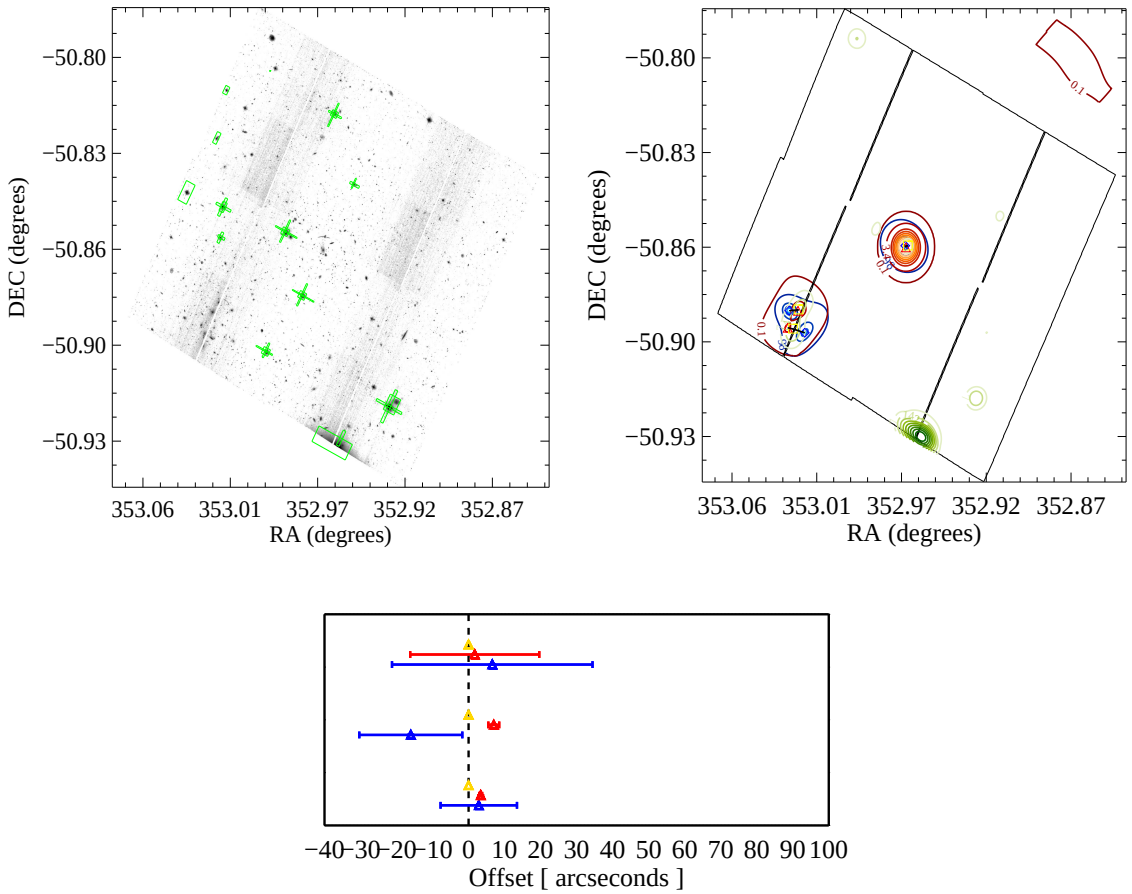

Figure 6.34: SPTCL2332

SPTCL2332

SPTCL2332 consists of one virialised halo and a multiple system halo to east. The eastern halo halo consists of two interacting systems, with bimodality observed in the optical, the X-ray and the weak lensing reconstruction. The positions of the dark matter are well constrained. It is not clear whether this system is post of pre merger, or if in-fact they merging at all and they are just accreting onto the main halo.

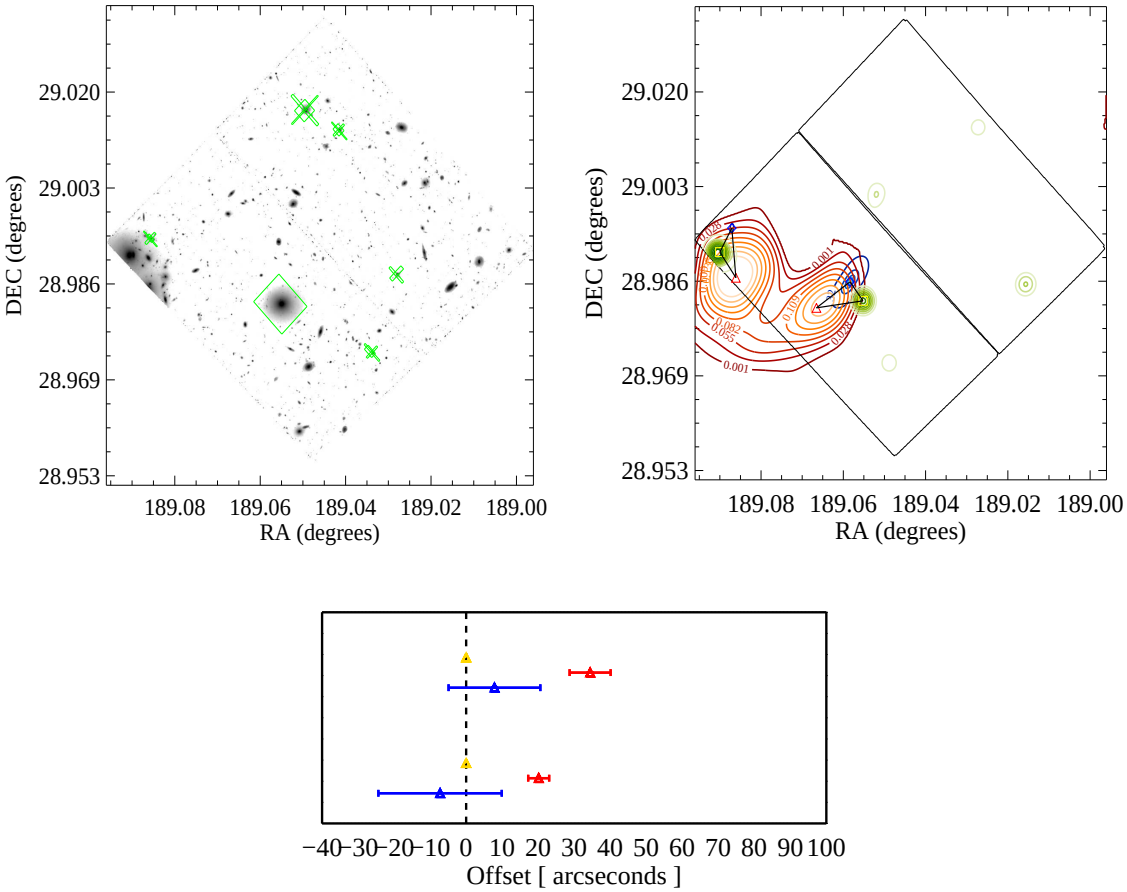

Figure 6.35: ZWCL1234

ZWCL1234

The merging cluster ZWCL1234, or the Burst Cluster, contains two haloes one that is near to the eastern edge of the field, and is coincident with its associated galaxy halo, and a westerly peak that is offset from the massive galaxy associated with this system. The morphology of this western halo is also indicative of an interacting gas halo, furthermore the lensing peak tends to lie coincident with the galaxy peak. However, the eastern peak, with overlapping gas and galaxy distributions, has an offset dark matter peak. This may be because the posterior to this dark matter peak is cut but the edge of the field, however the study by Dahle et al. (2013), which used VLT and HST data, shows that not only are the most massive galaxies are within the HST field (and hence not being biased), but their weak lensing peak is consistent with the one found in this study.

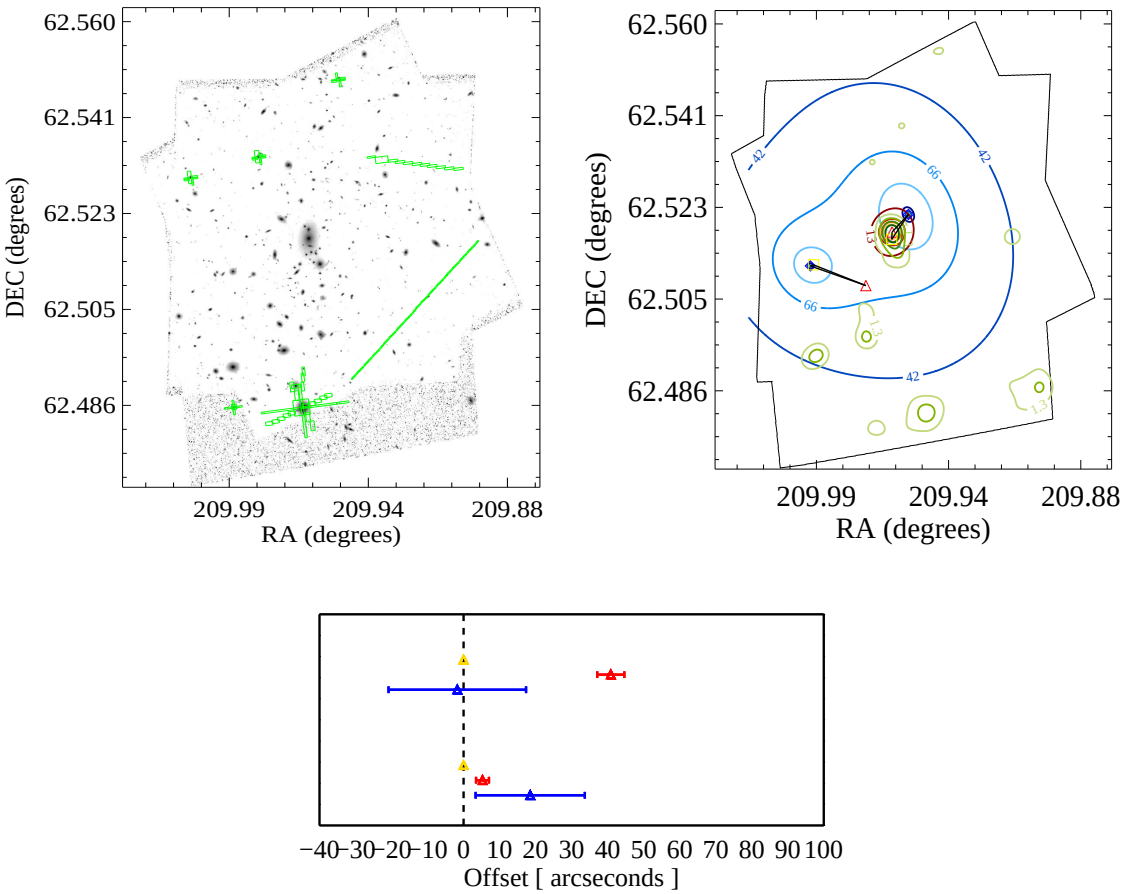

Figure 6.36: ZWCL1358

ZWCL1358

This seemingly virialised halo has a very faint excess of gas in the south of the field. This may be an extension of the gas distribution from the main halo, however the distribution of galaxies that lie close to it implies that in-fact supports evidence for a separated halo. Contrary to the previous assumptions on the dynamical state of this system, the dark matter reconstruction preferred the halo to lie to the east of this region. At this point there is clearly a large group of galaxies here. The consequences of this are a much more complicated merging system, and although this may be a result of the LENSTOOL sampler getting stuck in a local likelihood maxima, I note that I preferred not to introduce my own preconceptions of a cluster in the case where it is not obvious what is happening. I therefore chose to allow the dark matter halo to move this region in the field.

This system is a good example of how I associate the galaxies and iterate on the dark matter reconstruction. In this system the gas region to the south of the main halo is weak, so I place a large prior over this that incorporates the galaxies and the gas. I then associate the dark matter to the closest galaxies (which turn out to be a different system). I then re-run the dark matter reconstruction which is centred on this galaxy distribution.

6.4.2 Estimating errors in offsets

Figure 6.37 shows the combined offsets of the three mass components when projected on to the **SG** vector, from all the clusters. The red points represent the separation of the gas with its associated error, the blue the separation of the dark matter when projected on to this vector, and the green the position of the galaxies (always to be at 0). Figure 6.38 shows the collated offsets binned up, in order to show the distribution. Estimating the offsets between the positions of various mass components is relatively simple, however estimating the errors in these offsets is a non-trivial measurement. I initially estimate the local error for each cluster as laid out in Section 6.3 and propagate the errors on individual mass components through to error in the offsets. However, I find that although these errors appear to be a good estimate in a large proportion of the clusters, in some cases this fail drastically.

The "outliers" were clusters that had well constrained dark matter, gas and galaxy haloes, resulting in small errors, but their merging scenario was unclear, resulting in spurious signals from (potentially) mis-associated haloes. Examples of such clusters are A520 and A2744 (the westerly most peak). These spurious signals would then dominate when I combine the sample together to make a estimate of the mean offsets as weighted by the likelihood of that system. It seemed that in some specific cases the uncertainties were being underestimated.

In order to deal with this additional uncertainty associated with interpreting each merging scenario, I estimate a global error using the variance in the offset, $\delta_{\rm DI}$. In the event that the dark matter will lie along the vector **SG** (which on average I find to be true) the distance $\delta_{\rm GI}$, will inform me on the scatter due to all uncertainty within the system. However this itself will have some error (error in the error) since, for some clusters the lensing peak will randomly lie on the vector **SG**, and hence I will falsely up-weight this system. Using this variance

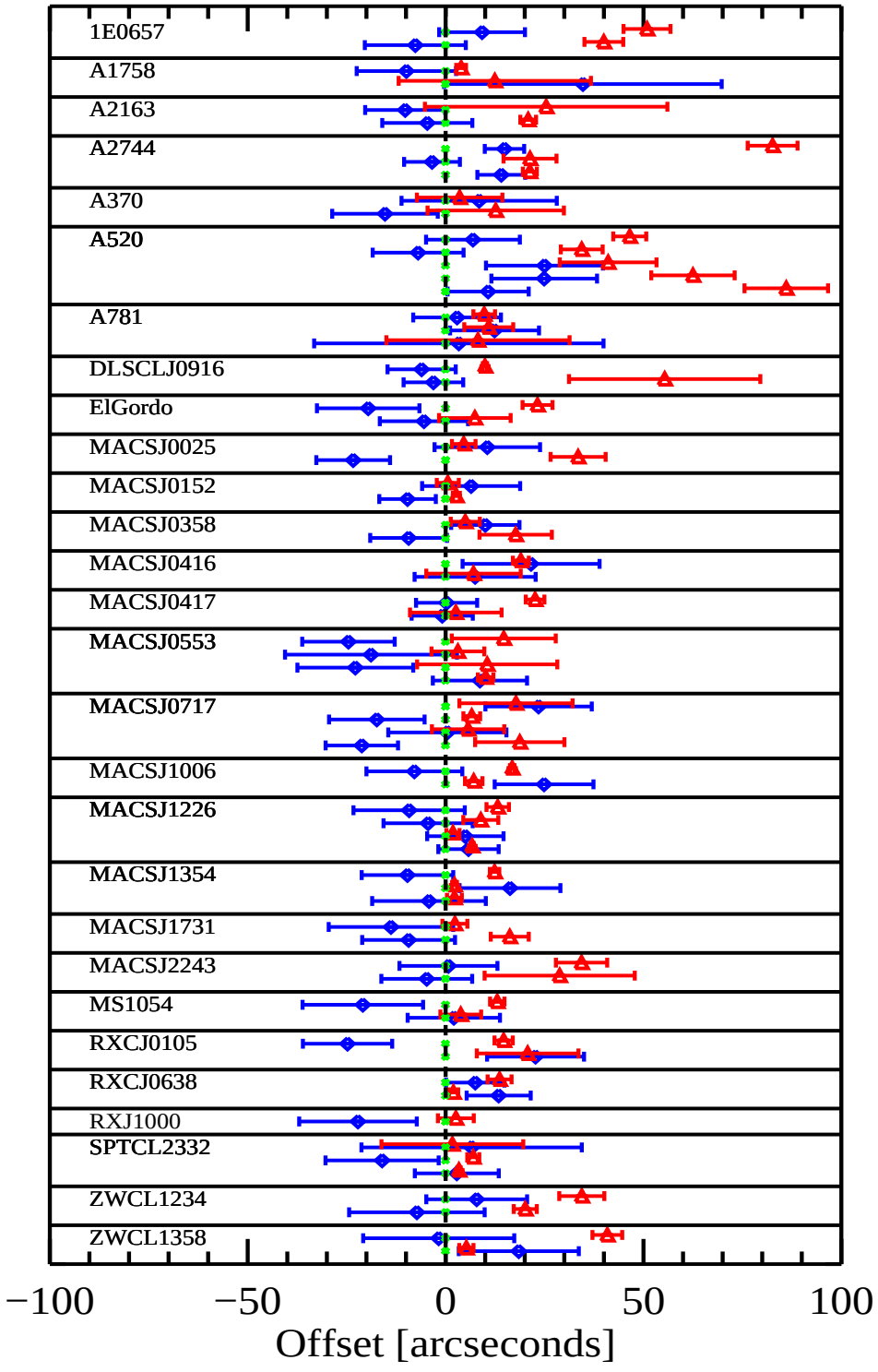

Figure 6.37: An overview of the 68 extracted merging haloes. In each case I show the magnitude separation between galaxies and gas, δ_{SG}, and associated error in red, and the separation of the dark matter with respect to the galaxies, projected onto the SG vector, δ_{SI} and associated error in blue. The error bars show the locally estimated errors.

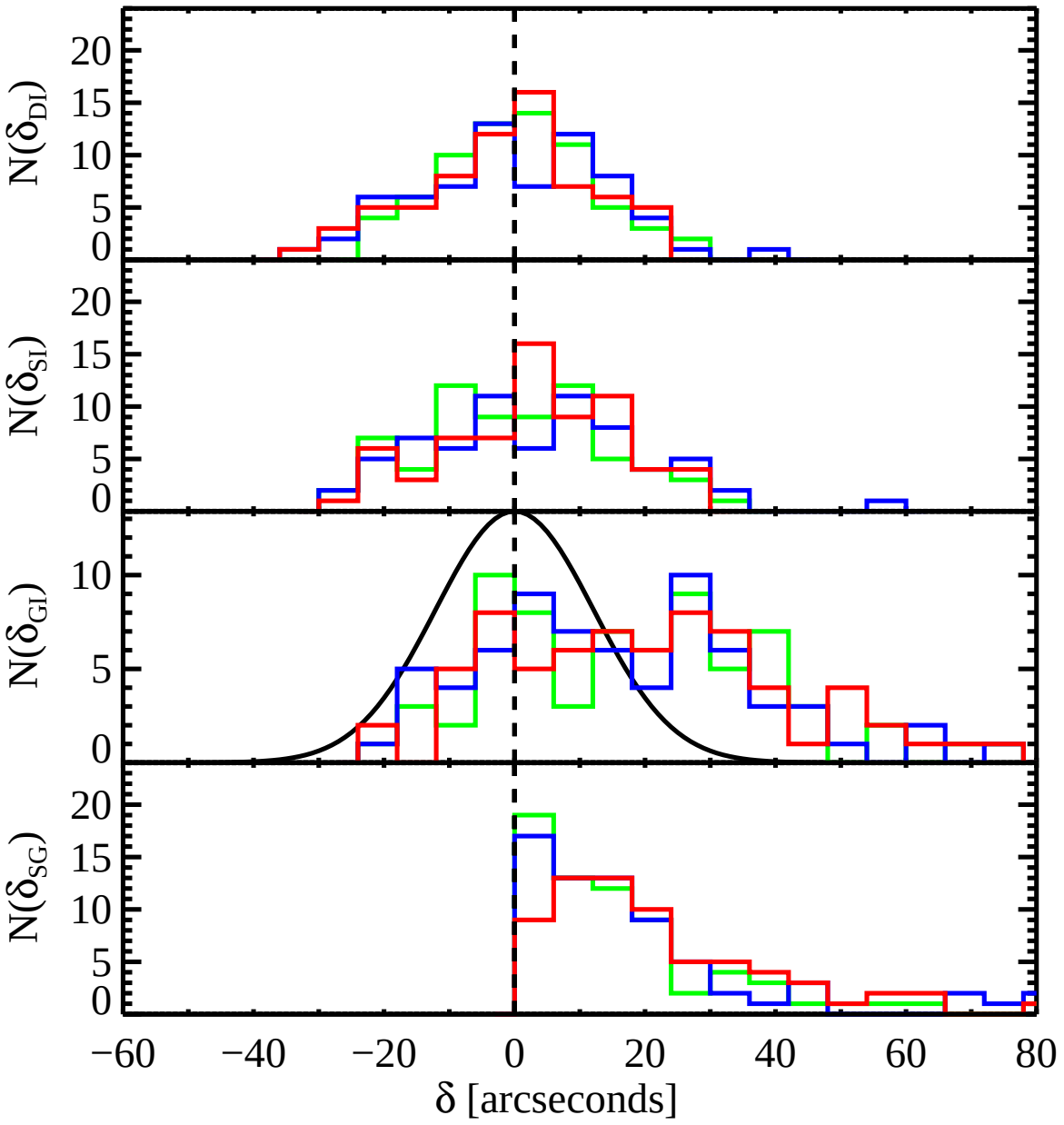

Figure 6.38: The distribution of each mass offset from the previous figure, binned to show overall distributions. From the top panel down, the panels show the distribution of $\delta_{\rm DI}$, $\delta_{\rm SI}$, $\delta_{\rm GI}$ and then finally $\delta_{\rm SG}$. The important panel here is the second panel as any noticeable offset will be evidence for interacting dark matter. The different colours represent the different proxies for the galaxy distribution. In green is the flux weighted number density. the red is the number weighted density and the blue is the BGG proxy.

is particularly attractive as it is sensitive to all three haloes in the system, and therefore provides a total uncertainty in the system and its merging scenario. I therefore make an estimate of the error over the entire sample and apply this error to the offsets i.e. $\sigma_{\rm SG} = \sigma_{\rm SI} = \sigma_{\rm GI} = \sigma_{\rm DI} \approx 11'' \approx 60$kpc. I can see that here the large uncertainty in the lensing peak will potentially overestimate the uncertainty in the error in $\delta_{\rm SG}$, since this is very well constrained, and therefore note that this handling of errors is a conservative method. Moreover, since I apply the same error to all offsets, I will apply roughly equal weights to each system and offset, thus not being dominated by a single unknown merging scenario.

6.4.3 Dark matter exists

Gravitational lensing measures the position of total mass, rather than that of just dark matter. In order to analyse the data I correct the measured offsets $\delta_{\rm SI}$ and $\delta_{\rm GI}$ for the contribution from the next most massive component. To calibrate this correction, I analyse mock lensing data from a dominant mass component (with an NFW profile) plus a less massive component at some offset δ. The corrections are always small but, for a subdominant component with the same profile, normalised to contain a fraction f of the total mass, I find that the lensing position is pulled by an amount

$$\Delta = f\delta e^{-0.01\delta}. \tag{6.3}$$

To test the hypothesis that dark matter *does not* exist, I require a model of the $\delta_{\rm GI}$ data expected if this were true. To generate that model, I assume the true positions of the X-ray and lensing signals coincide, but that the observed positions are offset by a random amount determined by the appropriate level noise in each (see Section 6.3). I calculate the 2D offset, then project this onto the direction to the stars, which is also selected at random. I could slightly increase the model $\delta_{\rm GI}$ offset to account for the mass in stars (the increase must be positive because the vector $\delta_{\rm SG}$ is defined from the galaxies to the gas). However, it is better to instead decrease the observed $\delta_{\rm GI}$ offset. The two approaches are equivalent in principle, but the latter allows information to be added to our analysis because the absolute value of $\delta_{\rm SG}$ is known in each system. To do so I use a value of $f = 0.03$ in equation (6.3) (Giodini et al., 2009b). When comparing the model

and observed $\delta_{\rm GI}$ offsets via a Kolmogorov-Smirnov test (in which I compute critical values using a Taylor series), I also use the errors on $\sigma_{\delta_{\rm GI}}$ determined for each system individually.

The third panel down in Figure 6.38 shows the distribution of the three galaxy tracers, in green, red and blue (flux, number and BGG) and the theoretical line that represents the expected $\delta_{\rm GI}$ signal in the case that dark matter does not exist in solid black. A Kolmogorov-Smirnov test to compare each histogram with the theoretical line indicates that the observed offsets between gas and mass are inconsistent with the null hypothesis at $1 - 1.5 \times 10^{13}$ or 7.4σ using the flux weighted galaxy tracer (without compensation for the mass of stars, this is 7.5σ). I also find that the null hypothesis is rejected at 7.7σ and 6.6σ for the number density and BGG galaxy tracer respectively. This test thus provides direct evidence for a dominant component of matter in the clusters that is not accounted for by the standard model components.

6.4.4 Removing line of sight projections with β

As I showed earlier in this this thesis it is possible to remove any inherent line of sight projections with β:

$$\beta \; = \; \frac{\delta_{SI}}{\delta_{SG}}. \tag{6.4}$$

Not only this but I showed that it can be physically related to the cross-section of dark matter. I therefore calculate β for each individual halo, and generate the PDF from the sample of β estimates (assuming Gaussian statistics). However this is currently a biased estimator of β since the lensing peak will have a non-zero contribution from the gas peak. Although I found in chapter 5 that the affect on β to be very small, these were using an order of magnitude smaller haloes. In this case, I am using minor and major mergers. I therefore calibrate the bias by estimating the systematic error in β using the functional form in equation (6.3) I found earlier from the simulations where $f = 0.16$ (Planck Collaboration et al., 2013a). Figure 6.39 shows the expected bias on β as a function of the distance the gas halo is from the dark matter peak.

Correcting for the bias, Figure 4.2 shows the constraints on the parameter β. I find that for two of the three galaxy proxies I find that $\beta = -0.04 \pm 0.07$ and

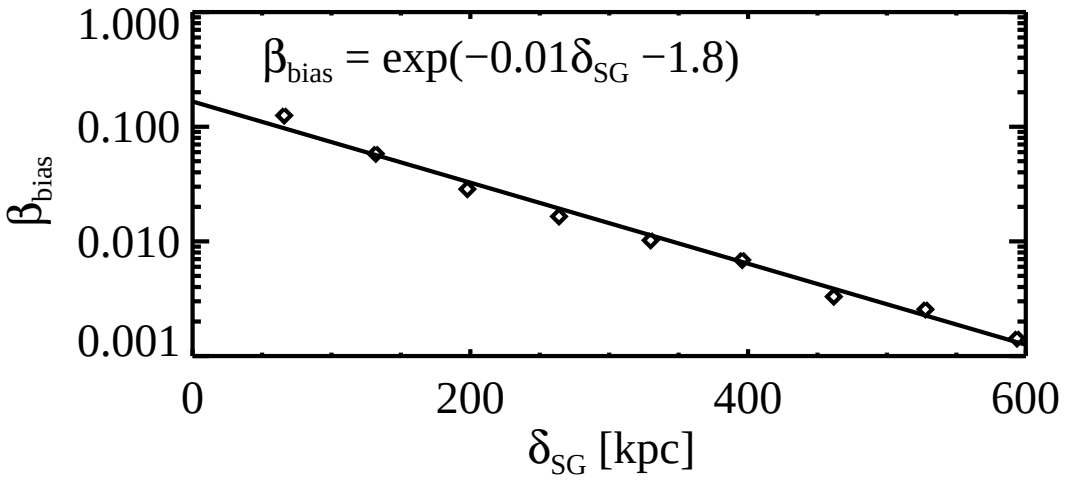

Figure 6.39: The expected bias on β caused by the gas halo shifting the estimated lensing peak, as a function of the distance the gas peak from the dark matter peak.

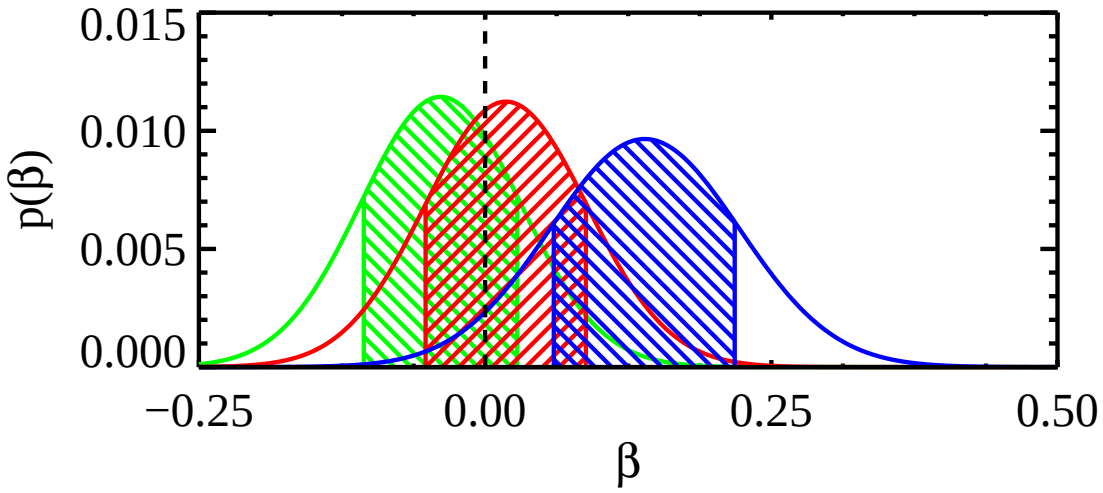

Figure 6.40: The probability distribution of β. Green represents the estimate using the flux weighted sample of galaxies, the red the number density and the blue to BGG. I observe a slight tendency for the dark matter to be offset from the BGG at the 1.8σ confidence level.

$\beta = 0.03 \pm 0.06$ for the flux weighted galaxy density and number density and is consistent with zero and collisionless dark matter, however the BGG proxy is offset by 1.85σ at $\beta = -0.15 \pm 0.08$, implying a potential offset between dark matter and galaxies. I address this potential offset in Section 6.5.

6.4.5 Cross-Section

In chapter 5, I showed that during in-fall, haloes separate due to their differing interaction properties, these separations equate to a effective cross-section. I showed that one could test for a dark matter interaction by measuring offsets between galaxies and the dark matter itself. This method would probe interactions that are highly angular dependent with the majority of scatterings occurring along the direction of motion. I found that the relation between the parameter β and the cross-section, $\sigma_{\rm DM}$ is:

$$\sigma_{\rm DM} = -\sigma^*_{\rm DM} \log(1 - \beta), \tag{6.5}$$

where $\sigma^*_{\rm DM}$ is dependent on the geometrical properties of the halo and is given by:

$$\sigma^*_{\rm DM} = \frac{\pi s^2}{M}, \tag{6.6}$$

where s is the size of the galaxy, and M is the mass. As an estimate of $\sigma_{\rm DM}$ for each halo will be noisy, because the estimate of $\sigma^\star_{\rm DM}$ will be noisy, I make a global estimate of $\sigma^\star_{\rm DM}$ from the sample. Assuming the Macciò et al. (2008) relation between the NFW concentration and mass of the halo, I determine the relationship between the scale radius of a halo, r_{200} and the mass, M_{200} and hence the relationship between mass and $\sigma^\star_{\rm DM}$. The top panel of 6.41 shows the values of $\sigma^*_{\rm DM}$ for different masses of haloes (M_{200}). Using the estimates from the flux weighted galaxy estimates, the bottom panel shows how various values of $\sigma^*_{\rm DM}$ (representative of the sample) affect $\sigma_{\rm DM}$. I find that the estimate of $\sigma_{\rm DM}$ is quite insensitive to what value of $\sigma^*_{\rm DM}$, I choose, and the width is also stable, varying from $\sigma_{\rm DM} = -0.23 \pm 0.6$ for a halo of $M = 10^{13} M_\odot$ to $\sigma_{\rm DM} = -0.1 \pm 0.28$ for a halo of $M = 10^{15}_\odot$, and that even in the most conservative estimate of the $\sigma^*_{\rm DM}$, the constraints are the current best in the literature, with the previous from Randall

Table 6.2: Mean results from initial analysis using flux

Galaxy Proxy	$\sigma_{\rm DM}$ [cm^2/g]	one-tailed (95% CL)	Statistical Sig
Flux	$-0.25^{+0.44}_{-0.41}$	< 0.50cm^2/g	0.57
Number	$0.20^{+0.49}_{-0.44}$	< 1.01cm^2/g	0.45
BGG	$1.04^{+0.67}_{-0.57}$	N/A	1.83

et al. (2008) of < 0.7cm^2/g.

Having seen that the error induced by $\sigma^*_{\rm DM}$ is negligible, I choose a value that well represents the sample and fold in the uncertainty in $\sigma^*_{\rm DM}$ in to the error in $\sigma_{\rm DM}$. Since many of the haloes in this sample are very large, I choose a conservative halo mass of $\log(M_{200}/M_\odot) = 14 \pm 1$, which equates to $\sigma^*_{\rm DM} = 6.5^{+3.0}_{-2.1}$cm^2/g. Folding the uncertainty in $\sigma^\star_{\rm DM}$ in to each estimation of the cross-section of dark matter I calculate $\sigma_{\rm DM}$ using equation (6.5) and present the resulting PDFs in Figure 6.42, where the green shows the flux weighted galaxy estimator, red shows the number density estimator and blue the brightest group galaxy estimator. I present the peak values with their one standard deviation error inTable 6.2.

From the three estimations of the cross-section of dark matter I find two consistent with zero with one-tailed upper limits of $\sigma_{\rm DM} < 0.50$cm^2/g and $\sigma_{\rm DM} < 0.93$cm^2/g (95% CL) for the flux weighted and number density respectfully. I find that the brightest group galaxy is offset from zero by $\sim 1.8\sigma$ implying a non-zero dark matter interaction cross-section of $1.04^{+0.69}_{-0.58}$cm^2/g.

6.5 Astrophysical Implications

I have seen from the analysis of the sample of galaxy clusters that the number density and flux density are consistent with collisionless dark matter, interestingly however, the results infer that the BGG tends to lead the dark matter during infall, a result that is also seen in Williams & Saha (2011). This can be seen in the second panel of Figure 6.38 where the mean of the blue distribution is shifted to the right. Figure 6.43 shows the system configuration as suggested by the results and although only to 1.8σ confidence, it is interesting to entertain some astrophysical interpretations of this.

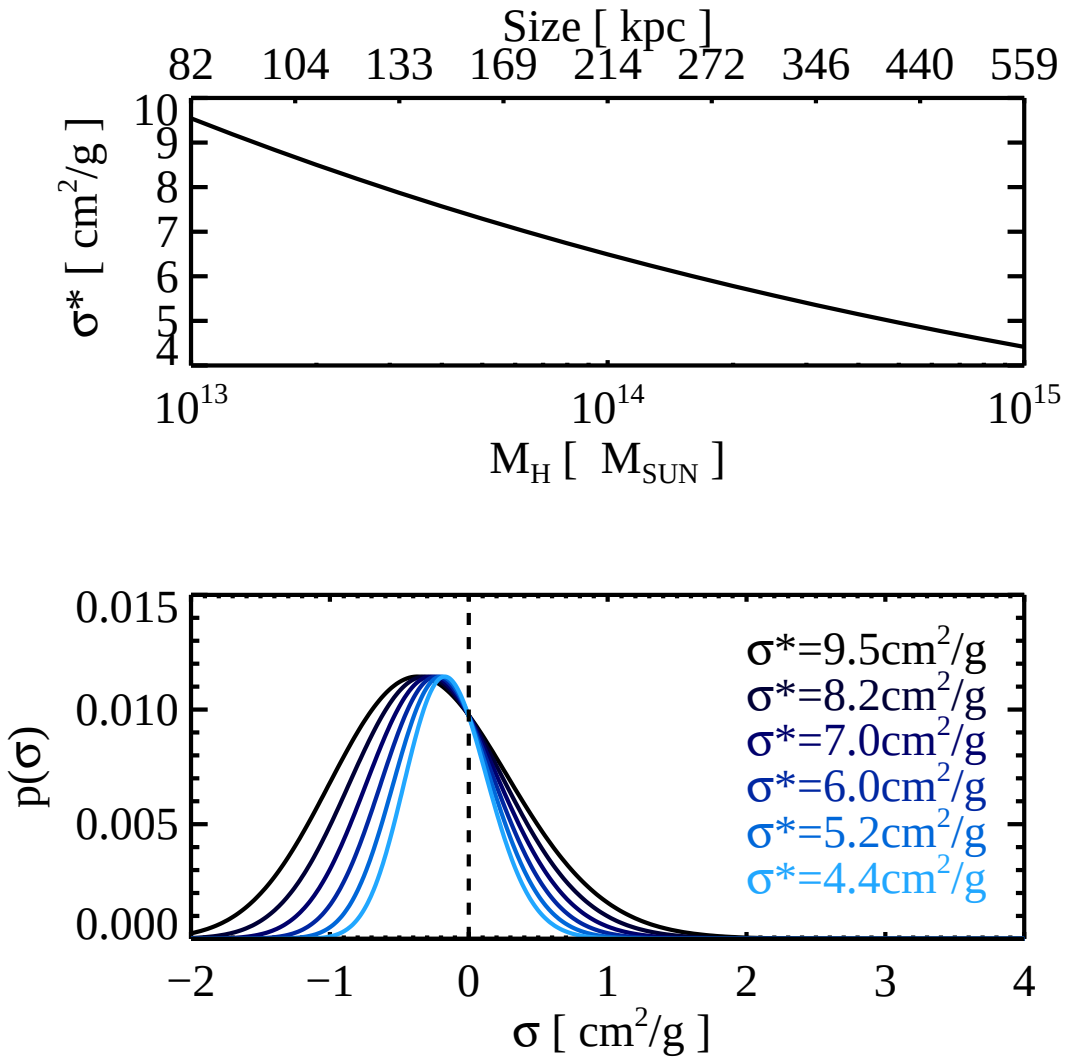

Figure 6.41: Here I test the affect of $\sigma^*_{\rm DM}$, on the estimation of the cross-section of dark matter. The top panel shows the corresponding values of $\sigma^*_{\rm DM}$ for different halo masses assuming a mass - concentration relation. The bottom panel shows how a few of those values affect the estimation of the cross-section. I find that the effect is not significant, and sub-dominant to the statistical error. For the final estimation I therefore use a value of $\sigma^*_{\rm DM} = 6.5{\rm cm}^2/{\rm g}$, corresponding to $M = 10^{14} M_\odot$.

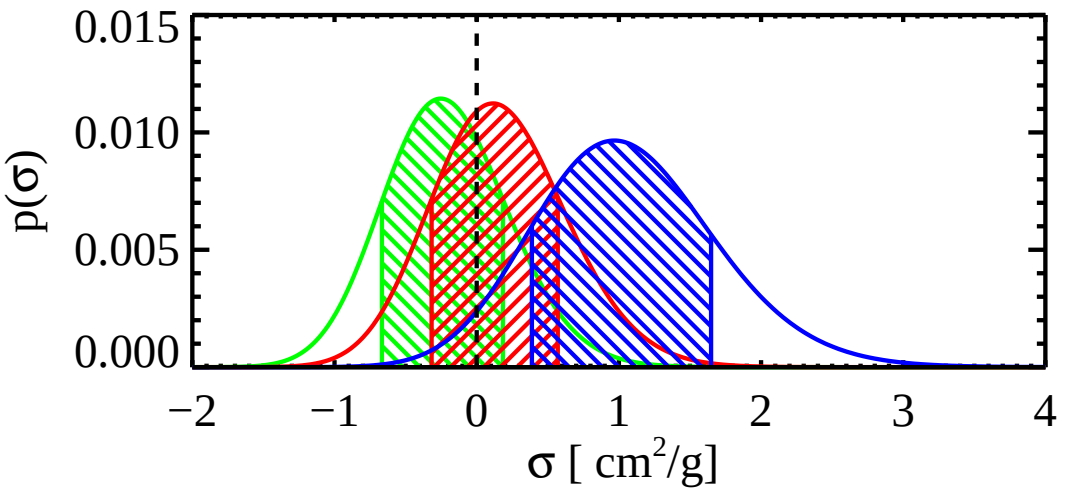

Figure 6.42: The PDFs for the cross-section of dark matter assuming $\sigma^*_{\rm DM} = 6.5 {\rm cm}^2/{\rm g}$. The green represents the PDF using the flux weighted estimator for the galaxy distribution, the red shows the PDF of the number density estimator and blue, the brightest group galaxy estimator.

6.5.1 Interpretation 1: Self-Interacting Dark Matter

During in-fall it is plausible to expect a galaxy distribution that is symmetric around a BGG, with some error. If it is true that the BGG is at the centre, those galaxies in the halo that precede the BGG will exhibit galaxy harassment, and potentially ram pressure stripping. This could lead to the distribution of galaxies being stripped on the leading edge and causing the positional estimate to shift backwards, thus not providing an accurate proxy for a collisionless particle. If indeed dark matter does interact often, with small amounts of momentum exchange, then the dark matter halo would also shift backwards, keeping the two distributions coincident. However, the BGG would not feel this tidal force (or at least much less) and continue on through the halo, acting truly collisionless. I would then observe the true signal of SIDM, and not a biased tracer from the distribution proxies. Interestingly, RXJ1000 (and Figure 6.4.1), as an example, represents this case nicely. Here were see that although the three components are peaked near the same area, the galaxy flux weighted distribution trails behind the system, and would therefore have a shifted estimated peak whereas the BGG estimate would not be biased backwards.

Interestingly this offset would provide evidence for a particular type of

scattering. As showed in K13, for an actual offset between dark matter and galaxies to exist the scattering needs to be highly angular dependent, with many scatterings occurring with small amounts of momentum exchange. Such a scattering model could imply a more exotic dark sector including dark photons (e.g. Berezhiani et al., 1996; Mohapatra et al., 2002; Hodges, 1993; Feng et al., 2009).

6.5.2 Interpretation 2: Bias of the BGG

During selection, I assume that the brightest group galaxy is the brightest galaxy within the dark matter prior used for the reconstruction. It is likely that the distribution of member galaxies will exceed this prior, and in the event that a very bright galaxy in a neighbouring halo falls within this prior, I could select a galaxy that is in-fact associated with a different halo, and not the one I am estimating. In this scenario this will cause me to preferentially select galaxies towards the other halo, and since I use this as the coordinate origin, will cause a bias in the cross-section.

6.5.3 Interpretation 3: Statistical Fluctuation

At 1.8σ confidence, this is only $\sim 93\%$ certain that this is a true signal, that is roughly 1/10 I would expect to be a random fluctuation. It is foreseeable that with future surveys and observations, this tension could be eased to become consistent with zero.

6.5.4 Interpretation 4: Unknown Astrophysical Process

It is plausible that in-fact during a merger those galaxies that precede the centre of the dark matter halo instigate star formation, and cause one of the leading galaxies to become brighter than the BGG. In this case, such a galaxy would be selected, and would preferentially leading the dark matter halo. Other possible explanations can be that of dynamical friction, as the dark matter falls in, it experiences gravitational drag from the surrounding environment and therefore pushes back naturally without cause for dark matter interactions. Finally the finite mass of the gas may pull the dark matter back as they separate. If each halo in question here were point masses this would not be a problem, however

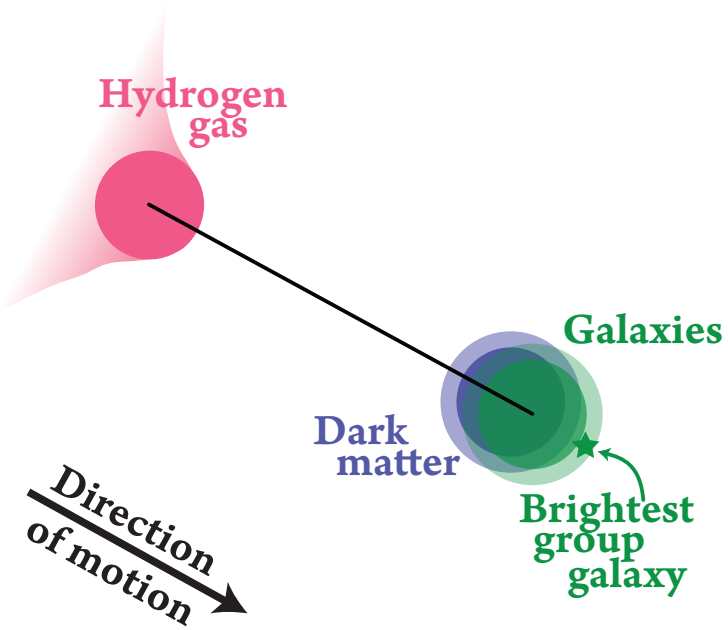

Figure 6.43: It seems that the two estimations of the distribution of galaxies is coincident with the dark matter, however the BGG seems to be slightly offset from the dark matter, with the non-baryonic component lagging behind the galaxy implying some non-zero dark matter cross-section.

since they are distributions of masses this could result in a finite separation of dark matter even if it did not interact. Such issues will need to be taken in account for future work.

It is clear from these results and the various possible scenarios that the astrophysics of the systems and the BGG in particular are very complicated and the simple modelling of this particular tracer may not be sufficient. Studies prior to this concerning the behaviour of the BGG in groups and cluster, both isolated and merging have shown that the BGG is not necessarily at the base of the potential, and is even not always the closest galaxy to the centre (e.g. Martel et al., 2014; Skibba et al., 2011), which could result in various biases in the case. To this end, although a very interesting finding I ignore this estimate and focus on the number and flux weighted estimators as these seem to be more reliable. I find that the flux weighted number density provides me with the strongest constraints on the self-interacting cross-section of dark matter at $\sigma_{\rm DM} = -0.19^{+0.43}_{-0.42}{\rm cm}^2/{\rm g}$, a significant improvement on the current best estimates of $\sigma_{\rm DM} < 0.7{\rm cm}^2/{\rm g}$ Randall et al. (2008).

6.6 Conclusions

I make the first multi-wavelength analysis of a sample of 30 merging galaxy clusters. In order to exploit the entire HST archive I adapt the RRG shape measurement pipeline, in conjunction with LENSTOOL to determine the positions of dark matter haloes in these merging groups. In order to map the highly ionised Hydrogen gas I utilise the Chandra Observatory and reduce and smooth using (amongst other *Ciao* tools) *Wavdetect*. I finally choose three different tracers to map out the stellar component of the cluster; the flux weighted number density, the number density and the brightest group galaxy (BGG).

From the 30 clusters in the sample I use 28 to construct 68 systems consisting of dark matter, gas and each of the galaxy tracers. I construct four different observables for the analysis; $\delta_{\rm SG}$ (the separation between galaxies and gas), $\delta_{\rm DI}$ (the separation between the dark matter and the point along the vector joint the stars and gas that is closest to the dark matter, the intersection point), $\delta_{\rm GI}$ (the separation between the gas and the intersection point), and $\delta_{\rm SI}$ (the separation between the galaxies and the intersection point).

By comparing the observed $\delta_{\rm GI}$ signal with the null hypothesis that all the mass in a cluster lies in the gas I measure a 7.4, 7.7 and 6.6σ that the major component of a merging cluster is an un-observable dark mass that is not a Standard Model particle (from the flux, number density and BGG galaxy tracers respectively) providing significant evidence for the existence of dark matter.

From the sample of 68 systems I construct the line of sight independent parameter, β, which measures the fraction that dark matter lies along the galaxy-gas vector ($\delta_{\rm SI}/\delta_{\rm SG}$). I gain the tightest constraints on the cross-section of dark matter from the flux weighted number density $\sigma_{\rm DM} = -0.25^{+0.44}_{-0.41}{\rm cm}^2/{\rm g}$ (two-tailed 68% CL), $< 0.50{\rm cm}^2/{\rm g}$ (one-tailed, 95%CL). This estimate is a factor of three better than the current best limits in the literature on any cross-section, and the first attempt to measure a cross-section that would imply a scattering that occured often with small amounts of momentum exchange. Also consistent with zero the number density tracer for galaxy distribution gives an estimate of $\sigma_{\rm DM} = 0.20^{+0.49}_{-0.44}{\rm cm}^2/{\rm g}$ (two-tailed 68% CL), $< 1.01{\rm cm}^2/{\rm g}$ (one-tailed, 95%CL).

I also find an offset between the BGG and the dark matter potential intimating a positive cross-section $\sigma_{\rm DM} = 1.04^{+0.67}_{-0.57}$ cm^2/g at the 1.8σ confidence level. This

offset between dark matter and the BGG has been seen previously in the study by Williams & Saha (2011). Although I interpret this as a positive cross-section, I am cautious in making assumptions on the behaviour of the BGG during a merger. I therefore clearly state that although tantalising evidence and definite grounds for further observations, I require increased understanding of the behaviour of galaxies during mergers to make a concrete statement about the interacting nature of dark matter.

Having made the most detailed study of interacting dark matter in galaxy clusters, I have not found conclusive evidence for interacting dark matter. However it is clear that merging clusters are a powerful tool to probe the properties of dark matter. the method is easily extendible for future surveys where I can see if the offset between dark matter and the BCG continues to grow in samples of clusters orders of magnitude than I have used here. It is plausible that future surveys will return order of ten thousand merging clusters returning statistical errors of $\pm 0.001 \mathrm{cm}^2/\mathrm{g}$, where systematics will be prevalent. It is important therefore to develop SIDM simulations alongside the data as the understanding of these environments will become vital in interpreting the observations.

7 Conclusions & Future Work

"For one change always leaves a dovetail into which another will fit."

In this thesis I have critically analysed the self-interacting dark matter (SIDM) paradigm. SIDM as a theory has the potential to solve the observed discrepancies and inconsistencies that currently exist between theory and observations. However as highlighted throughout this study, testing and interpreting SIDM is complicated, from making measurements, to their implications on the particle physics models.

Tests into SIDM have been carried out, however, each study has relied on either single clusters that have many unknown impact parameters and merging scenarios or halo sphericity that suffer from lack of sensitivity. In preliminary work it was proposed that the SIDM paradigm could be tested with cluster bulleticity, an idea that used accreting substructure experiencing bullet cluster effects. The main advantage of this technique is that clusters that are forming hierarchically, would harbour many sub-haloes, increasing the statistical sample of major merging events by an order of magnitude.

Detecting offsets between in-falling and merging haloes during cluster formation is an advantageous method to measuring the cross-section of dark matter. However, the initial study of cluster bulleticity predicted that a large detected

offset resulted in a very small measured signal and hence a new method was required. This led to introducing the stellar component as a probe for the direction of motion. By centering the co-ordinate system on the member galaxies such that they were the collisionless particle leading the way for the merger, we could calibrate the dark matter interaction cross-section by where it lay between the collisionless galaxies and the highly interacting baryonic gas. However in order to do this I would require a better theoretical understanding of the behaviour self interacting dark matter and sub halo in-fall.

In chapter 4 I carried out an analytical study of the forces acting on the three components of in-falling haloes; the galaxies, dark matter and gas. I constructed a simple mapping between the line of sight invariant quantity $\beta = \delta_{\rm SI}/\delta_{\rm SG}$, where $\delta_{\rm SI}$ is the distance the dark matter laid along the vector joining the centre of the galaxy distribution to the centre of the gas halo, $\delta_{\rm SG}$, to the cross-section of dark matter, $\sigma_{\rm DM}$. Conveniently time independent and directly relatable to $\sigma_{\rm DM}$, this method of constraining the cross-section of dark matter is also easily extendable to future surveys such as Euclid, where β can be stacked as it should be merger independent. Moreover, after considering the observational implications of an offset (and hence drag of a dark matter halo), I found that this method would be probing a particular type of scattering method, one where the interactions were over long distances, and highly angular dependent (such that scatterings occurred along the direction of motion). This meant that the method would be probing interactions that occurred often with little momentum exchange resulting in an overall shift in the haloes velocity, and hence giving large implications type of particle dark matter maybe.

Having constructed a new, convenient method to probe the cross-section of dark matter I examined its constraining power, testing on collisionless dark matter simulations. I found that with a sample of 30 galaxy clusters, with roughly two sub-haloes each (resulting in 60 stacked offsets), I would constrain $\Delta\beta \approx 0.1$ and $\Delta\sigma_{\rm DM} \approx 1{\rm cm}^2/{\rm g}$ and hence would be not only competitive with current constraints, but would not suffer from uncertainties in light of sight projections or time of in-fall.

In order to critically analyse the feasibility of such an idea and to test the implications of potential weak lensing systematics, I determined the accuracy in which dark matter substructure in galaxy clusters can be located. Accurately

estimating the positions of sub-haloes in galaxy clusters is important since any bias would lead to a bias in the estimate of the self interaction cross-section, $\sigma_{\rm DM}$. Moreover, understanding the behaviour of single point estimators of two dimensional likelihoods and determining which is the best estimator of the position of haloes, was equally important.

To carry out a feasibility test, I constructed simulated shear fields in the presence of a galaxy cluster using analytical, realistic density profiles. Using various different configurations I made the first estimate of how accurate the positions of sub haloes can be estimated in the presence of different noise contaminants. I found that the public LENSTOOL software can measure the position of individual $1.5 \times 10^{13} M_{\odot}$ peaks with $\sim 0.3''$ systematic bias. Any sub-haloes detected above this threshold will be real and only biased to $\sim 0.3''$. Moreover, I found that the maximum likelihood value of the 2 dimensional position likelihood surface is found to be the best point source estimator, being negligibly biased in the noise free case compared to the mean value estimator. I found that the dominant source of bias is caused by a preferred direction to the shape of galaxies introduced by an biased shape measurement algorithm. This gives me confidence since any estimate of the cross-section now will be using archival data which is randomly orientated (since it will be from many different observing runs).

From this initial study, I estimated that typical clusters will each have on average 1 in-falling groups of galaxies containing $\sim 10\%$ of their mass, and hence found that I will need between $20 - 50$ clusters to detect an offset between dark and baryonic matter. Although this method would need to be tested on full hydrodynamical simulations (containing a more complex distribution of mass) in parallel with real data to show that the displacement obtained from data is reliable, this vital preliminary work gave me confidence to pursue offsets as a technique in the measurement of the dark matter cross-section.

Although this study showed that roughly 50 clusters are required to detect an offset between baryonic matter and dark matter, I found that the predicted signal to constrain SIDM ($\approx 2h^{-1}$kpc),was inaccessible by current data archives. Moreover, to make any estimate of the cross-section of dark matter I would require simulations to calibrate any cross-section. It was clear that in order to exploit the magnitude offset of $\approx 18h^{-1}$kpc, I would require extra information from the

stellar material in galaxy clusters.

Having systematically tested the reliability and robustness of LENSTOOL and developed a technique to constrain the cross-section of dark matter directly from observations, I made a full analysis of a sample of merging galaxy clusters where both Hubble Space Telescope and Chandra X-ray Observatory archival data exists. Developing a unique pipeline that measure the shapes of galaxies to estimate the position of haloes and sub-haloes in clusters, and smooth optical and X-ray emission to estimate the distribution of stellar and baryonic gas I measured the separation of mass components in 68 merging systems. From these 68 merging systems I followed the analysis technique previously developed in order to place the tightest constraints of the cross-section of dark matter of $\sigma_{\rm DM} < 0.50 {\rm cm}^2/{\rm g}$ (tailed 95% CL). This estimate used the flux weighted number density of galaxies as a tracer for the stellar component, which also found in a two-tailed probability that $\sigma_{\rm DM} = -0.25^{+0.44}_{-0.41} {\rm cm}^2/{\rm g}$. By repeating the same analysis however using the number density of galaxies instead of the flux weighted, I found that $\sigma_{\rm DM} = 0.20^{+0.49}_{-0.44} {\rm cm}^2/{\rm g}$ (two-tailed, 68% CL) and $\sigma_{\rm DM} < 1.01 {\rm cm}^2/{\rm g}$ (one-tailed 95% CL). Interestingly I found that the brightest group galaxy (BGG) leads the dark matter, and in-fact implies some finite cross-section of $\sigma_{\rm DM} = 1.04^{+0.67}_{-0.57} {\rm cm}^2/{\rm g}$. The reason for this is unknown, however the physics of BGGs is complicated, and this could represent a bias (and not interacting dark matter) and could have insights into galaxy formation during mergers. However, it does highlight the need to understand the formation and dynamics of haloes during mergers and in-fall. Effects such as dynamical friction and drag caused by distribution of baryonic gas in the halo both can induce a finite displacement of dark matter even if dark matter is collisionless. For future surveys where the constraints will be sensitive enough to resolve such effects, simulations will be required to calibrate any detection.

An advantage of such a technique laid out here is that it is trivially extended to large surveys. The future is expecting the advent of a new age of data where by telescopes are providing the deepest and widest coverage of the sky. The surveys carried out with telescopes such as EUCLID (Laureijs et al., 2011), LSST (Ivezic et al., 2008), WFIRST (Spergel et al., 2013) and new X-ray Observtaory, Athena (Barret et al., 2013), will bring orders of magnitude more merging systems. In this case it will be impossible to simulate and study each cluster to the accuracy that

currently exists in the literature. Methods such as these that can extract haloes from their individual environments and treat them as individual merging systems, and measure a stackable parameter such as β will be vital in efforts to understand the nature of dark matter. In this study I have acquired the largest sample of 68 merging clusters resulting in errors of $\approx 0.5\text{cm}^2/\text{g}$, however if statistically I increase the number of haloes in a survey by $10,000$ then the statistical errors will reach $\Delta\sigma_{\text{DM}} \approx 0.001\text{cm}^2/\text{g}$, where the affect of SIDM will have no observable affect on structure formation, but will however still have large implications for the nature of dark matter.

In order to attain the potential level of accuracy accessible by future experiments it will be vitally important to understand and control systematics. These systematics will vary from theoretical limitations to software limitations. In a survey where the sky is systematically observed, and coherent shape measurement will be made, any bias will impact any estimate. I showed earlier that the dominant source of contamination on an estimate is bias in the shape measurement technique. It is clear therefore that we must improve shape measurement algorithms for the future experiments. How algorithms are developed to improve the accuracy and precision are widespread. We saw in this thesis that competitions such as GREAT and STEP challenges are a fruitful approach. In my thesis I carried a similar experiment where I attempted to exploit citizen science as a method to improve algorithm quality. I set up a weak gravitational lensing competition with the company Kaggle[1], which exploits expert crowd sourcing, in an attempt to improve mass reconstruction algorithms. The results and set-up of this competition are laid out in Appendix A where we show that the crowd can improve on current state-of-the-art algorithms, however, such approaches also have their drawbacks.

Shape measurement and observational analysis aside it is equally important to continue theoretical work on self-interactions and how these correspond to the observations we make. At the time of writing this thesis, the model laid out here is the most sophisticated analytical method to derive the cross-section of dark matter. However in order to fully exploit future surveys, a better method that does not require conservative assumptions on the gas fraction or shape of the halo will be required. The only way this will be done is with accurate simulations of

[1] `www.kaggle.com`

interacting dark matter. However, the current level of such simulations is limited, with most simulating hard-sphere interactions. In order to understand how haloes can separate in cluster mergers, increasingly sophisticated scattering mechanisms will need to be tested. Only then will it possible to make accurate conclusions on the interacting nature of dark matter. In this study I have shown that with a small sample of galaxy clusters it is possible to make more reliable estimates of the cross-section of dark matter. However, theoretically, improvements need to be made in order to fully exploit future experiments.

It still remains an unanswered question of what dark matter is, and any detection of self-finteraction will have dramatic implications for the probable particle physics models. The technique here can be used on future surveys and for now presents the tightest constraints to-date, inferring that dark matter is indeed collisionless. However with the advent of future surveys, and the improvement of a theoretical framework, we will be able to probe deeply the particle properties of dark matter and finally untangle the mystery of exactly what it is.

A Observing Dark Worlds: A crowdsourcing experiment for dark matter mapping

"The first method for estimating the intelligence of a ruler is to look at the men he has around him."

A.1 Introduction

In this thesis we have shown how gravitational lensing can be used as a tool to probe the distribution of dark matter in galaxy clusters, and thus constrain its interaction properties. In this appendix we will focus on an innovative method to develop techniques which use weak gravitational lensing as a probe of the dark matter distribution. We have seen in Chapter 1 that there are many different methods to reconstruct the lensing potential and in Chapter 2, how that method determines the feasibility of methods such as that in Massey et al. (2011).

In this appendix we will present the analysis of simulated weak lensing data around simulated galaxy clusters. The analysis of these simulations, in an effort to improve the algorithms that are used to infer the mass distribution from weak lensing data, were used to define a citizen science competition that was crowdsourced to the public.

A.1.1 Standard approaches to dark matter reconstruction

The fidelity with which algorithms are required to map the dark matter distribution in galaxy clusters depends on the range of scales in question. Although it is possible to map the distribution of matter using galaxy velocities it has become increasingly popular to use gravitational lensing to determine the total matter distribution. There are several approaches that have been developed within the field of weak lensing where algorithms are split mainly into two categories based on the type of model used:

- Parametric methods involve fitting a physical model to the data and constraining a number of parameters in that model.

- Non-parametric methods attempt to directly convert from the measured shear to some projected mass density.

For a recent review of the standard approaches see Jullo et al. (2013).

Throughout this appendix we shall refer to the benchmark code LENSTOOL. LENSTOOL (Jullo et al., 2007) is a public strong and weak lensing gravitational mass reconstruction method that fits dark matter haloes, parameterised by a parametric radial profile, to data and determines posterior probabilities for the parameters via a Bayesian sampling method. For a full description of how LENSTOOL works please see Jullo et al. (2007), however, simply, it works by:

1. Taking a user input number of haloes, which have with them the desired halo profile and associated parameters (e.g. mass, position etc.)

2. It then selects a random sample of parameters from within the priors given by the user and then converts the data, which are the shapes galaxies in the image plane, back to the source plane, undoing the lensing effect caused by the sampled dark matter halo.

3. These unlensed galaxies should represent the intrinsic shape of the galaxy which will be drawn from an assumed Gaussian distribution with a mean of zero and variance also given by the user. Using a chi-square test it then finds how well the parameters which converted the galaxies to the source plane did at recovering the expected intrinsic ellipticity distribution.

4. It then resamples the posterior depending on the likelihood of the next parameter set chosen.

5. It will continue to build up a representation of the posterior surface, over a predetermined number of samples.

6. 10 simultaneous sampling chains are run, each with 1000 samples, in order to avoid local maxima, after which the maximum likelihood position is chosen and selected as the estimate for the position of the halo.

Given 50″ priors (not applied to this competition), Harvey et al. (2013a) found that the accuracy of LENSTOOL is roughly $\sim 10''$ for a halo of mass $\sim 10^{13} M_{\odot}$, and is robust to most potential systematics involved in parametric fitting. This code was run on the competition and presented in this appendix in order to provide benchmark analysis on individual scores.

A.1.2 Expert citizen science

Citizen science has recently become a productive tool in the analysis of large complicated databases for which algorithms are unable to provide reliable results. Pioneering this work in science is the Zooinverse[1]. The Zooniverse is a database of various projects including (amongst others), Moon craters, whale sounds and galaxies. In each case, a sample of images/sounds or other data is presented to a user (a 'citizen'), who is then guided through steps to classify that sample into a particular category based on their personal judgement. In many cases, such as the identification of complex galaxy morphologies, human-based classification is more reliable than current automated algorithms. The science is achieved through the statistical analysis of the human-classified data sets.

The success of using humans to classify large databases of complicated objects relies on the number of humans doing the classification to be large, to avoid individual subjectivity (although there are common inter-subjective biases in human object recognition that need to be found and quantified). There are many advantages of using a large population to solve a classification problem (i.e. 'crowdsourcing'). However there are two regimes in which the human-classification mode of crowdsourcing a problem is limited:

[1] `https://www.zooniverse.org`

- When the dataset, or the number of classification categories, becomes too large for a population of humans to analyses in a reasonable time period. An example would be a database of several billion astronomical objects, each of which needed many minutes of classification.

- When the precision required for a measurement is very high. An example would be in weak lensing measurements where the accuracy required is sub-percent in the bias of ellipticity measurements of galaxies.

In these regimes algorithms are required to analyse the data. However the crowd can still be used, but in a different mode: instead of classifying, the crowd can be asked to write computer algorithms to solve the task at hand. In this regime one needs to set the problem to a targeted group of computer programming literate individuals or teams, with sufficient motivation (either in the form of a prize for writing the best algorithm or other), and with a clearly defined objective measure for what is meant by the best algorithm, i.e. a metric for success. The algorithm-writing mode of crowdsourcing in astronomy has only recently been utilised for example in a competition (Kitching et al., 2012b), in partnership with Kaggle[2], where the problem of weak lensing shape measurement was set to the public (see also Bridle et al. (2010); Kitching et al. (2012a); Mandelbaum et al. (2013); Heymans et al. (2006); Massey et al. (2007a) for more complex challenges in the same area). This initial competition called 'Mapping Dark Matter', outlined the potential that competitive crowdsourcing may have for astronomy. They found they could make a factor of 3 improvement on high signal-to-noise galaxies over previously published results in only 2 months. With new astronomical surveys on the horizon that will require increasingly sophisticated algorithms, expert crowdsourcing, such as Kaggle is an innovative way to utilise expertise that may not exist in astronomy. To this end we decided to crowdsource the problem of dark matter reconstruction in galaxy clusters to the expert public.

In this appendix we present the results of crowdsourcing the problem of using weak lensing measurement to create maps of the dark matter distribution around galaxy clusters. 'Observing Dark Worlds' was a competition in partnership with Kaggle, whereby we asked participants to reconstruct the positions of simulated dark matter haloes in fields of galaxies. By varying the parameters of the fields,

[2] `http://www.kaggle.com`

such as the mass and the galaxy density, we aimed to probe the sensitivity and behaviour of the reconstruction algorithms. In a bid to develop an algorithm that was systematically unbiased and statistically precise, we supplied 120 clusters ranging in mass from the group scale ($10^{13} M_{\odot}$) to super-cluster scale ($10^{15} M_{\odot}$).

This appendix is organised as follows, in Section A.2 we will outline the premise of the competition, including a description of the data provided to participants. In Section A.3 we present our results. Section A.4 gives a detailed description of the winning three algorithms and in Section A.6 make our conclusions.

A.2 Observing Dark Worlds

Determining the distribution of dark matter in galaxy clusters has generally been focused on how well one can reproduce the macroscopic properties of dark matter including the mass and concentration parameter (Bradač et al., 2005; Cacciato et al., 2006; Diego et al., 2007; Merten et al., 2009) . Massey et al. (2011) and later Harvey et al. (2013b), developed a method to constrain the self-interaction cross-section of dark matter using the position of dark matter substructure. In order to avoid systematic errors, this technique required accurate estimation of substructure and systematic errors to be $< 0.5''$ (Harvey et al., 2013a). Any biased estimate of position of galaxies would result in a spurious constraint of SIDM. With this in mind our aim for the competition 'Observing Dark Worlds' (ODW) was to encourage the development of new algorithms to reconstruct the position of dark matter haloes in galaxy clusters with a systematic bias $< 0.5''$.

A.2.1 The Competition

In order to achieve our competition aim, we required competitors to reconstruct the positions of dark matter haloes in a number of simulated galaxy clusters with varying parameters. We provided users with data to 'train' on and a test set on which they submitted blind answers. Participants had two months to improve their algorithms and make submissions to the Kaggle website. After two months, on the proviso that they provided the correct documentation concerning their algorithm, the top three participants received a reward: in the case of ODW this

was generously provided by Winton Capital Management[3].

A.2.2 The Data

The competition consisted of three different types of data sets (this is similar for the majority of Kaggle competitions);

Training Set: The set on which users could train their algorithms. Users had access to the galaxy catalogues that included positions and ellipticities in the field **and** the true positions of each dark matter halo.

Public Test Set: The set on which users were tested. They had access to catalogues of galaxies which contained positions and ellipticities, however the positions of the dark matter haloes were unknown. Users had to submit their predictions to the Kaggle website and were scored according to some metric (see section A.2.3) and the result published on a leaderboard. However the final results *were not* based on these results.

Private Test Set: Similar to the public test set, users were required to submit predictions for the positions of the dark matter haloes in these fields, however they did *not* receive any feedback on their score via the live leaderboard. These scores were kept secret (private) until the competition finished at which point they were revealed and the final result was be based on these. This is designed to prevent people over-fitting to the data. Note that competitors did not know which galaxy clusters were in the private or public test set.

Typical training sets supplied for machine learning problems usually incorporate a large number of training samples (many more than the test sets), from which a computer program can 'learn', and then a test set for which competitors have to submit their predictions to a blind sample. However such training sets may not be possible in real world astronomical situations. In the decision for the set size for the training and test we considered;

- What sized data set well reflects what one would see in real observational data?

[3] `https://www.wintoncapital.com`

- Do you want to place emphasis on quick accurate algorithms, or complex precise algorithms?

The latter was an important factor when we considered the sample size since we did not want to limit the complexity/run-time of algorithms. Currently LENSTOOL takes $\sim$ 30minutes/cluster, which is acceptable for samples of ~ 100 clusters (on a current machine). The number of clusters that one asked users to use was inevitably going to affect the type of algorithm submitted throughout the competition. Moreover, the properties of the clusters themselves affected the set sizes since if one requested many haloes per cluster then one was requiring users to constrain many more parameters. In addition, small mass haloes (or a high un-sheared/intrinsic ellipticity noise), which are harder to constrain, may require many likelihood evaluations during fitting. We therefore considered; the number of dark matter haloes in each cluster, the properties of the haloes in each cluster including; mass, profile, shape and concentration and their distribution in the field, the number of background lensed galaxies per cluster and the noise on the galaxies. Taking this also into account we choose the following set of parameters:

- 360 training haloes and 120 test clusters, of which three quarters are the private test set and one quarter is the public test set. This reflected the number of clusters one may expect to get with the Hubble archive and would allow competitors to develop methods that were of similar speed to LENSTOOL.

- For each set exactly one third of the clusters have one, two and three haloes in them and are randomly distributed in the field.

- Each cluster has one main halo which has a mass randomly chosen between $1 - 10 \times 10^{14} M_{\odot}$. Where there is greater than one halo in the cluster the second (and third) halo mass is randomly selected between $1 - 10 \times 10^{13} M_{\odot}$ imitating an in-falling galaxy group.

- To reflect the field of view and depth of the Hubble Space Telescope and the typical intrinsic ellipticity from the COSMOS field (Leauthaud et al., 2007a), we randomly select the source galaxy density between $30 - 80$ galaxies/arcmin^2 and apply a intrinsic ellipticity with a mean, $\langle \epsilon_{\rm int} \rangle = 0$ and a dispersion, $\sigma_{\epsilon} = 0.3$ and place them randomly in a field of 3×3 arcminutes.

Data Set Parameters	
# Clusters [Training, Public, Private]	[360, 30, 90]
1 Halo [Training, Public, Private]	[120, 10, 30]
2 Halo [Training, Public, Private]	[120, 10, 30]
3 Halo [Training, Public, Private]	[120, 10, 30]
NFW [Training, Public, Private]	[180, 15, 45]
SIS [Training, Public, Private]	[180, 15, 45]
1st Halo Ellipticity	[0, 0.3]
1st Halo Mass	$[1-10]\times 10^{14} M_{\odot}$
2nd Halo Mass	$[1-10]\times 10^{13} M_{\odot}$
3rd Halo Mass	$[1-10]\times 10^{13} M_{\odot}$
Intrinsic ellipticity dispersion	0.3
Galaxy Density	[30-80] galaxies/arcmin^2
Field of View	3×3 arc minutes

Table A.1: The parameters used for the data sets provided for the "Observing Dark Worlds" competition.

- We randomly chose half the haloes to have a single isothermal sphere density profile (SIS), and the other half to have a Navarro, Frenk and White profile (hereafter NFW, Navarro et al. 1997).
- Finally, we told the competitors exactly how many haloes were in each field.

This is shown in more detail in Table A.2.2 and an example sky (Training Sky 233) is shown in Figure A.1

A.2.3 The Metric

One of the most important aspects of a competition such as ODW is how one measures the success of an algorithm. A good metric should accurately reflect how well an algorithm is doing at achieving the aims which you have set. The consequences of this are that it rewards and penalises aspects of the problem that you are interested, and not interested in, respectively. Specifically in the

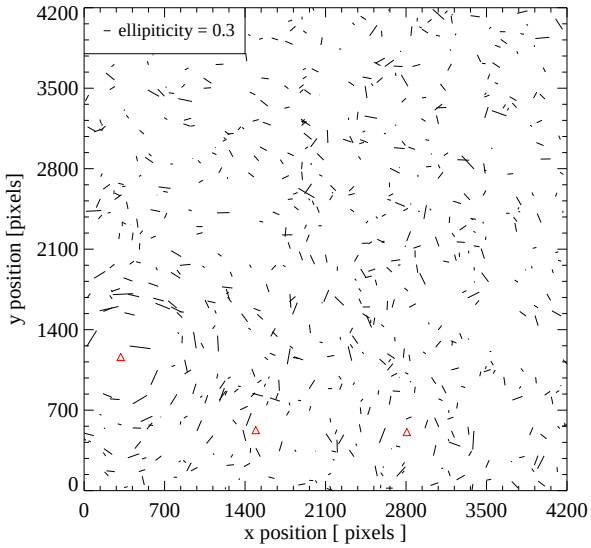

Figure A.1: An example of one of the training skies given to the participants. Here there are three haloes, with these positions shown by the red triangles. The black tick marks show the ellipticity and positions of each galaxy in the field.

context of this competition, the metric was required to achieve the aims set out in Section A.2. To this extent, we required a metric that not only rewarded competitors for providing solutions that were close to the halo positions, but also rewarded solutions that were not systematically biased in a particular angular direction, i.e. an unbiased solution would be angularly invariant on average to the true position of the halo. We therefore constructed a metric of two parts, a distance part, F, and an angular part, G and combined them such that the overall score, m, was,

$$m = \frac{F}{1000} + G, \tag{A.1}$$

where the factor of 1000 down-weighted the F part of the metric such the two parts to the metric were of equal order (since they were perceived as equally important) and that LENSTOOL achieved a score of approximately 1.0.

The Distance, F Metric

The first part of the metric quantified the ability of an algorithm to produce halo positions that were as close as possible to the true positions. However, one

issue we met was that in the case of clusters with more than one halo, it was not always clear which halo users were predicting, i.e. if they had named their first prediction, "halo1", it was ambiguous to which halo this referred to. We therefore selected the halo pairs (users haloes to true haloes) such that it optimised the distance part of the metric. The 'F' part of the metric was in the form,

$$F = \sum_{k=0}^{\text{nClusters}} \arg\min \left\{ \sum_{i=0}^{\text{nHaloes}} \sqrt{(x_{ik} - x_{jk})^2 + (y_{ik} - y_{jk})^2} \right\}_j^{\text{config}} \tag{A.2}$$

where the min function is over all the pair configurations in the cluster, where for two haloes there was two and for three there was six. We normalised the F metric to provide an approximately unit score for LENSTOOL.

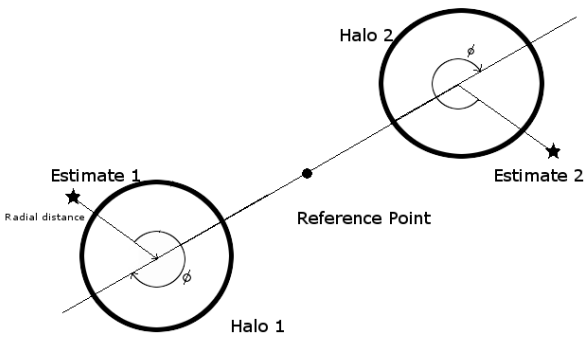

Figure A.2: The angular, G metric. ϕ was calculated as the angle between the the vector joining the true and users predicted position and the vector joining the centre of mass of the system (reference point) and the true position.

The Angular, G Metric

In any public competition where money and pride is at stake, competitors will be less concerned with the scientific goals of the competition, and more concerned with gaining a good score on the leaderboard. Not only is this because they compete for money or pride, but also because they will assume that the organisers will have constructed a metric that will mean that a good score naturally results in a good algorithm. This means that competitors will optimise their algorithms such that they achieve the best metric score possible. In the case where $m \propto F$, participants could have continued developing their algorithm such that they

reduced the separation between predicted and true position of haloes. Although this may have resulted in predictions that are very close to the true halo positions, it would not have solved the second aim of developing an algorithm that is systematically unbiased. We therefore included a second part to the metric that rewarded angular invariance of predictions.

To calculate the angular invariance, we derived the angle of the vector between the true and the predicted position with respect to the vector that connected the true position and the centre of mass of the system (or reference point as it was denoted). Once we had this angle, ϕ, we took the average vector that this angle defined in a unit circle, i.e.

$$G = \sqrt{\left(\frac{1}{N}\sum_{i=0}^{N}\cos(\phi_i)\right)^2 + \left(\frac{1}{N}\sum_{i=0}^{N}\sin(\phi_i)\right)^2}, \tag{A.3}$$

where the sum N is over all haloes in all clusters. Figure A.2 shows diagrammatically how we calculated ϕ.

A.3 Results

Here we present the results from the ODW competition. We present the original metric, and also results that were calculated using only the distance part of the metric, which we found to dominate the total metric. Figure A.3 shows the results for the two metrics normalised to the score of LENSTOOL, (in other words a score of 1.0 is the same score as LENSTOOL), as a function of competitor for the top 150 competitors. We have sorted the results such that the total score does not correspond with the radial score of the same participant.

From the initial results we find that of the 357 participants, 143 had a score better than the LENSTOOL benchmark with the top 27 competitors registering better than a 20% improvement, and the top competitors recording a $> 30\%$ improvement. We find that the act of removing the angular part of the metric slightly reduces the relative score of the competitors with respect to LENSTOOL, with 150 of the 357 competitors (42%) achieving a better score than LENSTOOL, and that the top competitors still recorded a $> 30\%$ improvement.

Figure A.4 shows the incremental improvement of the best scoring algorithm with time. It can be seen that in the initial periods of the competition

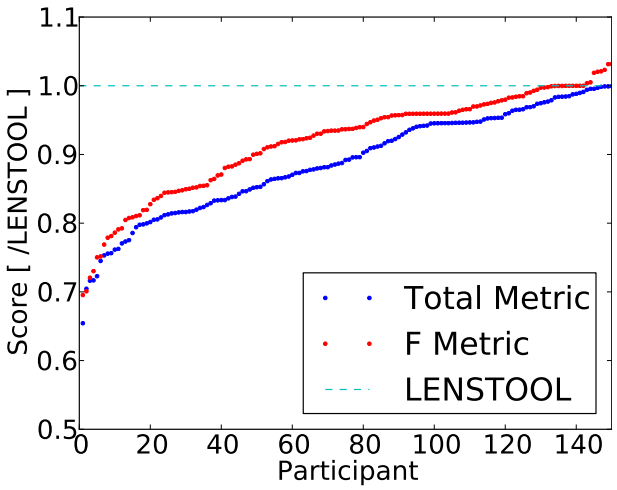

Figure A.3: The figure shows the score of the top 150 competitors normalised to the score of LENSTOOL for easy direct comparison (where LENSTOOL = 1.0) as a function of the participants final leaderboard rank. The blue points refer to the total score of the competitor and the red the radial part. The scores have been sorted and therefore the points in the radial do not directly correspond to the points in the blue.

regular, large improvements are made, and as the competition continues these improvements become less frequent. This is typical of a machine learning competition, however a typical machine learning competition will then at later times see smaller, fewer, incremental improvements [4], tending to some limit which is typically the limit of information in the data. ODW saw slightly more regular improvement and increased late-time large improvements than a typical competition. This can be attributed to either the competitors had not reached the information threshold of the data set, and improvements could be still made, or more likely the uncertainty in the metric meant that given sufficient submissions to the leaderboard a participant would strike lucky and their score would jump up, causing the best score to improve. Since this would be largely random, improvements would continue at a steady rate, until competitors were gaining scores that were so low that it was unlikely that a lucky strike would improve it.

Figure A.5 shows how the average of the top 150 competitors performed as a function of various components of the competition. We find that the mass of the halo is the dominant variable in the estimation of the position of dark matter

[4] e.g. `https://www.kaggle.com/c/facebook-recruiting-iii-keyword-extraction/leaderboard`

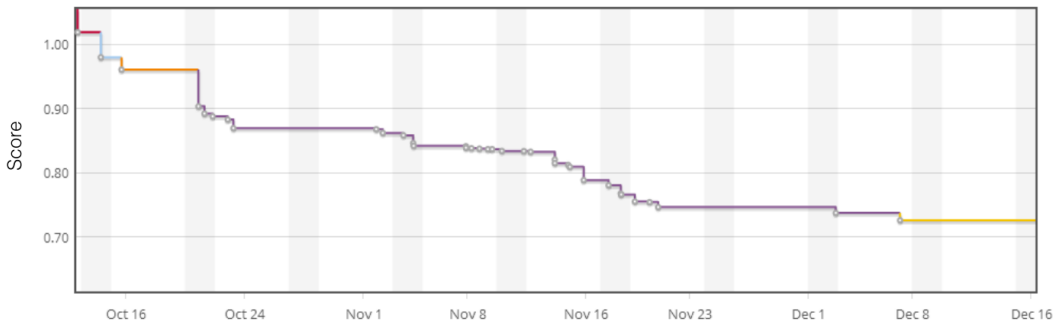

Figure A.4: Timeline for the improvement of the best scoring algorithm. Initially, a significant amount of progress is made, however towards the end, progress plateaus with few and small incremental improvements. Although typical, this competition saw more more regular improvements than typical machine learning problems.

haloes, and the methods were unaffected by the number of source galaxies. We see that below $10^{14} M_{\odot}$, there seems to be no trend. In order to constrain this better, future competitions would require more estimates of the positions of haloes of these masses. Interestingly competitors did better when the halo was a SIS and not an NFW profile. We hypothesise that this is because the very centre of a SIS is much denser than a NFW, with no core, and therefore estimating its peak is easier. We find a weak trend between the ellipticity of the main halo and the position estimates.

Figure A.6 shows graphically the distribution of estimates of the 150 participants. We can clearly see that in the left hand panel, that shows the main halo estimates, positions are much more concentrated and clustered about the true position than the sub haloes shown in the second two panels. First place submissions (Tim Saliman's) are shown as blue stars and the cyan dot is the original position of the halo.

In order to quantify the statistical accuracy of the best submissions, we binned up the submissions in mass. Figure A.7 shows the results of the top three placing algorithms. The error bars show the error in the mean radial position for that particular mass bin. We find that the best algorithms could constrain the large mass haloes to $< 5''$ rising to $\sim 60''$ for smaller mass haloes. In hindsight, this strong trend between mass of the halo and the accuracy means that we may have taken more care when sampling the distribution of mass haloes for both the

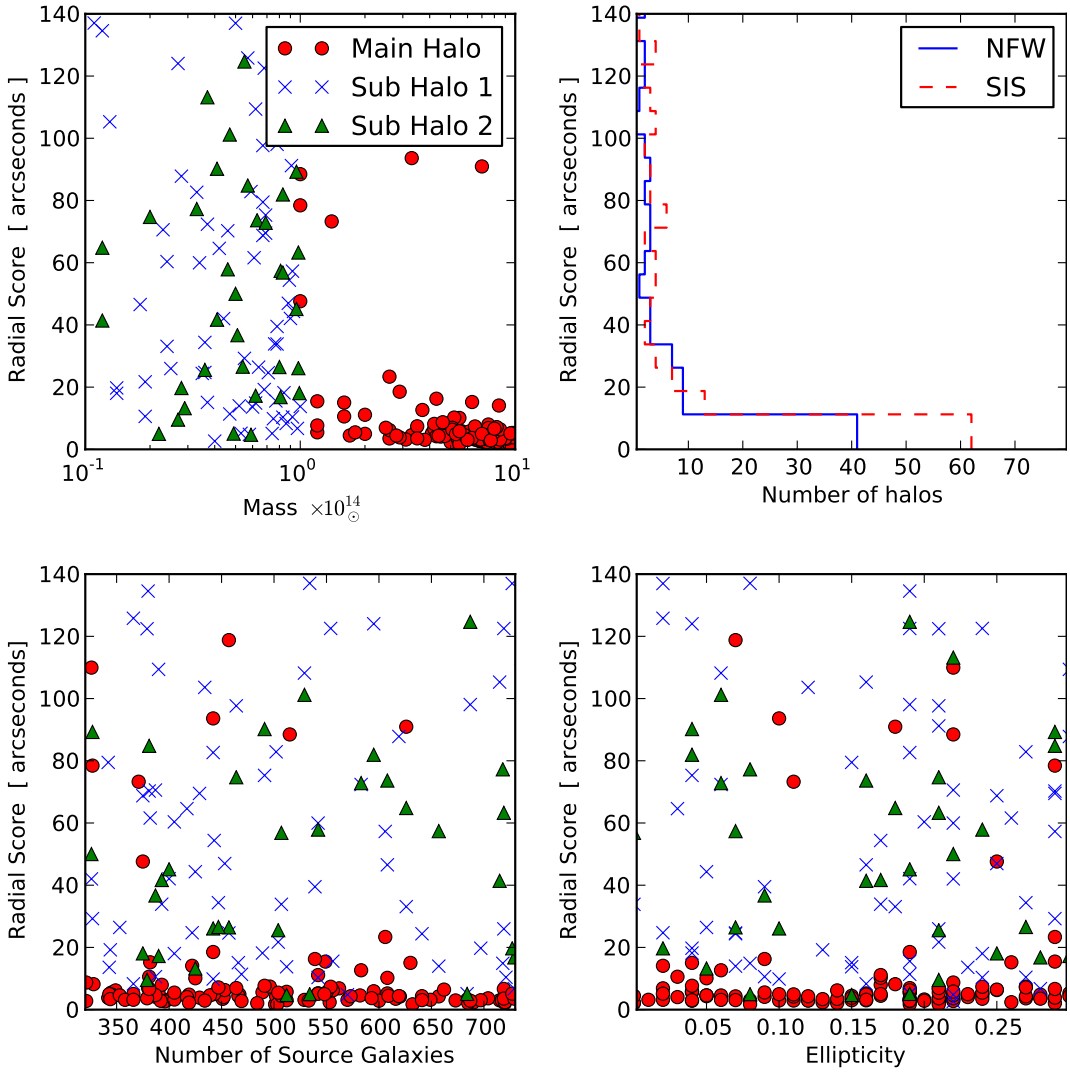

Figure A.5: The figure shows the average score of the top 150 competitors radial score as a function of various competition parameters. We see that there is a trend with respect to the mass of the halo, showing that estimates are more uncertain with decreasing mass. Below $10^{14} M_{\odot}$, estimates seem to be extremely varied, and in order to constrain this trend further, we would require more estimates of haloes of that mass. Also the top right panel shows how more SIS haloes were constrained to within 15″ than NFW.

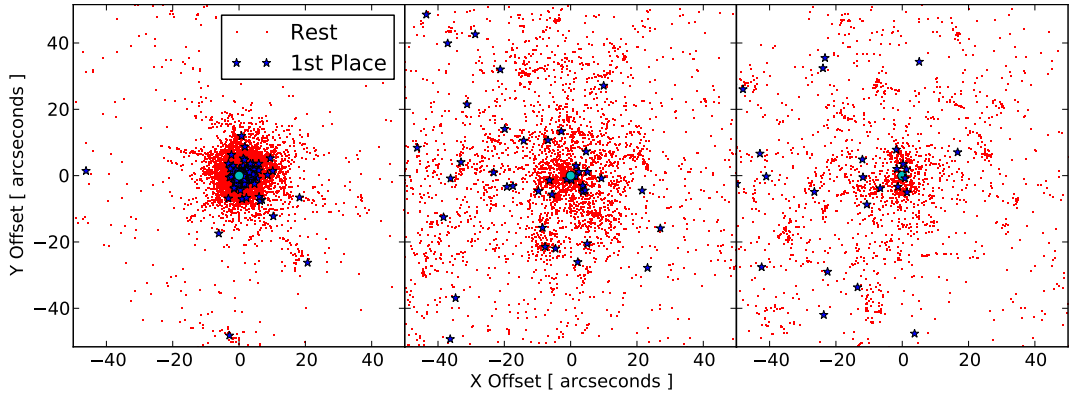

Figure A.6: The red points are the best radial position of each halo for the top 150 competitors. The first panel shows the results of the main halo in each case, and the second two panels, the sub halo. The blue stars in each case represent the winner's (Tim Saliman's) estimated positions. One can clearly see that the points are much more clustered for the main halo.

test and training set. By drawing from a uniform distribution we overestimated the number of larger mass haloes than one would expect in a sample of galaxy clusters such as this. Future competitions may look to draw from a more realistic sample such as a Press-Schechter function thus supplying participants with a more realistic sample of clusters.

A.3.1 Metric Stability

In order for the competition to provide accurate feedback to participants, the metric needs to be able to distinguish between two algorithms that are very similar, and determine which is better at achieving the research goal. There are many ways that one can reduce the uncertainty in the metric and ensure the correct algorithms win.

The first method to minimise the uncertainty is to have a well defined metric that is simple and has minimal intrinsic variability. The metric set out in this competition had two parts; the distance part and the angular part. The former was a direct probe for the precision of an algorithm, and the second part was used to determined any systematics in the algorithm. However the angular part of the metric was also intrinsically more uncertain than the radial part. Figure A.8 shows the variance in a random set of submissions, whereby each halo was a random guess within the field of view of the cluster. It can be seen that there was

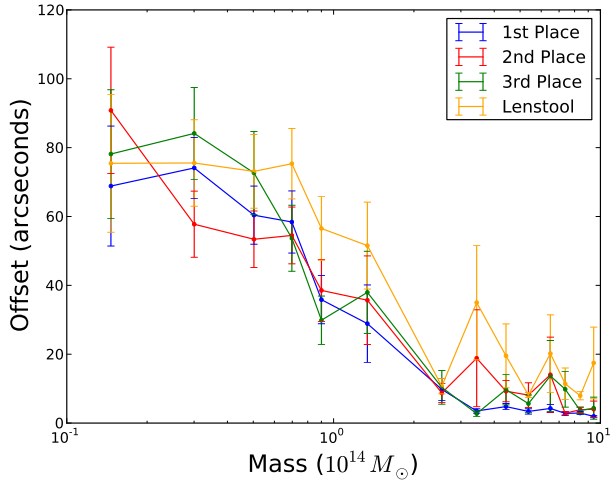

Figure A.7: The Figure shows the radial distance the top three competitors and LENSTOOL estimates are from the true position in arcseconds. The submissions have been binned by mass, and the error bars are the error in the mean of the radial distances in the mass bin.

a large variance in scores due to the nature of the metric. In the limit that the number of clusters tends to a large number, noise will average out and the score on the metric will tend to truly reflect the quality of the algorithm. However in a bid to reflect the expected number of clusters from typical data sets from future surveys we only provided a small number of clusters. Moreover, we did not want to limit participants to algorithms that had requirements of > 1 second/cluster reconstruction times. In normal machine learning competitions, data sets are of the order 10^5 samples, and in the scenario where a lot of people enter with similar algorithms, the scores at the top of the leader board can be separated by $\sim 0.01\%$. This requires the uncertainty to be another order of magnitude less than this.

Another consequence of small training and test sets is the effective Poisson noise in the sampling of parameters for the data. We sampled each parameter for the field in Table 1 from a uniform distribution. As a result the mass of the haloes in each test set varied by a large amount, The public test set consisted of smaller sub haloes than the private test set. In this sense, the public test set was not only harder, but below a certain halo mass the uncertainty in the positions was larger, making the public leaderboard noisier than the private leaderboard; this is something that should be addressed in designing future competitions.

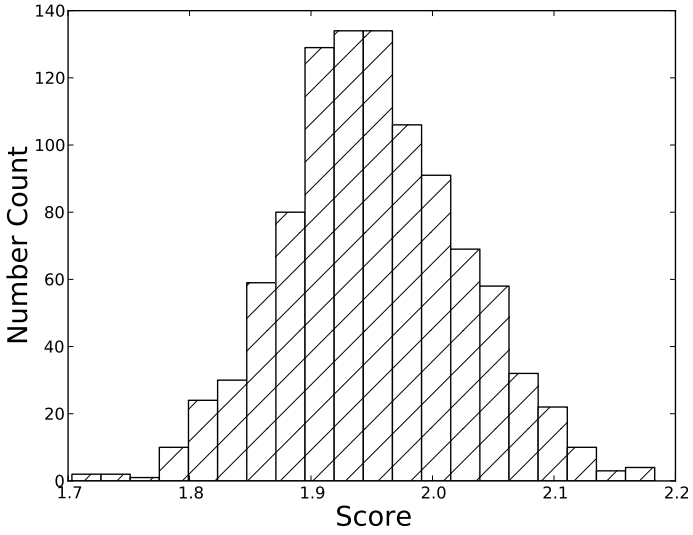

Figure A.8: The score of a random sample of fake entries; 1000 fake submissions with random guesses were scored. This uncertainty on the metric led to less efficient feedback from the leaderboard given to participants.

A.4 Successful Algorithms

Competitions such as these will often not return a complete algorithm that will revolutionise the problem at hand. Often they will give a new insight, or tool. Kitching et al. (2012b) found that improvements to shape measurement were made with increasingly sophisticated sampling methods. Although it is hard to say statistically that Lenstool has been improved on, many insights were made during this competition.

Methods to try and solve the problem of dark matter reconstruction were reasonably varied. Although many participants attempted new methods involving classical machine learning techniques such as neural networks and random forests, many found it difficult to extract a distinct set of features that could be trained on. It was found that the most successful solutions were Bayesian ones, that fitted parametric models to the data and then sampled the parameter space and found the most likely parameters.

Most importantly, these techniques, which were similar to Lenstool, then optimised the final point estimator according to the metric defined by the competition. It is this reason why many of the techniques did better than the public code Lenstool. Although Lenstool finds the best fitting position by

maximising the likelihood of a set of parameters, those that did particularly well used a sophisticated method to select the point estimator that gained the best 'score' from the set of samples where as LENSTOOL just returned the score with the best reduced chi-square.

An interesting point to be raised post-competition, was that Iain Murray, who came second, found that, ultimately, sampling the posterior surface did not take the majority of the computational time, but in-fact it was the interpretation of the samples as a point estimator that did (as for required by the competition). Iain stated that he would have preferred to just supply a set of samples to expected positions and that this way we could evaluate the algorithm much more accurately. As a result, future competitions should examine whether point estimators are what is required or whether likelihoods would be of more use. Moreover, this competition served as a example that in astronomy, often we endeavour to attain a single point estimator for a parameter, an estimator that may be biased, when in-fact this parameter is not the end goal and we should consider using the full posterior distribution.

The top three competitors were only separated by 4% in accuracy, and therefore it is difficult to make a statistical significant conclusion of why Saliman's algorithm did better than Murray and Pires. Although the three competitors did conduct a similar model fitting technique, Tim used metropolis hastings Monte Carlo Markov Chain sampler, where as Iain used slice sampling. The latter is useful as it determines its own step sizes during sampling and therefore requires little tweaking, however metropolis hastings sampling may have been more effective for this competition. Since the score separation is not statistically significant we will refrain from making claims that the algorithms were statistically better than one another, however it is clear, that assuming no knowledge of physics (such that direct inversion techniques are not available) parametric model fitting was clearly the most effective method to reconstruct the positions of dark matter haloes.

As part of the competition, a requisite for claiming the prize was that both the code and a detailed description was made public. As such, we now present the main properties of the winning solutions. Note that since these models were presented as non-astronomically motivated algorithms (the motivation was to win the competition), many of the parameters used have no physical units and were

based on the experience of the data. These are brief summaries of the solutions, and we encourage the reader to use the embedded URL's to find more information.

A.4.1 First place: Tim Salimans

This was a Bayesian solution[5] to the problem and was made publicly available[6]. There were three main steps in this code;

1. From the data, formulate some model for the likelihood of a dark matter halo position given some galaxy information, $p(e|x)$,

$$p(e_i|x) = N(\sum_{j=0}^{\text{all haloes}} d_{i,j} m_j f(r_{i,j}), \sigma^2), \tag{A.4}$$

   where the probability is assumed to be a normal distribution, N. $d_{i,j}$ is the tangential direction to the vector joining halo j to galaxy i, (i.e. the direction in which the galaxy is lensed), m_j is the mass of the the halo, r_{ij} is the euclidean distance between the halo centers and the galaxies and $f(r_{ij})$ is a radial profile of the halo. In order to determine the model settings he first placed priors on the masses, $p(m|q)$, where q is the set of parameters determining the shape of the prior and the functional form of $f(r; w)$, with w parameterizing $f()$, he then calculated the marginal likelihood of the ellipticities on the training data (since there the positions of the haloes are known):

$$p(e|q, w, \sigma^2) = \int p(e|f(r; w), m, \sigma^2) p(m|q) dm, \tag{A.5}$$

   By maximizing the marginal likelihood with respect to q, w, σ^2, he got efficient and consistent estimates of the true profile parameters and priors, assuming the model is correct. From this he fixed the dispersion of the likelihood model at $\sigma^2 = 0.05$. The main halo mass was selected from a log uniform distribution between 40 and 180 and the sub-halo mass was fixed to be 20, i.e. $M_{\text{S}}/M_{\text{M}} = [0.11, 0.5]$. The halo profiles were a simple inverse

[5] `http://timsalimans.com/observing-dark-worlds/`
[6] `http://timsalimans.com/code-for-the-dark-worlds-competition/`

distance profile with a core,

$$f(r_{i,j}, r_{\mathrm{c}}) = \frac{1}{\max(r_{i,j}, r_{\mathrm{c}})}, \tag{A.6}$$

where the core radius, r_{c} was fixed at $r_{\mathrm{c}} = 240$ and $r_{\mathrm{c}} = 70$ for the main and sub haloes respectively.

2. Using Bayes's theorem, calculate the probability of a dark matter halo position, given some galaxy information via

$$p(x|e) = \frac{p(e|x)p(x)}{p(e)} \tag{A.7}$$

3. Finally minimise the ODW metric with respect to the parameters of the dark matter haloes, i.e.

$$\hat{x} = \arg\ \min_{\mathrm{q}} \mathbb{E}_{p(x|e)} L(\mathrm{q}, x), \tag{A.8}$$

where q are the predictions of the positions of the dark matter haloes. This was implemented via a Monte Carlo Markov Chain (MCMC) Metropolis Hastings sampler, and a simple gradient descent. The sampler was also restarted at random points to avoid local minima.

A.4.2 Second place: Iain Murray

In a similar fashion, second place solution also followed a Bayesian solution and the code is also publicly available[7]. Using the same halo profile, this algorithm used slice sampling instead of Metropolis Hastings, as Salimans used. Since it was assumed that this radial profile was not quite accurate, the variance inside the core radius was increased to account for this lack of knowledge. The expected loss with respect to the ODW metric was then minimised.

Interestingly, once Murray had sampled the posterior surface, he developed an innovative way to determine a single point estimator, which he said was what took the most computation. In order make an estimate as required by the competition, he constructed a fake test set with the positions of the haloes from the samples in the MCMC and then chose the sample which gave the best score on this fake

[7] `http://blog.kaggle.com/2012/12/19/a-bayesian-approach-to-observing-dark-worlds/`

test set. This is conceptually similar to stage 4 in Tim Salimans and the final stage in Ana Pires's method.

A.4.3 Third place: Ana Pires

The third solution was slightly different from the previous two. Pires assumed the haloes were sized such that there were (in the case of three haloes) a large, medium and small halo. This approach also defined a distinct "elliptical distance" between the ith galaxy, kth halo,

$$d_{i,k} = \sqrt{(x_i - x_k)^2 + r_{\sigma,k}(y_i - y_k)^2 + 2\rho_k(x_i - x_k)(y_i - y_k)} \tag{A.9}$$

where $r_{\sigma,k}$ and ρ_k are free parameters and represent the ratio of the absolute strength of the shear in vertical, y and horizontal, x directions and ρ_k represents a "distortion". The motivation for this was to represent the distances between haloes and galaxies not as "geometric" distances, but "physical" distance, such that two galaxies may be at different geometrical distances from the centre of the halo but experience the same distortion (due to dark matter halo ellipticity for example).

Using the definition for elliptical distance, a model was constructed for the two components of ellipticity, χ_1 and χ_2 for the ith galaxy;

$$\chi_{1i} = -\sum_{k=0}^{\text{nHaloes}} \cos(2\phi_{i,k}) f_k(d_{i,k}) + \alpha_0 + \epsilon_{1i} \tag{A.10}$$

and

$$\chi_{1i} = -\sum_{k=0}^{\text{nHaloes}} \sin(2\phi_{i,k}) f_k(d_{i,k}) + \alpha_0 + \epsilon_{1i}, \tag{A.11}$$

where ϵ refers to the intrinsic ellipticity of the galaxy with some variance σ^2 and mean, $\langle\epsilon\rangle = 0$, α_0 is some free parameter and the function f was given by

$$f_k(x) = \alpha_k e^{-\beta x} \tag{A.12}$$

where α_k and β are further free parameters. In order to estimate parameters, she

constructed a maximum likelihood criterion, η, such that

$$\eta = \arg\min \left(\sum_{0}^{\text{nSkies}} h(\chi_{1i} - \hat{\chi}_{1i};\ 0.6) + \sum_{0}^{\text{nSkies}} h(\chi_{1i} - \hat{\chi}_{1i};\ 0.6) \right) \tag{A.13}$$

where

$$h(x;\delta) = \begin{cases} x^2, & \text{if } |x| < \delta \\ \delta^2, & \text{if } |x| \geq \delta. \end{cases} \tag{A.14}$$

η was then solved via the Nelder-Mead method to derive optimal parameters for the fields.

A.5 Implications for future competitions

Many of the results and conclusions from this experiment may have benefitted from the experiences gained during the competition. Similar types of competitions have reported guidelines to run such crowdsourcing efforts (e.g. Goodfellow et al., 2013), however here we outline some other important factors that arose during the competition.

1. Although it is difficult to completely full-proof data before releasing the public, data should have no discrepancies, especially if explicit constraints are explained prior, for example, ellipticity is always bound by 1. In order to check, use example code and submit to check the returned results. Any changes in the data post launch can cause disruption and loss of participation.

2. Prior to the competition, test the uncertainty on the metric via Monte Carlo simulations. This is especially important if the metric is unique to the competition. The metric must be sensitive enough to distinguish between good and bad models and return scores that reflect the competency of the algorithm.

3. Check the distribution of parameter choices between sets. Ensure that if there exist significant discrepancies between the test and training set that these are intended. Users will use the training set to estimate their score

away from the leaderboard, so consistent data between the training and public test set is important. Moreover ensure that, in the event of no overfitting to the data, scores are consistent between private and public test sets. Users will base their decision of which scores to submit at the end of the competition on the scores given on the public leaderboard and so need to be reliable.

4. Keep the metric as simple as you can and avoid weighting parts of the test set (natural competition normally negates the need for this).

5. Bare in mind the overall scientific goal of the competition, and ask if point like estimates are what is required. Would it be more beneficial instead to return probabilities or posterior surfaces?

6. Only provide benchmark code that will be useful. If public code exists (e.g. LENSTOOL) be aware that competitors will attempt to use it and will require assistance to install and run it. If this isn't desired then do not allow access to it.

A.6 Conclusions

We have presented the results of the expert crowdsourcing competition 'Observing Dark Worlds'. The competition was designed to develop weak gravitational lensing algorithms to reconstruct the position of the peak positions of dark matter haloes in galaxy clusters. We found that, of the 357 participants that competed in 'Observing Dark Worlds', 150 scored better than the LENSTOOL benchmark with the top 27 competitors registering better than a 20% improvement; and the best algorithms registering a $> 30\%$ improvement.

Notably, the majority of the algorithms were similar Bayesian fitting methods that fitted various functional forms and then optimised with respect to the Observing Dark Worlds metric. Those that attempted innovative machine learning techniques struggled to extract important features and therefore did not do as well. The top three algorithms were all Bayesian, model fitting methods, however uniquely had sophisticated methods to determine a point like estimator from the bayesian inference which gave the best score. It is this step that we find to be the most important in the context of this competition. We found that the

top three algorithms could constrain the large mass haloes ($\sim 3 - 10 \times 10^{14} M_{\odot}$) to within $< 5''$, which is an accuracy required to used dark matter peak positions to measure dark matter cross section (Harvey et al., 2013b). However for smaller mass ($< 10^{14} M_{\odot}$) this rose to $> 60''$. We conclude that these algorithms performed significantly better than the public code LENSTOOL, however to make a direct comparison further tests will be required on both the winning algorithms and LENSTOOL on more realistic simulations, and data.

Many of the results and conclusions from this experiment may have benefitted from the experiences gained during the competition. Similar types of competitions have reported guidelines to run such crowdsourcing efforts (e.g. Goodfellow et al., 2013) and should be considered before embarking on similar competitions.

We found that competitions such as these are a useful approach to developing computer algorithms within the astronomical context. We note that although this method of developing algorithms is efficient, work must be done post-competition to develop these ideas such that they can work on real data, avoiding situations where they become black boxes. However, we do see that using expert data scientists significant improvements can be made in a relatively short amount of time.

Bibliography

Aalseth C. E. et al., 2011, Physical Review Letters, 106, 131301

Agertz O. et al., 2007, MNRAS , 380, 963

Aguilar M. et al., 2013, Physical Review Letters, 110, 141102

Allen S. W., Rapetti D. A., Schmidt R. W., Ebeling H., Morris R. G., Fabian A. C., 2008, MNRAS , 383, 879

Alner G. J. et al., 2005, Nuclear Instruments and Methods in Physics Research A, 555, 173

Amara A., Refregier A., 2006, in COSPAR Meeting, Vol. 36, 36th COSPAR Scientific Assembly, p. 2118

Angloher G. et al., 2012, European Physical Journal C, 72, 1971

Angulo R. E., Springel V., White S. D. M., Jenkins A., Baugh C. M., Frenk C. S., 2012, MNRAS , 426, 2046

Aprile E. et al., 2012, Physical Review Letters, 109, 181301

Arnaud M., 2005, in Background Microwave Radiation and Intracluster Cosmology, Melchiorri F., Rephaeli Y., eds., p. 77

Bacon D. J., Goldberg D. M., Rowe B. T. P., Taylor A. N., 2006, MNRAS , 365, 414

Bacon D. J., Refregier A. R., Ellis R. S., 2000, MNRAS , 318, 625

Bania T. M., Rood R. T., Balser D. S., 2002, Nature , 415, 54

Barret D. et al., 2013, in SF2A-2013: Proceedings of the Annual meeting of the French Society of Astronomy and Astrophysics, Cambresy L., Martins F., Nuss E., Palacios A., eds., pp. 447–453

Bartelmann M., Schneider P., 2001, Phys. Rep. , 340, 291

Battaglia N., Bond J. R., Pfrommer C., Sievers J. L., 2013, ApJ , 777, 123

Bekenstein J., 2006, Contemporary Physics, 47, 387

Bekenstein J., Milgrom M., 1984, ApJ , 286, 7

Berezhiani Z. G., Dolgov A. D., Mohapatra R. N., 1996, Physics Letters B, 375, 26

Bernabei R. et al., 2013, International Journal of Modern Physics A, 28, 30022

Bertotti B., Iess L., Tortora P., 2003, Nature , 425, 374

Beskidt C., de Boer W., Kazakov D. I., Ratnikov F., 2012, European Physical Journal C, 72, 2166

BICEP2 Collaboration et al., 2014, ArXiv e-prints

Bondi H., Gold T., 1948, MNRAS , 108, 252

Booth C. M., Schaye J., 2009, MNRAS , 398, 53

Bosma A., 1978, PhD thesis, PhD Thesis, Groningen Univ., (1978)

Bourdin H. et al., 2011, A&A , 527, A21

Boylan-Kolchin M., Bullock J. S., Kaplinghat M., 2011, MNRAS , 415, L40

Bradač M., Allen S. W., Treu T., Ebeling H., Massey R., Morris R. G., von der Linden A., Applegate D., 2008, ApJ , 687, 959

Bradač M. et al., 2006, ApJ , 652, 937

Bradač M., Schneider P., Lombardi M., Erben T., 2005, A&A , 437, 39

Bridle S. et al., 2010, MNRAS , 405, 2044

Burles S., Nollett K. M., Turner M. S., 2001, ApJ , 552, L1

Cacciato M., Bartelmann M., Meneghetti M., Moscardini L., 2006, A&A , 458, 349

Carr B. J., 1980, A&A , 89, 6

Cavaliere A., Fusco-Femiano R., 1976, A&A , 49, 137

CDMS Collaboration et al., 2013, ArXiv e-prints

Clowe D., Bradač M., Gonzalez A. H., Markevitch M., Randall S. W., Jones C., Zaritsky D., 2006, ApJ , 648, L109

Clowe D., Gonzalez A., Markevitch M., 2004, ApJ , 604, 596

Clowe D., Markevitch M., Bradač M., Gonzalez A. H., Chung S. M., Massey R., Zaritsky D., 2012, ApJ , 758, 128

Coe D. et al., 2012, ApJ , 757, 22

Cohn J. D., 2012, MNRAS , 419, 1017

Comerford J. M., Natarajan P., 2007, MNRAS , 379, 190

Crain R. A., Eke V. R., Frenk C. S., Jenkins A., McCarthy I. G., Navarro J. F., Pearce F. R., 2007, MNRAS , 377, 41

Dahle H. et al., 2013, ApJ , 772, 23

Davis M., Lecar M., Pryor C., Witten E., 1981, ApJ , 250, 423

Dawson W. A. et al., 2012, ApJ , 747, L42

Daylan T., Finkbeiner D. P., Hooper D., Linden T., Portillo S. K. N., Rodd N. L., Slatyer T. R., 2014, ArXiv e-prints

de la Torre S. et al., 2013, A&A , 557, A54

Dicke R. H., Peebles P. J. E., Roll P. G., Wilkinson D. T., 1965, ApJ , 142, 414

Diego J. M., Tegmark M., Protopapas P., Sandvik H. B., 2007, MNRAS , 375, 958

Dietrich J. P., Böhnert A., Lombardi M., Hilbert S., Hartlap J., 2012, MNRAS , 419, 3547

Dressler A., Lynden-Bell D., Burstein D., Davies R. L., Faber S. M., Terlevich R., Wegner G., 1987, ApJ , 313, 42

Dubinski J., Carlberg R. G., 1991, ApJ , 378, 496

Duffy A. R., Schaye J., Kay S. T., Dalla Vecchia C., 2008, MNRAS , 390, L64

Duffy A. R., Schaye J., Kay S. T., Dalla Vecchia C., Battye R. A., Booth C. M., 2010, MNRAS , 405, 2161

Dyson F. W., Eddington A. S., Davidson C., 1920, Royal Society of London Philosophical Transactions Series A, 220, 291

Eke V. R., Navarro J. F., Frenk C. S., 1998, ApJ , 503, 569

Ettori S., Gastaldello F., Leccardi A., Molendi S., Rossetti M., Buote D., Meneghetti M., 2010, A&A , 524, A68

Faber S. M., Jackson R. E., 1976, ApJ , 204, 668

Felten J. E., Gould R. J., Stein W. A., Woolf N. J., 1966, ApJ , 146, 955

Feng J. L., 2010, ARA&A , 48, 495

Feng J. L., Kaplinghat M., Tu H., Yu H.-B., 2009, Journal of Cosmology and Astroparticle Physics, 7, 4

Fields B. D., Freese K., Graff D. S., 2000, ApJ , 534, 265

Finoguenov A. et al., 2007, ApJS , 172, 182

Freese K., Fields B., Graff D., 2000, ArXiv Astrophysics e-prints

Frisch U., 1995, Turbulence. The legacy of A. N. Kolmogorov. Cambridge University Press

Fruscione A. et al., 2006, in Society of Photo-Optical Instrumentation Engineers (SPIE) Conference Series, Vol. 6270, Society of Photo-Optical Instrumentation Engineers (SPIE) Conference Series

Fukugita M., Hogan C. J., Peebles P. J. E., 1998, ApJ , 503, 518

Gamow G., 1946, Physical Review, 70, 572

Gavazzi R., Treu T., Rhodes J. D., Koopmans L. V. E., Bolton A. S., Burles S., Massey R. J., Moustakas L. A., 2007, ApJ , 667, 176

George M. R. et al., 2012, ApJ , 757, 2

Gilmour R., Best P., Almaini O., 2009, MNRAS , 392, 1509

Giodini S. et al., 2009a, ApJ , 703, 982

Giodini S. et al., 2009b, ApJ , 703, 982

Gnedin O. Y., Ostriker J. P., 2001a, ApJ , 561, 61

Gnedin O. Y., Ostriker J. P., 2001b, ApJ , 561, 61

Gonzalez A. H., Sivanandam S., Zabludoff A. I., Zaritsky D., 2013, ApJ , 778, 14

Goodfellow I. J. et al., 2013, ArXiv e-prints

Guth A. H., 1981, Phys. Rev. D , 23, 347

Hamana T., Takada M., Yoshida N., 2004, MNRAS , 350, 893

Harvey D., Massey R., Kitching T., Taylor A., Jullo E., Kneib J.-P., Tittley E., Marshall P. J., 2013a, MNRAS , 433, 1517

Harvey D. et al., 2013b, ArXiv 1310.1731

Heymans C. et al., 2006, MNRAS , 368, 1323

Hodges H. M., 1993, Phys. Rev. D , 47, 456

Hoekstra H., 2001, A&A , 370, 743

Hoekstra H., Donahue M., Conselice C. J., McNamara B. R., Voit G. M., 2011, ApJ , 726, 48

Hoekstra H., Jain B., 2008, Annual Review of Nuclear and Particle Science, 58, 99

Hoyle F., 1948, MNRAS , 108, 372

Hubble E., 1929, Proceedings of the National Academy of Science, 15, 168

Israel H., Reiprich T. H., Erben T., Massey R. J., Sarazin C. L., Schneider P., Vikhlinin A., 2014, ArXiv e-prints

Ivezic Z. et al., 2008, ArXiv e-prints

Jain B., Seljak U., White S., 2000, ApJ , 530, 547

Jedamzik K., 1995, ApJ , 448, 1

Jee M. J., Mahdavi A., Hoekstra H., Babul A. ., Dalcanton J. J., Carroll P., Capak P., 2012, ApJ , 747, 96

Jetzer P., Koch P., Piffaretti R., Puy D., Schindler S., 2002, ArXiv Astrophysics e-prints

Johnston D. E. et al., 2007, ArXiv e-prints

Jullo E., Kneib J.-P., Limousin M., Elíasdóttir Á., Marshall P. J., Verdugo T., 2007, New Journal of Physics, 9, 447

Jullo E., Pires S., Jauzac M., Kneib J.-P., 2013, ArXiv e-prints

Kahlhoefer F., Schmidt-Hoberg K., Frandsen M. T., Sarkar S., 2014, MNRAS , 437, 2865

Kaiser N., 1984, ApJ , 284, L9

Kaiser N., Squires G., 1993, ApJ , 404, 441

Kaiser N., Squires G., Broadhurst T., 1995, ApJ , 449, 460

Kaiser N., Wilson G., Luppino G. A., 2000, ArXiv Astrophysics e-prints

Kay S. T., Thomas P. A., Jenkins A., Pearce F. R., 2004, MNRAS , 355, 1091

Kilbinger M. et al., 2013, MNRAS , 430, 2200

King L. J., Mead J. M. G., 2011, MNRAS , 416, 2539

King S. F., Merle A., 2012, Journal of Cosmology and Astroparticle Physics, 8, 16

Kitching T. et al., 2010, ArXiv e-prints

Kitching T. D. et al., 2012a, MNRAS , 423, 3163

Kitching T. D. et al., 2012b, ArXiv e-prints

Klypin A., Kravtsov A. V., Valenzuela O., Prada F., 1999, ApJ , 522, 82

Kochanek C. S., White M., 2000, ApJ , 543, 514

Larson D. et al., 2011, ApJS , 192, 16

Lasky P. D., Fluke C. J., 2009, MNRAS , 396, 2257

Laureijs R. et al., 2011, ArXiv e-prints

Layzer D., 1957, AJ , 62, 23

Leauthaud A. et al., 2010, ApJ , 709, 97

Leauthaud A. et al., 2007a, ApJS , 172, 219

Leauthaud A. et al., 2007b, ApJS , 172, 219

Leauthaud A. et al., 2012, ApJ , 744, 159

Linde A. D., 1983, Physics Letters B, 129, 177

Livio M., Silk J., 2014, Nature , 507, 29

Lovell M. R. et al., 2012, MNRAS , 420, 2318

LUX Collaboration et al., 2013, ArXiv e-prints

Lynds R., Petrosian V., 1986, in Bulletin of the American Astronomical Society, Vol. 18, Bulletin of the American Astronomical Society, p. 1014

Macciò A. V., Dutton A. A., van den Bosch F. C., 2008, MNRAS , 391, 1940

Mahdavi A., Hoekstra H., Babul A., Balam D. D., Capak P. L., 2007, ApJ , 668, 806

Mandelbaum R. et al., 2013, ArXiv e-prints

Mantz A. B., Allen S. W., Morris R. G., Rapetti D. A., Applegate D. E., Kelly P. L., von der Linden A., Schmidt R. W., 2014, ArXiv e-prints

Markevitch M., Gonzalez A. H., Clowe D., Vikhlinin A., Forman W., Jones C., Murray S., Tucker W., 2004, ApJ , 606, 819

Marshall P. J., Hobson M. P., Gull S. F., Bridle S. L., 2002, MNRAS , 335, 1037

Martel H., Robichaud F., Barai P., 2014, ArXiv e-prints

Massey R., 2010, MNRAS , 409, L109

Massey R. et al., 2007a, MNRAS , 376, 13

Massey R., Kitching T., Nagai D., 2011, MNRAS , 413, 1709

Massey R., Kitching T., Richard J., 2010, Reports on Progress in Physics, 73, 086901

Massey R. et al., 2007b, Nature , 445, 286

Mateo M. L., 1998, ARA&A , 36, 435

Mather J. C. et al., 1990, ApJ , 354, L37

Maughan B., 2005, XMM-Newton Proposal, 87

Maughan B. J., 2007, ApJ , 668, 772

Medezinski E. et al., 2013, ApJ , 777, 43

Melchior P., Viola M., 2012, MNRAS , 424, 2757

Meneghetti M., Yoshida N., Bartelmann M., Moscardini L., Springel V., Tormen G., White S. D. M., 2001, MNRAS , 325, 435

Merten J., Cacciato M., Meneghetti M., Mignone C., Bartelmann M., 2009, A&A , 500, 681

Merten J. et al., 2011, MNRAS , 417, 333

Milgrom M., 1983, ApJ , 270, 365

Miller L., Kitching T. D., Heymans C., Heavens A. F., van Waerbeke L., 2007, MNRAS , 382, 315

Miralda-Escudé J., 2002, ApJ , 564, 60

Mohammed I., Liesenborgs J., Saha P., Williams L. L. R., 2014, MNRAS , 439, 2651

Mohapatra R. N., Nussinov S., Teplitz V. L., 2002, Phys. Rev. D , 66, 063002

Mollerach S., Harari D., Matarrese S., 2004, Phys. Rev. D , 69, 063002

Moore B., Ghigna S., Governato F., Lake G., Quinn T., Stadel J., Tozzi P., 1999, ApJ , 524, L19

Nagai D., Vikhlinin A., Kravtsov A. V., 2007, ApJ , 655, 98

Navarro J. F., Frenk C. S., White S. D. M., 1997, ApJ , 490, 493

Newman A. B., Treu T., Ellis R. S., Sand D. J., Nipoti C., Richard J., Jullo E., 2013, ApJ , 765, 24

Newton R. D. A., Kay S. T., 2013, ArXiv e-prints

Nuza S. E. et al., 2013, MNRAS , 432, 743

Okabe N., Smith G. P., Umetsu K., Takada M., Futamase T., 2013, ApJ , 769, L35

Oort J. H., 1932, Bull. Astron. Inst. Netherlands , 6, 249

Parkinson D. et al., 2012, Phys. Rev. D , 86, 103518

Peacock J. A., 1999, Cosmological Physics

Peacock J. A., Heavens A. F., 1990, MNRAS , 243, 133

Peccei R. D., Quinn H. R., 1977, Physical Review Letters, 38, 1440

Peebles P. J. E., 1980, The large-scale structure of the universe

Penzias A. A., Wilson R. W., 1965, ApJ , 142, 419

Percival W. J. et al., 2001a, MNRAS , 327, 1297

Percival W. J. et al., 2001b, MNRAS , 327, 1297

Perlmutter S. et al., 1998, Nature , 391, 51

Peter A. H. G., Rocha M., Bullock J. S., Kaplinghat M., 2013, MNRAS , 430, 105

Phillips M. M., 1993, ApJ , 413, L105

Planck Collaboration et al., 2013a, ArXiv e-prints

Planck Collaboration et al., 2013b, ArXiv e-prints

Planck Collaboration et al., 2011, A&A , 536, A1

Planelles S., Borgani S., Dolag K., Ettori S., Fabjan D., Murante G., Tornatore L., 2013, MNRAS , 431, 1487

Pontzen A., Governato F., 2014, Nature , 506, 171

Postman M. et al., 2012, ApJS , 199, 25

Powell L. C., Kay S. T., Babul A., 2009, MNRAS , 400, 705

Press W. H., Schechter P., 1974, ApJ , 187, 425

Randall S. W., Markevitch M., Clowe D., Gonzalez A. H., Bradač M., 2008, ApJ , 679, 1173

Refregier A., 2003, ARA&A , 41, 645

Rhodes J., Refregier A., Groth E. J., 2000, ApJ , 536, 79

Rhodes J. D. et al., 2007, ApJS , 172, 203

Riess A. G. et al., 1998, AJ , 116, 1009

Riess A. G. et al., 2011, ApJ , 730, 119

Rocha M., Peter A. H. G., Bullock J. S., Kaplinghat M., Garrison-Kimmel S., Oñorbe J., Moustakas L. A., 2013, MNRAS , 430, 81

Rubin V. C., Ford W. K. J., . Thonnard N., 1980, ApJ , 238, 471

Sánchez A. G. et al., 2012, MNRAS , 425, 415

Sarazin C. L., 1988, X-ray emission from clusters of galaxies

Schmidt F., Leauthaud A., Massey R., Rhodes J., George M. R., Koekemoer A. M., Finoguenov A., Tanaka M., 2012, ApJ , 744, L22

Schneider P., Bartelmann M., 1997, MNRAS , 286, 696

Schrabback T. et al., 2010, A&A , 516, A63

Scoville N. et al., 2007, ApJS , 172, 1

Semboloni E., Hoekstra H., Schaye J., van Daalen M. P., McCarthy I. G., 2011, MNRAS , 417, 2020

Sersic J. L., 1968, Atlas de galaxias australes

Shan H. Y., Qin B., Zhao H. S., 2010, MNRAS , 408, 1277

Shane C. D., Wirtanen C. A., Steinlin U., 1959, AJ , 64, 197

Skibba R. A., van den Bosch F. C., Yang X., More S., Mo H., Fontanot F., 2011, MNRAS , 410, 417

Soucail G., Mellier Y., Fort B., Mathez G., Cailloux M., 1988, A&A , 191, L19

Spergel D. et al., 2013, ArXiv e-prints

Spinelli P. F., Seitz S., Lerchster M., Brimioulle F., Finoguenov A., 2012, MNRAS , 420, 1384

Springel V., 2005, MNRAS , 364, 1105

Springel V. et al., 2008, MNRAS , 391, 1685

Sunyaev R. A., Zeldovich Y. B., 1970, Ap&SS , 7, 3

Taylor A. N., Kitching T. D., Bacon D. J., Heavens A. F., 2007, MNRAS , 374, 1377

Teague M. R., 1980, Journal of the Optical Society of America (1917-1983), 70, 920

Thacker R. J., Tittley E. R., Pearce F. R., Couchman H. M. P., Thomas P. A., 2000, MNRAS , 319, 619

The Fermi-LAT Collaboration et al., 2013, ArXiv e-prints

Tully R. B., Fisher J. R., 1977, A&A , 54, 661

Van Waerbeke L. et al., 2013, ArXiv e-prints

Van Waerbeke L. et al., 2000, A&A , 358, 30

Viel M., Lesgourgues J., Haehnelt M. G., Matarrese S., Riotto A., 2005, Phys. Rev. D , 71, 063534

Viola M., Melchior P., Bartelmann M., 2012, MNRAS , 419, 2215

Vogelsberger M., Zavala J., Loeb A., 2012, MNRAS , 423, 3740

von der Linden A. et al., 2012, ArXiv e-prints

von der Linden A. et al., 2014, ArXiv e-prints

Walsh D., Carswell R. F., Weymann R. J., 1979, Nature , 279, 381

Watson W. A., Iliev I. T., Diego J. M., Gottlöber S., Knebe A., Martínez-González E., Yepes G., 2013, ArXiv e-prints

Weinberg S., 1978, Physical Review Letters, 40, 223

Whalen D. J., Smidt J., Johnson J. L., Holz D. E., Stiavelli M., Fryer C. L., 2013, ArXiv e-prints

White S. D. M., 1976, MNRAS , 177, 717

White S. D. M., Frenk C. S., Davis M., 1983, ApJ , 274, L1

Williams L. L. R., Saha P., 2011, MNRAS , 415, 448

Wittman D., Tyson J. A., Margoniner V. E., Cohen J. G., Dell'Antonio I. P., 2001, ApJ , 557, L89

Wittman D. M., Tyson J. A., Kirkman D., Dell'Antonio I., Bernstein G., 2000, Nature , 405, 143

Wright C. O., Brainerd T. G., 2000, ApJ , 534, 34

Yoshida N., Springel V., White S. D. M., Tormen G., 2000, ApJ , 544, L87

Young O. E., Thomas P. A., Short C. J., Pearce F., 2011, MNRAS , 413, 691

Zhang Y.-Y., Finoguenov A., Böhringer H., Kneib J.-P., Smith G. P., Czoske O., Soucail G., 2007a, A&A , 467, 437

Zhang Y.-Y., Finoguenov A., Böhringer H., Kneib J.-P., Smith G. P., Czoske O., Soucail G., 2007b, A&A , 467, 437

Zhao H., Li B., Bienaymé O., 2010, Phys. Rev. D , 82, 103001

Zuntz J., Kacprzak T., Voigt L., Hirsch M., Rowe B., Bridle S., 2013, MNRAS , 434, 1604

Zwicky F., 1933, Helvetica Physica Acta, 6, 110

Publications

Dark matter astrometry: accuracy of subhalo positions for the measurement of self-interaction cross-sections., Harvey D., Massey R., Kitching T., Taylor A., Jullo E., Kneib J. P., Tittley E. and Marshall P., 2013,*MNRAS*, **433**, 151.

On the cross-section of dark matter using substructure infall into galaxy clusters. Harvey D., Tittley E., Massey R., Kitching T., Taylor A., Pike S.; Kay S., Lau E. and Nagai D., 2014,*MNRAS*, **441**, 404.

Observing Dark Worlds: A crowdsourcing experiment for dark matter mapping. Harvey D., Kitching T., Noah-Vanhoucke J., Hamner B., Salimans T. and Pires A., 2014, *Astronomy & Computing*, **5**, 35.

Astronomical Particle Colliders. Harvey D., Massey R., Kitching, T., Taylor, A. and Tittley, E., *Nature Submitted*

Origins of weak lensing systematics, and requirements on future instrumentation (or knowledge of instrumentation.) Massey, R., Hoekstra, H., Kitching, T., Rhodes, J., Cropper, M., Amiaux, J., Harvey, D., Mellier, Y., Meneghetti, M., Miller, L., Paulin-Henriksson, S., Pires, S., Scaramella, R., Schrabback, T., 2013, *MNRAS*, **429** 661